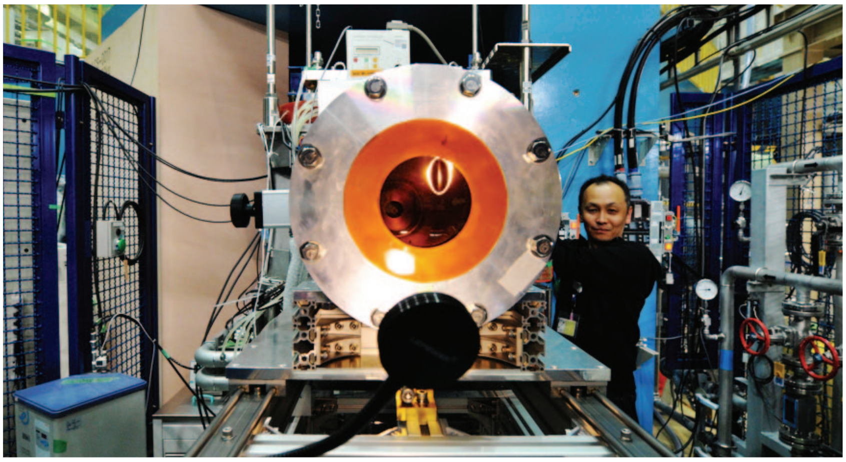

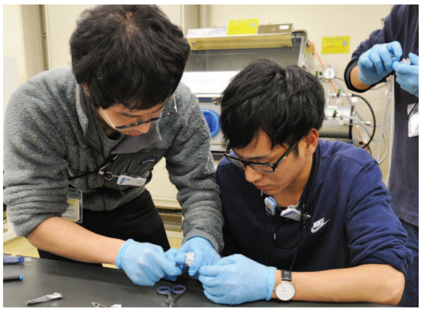

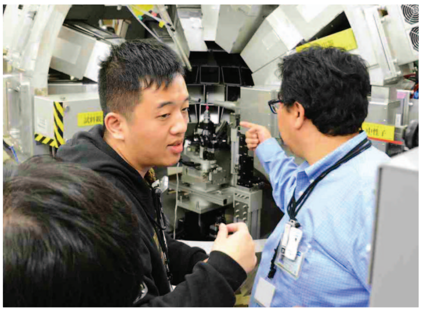

J-PARC

ANNUAL REPORT 2018

Vol.2: Materials and Life Science Experimental Facility

MLF ANNUAL REPORT

J-PARC MLF
Materials and Life Science Division
J-PARC Center
https://mlfinfo.jp/en

J-PARC was jointly constructed and is now operated by the High Energy Accelerator Research Organization (KEK) and the Japan Atomic Energy Agency (JAEA).

CROSS
Comprehensive Research Organization for Science and Society
https://neutron.cross.or.jp/en

J-PARC 19-02

Preface

Toshiji Kanaya
Division Head of Materials and Life Science Division, MLF

In fiscal year 2018, the operation of Materials and Life Science Experimental Facility (MLF) started with the neutron production mercury target (#8), which had helium bubbling system. On April 19, the proton beam power delivered to the target was increased from 400 kW to 500 kW and the operation continued very stably until July 2, 2018, followed by a 1-MW test operation for one hour on July 3. The beam availability of the target (#8) to the scheduled beam time was 92%. In the summer maintenance period, the target was replaced from #8 to #9. The neutron production started on October 22 and continued stably until March 26, 2019.

The muon rotating target system has been delivering a stable muon beam to users without troubles since 2014. However, the potential damage of a flexible joint for transferring motor rotation to the graphite disk target has been a cause for concern. Some measures were taken to minimize the potential hazards expected in case of suspended target rotation. By ensuring that those measures were effective, the muon user program was resumed in the beginning of November after two weeks delay behind the original schedule. The operation continued until March 26, 2019, without troubles.

Due to the stable operation of the facility, the MLF was able to produce many excellent outcomes in various research fields, such as hard matter, soft matter, energy materials, engineering materials, biomaterials and so on. In addition to the research outcomes, there were many activities in the MLF in 2018 to enhance the collaboration with international and domestic users in academia and various industries. The Annual Meeting of Industrial Application at J-PARC MLF was held on July 23 and 24 at Akihabara Convention Hall. The total number of attendees has increased to 303. The 3rd Neutron and Muon School was held from November 20 to 24. 35 young researchers and graduate students from China, India, Korea, Thailand, Russia, United Kingdom, as well as Japan participated in the school to enjoy the lectures and hands-on experiments. The 3rd ESS-J-PARC Workshop was held from November 13 to 15. 24 participants from ESS visited J-PARC to exchange information on a wide range of items. On the first day of the workshop, the Swedish Ambassador Magnus Robach delivered his greetings. The Quantum Beam Science Festa, which is a conference mainly for domestic users for MLF J-PARC and IMSS KEK, was held in Tsukuba (EPOCHAL TSUKUBA) on March 12 and 13 with about 580 participants. In this Festa, an MLF symposium was held on March 13 where the MLF facility status, scientific results and developments were reported.

In the annual report, the research highlights, technical developments and collaboration activities with users in 2018 are described in detail.

Materials and Life Science Division, Japan Proton Accelerator Research Complex
https://mlfinfo.jp/en

Preface

Hideaki Yokomizo
Director, CROSS

CROSS (Comprehensive Research Organization for Science and Society) has served as a registered institution of specific neutron beam Facilities of J-PARC appointed by the Government since 2011. We have been supporting the appropriate user program operation of the Public Beamlines at Materials and Life Science Experimental Facility (MLF). We have also been engaged in facility promotion activities, such as operating a fair and open proposal selection system for the MLF Public Beamlines, providing high-quality user support and promoting facility utilization for both academic and industrial researchers. As of 2018, CROSS has four science coordinators who counsel various kinds of users on the neutron sciences and encourage new users in utilizing the neutron beams as advanced and incomparable research tools.

CROSS supported the user programs at seven fully operational Public Beamlines: BL01 *4SEASONS*, BL02 *DNA*, BL11 *PLANET*, BL15 *TAIKAN*, BL17 *SHARAKU,* BL18 *SENJU and* BL22 *RADEN*. In 2018, the beam power was operated at 500 kW using the improved target vessel, which is equipped with pitting protection system. We accomplished a stable and highly reliable machine operation, which ensured 93% usage of the planned users' time.

The special program for New User Promotion (NUP) started in 2016 to provide sufficient guidance and assistance for scientists who are new to the neutron research. NUP has a preferential beam time allocation to first-time or novice users who need to learn how to use the neutron facility. NUP is expected to cultivate a new scientific field by conducting those users' first experiments successfully with the sufficient and generous support by our staffs. In the 2017B proposal round, a new program called Long-Term Proposal was started to select and approve the experimental plans that will be carried out in a period of three years. Complementary Use is a program that encourages and facilitates the complementary and collaborative use of pulsed neutrons (J-PARC MLF), synchrotron radiation (SPring-8), and the supercomputer (K computer).

I hope this Annual Report would serve as a useful information source for anyone wishing to know more about the current status of MLF, its recent scientific achievements, the technical R&D projects that support the science program, and the operational details of our facility.

On behalf of the CROSS, I extend a warm welcome to all researchers who wish to use the Public Beamlines at J-PARC MLF.

Neutron Science and Technology Center, Comprehensive Research Organization for Science and Society
https://neutron.cross.or.jp/en

Contents

Research and Development Highlights

Neutron Source

Neutron Science

Muon Science

MLF Safety

MLF Operations in 2018

Organization Chart

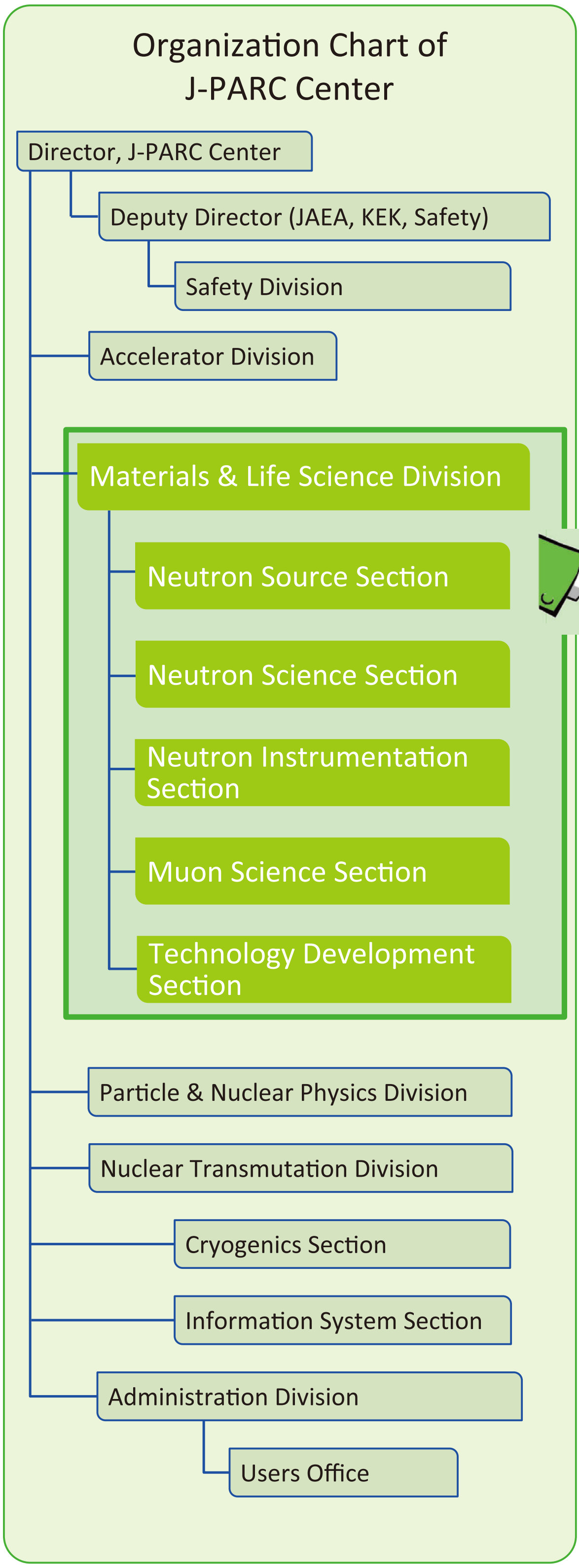

Organization Chart of J-PARC Center

- Director, J-PARC Center
  - Deputy Director (JAEA, KEK, Safety)
    - Safety Division
  - Accelerator Division
  - Materials & Life Science Division
    - Neutron Source Section
    - Neutron Science Section
    - Neutron Instrumentation Section
    - Muon Science Section
    - Technology Development Section
  - Particle & Nuclear Physics Division
  - Nuclear Transmutation Division
    - Cryogenics Section
    - Information System Section
  - Administration Division
    - Users Office

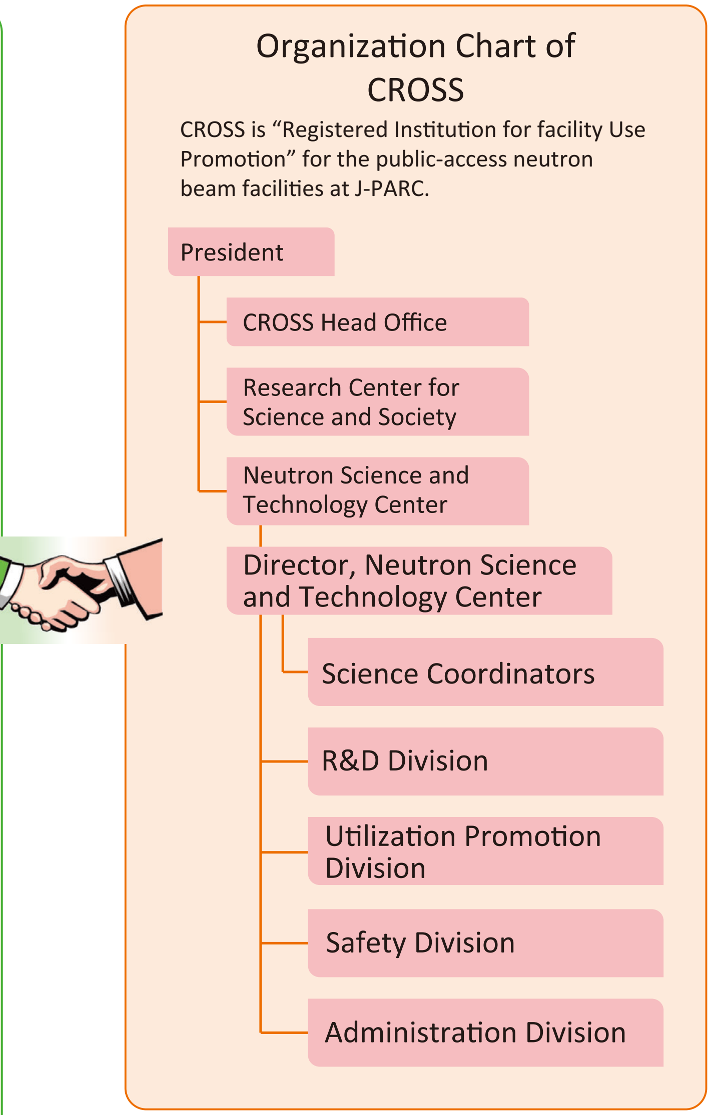

Organization Chart of CROSS

CROSS is "Registered Institution for facility Use Promotion" for the public-access neutron beam facilities at J-PARC.

- President
  - CROSS Head Office
  - Research Center for Science and Society
  - Neutron Science and Technology Center
    - Director, Neutron Science and Technology Center
      - Science Coordinators
      - R&D Division
      - Utilization Promotion Division
      - Safety Division
      - Administration Division

The Role of CROSS

Under the terms of the legislation that supports the Public Neutron Beam Facility, CROSS is entrusted with specific responsibilities. In practical terms, the core functions of CROSS can be summarized as follows:

- *Proposal Selection and Beamtime Allocation on the Public Beamlines*
- *User Support on the Public Beamlines*
- *Establishment of an Information Resource for Facility Users*
- *Outreach and Facility Utilization Promotion*
- *Contract Beamline Assessment and Selection*

J-PARC Map

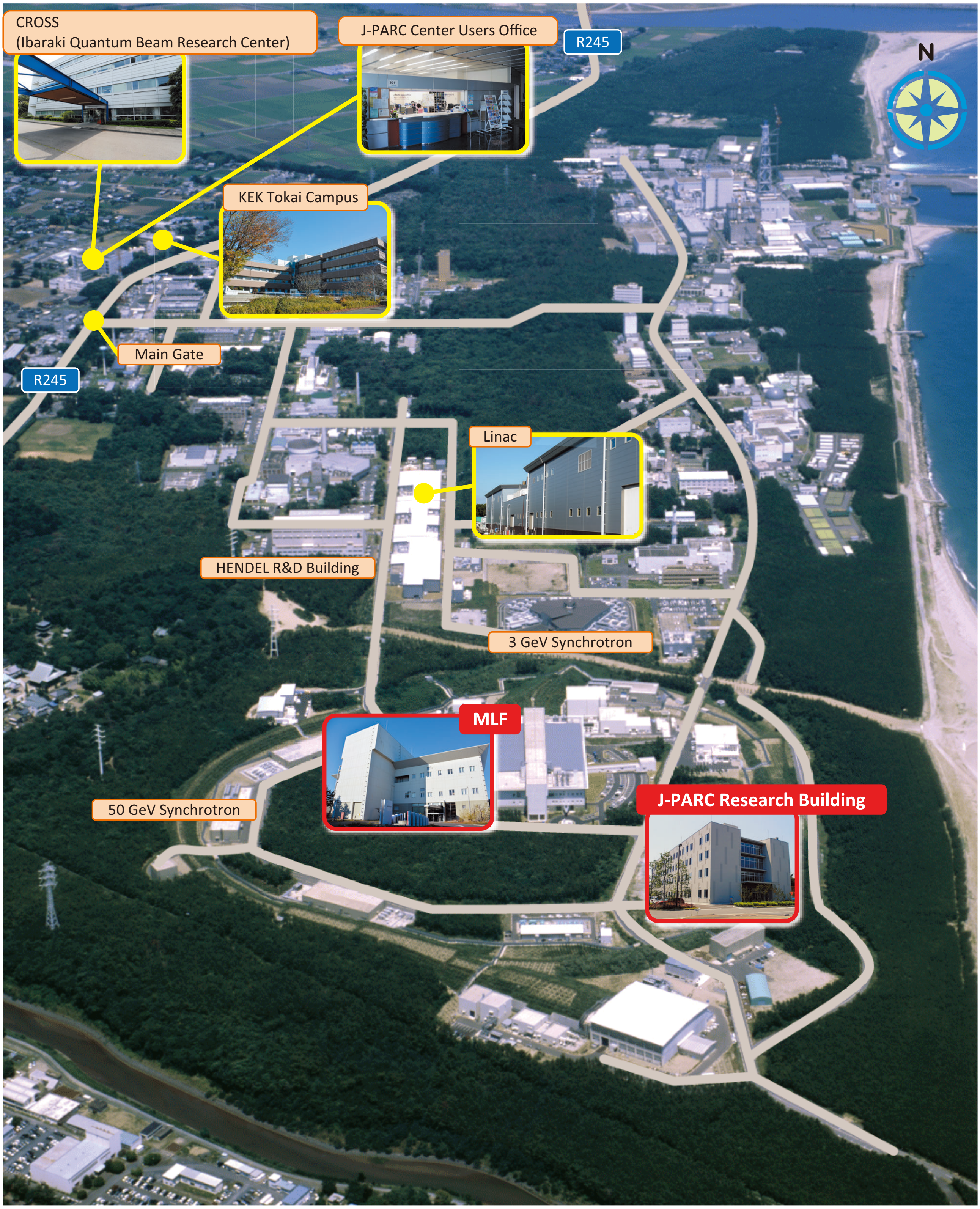
CROSS
(Ibaraki Quantum Beam Research Center)
J-PARC Center Users Office
R245
N
KEK Tokai Campus
Main Gate
R245
Linac
HENDEL R&D Building
3 GeV Synchrotron
MLF
50 GeV Synchrotron
J-PARC Research Building

Muon and Neutron Instruments

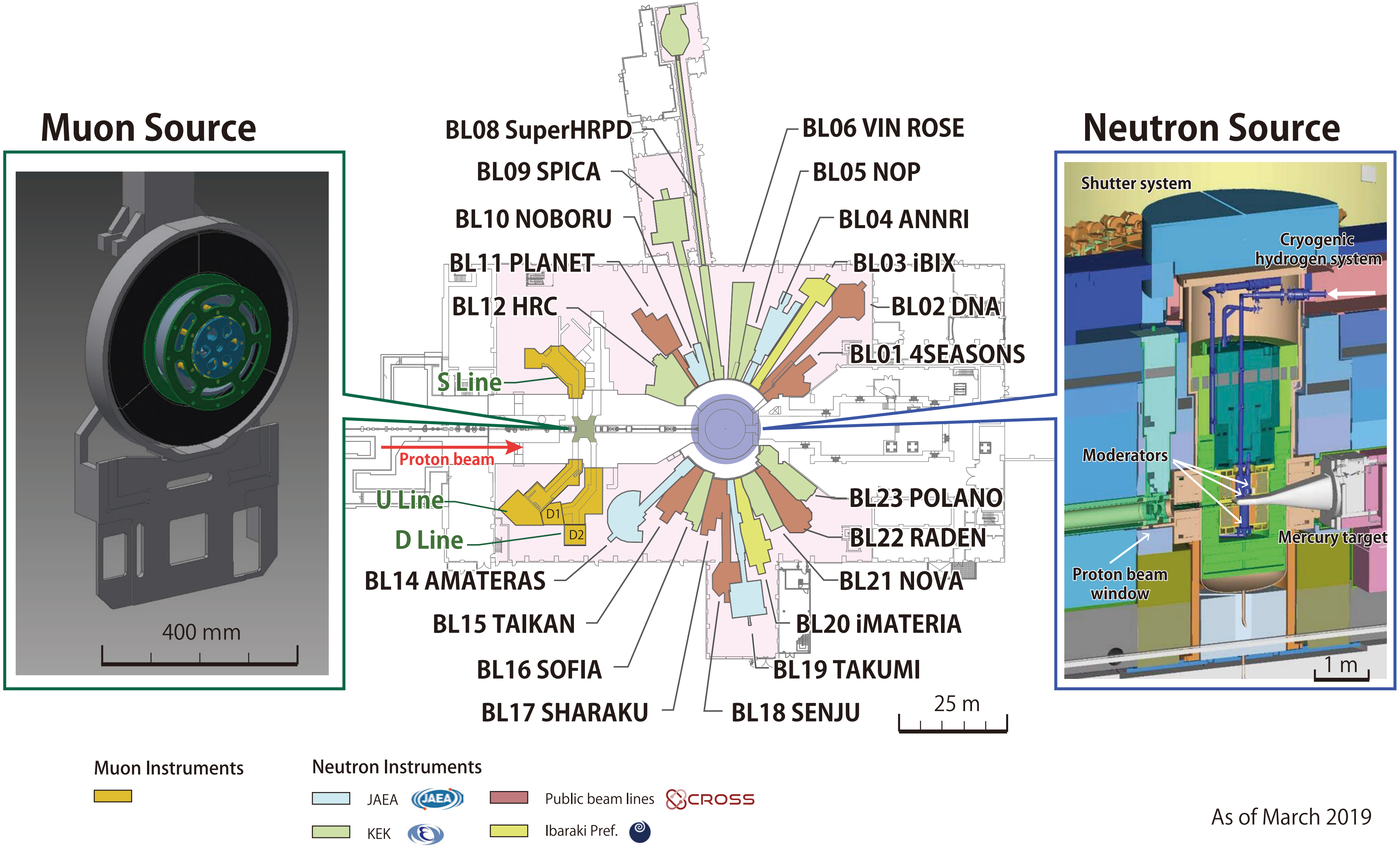

As of March 2019

Research and Development Highlights

Four-Dimensional Mapping of Dirac Magnons

1. Introduction

Following the remarkable discovery of topological insulators, exploration of topological band structures in crystalline materials has been a topical line of research in condensed matter physics. The notion of band topology lies in the mapping from momentum space, which follows from the lattice translational symmetry, to Hilbert space, which follows from the fact that band structures can be understood as solution to an eigen-value problem. Importantly, topological bands are not restricted to fermions as the constituent (quasi)particles. Since the existence and categorization of topological bands depend on symmetry and dimensionality, prediction and experimental discovery of topological bands of classical and bosonic excitations have been an active line of research in recent years – they offer more possibilities of symmetry that can be materialized realistically.

In 2017, we predicted [1] that there can be a (back then) new type of Dirac points in the band structure of magnons in three-dimensional antiferromagnets with *PT* and U(1) symmetry. The U(1) symmetry requires collinear magnetic structure, and the *PT* symmetry requires that the material has inversion symmetry which relates up-spin sub-lattice to down-spin sub-lattice. Importantly, the prediction can in principle apply to a large class of materials, and a specific example was recognized: Cu_3TeO_6. This is a material that can be grown into large single crystals and hence suitable for inelastic neutron scattering experiments for verifying the theoretical predictions. At J-PARC, we have successfully performed such experiments and confirmed the theory [2]. The experimental data were very clean and they proved that there are long-range spin interactions in the system, which suppress quantum fluctuations and facilitate the observation of highly harmonic magnon bands.

2. Technical Advantages

There are several advantages of using time-of-flight inelastic neutron scattering (ToF-INS) to determine band topology: (1) ToF-INS can reliably measure band structures with good momentum resolution in all three dimensions, in contrast to ARPES which has limited resolution perpendicular to the sample surface; (2) the scattering matrix elements are quantitatively known, therefore S(**Q**,w) can be used to verify the theoretically predicted wave functions which are the carrier of the non-trivial topology; (3) for materials with high crystallographic symmetry, cubic symmetry in particular, the 4-dimensional data set obtained by ToF-INS can be folded according to the symmetry, in which way the statistical accuracy can be greatly improved.

Our experiment was carried out on the high-flux thermal ToF-INS spectrometer BL-01 (4SEASONS) at the MLF. Figure 1 displays an overview of our

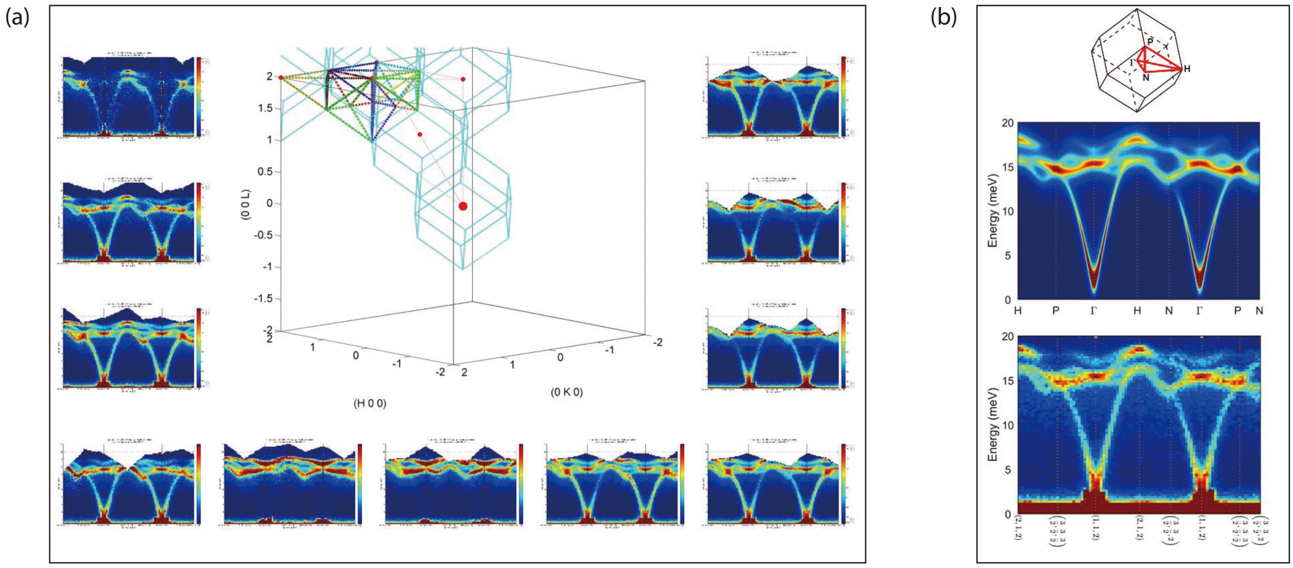

Figure 1. (a) Illustration of symmetry-allowed folding of Tof-INS data into the physically meaningful sector (indicated by red dotted lines), which contains many different Brillouin zone sectors. Intensity as functions of energy and momentum transfer along the high-symmetry lines (colored dotted lines) of the Brillouin zone sectors are displayed as contour plots in the insets that surround the main figure. (b) Comparison between theoretical calculation (middle panel) and experimental data (bottom panel) for a given Brillouin zone along high-symmetry lines, showing excellent agreement.

symmetry-folded data set that contained S(**Q**,w) information for many different Brillouin zone sectors. As the dispersion relationship has to be identical in all these sectors but the intensity can vary, these data can be used to over-determine the theoretical model's interaction parameters. The outcome of the global fitting is extremely satisfactory, and we are able to reproduce the experimentally observed S(**Q**,w) to a high level of accuracy (Fig. 1(b)).

3. Visualization of a Topological Dirac Point

After the theoretical model was successfully fitted using the highly accurate 4D experimental data set, we used the model to precisely predict favorable locations for observing the topological magnon Dirac points. One of such points was predicted to be P(1.5, 0.5, 1.5) near 17.8 meV (Fig. 2), and indeed, by sufficiently utilizing the statistical accuracy of the data allowed (again) by symmetry-related folding, we were able to obtain a sub-resolution visualization of the magnon Dirac point in constant-*E* slices that were separated by only 0.2 meV (compared to FWHM energy resolution of about 0.58 meV). The dispersion near the Dirac point is evident from these data.

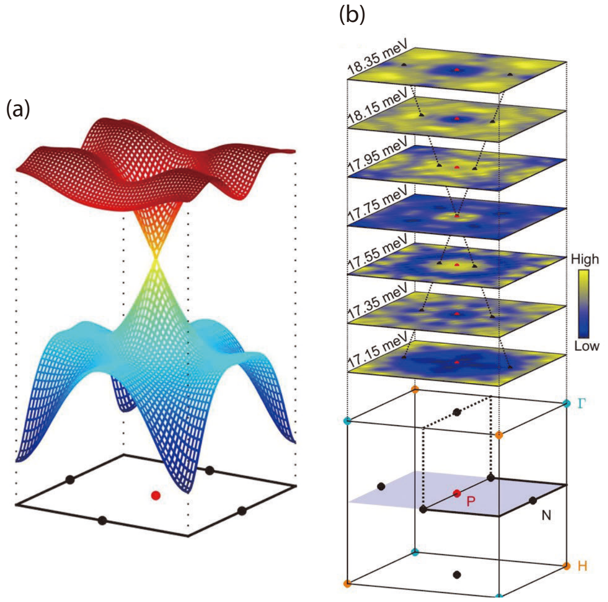

Figure 2. (a) Theoretical calculation of magnon dispersion near a Dirac point at the Brillouin zone P-point at about 17.8 meV. (b) Experimental intensity profiles generated by symmetrizing ToF-INS data at P(1.5, 0.5, 1.5) and plotting them in constant-*E* slices.

4. Future Plans

For the Cu_3TeO_6 system, we estimate that what we have successfully observed is essentially what can be resolved by today's state-of-the-art instrumentation. Generally speaking, the INS technique can be further used to visualize topological bosonic excitations' wave-function structure, *e.g.*, by using spin-polarized neutrons to measure magnons. In addition, it remains a technical challenge to measure the topological magnon surface states, as well as to observe topological magnons' transport properties such as topological thermal Hall effects. We have on-going collaborations for these purposes involving the use of our high-quality Cu_3TeO_6 single crystals.

References

[1] K. Li *et al.*, *Phys. Rev. Lett.* **119**, 247202 (2017).
[2] W. Yao *et al.*, *Nat. Phys.* **14**, 1011 (2018).

Yuan Li[1], Weiliang Yao[1], Kazuki Iida[2], and Kazuya Kamazawa[2]
[1]*International Center for Quantum Materials, Peking University, China;* [2]*Neutron Science and Technology Center, CROSS*

Diffusion Behavior of Methanol Molecules Confined in Cross-Linked Phenolic Resins Studied Using Neutron Scattering and Molecular Dynamics Simulations

1. Introduction

Phenolic resin is a thermosetting polymer widely used in many industrial applications, such as automobiles, semiconductors, and aerospace equipment. Its excellent properties, such as strong mechanical properties, thermal stability, electric resistance, and solvent resistance, are due to the dense chemically bonded network structure [1]. These applications, especially automotive parts and semiconductor packages, require high solvent resistance because they may be exposed to various solvents under prolonged conditions of high temperature and pressure. Solvent penetration into the cured thermosetting resins causes many problems, including dimensional changes, decreases in mechanical strength and modulus leading to solvent stress cracking, and short-circuiting. In designing thermosetting materials, it is necessary to understand the relationships between a cross-linked structure and solvent resistance from the perspective of atomistic structure. Elucidation of the diffusion mechanism of small molecules, such as water, methanol, or ethanol, in cured resins is of special importance for achieving high solvent resistance [2]. In this study, we investigated the diffusion dynamics of methanol confined in highly cross-linked phenolic resins using quasi-elastic neutron scattering (QENS) and atomistic molecular dynamics (MD) simulations.

2. Experimental

We prepared highly deuterated cross-linked phenolic resins via two processes: synthesis of deuterated novolac resin from phenol-d_6 and formaldehyde-d_2 under acidic condition, and subsequent crosslink reaction using hexamethylenetetramine (HMTA) as a curing agent [3]. After molding, cured phenolic resin (dNVH) and solvent (CH_3OH or CD_3OD) were sealed in a pressure vessel and allowed to stand for 72 hours in an 80°C oven. Then, the sample was dried in the air and pulverized with a mill for QENS measurement. The amount of penetrant methanol in the sample was estimated to be about 8 wt% from the weight change measurement value after heating in a vacuum oven. From the composition of dNVH and methanol in dNVH–CH_3OH, the ratio of incoherent scattering cross-sections (σ_{inc}) is estimated to be σ_{inc} (H_{dNVH}) : σ_{inc} (D_{dNVH}) : σ_{inc} (H_{CH3OH}) = 6.9 : 1 : 11.1. This suggests that sufficient incoherent scattering intensity from the CH_3OH in the dNVH–CH_3OH can be obtained by the QENS measurement for dNVH–CH_3OH.

QENS experiments were performed using the time-of-flight near-backscattering spectrometer installed at J-PARC/MLF BL02 DNA [4]. Powder samples were lapped with thin aluminum foil and loaded in a cylindrical aluminum sample holder. The dynamic scattering functions $S(Q, \omega)$ were measured at 296 K, in a momentum transfer range $0.1 < Q < 1.8$ Å^{-1}. The energy window and resolution were -40 μeV $\leq \hbar\omega \leq 100$ μeV and $\Delta E = 3.6$ μeV, respectively. The QENS data reduction and analyses were performed using software provided by the DNA group of J-PARC/MLF.

3. Results and Discussion

Figure 1 shows the measured QENS profiles of dNVH–CH_3OH, dNVH–CD_3OD, and dried dNVH normalized by the elastic intensity at Q = 1.7 Å^{-1}. The difference in scattering intensity between dNVH–CH_3OH and dNVH–CD_3OD indicates the existence of quasi-elastic broadening from methanol. Furthermore, the intensity in dNVH–CD_3OD, larger than that of dried dNVH in the quasielastic region, implies the induction of resin dynamics derived from solvent invasion. Accordingly, the QENS profile of dNVH–CH_3OH is represented by the sum of methanol and dNVH components as follows:

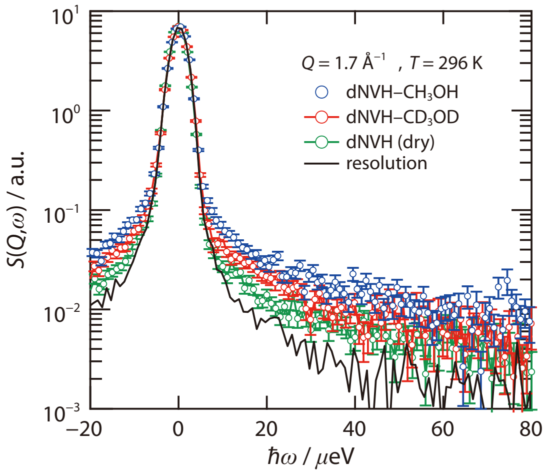

Figure 1. Typical QENS spectra for dNVH–CH_3OH, dNVH–CD_3OD, and dried dNVH at Q = 1.7 Å^{-1}. The spectra are normalized by the elastic intensity.

$$S(Q, \omega) = [A^{\mathrm{M}}_{\mathrm{el}}(Q)\delta(\omega) + A^{\mathrm{M}}_{\mathrm{qe}}(q)L^{\mathrm{M}}(Q, \omega) + A^{\mathrm{R}}_{\mathrm{el}}(Q)\delta(\omega) + A^{\mathrm{R}}_{\mathrm{qe}}(q)L^{\mathrm{R}}(Q, \omega)] \otimes R(Q, \omega) + \mathrm{bkg.},$$

where $R(Q, \omega)$, $\delta(\omega)$, and $L(Q, \omega)$ are the resolution function of the DNA spectrometer, the delta function, and the Lorentz function, respectively, and bkg. denotes the background. A_{el}, and A_{qe} denote the coefficients of each scattering component for elastic and quasielastic scatterings, and superscripts M and R indicate methanol and cured resin (dNVH), respectively.

Figure 2 shows the Q^2-dependence of Γ, where Γ indicates the HWHM in the Lorentz function of methanol. The Q-dependency of Γ for methanol in cured resin closely followed a fitting curve of the random-jump diffusion model, $\Gamma = DQ^2 / (1 + \tau_0 DQ^2)$, though the continuous diffusion model, $\Gamma = DQ^2$, did not match in the high-Q range. Here D is the translational diffusion coefficient. The fitting results in $D = 1.6 \times 10^{-6}$ cm^2/s for methanol confined in cured resin, which is one order of magnitude smaller than the value in the bulk, $D = 2.3 \times 10^{-5}$ cm^2/s.

Full atomistic MD simulations were carried out on the methanol dispersed cross-linked phenolic resin model systems. The details of the MD simulation were described in references [4–6]. Figure 3 shows a 3D image of methanol dispersed in a cross-linked phenolic resin. Methanol molecules in the resin network reside in void spaces near hydroxyl groups of phenolic units form hydrogen bonds to the phenolic hydroxyl group or other methanol molecule.

Figure 4 shows the trajectory lines of 20 randomly chosen methanol molecules in 2 ns acquired every 10 ps. These molecular trajectories in the MD simulation clearly indicate that some methanol molecules diffuse by moving a small distance in a limited space, although most methanol molecules are not moving. Such a leaping movement corresponds well to the jump-diffusion model, as suggested from the QENS results. Furthermore, the diffusion coefficient D of diffusive methanol was estimated from the time dependence of the mean squared displacement using Einstein's relation. The estimated D for diffusive molecules is 1.63

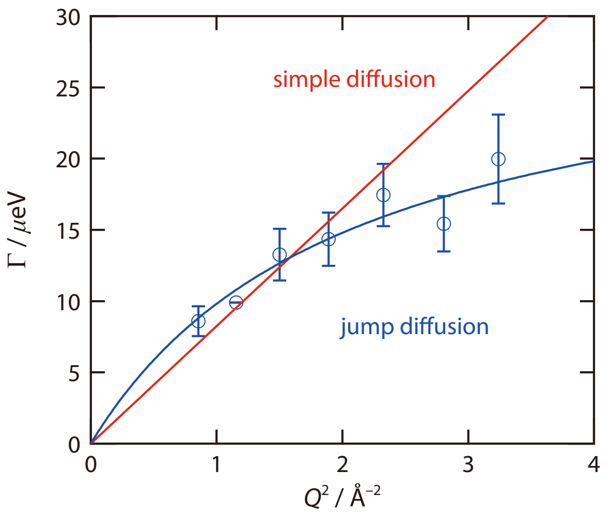

Figure 2. Q^2-dependence of Γ of CH_3OH for dNVH–CH_3OH obtained from QENS fitting at T = 296 K. The red and blue lines are fitting results by the simple-diffusion and jump-diffusion models, respectively.

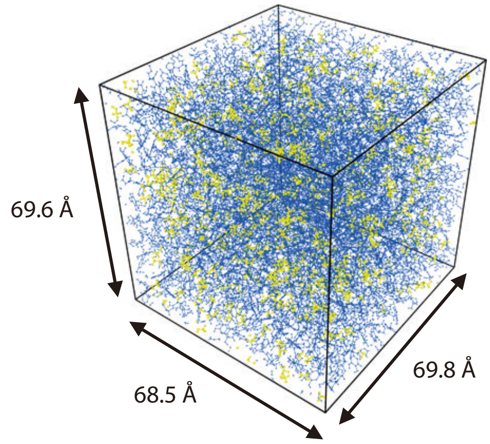

Figure 3. 3D model of methanol molecules (yellow), confined in cured phenolic resins (blue), used in the MD simulation.

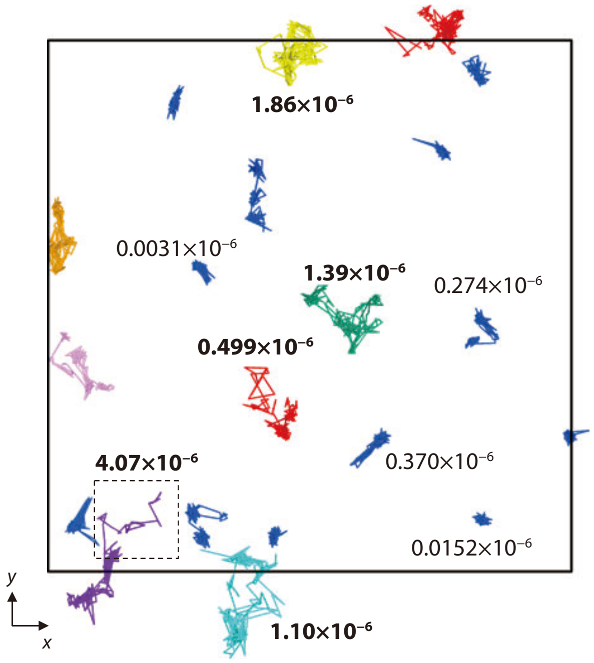

Figure 4. Representative trajectory lines of methanol molecules in 2 ns acquired every 10 ps. The values shown close to the particles indicate D (cm^2/s). Lines of non-diffusive methanol are shown in blue, and lines of diffusive methanol are displayed with different colors.

× 10^{-6} cm^2/s, which is well consistent with the QENS experiments, i.e., $D = 1.6 \times 10^{-6}$ cm^2/s. This agreement suggests that our constructed MD model is very reasonable and the existence of confined dynamics for methanol is highly probable.

Acknowledgements

The QENS experiments were executed using the BL02 (DNA) beamline at the Materials and Life Science Experimental Facility (MLF) of J-PARC under Proposal No. 2015A0077 and 2016A0177. This research used computational resources of the K computer provided by the RIKEN Advanced Institute for Computational Science through the HPCI System Research project (Project ID: hp160089).

References

[1] J.-P. Pascault, H. Sautereau, J. Verdu, R. J. J. Williams, Thermosetting Polymers; Marcel Dekker: New York, 2002.
[2] M. L. Kaplan, Polym. Eng. Sci., **31**, 689 (1991).
[3] A. Izumi, T. Nakao, and M. Shibayama, J. Polym. Sci. A., **49**, 4941 (2011).
[4] Y. Shudo, A. Izumi, K. Hagita, T. Yamada, K. Shibata and M. Shibayama, Macromolecules, **51**, 6334 (2018).
[5] Y. Shudo, A. Izumi, K. Hagita, T. Nakao, and M. Shibayama, Polymer, **103**, 261 (2016).
[6] Y. Shudo, A. Izumi, K. Hagita, T. Nakao, and M. Shibayama, Polymer, **116**, 606 (2017).

Y. Shudo[1], A. Izumi[1], K. Hagita[2], T. Yamada[3], K. Shibata[4], and M. Shibayama[5]

[1]Corporate Engineering Center, Sumitomo Bakelite, Co., Ltd.; [2]Department of Applied Physics, National Defense Academy of Japan; [3]Neutron Science and Technology Center, CROSS; [4]Neutron Science Section, Materials and Life Science Division, J-PARC Center; [5]Neutron Science Laboratory, Institute for Solid State Physics, The University of Tokyo

Angular Distribution of γ Rays from Neutron-Induced Compound States of ^{140}La

1. Introduction

Very large parity violations with a maximum size of 10^{-1} have been observed in several compound nuclei formed after neutron capture by several nuclides such as ^{139}La, ^{131}Xe, ^{117}Sn, and ^{81}Br [1]. It is theoretically understood that the tiny parity violation with the size of 10^{-7} caused by the weak interaction is enhanced by up to 10^6 with the interference between s- and p-wave amplitudes. This hypothesis is referred to as s-p mixing. The parity violation in the compound nuclei is described with the weak matrix element W and a ratio of the partial neutron width of the p-wave resonance x. Additionally, an enhancement of the time reversal (T) violation in the compound nucleus can also be calculated using x. A T-violating cross section $\Delta\sigma_T$ in the compound nucleus is described as [2]

$$\Delta\sigma_T = \kappa(x)\frac{W_T}{W}\Delta\sigma_P\,,$$

where $\Delta\sigma_P$ is the P-violating cross section in the compound nucleus, W_T is the T-violating matrix element, and $\kappa(x)$ is the spin factor, corresponding to a conversion constant from the P-violating cross section to the T-violating cross section. Since the T-violation can be a key to reveal the origin of our matter-dominant universe under the assumption of CPT theorem [3, 4], $\kappa(x)$ is an important parameter to evaluate the potential to search for a new physics.

Therefore, x and W are essential parameters for the study of the discrete symmetry violation in the compound nuclei. The product of W and x has been measured in several nuclei, however, the individual values of x and W have not yet been determined. The value of x can be extracted from the neutron energy dependence of the angular distribution of the γ-rays from the p-wave resonance of the compound nucleus [5]. We conducted an experiment to measure the angular distributions of the γ-rays from the 0.74 eV p-wave resonance of the ^{139}La, where an extremely large parity violation with the size of the $(9.56 \pm 0.35)\%$ was observed [6].

2. Experiment and result

The experiment was performed using a germanium detector assembly in BL04, ANNRI. The Germanium detector assembly consists of 22 individual germanium crystals, whose angles are 36°, 71°, 72°, 90°, 108°, 109°, and 144° with respect to the direction of the incident neutron momentum. A $^{\mathrm{nat}}$La plate with the dimensions of $40 \times 40 \times 1$ mm was used as a sample. The measurement time was 60 h, and the average beam power was 150 kW during the experiment. We investigated the angular distribution of γ-rays with the energy of 5161 keV, which is the Q value of the ^{139}La+n state. Figure 1 shows the neutron spectra in the vicinity of the 0.74 eV p-wave resonance gated with the full absorption peak of 5161 keV γ-rays. We can see that the shape of the p-wave resonance is distorted according to the detector angle. Note that the neutron spectrum was divided by the incident neutron spectrum measured using a ^{10}B sample and the background caused by the Compton scattering from the high energy γ-rays was subtracted. The detection efficiencies of each detector were corrected by constructing a GEANT 4 simulation [7].

3. Analysis

In order to quantify the distortion of the peak, we defined the asymmetry of the p-wave resonance with respect to the peak energy A_{LH} as

$$A_{\mathrm{LH}} = \frac{N_L - N_H}{N_L + N_H}\,,$$

where N_L and N_H are the integral values of the neutron spectrum in the region of low energy (0.66–0.74 eV) and high energy (0.74–0.82 eV), respectively. The angular distribution of the A_{LH} is shown in Fig. 2. We found the clear angular dependence in the γ-rays from the 0.75 eV p-wave resonance to the ground state of ^{140}La as shown in Fig. 2.

The angular distribution of A_{LH} was analyzed by comparing it to a theoretical calculation based on the s-p mixing model. Finally, the values of x and W were obtained as

$$x = -0.16^{+0.09}_{-0.11},\ -0.95^{+0.04}_{-0.03},$$

$$W = (13.2^{+18.1}_{-5.3})\mathrm{meV},\ (2.21^{+0.10}_{-0.06})\mathrm{meV}.$$

The value of $\kappa(x)$ was also determined using the value of x as

$$\kappa(x) = 4.84^{+5.58}_{-1.69},\ 0.99^{+0.08}_{-0.07}.$$

The fact that $\kappa(x)$ is the order of 1 implies that the T-violation is also enhanced by an order of 10^6 as the P-violation in the compound state of ^{140}La. This result shows that ^{139}La would be a strong candidate for the T-violation search experiment.

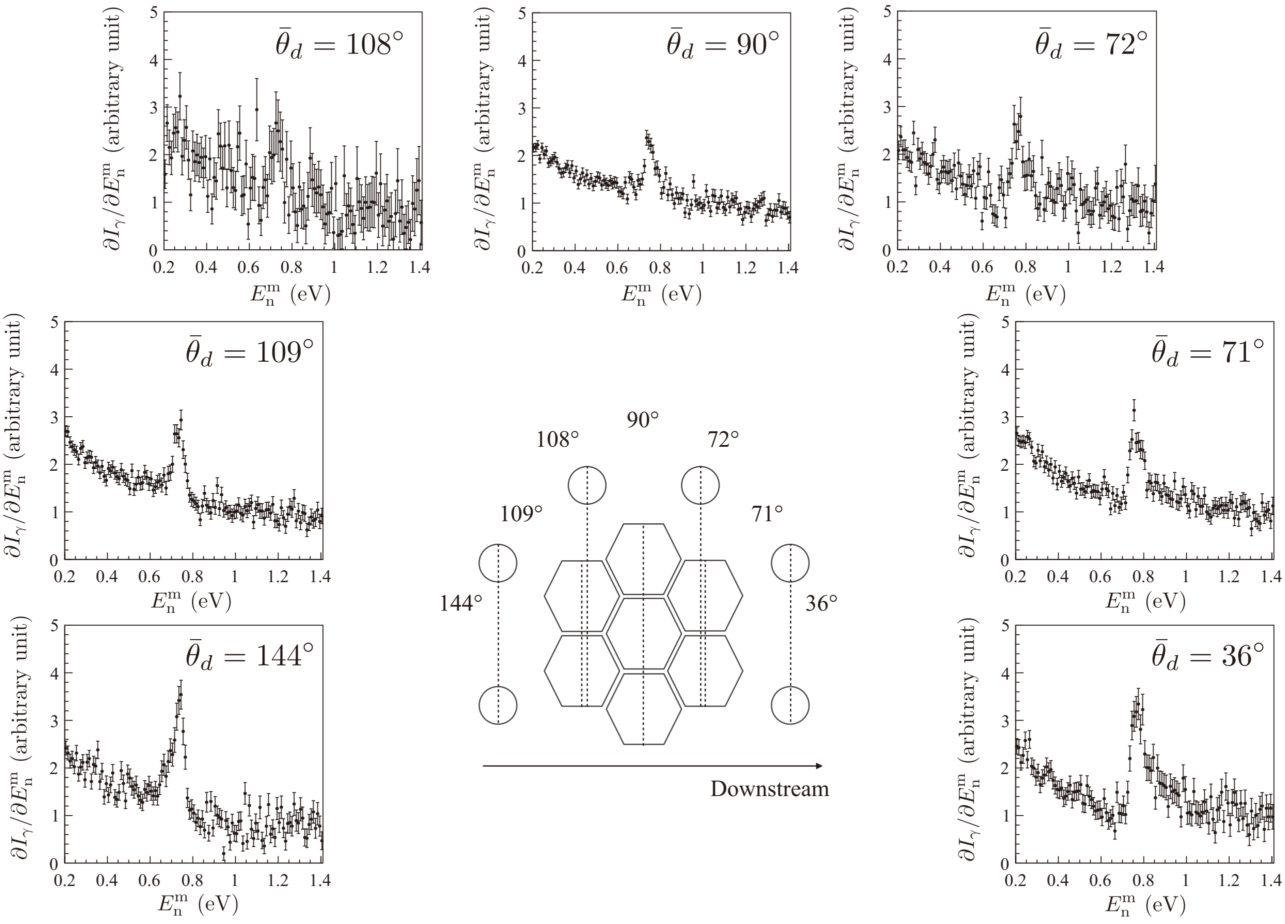

Figure 1. The neutron energy spectra in the vicinity of the 0.74 eV p-wave resonance for each detector angle. The central figure denotes each crystal of the detectors and its degrees. The valuable of $I_\gamma$in the vertical axis corresponds to the number of detected γ-rays.

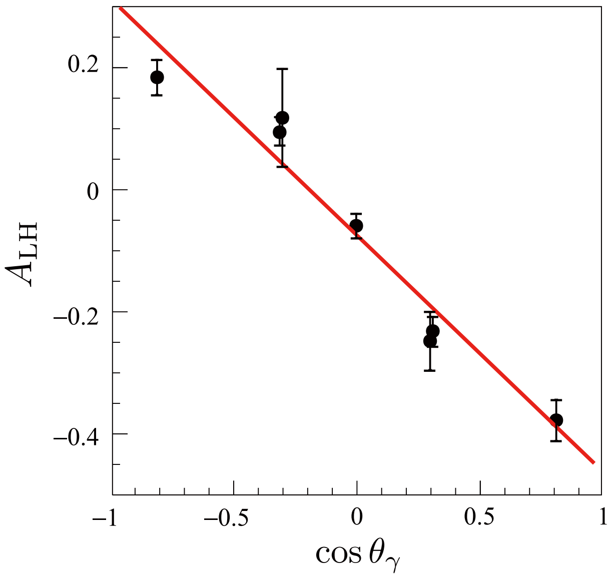

Figure 2. Angular dependence of A_{LH}. The sold line shows the best fit with a linear function.

4. Future plans

We limited *x* to the two values by conducting the measurement using the unpolarized neutrons. However, a measurement of the angular distribution of the γ-rays using polarized neutrons is necessary to finally determine the value of x. We have already complete the experiment using a ^{3}He spin filter in ANNRI [8], and the analysis is currently ongoing. Additionally, measurements of the angular distribution of the γ-rays with other nuclides such as ^{117}Sn [9], ^{81}Br, ^{131}Xe, ^{111}Cd, ^{113}In, and ^{127}I, which have enhanced P-violations, also are under way.

Our final goal is to search for an unknown T-violating effect in the compound nuclei. Several developments such as a polarized La target, the neutron polarizer, and a neutron detector [10] also are starting for the T-violation search experiment.

References

[1] G.E.Mitchell et al., Phys. Rep. **354**, 157 (2001).
[2] V. P. Gudkov, Phys. Rep. **212**, 77 (1992).
[3] A. D. Sakharov. JETP Lett., **5**, 24, (1967).
[4] J. Schwinger. Phys. Rev., **91**. 713, (1953).
[5] V. V. Flambaum et al., Nucl. Phys. A **435**, 352–380 (1985).
[6] V. P. Alfimenkov et al., Nucl. Phys. A **398**, 93 (1983).
[7] S. Takada et al., Journal of Instrumentation **13**, P02018 (2018).
[8] T. Yamamoto et al., JPS Conf. Proc. **22**, 011018 (2018).
[9] J. Koga et al., JPS Conf. Proc. **22**, 011035 (2018).
[10] S. Endo et al., JPS Conf. Proc. **22**, 011021 (2018).

T. Okudaira[1], S. Takada[2], K. Hirota[3], A. Kimura[4], M. Kitaguchi[3], J. Koga[2], K. Nagamoto[3], T. Nakao[4], A. Okada[3], K. Sakai[5], H. M. Shimizu[3], T. Yamamoto[3], and T. Yoshioka[2]

[1]*Technology Development Section, Materials and Life Science Division, J-PARC Center;* [2]*Kyushu University;* [3]*Nagoya University;* [4]*Nuclear Data Center, Nuclear Science and Engineering Center, JAEA;* [5]*Neutron Source Section, Materials and Life Science Division, J-PARC Center*

Synthesis, Structure and Magnetic Properties of $La_{0.5}Ba_{0.5}CoO_{2.75+x}$

1. Introduction

The cobaltite perovskites exhibit many unusual properties such as spin-state transition, metal–insulator transition, large magnetoresistance, negative thermal expansion and so on [1–4]. The coupling between the lattice, charge, orbital, and spin degrees of freedom is found to play an essential role. For example, $LaCoO_3$ with the Co valence being 3+, exhibits the spin-state transition upon heating, from the low-spin (LS) state (t_{2g}^6, $S = 0$) to the high-spin (HS) state ($t_{2g}^4 e_g^2$, $S = 2$) via the intermediate-spin (IS) state ($t_{2g}^5 e_g^1$, $S = 1$) [1, 5].

The hole-doping effect to $LaCoO_3$ has been researched extensively through substitution of divalent ion A (A = Ca, Sr, Ba) for La [6]. It is well established that the LS nonmagnetic ground state of $LaCoO_3$ undergoes a transition to IS or HS ferromagnetic (FM) state in $La_{1-x}A_xCoO_3$ [7]. Also, a large magnetoresistance effect was reported in $La_{1-x}A_xCoO_3$ [3].

However, hole doping to Co^{3+} ion can also be introduced by changing the oxygen content, which has not been widely exploited. For example, the nominal valence of Co ion in $La_{0.5}A_{0.5}CoO_{2.75}$ is 3+, and holes can be filled to the band by increasing the oxygen content. In a previous report [8–11], the A-site disordered $La_{0.5}Ba_{0.5}CoO_{2.75+x}$ ($x = 0.25$), shows FM transition at Curie temperature (T_C) 190 K. As the doping decreases to $x = 0.12$, the antiferromagnetic (AFM) correlation develops while the FM state survives at base temperature. When the oxygen content is further lowered to an electron doping side ($x = -0.15$), it shows pure AFM state with the Neel temperature (T_N) above room temperature.

Since the properties of cobaltite perovskites are very sensitive to external stimulus (temperature, pressure, etc.) or chemical compositions (rare-earth element, oxygen content *etc.*), we synthesized the sample $La_{0.5}Ba_{0.5}CoO_{2.75+x}$ with lighter hole doping level ($x = 0.08$ and $x = 0.16$) and characterized their magnetic properties. We found that sample $x = 0.08$ shows a magnetic behavior similar to the one of sample $x = 0.05$, but when compared with sample $x = 0.12$, a slight increase of the doping to $x = 0.16$ leads to the change from two phases with long range AFM and FM ordering to only one phase with long range FM ordering.

2. Experiment method

The samples of $La_{0.5}Ba_{0.5}CoO_{2.75+x}$ were synthesized by standard solid-state reaction. The raw materials La_2O_3, $BaCO_3$ and CoO were ground, pressed into a pellet and heated at 1200°C in air for 12 h. After grinding and heating were repeated 3 times, we could obtain the pure A-site disordered $La_{0.5}Ba_{0.5}CoO_{2.75+x}$ ($x = 0.16$). The sample $x = 0.08$ was obtained by annealing the attained sample under Ar flowing at 250°C for 12h. The oxygen content was determined by analysis of the neutron powder diffraction (NPD) pattern.

The high-resolution NPD measurement was performed by the Super High Resolution Powder Diffractometer (SuperHRPD) at MLF, J-PARC. The neutron diffraction patterns were analyzed by the Rietveld refinement method using both Z-Rietveld [12] and FULLPROF [13], and the representation analysis was utilized by SARAh [14]. The magnetization under field cooled (FC) and zero-field cooled (ZFC) was investigated by using superconducting quantum interference device (SQUID) magnetometer (MPMS) at the Cross-Tokai user laboratories.

3. Results and discussion

Figure 1 shows the temperature dependence of magnetization for $x = 0.08$ and $x = 0.16$ under 100 Oe. The FC magnetization [see Fig. 1(b)] of $x = 0.16$ exhibits a ferromagnetic transition at about 160 K. For sample $x = 0.08$, below 130 K the decrease of FC magnetization upon cooling indicates the AFM state at low temperature. However, the divergence between the magnetization of ZFC and FC in Fig. 1(a) and the hysteresis loop of the M/H curve [see the inset] at 13 K suggest that FM correlation also exists at low temperature. From the viewpoint of the phase diagram, $x = 0.08$ is located near the phase boundary of AFM and FM, therefore it is natural to see the coexistence of AFM and FM state, which comes from the electronic origin. Since it is in the vicinity of the boundary, the energy of the AFM and FM states is very close.

As shown in Fig. 2, the superlattice reflections (1/2 1/2 1/2) initiated at $T_N = 210$ K signify the AF ordering with propagation vector $\boldsymbol{k}_{AFM} = (1/2, 1/2, 1/2)$, while the increase in intensity of the reflection (100) initiated from $T_C = 160$ K upon cooling, indicates the ferromagnetic ordering with propagation vector $\boldsymbol{k}_{FM} = (0, 0, 0)$.

The pattern of sample $x = 0.08$ can be fitted well by the $Pm\bar{3}m$ cubic structure with the G-type AFM structure,

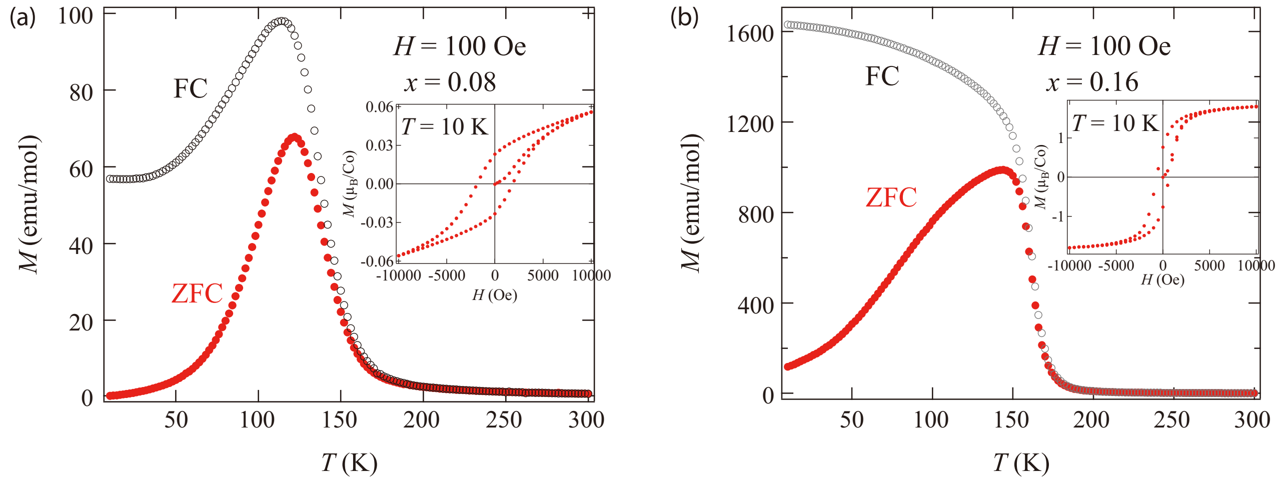

Figure 1. Temperature dependence of magnetization for $La_{0.5}Ba_{0.5}CoO_{2.75+x}$ (a) $x = 0.08$ and (b) $x = 0.16$.under 100 Oe in the ZFC and FC processes. The inset shows the M/H curve at 10 K.

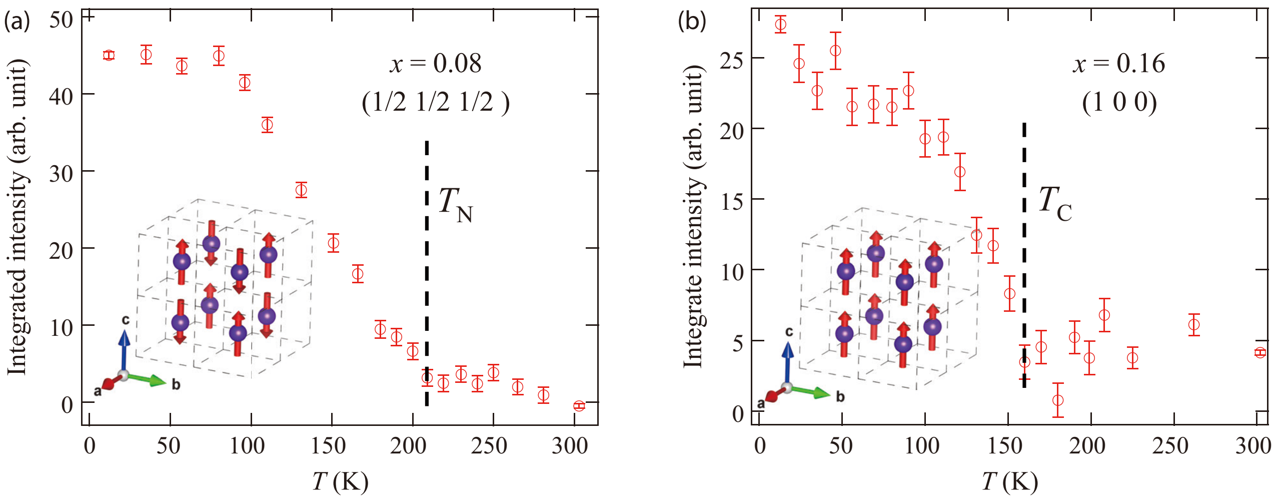

Figure 2. The temperature dependence of integrated intensity of (a) AFM reflection (1/2 1/2 1/2) for $La_{0.5}Ba_{0.5}CoO_{2.75+x}$ ($x = 0.08$) and (b) the FM reflection (1 0 0) for $La_{0.5}Ba_{0.5}CoO_{2.75+x}$ ($x = 0.16$). The inset of (a) and (b) shows the G-types AFM and FM structure, respectively. For clarity, only Co is displayed.

as shown in Fig. 3(a). In the G-type AFM structure, every Co ion aligns antiparallelly with the nearest Co neighbors, as shown in the inset of Fig. 2(a). As mentioned above, the magnetization of the $x = 0.08$ sample suggests the existence of FM correlation. Throughout the temperature range, we did not observe any ferromagnetic reflection in the NPD pattern, indicating that there is no long-range FM ordering. Therefore, we think that the FM correlation occurs in forms of short-range ordering together with a long-range AFM ordering at low temperature for sample $x = 0.08$.

Similarly, the simple FM structure found for $x = 0.16$ is depicted in the inset of Fig. 2(b) and the fitted pattern is shown in Fig. 3(b). In the NPD pattern of $La_{0.5}Ba_{0.5}CoO_{2.75+x}$ ($x = 0.16$) at low temperature we could not observe reflections (1/2 1/2 1/2) and (3/2 1/2 1/2). So, there is no long-range ordered AFM state at low temperature in this sample. It has been reported that FM state and small AFM clusters coexist in ground state in $La_{0.5}Ba_{0.5}CoO_{2.75+x}$ ($x = 0.25$) [15]. In the case of $x = 0.16$, a short-range ordered AFM state, which cannot be detected by NPD, may coexist with the long-range ordered FM state at low temperature as well. In order to clarify whether there is short-range ordered AFM state at low temperature, further experiments are needed, such as the muon-spin-relaxation experiment.

4. Conclusion

We synthesized the A-site disordered $La_{0.5}Ba_{0.5}CoO_{2.75+x}$ ($x = 0.08$ and 0.16) and investigated the crystal and

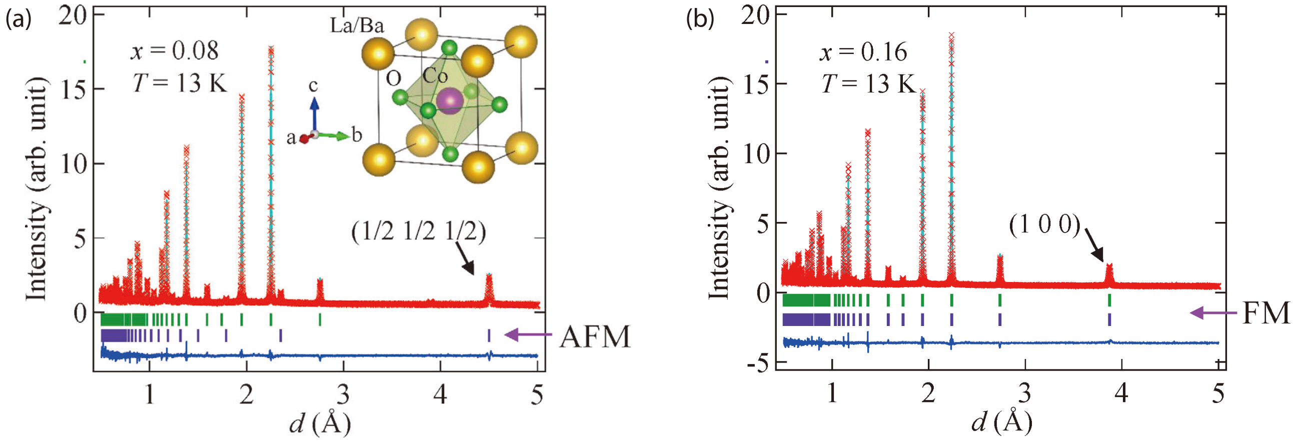

Figure 3. The NPD patterns of La$_{0.5}$Ba$_{0.5}$CoO$_{2.75+x}$ (a) $x = 0.08$, (b) $x = 0.16$ were collected at 13 K. The observed and calculated patterns are shown at the top with the cross markers and the solid line, respectively. The vertical green and purple marks in the middle show the calculated positions of Bragg reflections for nuclear and magnet diffraction, respectively. The bottom blue line represents the difference between observed and calculated intensities. The inset illustrates the cubic perovskite with the space group *Pm*$\bar{3}$*m*.

magnetic structures of the samples by magnetization and high-resolution NPD. By analyzing the NPD data, we found that the crystal structures remain in the cubic structure with space group *Pm*$\bar{3}$*m* in the whole temperature range. Sample $x = 0.16$ shows FM state at low temperature with the transition at 160 K. For the $x = 0.08$ sample, the short range ordered FM state occurs together with a long-range ordered AFM state at low temperature.

References

[1] M. A. Señarís-Rodriguez and J. B. Goodenough, J. Solid State Chem., **116**, (1995) 224.

[2] Y. Moritomo, M. Takeo, X. J. Liu, T. Akimoto and A. Nakamura, Phys. Rev. B, **58**, (1998) R13334.

[3] G. Briceño, H. Chang, X, Sun, P. G. Schultz, and X. D. Xiang, Science, **270**, (1995) 273.

[4] P. Miao, X. Lin, A. Koda, S. Lee, Y. Ishikawa, S. Torii, M. Yonemura, T. Mochiku, H. Sagayama, S. Itoh, K. Ikeda, T. Otomo, Y. Wang, R. Kadono, and T. Kamiyama, Adv. Mater., **29**, (2017) 1605991.

[5] T. Saitoh, T. Mizokawa, A. Fujimori, M. Abbate, Y. Takeda, and M. Takano, Phys. Rev. B, **55**, (1997) 4257.

[6] M. Kriener, M. Braden, H. Kierspe, D. Senff, O. Zabara, C. Zobel, and T. Lorenz, Phys. Rev. B, **79**, (2009) 224104.

[7] M. A. Señarís-Rodriguez and J. B. Goodenough, J. Solid State Chem., **118**, (1995) 323.

[8] T. Nakajima, M. Ichihara and Y. Ueda, J. Phys. Soc. Jpn., **74**, (2005) 1572–1577.

[9] V. Sikolenko, V. Efimov, I.O. Troyanchuk, D.V. Karpinsky, M.V. Bushinsky and D. Sheptyakov, J. Phys. Conf. Ser., **391**, (2012) 012106.

[10] I.O. Troyanchuk, M.V. Bushinsky, V. Sikolenko, V. Efimov, C. Ritter, T. Hansen, and D.M. Többens, Eur. Phys. J. B, **86**, (2013) 435.

[11] I. O. Troyanchuk, D. V. Karpinsky, M. V. Bushinsky, V. Sikolenko, V. Efimov, and A. Cervellino, JETP Lett., **93**, (2011) 139.

[12] R. Oishi-Tomiyasu, M. Yonemura, T. Morishima, A. Hoshikawa, S. Torii, T. Ishigaki, and T. Kamiyama, J. Appl. Crystallogr., **45**, (2012) 299.

[13] J. Rodrìguez-Carvajal, Physica B (Amsterdam, Neth.), **192**, (1993) 55.

[14] A. Wills, Physica B (Amsterdam, Neth.), **278**, (2000) 680.

[15] Devendra Kumar and A Banerjee, J. Phys.: Condens. Matter, **25**, (2013) 216005.

Z. Tan[1], P. Miao[1], M. Hagihala[1,2], S. Torii[1,2], and T. Kamiyama[1, 2]

[1]*Institute of Materials Structure Science, KEK;* [2]*Neutron Science Section, Materials and Life Science Division, J-PARC Center*

Crystal Structure, Ionic Conductivity and Li-Ion Diffusion Pathway in a La-Li-Co-O System

1. Introduction

The development of lithium (Li)-ion batteries is being driven by an ever-increasing demand to shift from fossil fuels to electricity, along with the use of more renewable energy on the grid. Enhancing the energy storage capacity remains a central objective of research on cathode, electrolyte and anode materials. For example, our previous study revealed a pronounced influence of the type of electrolyte on the capacity [1, 2].

Progress in the field of oxide electrolytes has been severely hampered due to the lack of new families of candidate compounds besides the classic d^0 and the main-group element systems (for example, Ti^{4+}, Ge^{4+} and Zr^{4+}) [3–5]. On the other hand, cobalt oxides have attracted great interest in recent years because of the observations of huge thermoelectric power [6], superconductivity [7] and a variety of peculiar physical properties reported by our group [8–11], which are generally considered to be associated with the valence state and the spin state of Co ions.

2. Experiments

Polycrystalline La-Li-Co-O samples were prepared by solid-state reaction. The details of the crystal structure analysis, sample characterization and ionic/electronic conductivity measurements were reported elsewhere [12]. The neutron time-of-flight diffraction data at room temperature and 100°C were obtained using a high-resolution neutron powder diffractometer at the BL09 (SPICA) beamline in the Materials and Life Science Experimental Facility (MLF) of J-PARC, Japan. The structural parameters were refined using the Z-Rietveld program [13, 14]. The maximum entropy method (MEM) calculations were performed using the Z-MEM algorithm in the Z-code software package [15]. The crystal structure and nuclear density distribution were visualized using the VESTA program [16].

3. Results and discussion

Li intercalation was performed on parent $La_2Li_{0.5}Co_{0.5}O_4$ with tuning x and y in $La_{4/3-x}Li_{3x+y}\square_{2/3}Li_{0.5}Co_{0.5}O_{4-\delta}$. The chemically fabricated materials exhibited electronic insulating and ionic conducting behavior. $La_{1.24}\square_{2/3}Li_{0.73}Li_{0.5}Co_{0.5}O_{3.23}$ ($x = 0.09$, $y = 0.46$, $\delta = 0.77$) exhibited the highest Li-ion conductivity (7×10^{-5} S cm^{-1} at 140°C) among all prepared samples.

The structural analysis carried out for the La-Li-Co-O system was the Rietveld refinement for the neutron diffraction profile. Figure 1(a) shows the neuron diffraction pattern of $La_{1.24}\square_{2/3}Li_{0.73}Li_{0.5}Co_{0.5}O_{3.23}$. The orthorhombic *Ammm* (No. 65) symmetry was applied and the intercalated Li ions were located at (0, 0, 0.25). The Li atoms together with vacancies were distributed in the interstitial sites. The lattice was refined as $a = 5.35$ Å, $b = 5.35$ Å and $c = 12.62$ Å, with $R_{WP} = 7.94\%$. The crystal structure of $La_{1.24}\square_{2/3}Li_{0.73}Li_{0.5}Co_{0.5}O_{3.23}$ is shown in Fig. 1(b). The MEM was applied to determine the precise nuclear densities. The Li nuclear density was indistinctly localized at room temperature (Fig. 2(a)). When the temperature was increased to 100°C, Li cations diffused throughout a quasi-one-dimensional (Q1D) pathway along the b–axis direction via exchange between interstitial Li and vacancies (Fig. 2(b)). An increase in the number of the Q1D pathway and/or the dimensionality of the pathway (i.e., isotropic diffusion) is desirable for realizing higher Li-ion conductivities.

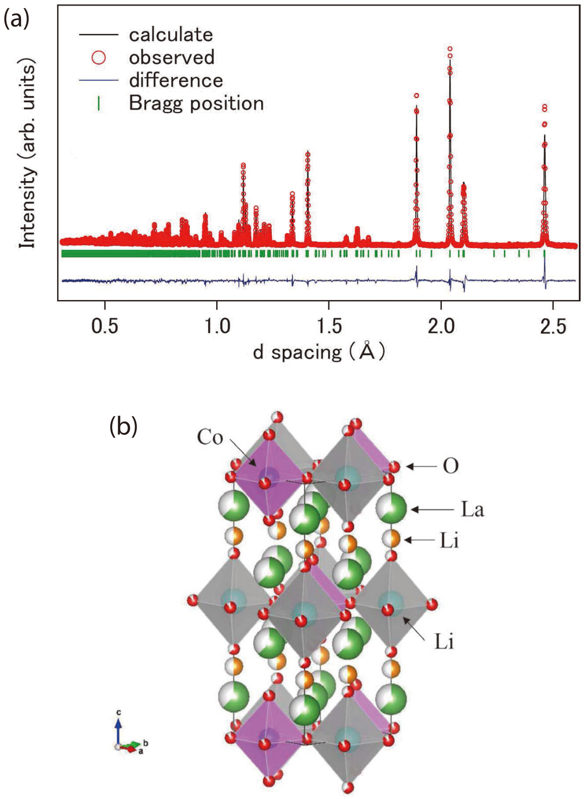

Figure 1. Structural characterization of La-Li-Co-O. (a) Neutron powder diffraction pattern of $La_{1.24}\square_{2/3}Li_{0.73}Li_{0.5}Co_{0.5}O_{3.23}$ and (b) its crystal structure.

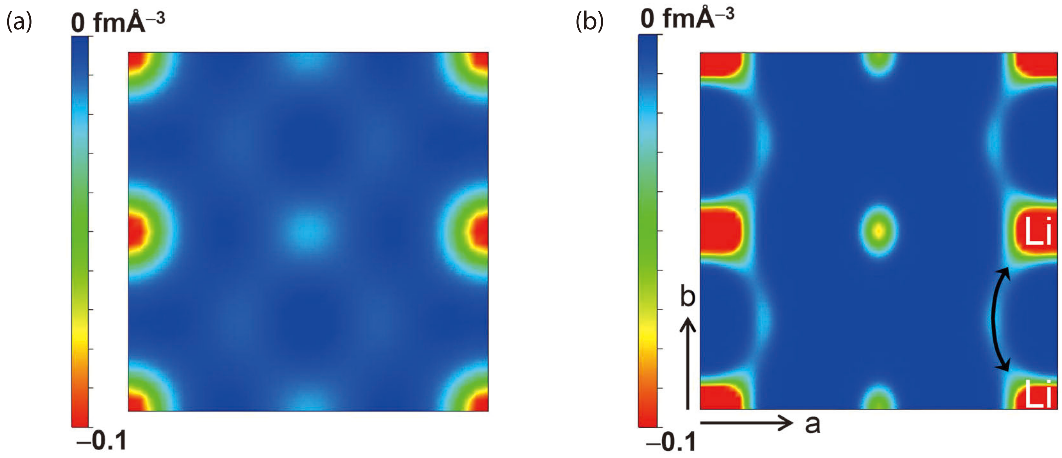

Figure 2. Nuclear density distribution at z≈0.25 calculated using the MEM with the neutron powder diffraction data at (a) room temperature and (b) 100°C for $La_{1.24}\square_{2/3}Li_{0.73}Li_{0.5}Co_{0.5}O_{3.23}$.

4. Conclusion

We discovered the La-Li-Co-O electrolyte as a leading contender. We applied the MEM to the neutron diffraction data. The MEM is expected to be effective for 3D visualization of diffusional pathways of other cations/anions in next-generation batteries such as sodium-ion batteries and fluoride-ion batteries, which currently is being developed.

References

[1] T. Takami *et al.*, J. Alloys Compd. **769**, 539 (2018).
[2] T. Takami *et al.*, AIP Advances **9**, 045301 (2019).
[3] U. v. Alpen *et al.*, Electrochimica Acta **23**, 1395 (1978).
[4] C. Wang *et al.*, J. Electrochem. Soc. **151**, A1196 (2004).
[5] H. Buschmann *et al.*, Phys. Chem. Chem. Phys. **13**, 19378 (2011).
[6] I. Terasaki *et al.*, Phys. Rev. B **56**, R12685 (1997).
[7] K. Takada *et al.*, Nature **422**, 53 (2003).
[8] T. Takami, Functional Cobalt Oxides: Funda mentals, Properties and Applications; Pan Stanford, (2014).
[9] T. Takami *et al.*, Phys. Rev. B **76**, 144116 (2007).
[10] T. Takami *et al.*, Appl. Phys. Lett. **99**, 072102 (2011).
[11] T. Takami *et al.*, Appl. Phys. Lett. **101**, 102409 (2012).
[12] T. Takami *et al.*, ACS Applied Energy Materials **1**, 2546 (2018).
[13] R. Oishi *et al.*, Nucl. Instrum. Methods Phys. Res., Sect. A **600**, 94 (2009).
[14] R. Oishi-Tomiyasu *et al.*, J. Appl. Crystallogr. **45**, 299 (2012).
[15] Y. Ishikawa *et al.*, ICANS XXI: International Collaboration on Advanced Neutron Sources, DAA-P08; J-PARC: Tokai, Japan, (2014).
[16] K. Momma and F. Izumi, J. Appl. Crystallogr. **41**, 653 (2008).

T. Takami[1], Y. Morita[1], M. Yonemura[2,3], Y. Ishikawa[2,3], S. Tanaka[4], M. Mori[4], T. Fukunaga[1], and E. Matsubara[1]
[1]Office of Society-Academia Collaboration for Innovation, Kyoto University; [2]Neutron Science Section, Materials and Life Science Division, J-PARC Center; [3]Institute of Materials Structure Science, KEK; [4]Research Institute of Electrochemical Energy (RIECEN), National Institute of Advanced Industrial Science and Technology (AIST)

High-Speed Neutron Imaging Using a Current-Biased Delay-Line Detector of Kinetic Inductance

1. Introduction

Recent progress in the development of intensive neutron sources and the required peripheral equipment has allowed us to perform simultaneously energy-resolved and high-spatial-resolution neutron imaging and tomography [1]. Much effort has been devoted to developing a neutron imager with high spatial and temporal resolution. Recent shortage of ^{3}He isotope, which is widely used as neutron absorber in neutron detectors, has also motivated the development of ^{3}He-free neutron detector.

The highest spatial resolution of 2 μm was achieved by a gadolinium-oxysulfide-scintillator camera detector with a reactor neutron source [2]. The scintillation light was magnified by an optical microscope and was imaged by a cooled sCMOS camera. To obtain a high spatial resolution image, the center-of-gravity corrections were applied to refine the scintillation-event positions. A ^{10}B-doped multichannel plate (MCP) combined with a Timepix readout was also investigated as a neutron imager for pulsed neutron sources [3, 4]. The spatial resolution was 55 μm and was improved down to 10 μm by using center-of-gravity corrections, while the detection-rate tolerance decreased due to the computational time.

We have been developing a ^{3}He free all solid-state neutron detector with high spatial and temporal resolution based on a superconducting detector [5–7]. Our developed system, a current biased kinetic inductance detector (CB-KID), can work as a neutron imager, while the detector should be cooled down to below superconducting transition temperature with sub-mA DC bias currents. We employ the delay-line method to obtain two-dimensional images with limited readout lines [7].

2. Detector structure and principle

Figures 1(a) and (b) show the schematic of our delay-line CB-KID system and cross-sectional image of the detector. Both the *X* and *Y* superconducting Nb striplines of 1 μm width are folded to meanderlines by every segment length of $h = 10.5$ mm with a spacing of 1 μm. The *X* and *Y* meanderlines are orthogonal to each other, and fabricated on a Nb ground plane. An enriched-^{10}B neutron-absorption layer is superimposed on top of the detector. The Nb meanderline with two end electrodes was fabricated in the Clean Room for Analog-Digital-Superconductivity (CRAVITY) at the National Institute of Advanced Industrial Science and Technology (AIST). The ^{10}B layer was deposited using a molecular beam technique under ultrahigh vacuum at Osaka Prefecture University.

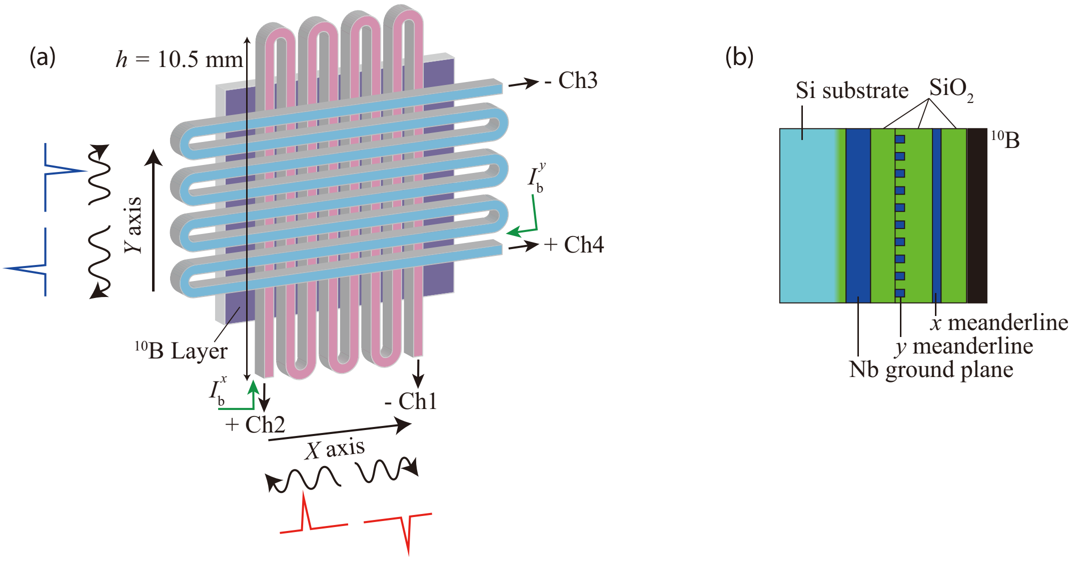

Figure 1. (a) Schematic of the CB-KID system. An *X* meander is orthogonal to a *Y* meander. The ^{10}B conversion layer is deposited on the CB-KID system. Bias currents I_b^x and I_b^y are fed to the *X* and *Y* meandelines independently. Both ends of the two meanderlines are connected to the channels, Ch1, Ch2, Ch3 and Ch4, of a Kalliope-dc readout circuit. (b) Schematic cross-sectional image of CB-KID system.

An incident neutron creates charged particles by the ^{10}B + n reaction at the neutron-absorption layer. The emitting charged particle to meanderlines induces rapid reduction of Cooper pair density n_s locally at a hot spot within a tiny segment of the meanderlines. Then, a transient change in the kinetic inductance L_k occurs, because L_k of a superconductor is a function of n_s. The voltage pulse across the hot spot arises from the transient change in L_k under DC bias current. The signals propagate as the electromagnetic waves along the meanderline toward the both ends with opposite polarity. In the present work, Ch1 and Ch2 (Ch3 and Ch4) were used for the collection of signals from the *Y* (*X*) meanderline.

We assume that the neutron incident event occurs at a certain elapsed time t_0 from the reference time, and then t_0 can be estimated as

$$t_0 = \frac{1}{2}\left(t_{\mathrm{Ch3}} + t_{\mathrm{Ch4}} - \frac{l}{v_x}\right) = \frac{1}{2}\left(t_{\mathrm{Ch1}} + t_{\mathrm{Ch2}} - \frac{l}{v_y}\right),$$

where t_{Ch1}, t_{Ch2}, t_{Ch3}, and t_{Ch4} are the time stamps of the signals received at Ch1, Ch2, Ch3, and Ch4, respectively. l (52.5 m) is the total length of the meanderline, and v_x (= 9.04×10^7 m/s) and v_y (= 7.24×10^7 m/s) are the propagation velocities for the *x* and *y* meanderlines, respectively. It is noteworthy that one can determine t_0 from the combination of $t_{\mathrm{Ch1}}$and t_{Ch2}, or t_{Ch3} and t_{Ch4}, independently. If the signals originate from the same event, t_0 in *X* and *Y* meanderlines should coincide with each other. We can identify a genuine combination of a signal quartet by using this coincidence criterion, even if several signals exist simultaneously on a meanderline. Therefore, a CB-KID has a good multi-hit tolerance. The neutron incident position *X* and *Y* is determined as

$$X = \mathrm{ceil}\left(\frac{\Delta t_x v_x}{2h}\right)p, \qquad \Delta t_x = t_{\mathrm{Ch4}} - t_{\mathrm{Ch3}},$$

$$Y = \mathrm{ceil}\left(\frac{\Delta t_y v_y}{2h}\right)p, \qquad \Delta t_y = t_{\mathrm{Ch2}} - t_{\mathrm{Ch1}},$$

where p is the repetition pitch for the meanderline.

The sensitivity of the CB-KID to γ-rays is negligibly small because of the low absorption probability of the constituent materials and the small effective thickness of the Nb meanderline for γ -rays.

3. Experimental method

Our neutron detector is cooled down to 4 K by using a Gifford-McMahon refrigerator. The mechanical vibration of the system is suppressed by an antivibration cryostat.

The signals are amplified and detected by a Kalliope-dc readout circuit, which has a 1-ns sampling multichannel time-to-digital converter (TDC). The Kalliope circuit was originally developed by Kojima *et al*. for muon-spin relaxation measurements [8]. We extend the time window from 64 μs to 4.2 s by increasing the bit width of the TDC from 16 to 32 bits. Thanks to this modification, the time-stamp measurements of 1-ns temporal resolution over a time window up to 4.2 s are possible without any dead time before and after data acquisition.

The neutron irradiation experiments were performed at BL10 of the Material and Life Science Experimental Facility (MLF), J-PARC [9] with the collimator ratio $L/D = 14$ m/0.1 m = 140 at 200 kW beam power. The energy resolution is achieved by the time-of-flight (TOF) method with 33 μs full width at half maximum at 10 meV.

4. Neutron transmission Image

Signal width of CB-KID is typically a few tens of ns. It implies the detection-rate tolerance to be as high as a few tens of MHz because CB-KID can handle multi-hit events. This relatively high detection-rate tolerance of CB-KID allows high-speed measurements and energy-dispersive neutron imaging with the combination of the TOF technique in a pulsed neutron source.

We conducted a neutron-imaging demonstration by using a well-shaped neutron absorber as a test pattern. The test absorber comprised a 50 μm-thick stainless-steel mesh, wherein 100 μm × 100 μm square holes were arrayed in a square lattice (with a lattice constant of 250 μm). Each hole was tightly filled by very fine ^{10}B particles. We show the neutron transmission image of the test pattern in Fig. 2(a). Measurements were performed at $T = 4.15$ K for 30.4 h with an incident neutron wavelength λ ranging 0.05–1.13 nm. The hole size and repetition period were in a fairly good agreement with those in the test pattern. The spatial resolutions were estimated from the sharpness of the dot boundary as 22 μm and 41 μm in the *y* and *x* directions, respectively. This variance was consistent with that in propagation velocities. We note that the origin of the error was partially due to the rounding of the etched edges of the holes in the metal mesh.

Figures 2(b)–(e) present the neutron transmission images of the test pattern corresponding to each λ with the width of $\Delta\lambda/\lambda = \pm 1\%$. Figure 2(b), which has the image for the $\lambda \sim 0.05$ nm slice, exhibits an unclear pattern of the test mask. This observation is consistent with the fact that the ^{10}B neutron-absorption cross-section becomes lower at shorter wavelengths. As shown in Figs. 2(c)–(e), we obtained successfully clear energy resolved neutron images.

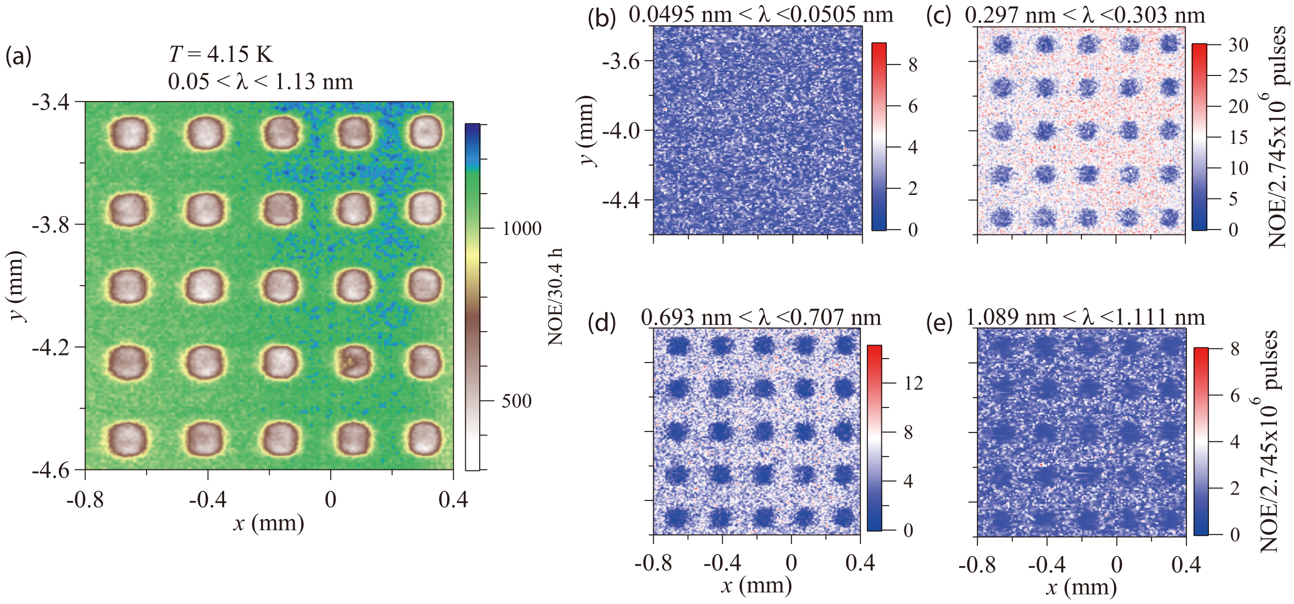

Figure 2. Neutron transmission images of the ^{10}B dot array contained in the stainless-steel mesh. Neutrons with the wavelength λ ranging (a) 0.05–1.13 nm, (b) 0.0495–0.0505 nm, (c) 0.297–0.303 nm, (d) 0.693–0.707 nm, and (e) 1.08–1.111 nm are used to construct the images.

5. Summary

We demonstrated the development of a high-speed neutron imaging system with capability suited for TOF method. We developed a set of analog signal discriminators from the preset threshold levels using a time-to-digital converter with 1 ns resolution over a time frame of 4.2 s. We reconstructed successfully the neutron image of a test pattern with a spatial resolution of 22 μm and the energy-resolved image was produced by the TOF method of pulsed neutrons.

References

[1] N. Kardjilov *et al.*, Mater. Today **14**, 248 (2011).
[2] D. S. Hussey, J. M. LaManna, E. Baltic, and D. L. Jacobson, Nuclear Instrum. Methods Phys. Res. A **866**, 9 (2017).
[3] A. S. Tremsin *et al.*, Sci. Rep. **7**, 40759 (2017).
[4] X. Llopart *et al.*, Nucl. Instrum. Methods Phys. Res. A **581**, 485 (2007).
[5] H. Shishido *et al.*, Appl. Phys. Lett. **107**, 232601 (2015).
[6] S. Miyajima *et al.*, Nucl. Instrum. Methods Phys. Res. A **842**, 71 (2017).
[7] H. Shishido *et al.*, Phys. Rev. Appllied **10**, 044044 (2018).
[8] K. Kojima *et al.*, J. Phys.: Conf. Ser. **551**, 012063 (2014)
[9] K. Oikawa *et al.*, Nucl. Instrum. Methods Phys. Res. A **589**, 310 (2008)

H. Shishido[1,2], T. D. Vu[3], K. M. Kojima[4,5], T. Koyama[5], K. Oikawa[6], M. Harada[6], S. Miyajima[7], M. Hidaka[8], T. Oku[3], K. Soyama[9], K. Aizawa[3], S. Y. Suzuki[10], M. M. Tanaka[11], and T. Ishida[1,2,5]

[1]*Department of Physics and Electronics, Graduate School of Engineering, Osaka Prefecture University;* [2]*NanoSquare Research Institute, Osaka Prefecture University;* [3]*Technology Development Section, Materials and Life Science Division, J-PARC Center;* [4]*Centre for Molecular and Materials Science, TRIUMF and Stewart Blusson Quantum Matter Institute, University of British Columbia;* [5]*Division of Quantum and Radiation Engineering, Osaka Prefecture University;* [6]*Neutron Science Section, Materials and Life Science Division, J-PARC Center;* [7]*Advanced ICT Research Institute, National Institute of Information and Communications Technology;* [8]*Advanced Industrial Science and Technology;* [9]*Materials and Life Science Division, J-PARC Center;* [10]*Computing Research Center, Applied Research Laboratory, KEK;* [11]*Institute of Particle and Nuclear Studies, KEK*

Symmetrization of Hydrogen Bond in δ-AlOOH under Earth's Mantle Condition

1. Introduction

The study of hydrogen bond under high pressure is important to understand the mineral physics under the Earth's mantle conditions. In general, hydrogen takes an asymmetric position between two neighboring oxygen atoms, which forms a long and relatively weak hydrogen bond on one side and a short and strong covalent bond on the other side. However, pressure changes this asymmetric geometry. It has been theoretically predicted that under high pressure, hydrogen re-locates at the center between two oxygen atoms. This phenomenon is called symmetrization of the hydrogen bond [e.g. 1]. Neutron diffraction is a powerful tool to investigate the position of hydrogen atom in the structure, however, so far the study on the symmetrization has been limited to indirect methods such as spectroscopic methods and X-ray diffraction studies.

In this study, we intended to observe directly the symmetrization in aluminous hydroxide phase δ-AlOOH using neutron diffraction [2]. This phase was found to be stable at extremely wide pressure range, above 134 GPa and 2000 K, thus it is an important candidate of water carrier into the Earth's core-mantle boundary at 2900 km depth.

2. High pressure experiment at PLANET

In this study we measured neutron diffraction on δ-AlOOH and its deuteride under high pressure at PLANET in MLF [3]. High pressure experiments were conducted using Paris-Edinburgh cell. Powder sample was sealed in TiZr encapsulating gaskets together with deuterated methanol-ethanol mixture, which maintains the quasi-hydrostatic condition. Diffraction patterns were collected for 4–7.5 h at several oil pressures upon compression. The obtained profiles were fitted by means of Rietveld method to refine the atomic positions including hydrogen.

3. Results and discussion

The diffraction profiles were successfully collected up to 18.1 GPa for δ-AlOOH and up to 17.4 GPa for δ-AlOOD (Fig. 1). Previous studies have determined the crystal structure at ambient pressure to be distorted rutile type with space group of $P2_1nm$. In this model, the AlO_6 octahedra make a single chain along c-axis and hydrogen bond is formed in the tunnel between the chains (Fig. 2(a)). The refinement was conducted using this model in the first step.

As pressure increased, we observed important features that indicate a phase transition. First, the difference of the interatomic distance of Al-O1 and Al-O2 atoms of AlO_6 octahedra becomes negligible at high pressure. This reflects the fact that two oxygen atoms, one of which is a donor and the other an accepter of hydrogen bond, become electrostatically equivalent. In addition, the intensity of 021 reflection around 1.7 Å continuously decreases at high pressure. The extrapolation of pressure evolution of the intensity of 120 shows that it disappears at 9 GPa. This additional extinction condition can be explained by the phase transition to

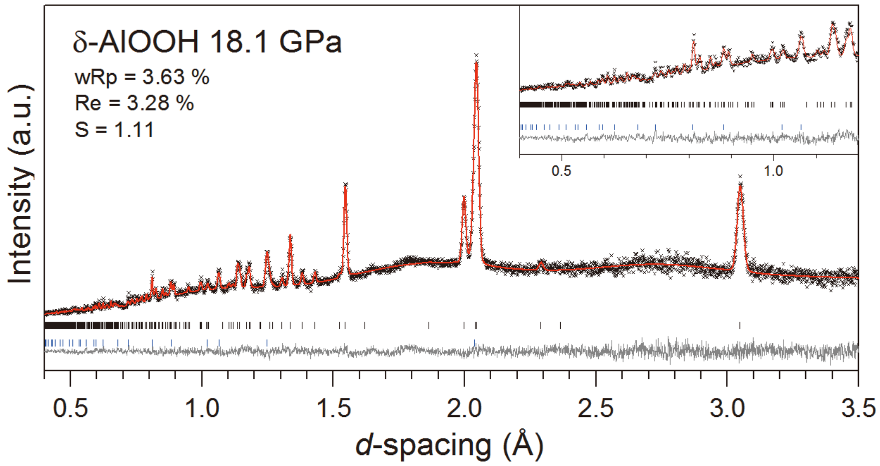

Figure 1. Neutron diffraction pattern of δ-AlOOH obtained at 18.1 GPa. The crosses, red and gray lines represent observed, calculated, and difference profiles, respectively.

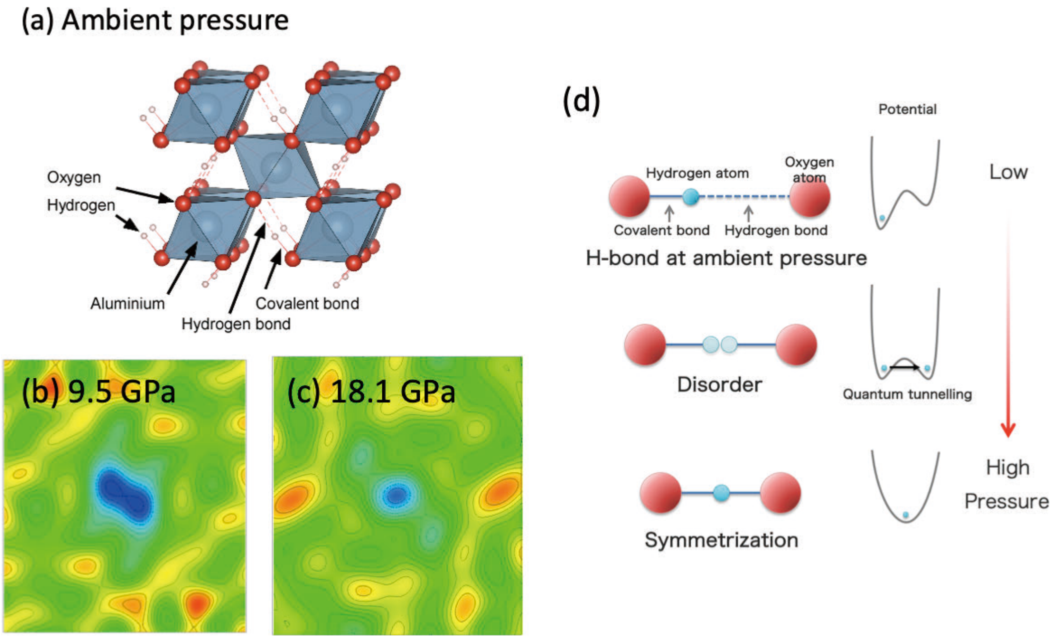

Figure 2. (a) Crystal structure of aluminous hydroxide δ-AlOOH at ambient pressure. (b, c) Change of nuclear density at high pressure obtained by neutron diffraction. The maps are enlarged around the hydrogen atom (pink spheres in (a)) and hydrogen is recognized as a negative (blue) peak. (d) Schematic diagram of the change of proton potential towards hydrogen bond symmetrization at high pressure.

Pnnm, which is a direct super group of $P2_1nm$.

The present study indicates that there is a phase transition in δ-AlOOH at 9 GPa, however, whether this relates to the symmetrization or not is still unclear. To investigate the hydrogen bond configuration precisely, the difference Fourier map was investigated. In the Fourier map, the hydrogen atom appears as a negative peak since it has a negative scattering length for neutron. At the transition pressure, nuclear density displays bimodal distribution around the center between two oxygen atoms (Fig. 2(b)). This result implies that the transition at 9 GPa originates from a disordering of hydrogen bond rather than the symmetrization. Further compression to 18.1 GPa results in the unimodal distribution, suggesting that the symmetrization was achieved at this pressure (Fig. 2(c)). The O...O distance reaches 2.41 Å at 18.1 GPa, which agrees with the theoretical prediction. It was fond that the deuterization of the sample led to an increase of the disorder pressure to 12 GPa. At up to 17.4 GPa, the deuterium atom remains in a disordered state and the symmetrization seems to occur at higher pressure.

Comparing the present result and previous studies, a link between the hydrogen bond symmetrization and the change of physical properties can be discussed. Previous X-ray diffraction studies have found stiffening behaviors along the *a* and *b* axes, where hydrogen bond lies in at around 10 GPa. Brillion scattering experiment also found anomalous increase in sound velocities in the pressure range of 6 to 15 GPa. The present study indicates that disorder of hydrogen induces these phenomena rather than the symmetrization.

4. Conclusion

Using neutron diffraction experiments, we observed for the first time that the hydrogen bond symmetrization occurs in aluminous hydrous phase δ-AlOOH. The results show that changes in physical properties of δ-AlOOH that had been reported previously can be explained by the symmetrization and its precursor phenomena of disorder of the hydrogen bond.

References

[1] Tsuchiya et al., Geophys. Res. Lett., **29** 1909 (2002).
[2] A. Sano-Furukawa et al., Sci. Rep. **8** 15520 (2018).
[3] T. Hattori et al., Nucl. Inst. Methods Phys. Res. A, **780** 55–67 (2015).

A. Sano-Furukawa[1], T. Hattori[1], K. Komatsu[2], H. Kagi[2], and T. Nagai[3]
[1]*Neutron Science Section, Material and Life Science Division, J-PARC Center;* [2]*Geochemical Research Center, The University of Tokyo;* [3]*Department of Earth and Planetary Science, Hokkaido University*

Neutron Spin Resonance in the 112-Type Iron-Based Superconductor*

1. Introduction

In unconventional superconductors, the neutron spin resonance mode is a crucial evidence for spin fluctuation mediated superconductivity in the proximity of an antiferromagnetic (AF) instability [1]. Although the spin resonance mode is theoretically believed to be a spin-1 exciton from the singlet-triplet excitations of the electron Cooper pairs in copper oxides and heavy fermions [2], solid proofs of its presence in iron-based superconductors (FeSC) is still rare. The proximity of superconductivity and AF order, together with the spin-orbit coupling (SOC) effect, add more complexity to the energy and momentum distribution of spin resonance. In order to seek for a convincing mechanism of high-Tc superconductivity, it is necessary to study the neutron spin resonance in more materials [3].

2. Experiments

We have prepared high quality single crystals of the newly discovered 112-type iron pnictide using the self-flux method [4, 5] and co-aligned 2.3 g $Ca_{0.82}La_{0.18}Fe_{0.96}Ni_{0.04}As_2$ (Tc = 22 K, see Fig. 1) single crystals (about 1500 pieces) with a small mosaic about 4° in the ab plane and 3° along the c axis. By using inelastic neutron scattering, we have comprehensively studied the low-energy spin excitations of this new 112-type FeSC [6].

3. Results

A neutron spin resonance mode around $E_R = 11$ meV was discovered for the first time in 112-type FeSC (Fig. 2) [6]. The resonance mode was almost two-dimensional, and the resonance energy was demonstrated to be almost temperature independent and could scale with T_c linearly (Fig. 3 and Fig. 4) [6]. Polarized neutron analysis revealed that the resonance mode was nearly isotropic in spin space (Fig. 3(c)). Because of the unique monoclinic structure with additional zigzag arsenic chains, the As 4p orbitals contribute to a three dimensional hole pocket around the Γ point and an extra electron pocket at the X point. Our results suggest that the energy and momentum distribution of the spin resonance does not directly respond to the k_z dependence of the fermiology, and the spin resonance intrinsically is a spin-1 mode from singlet-triplet excitations of the Cooper pairs in the case of weak spin-orbital coupling [6].

---

* This work has been published on Physical Review Letters [6]. The neutron-scattering experiment at HRC was performed with the J-PARC under user proposal program (2016B0068).

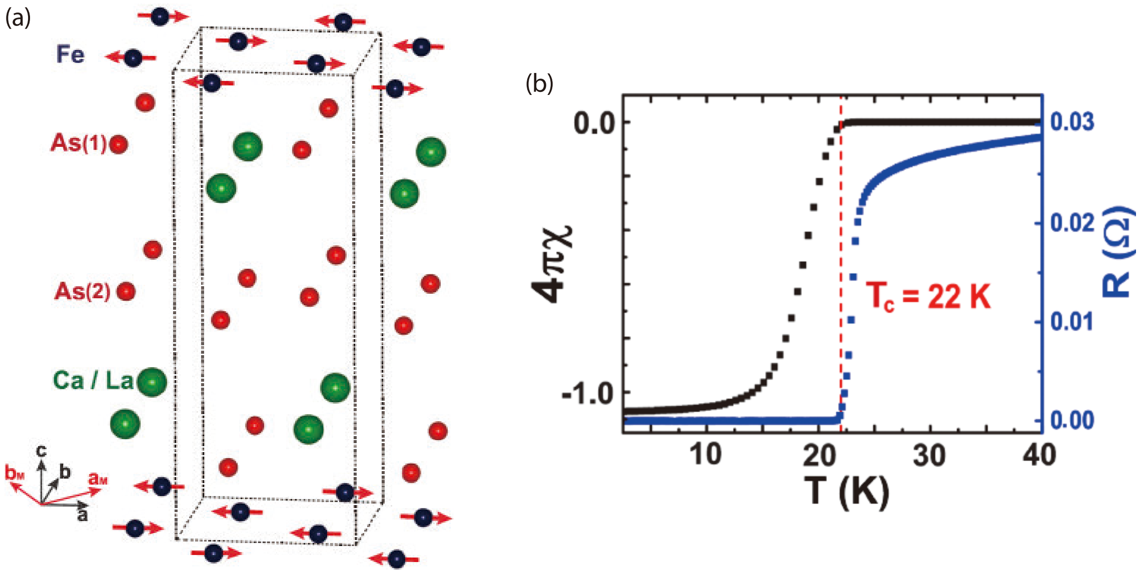

Figure 1. (a) Crystal and magnetic structure of the $Ca_{1-x}La_xFeAs_2$ system; (b) Superconducting transitions of $Ca_{0.82}La_{0.18}Fe_{0.96}Ni_{0.04}As_2$.

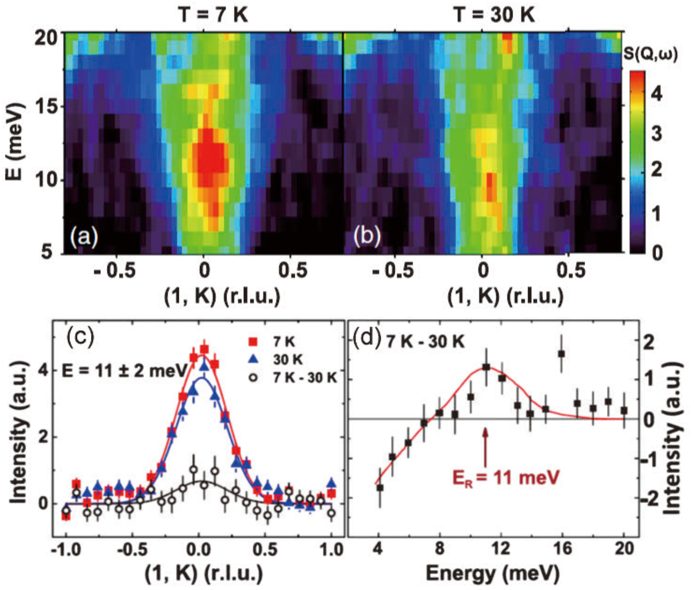

Figure 2. Neutron spin resonance mode around 11 meV in $Ca_{0.82}La_{0.18}Fe_{0.96}Ni_{0.04}As_2$. (Results from HRC-BL 12)

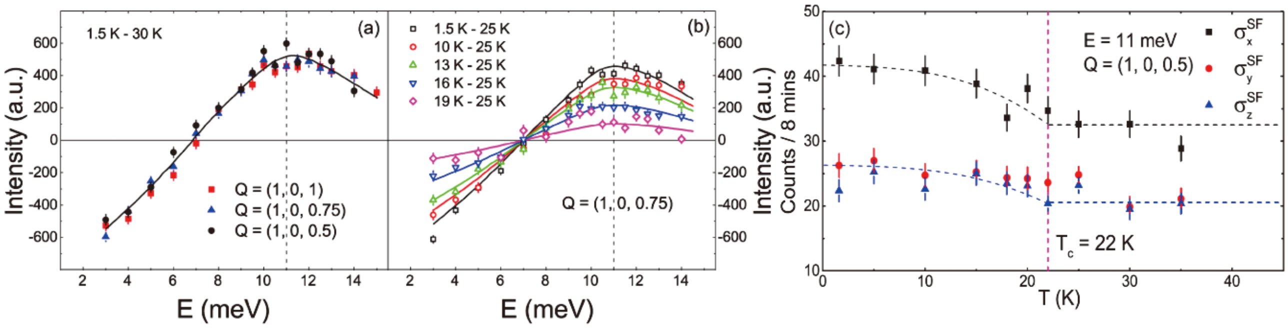

Figure 3. Two-dimensional, isotropic spin resonance in $Ca_{0.82}La_{0.18}Fe_{0.96}Ni_{0.04}As_2$.

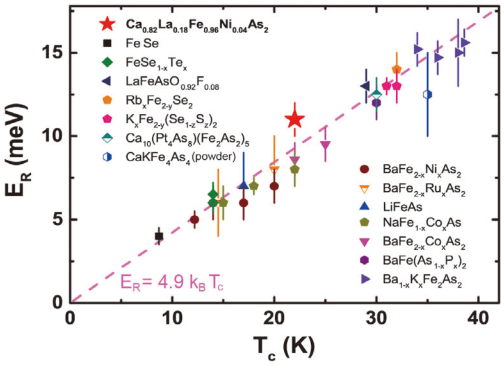

Figure 4. Linear scaling of spin resonance energy E_R and superconducting transition temperature T_c in FeSC.

References

[1] P. Dai, Rev. Mod. Phys. **87**, 855 (2015).

[2] M. Eschrig, Adv. Phys. **55**, 47 (2006).

[3] P.D. Johnson, G. Xu, and W.-G. Yin Iron-Based Superconductivity (Springer, New York, 2015).

[4] N. Katayama et al., J. Phys. Soc. Jpn. **82**, 123702 (2013).

[5] T. Xie et al.,Supercond.Sci. Technol. **30**, 095002 (2017).

[6] T. Xie et al., Phys. Rev. Lett. **120**, 137001 (2018).

T. Xie[1], D.L. Gong[1], H. Ghosh[2], A. Ghosh[2], M. Soda[3], T. Masuda[3], S. Itoh[4,5], F. Bourdarot[6], L-P. Regnault[7], S. Danilkin[8], S.L. Li[1], and H.Q. Luo[1]

[1]*Institute of Physics, Chinese Academy of Science;* [2]*HomiBhabha National Institute, AnushaktiNagar;* [3]*The Institute for Solid State Physics, The University of Tokyo;* [4]*Institute of Materials Structure Science,KEK;* [5]*Neutron Science Section, Materials and Life Science Division, J-PARC Center;* [6]*Université Grenoble Alpes, CEA;* [7]*Intitut Laue Langevin;* [8]*Australian Centre for Neutron Scattering, Australian Nuclear Science and Technology Organization*

Observation of Pressure-Tuned Molecular Reorientational Dynamics in Barocaloric Neopentylglycol

1. Introduction

Caloric effects are phase-transition thermal effects regulated by external fields. As a promising alternative to the vapor compression cycle technology that is currently in wide service, emerging refrigeration technologies based on solid-state caloric effects have been attracting attention in recent decades. Large isothermal entropy changes and adiabatic temperature changes are the most important requirements for a caloric material. Current caloric materials are characteristic of small isothermal entropy changes of about 50 J kg^{-1}K^{-1}, which is one of serious obstacles to the real applications. Very recently, we have discovered that plastic crystals exhibit excellent barocaloric effects with typical entropy changes higher than 400 J kg^{-1}K^{-1} induced by a small pressure, ~ 20 MPa, as shown in Fig.1 [1]. While these findings imply the solid-state refrigeration technologies based on caloric materials would be on the horizon, the underlying microscopic scenario on such colossal barocaloric effects has to be established, as far as the fundamental issue is concerned.

2. Experimental considerations

As plastic crystals are also called orientation-disordered crystals, the reorientational dynamics might play a decisive role in the colossal barocaloric effects. Thus, in-situ high-resolution inelastic neutron scattering (INS) as well as quasi-elastic neutron scattering (QENS) measurements are proposed on the representative plastic crystal neopentylglycol (NPG), whose chemical formula is $C_5H_{12}O_2$ and IUPAC name is 2,2-dimethyl-1,3-propanediol.

The cold neutron disk chopper spectrometer BL14 AMATERAS of MLF was chosen for such a study for its superior energy resolution in wide energy bands accommodated with the multi-E_i capacity [2]. A powder sample of around 0.29 g was wrapped with aluminium foil and further sealed into an aluminium can with indium wire. Such a geometry ensures about 80% transmission of neutrons, which is crucial for obtaining high-quality QENS data. A cryostat was used to access a broad temperature region. The chopper configurations were 300 Hz (CH01), 300 Hz (CH02) with a slit width of 10 mm, and 150 Hz (CH03), which enabled the selection of $E_i = 23.72$, 5.93, 2.64 meV with energy resolution of 0.42, 0.078, and 0.026 meV, respectively. The data reduction was performed using the Utsusemi suite [3]. The resulting $S(Q, E)$ data were visualized in Mslice of DAVE [4].

The high-pressure INS/QENS data were collected with the same E_i but with a slit size of 30 mm to enhance the intensity, using a clamped cell made of an Al–Zn–Mg-based alloy (Mesoalite). The powder sample was mixed with reagent-grade KBr powder (Kanto Chemical) to reduce multiple scattering and to ensure quasi-hydrostatic conditions. We note that KBr has very limited incoherent scattering length, which is very important for QENS measurements. A mixture of the sample and KBr powder at a volumetric ratio of 1:1 was used to fabricate a pellet of 6.5 mm diameter and 22.5 mm length, which was inserted into a sample cell made of Teflon. The sample was compressed to the desirable

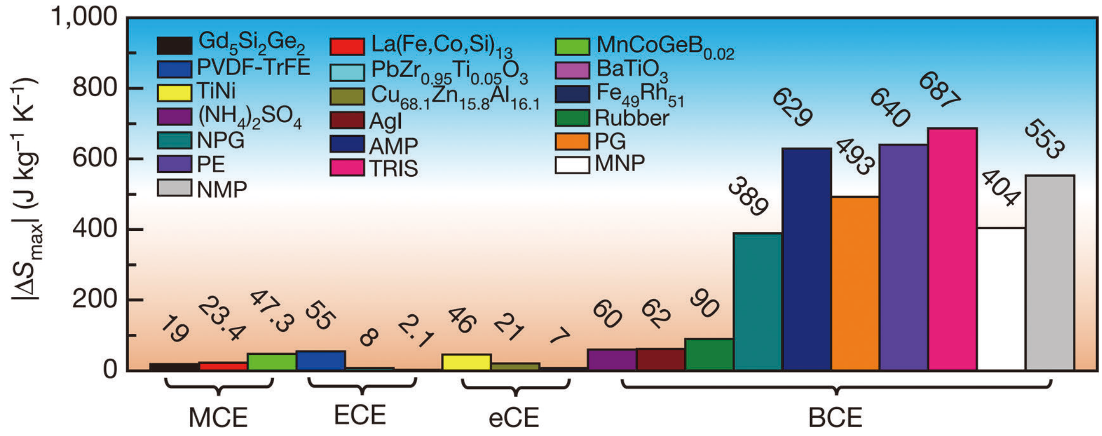

Figure 1. Absolute values of maximum entropy changes, $|\Delta S_{max}|$, for leading caloric materials. MCE, magentocaloric effect; ECE, electrocaloric effect; eCE, elastocaloric effect; and BCE, barocaloric effect.

loading with a hand press, using a load–pressure curve determined beforehand. The actual pressure generated in the cell was determined at the high-pressure neutron diffractometer (PLANET) [5] from the change of the lattice parameters of KBr using the equation of state [6].

3. Results and discussion

The molecular configuration of NPG is characteristic of a tetrahedral motif. The five carbon atoms form a tetrahedron, in which two carbon atoms are attached to hydrogen atoms in the methyl group, whereas two others form the hydroxymethyl group. At room temperature, the NPG molecules are ordered on a monoclinic lattice with space group $P2_1/n$. This ordered phase transforms into an fcc lattice at $T_t \approx 314$ K on heating under the ambient pressure.

We performed QENS measurements on NPG at selected temperatures near T_t. Shown in Fig. 2(a) are the contour plots of the dynamic structure factor $S(Q, E)$ as a function of momentum transfer (Q) and energy transfer (E) with $E_i = 2.64$ meV. The intense stripes centered at $E = 0$ represent the elastic line, which contains most of the scattering intensity. It can be seen that the elastic lines dominate the spectra at 250 K and 300 K. At 320 K, just above T_t, a less-intense signal spreads out from $E = 0$ and weakens as E increases, which corresponds to QENS originating from hydrogen atoms. The spectra fitting suggests that the hydrogen atoms in the methyl group are subjected to C_3 reorientation in both ordered and disordered phases (C_3 reorientation might be further frozen at about 60 K), while the whole molecule undergoes isotropic reorientation in the disordered phase.

More strikingly, the pressure-dependent QENS data directly provide insights into the microscopic dynamics of the system. It can be seen in Fig. 2(b), (c) that the QENS signal, which appears as a trail of the intense elastic line, is mostly suppressed under a pressure of 286 MPa. Indeed, the QENS intensity is already effectively suppressed even at a lower pressure of 178 MPa. These QENS data directly verify that orientational disorder is restrained by the pressure, inducing entropy changes. The pressure suppression of orientational disorder is also manifested in phonons. Shown in Fig. 2(d), (e) are $S(Q, E)$ with $E_i = 23.72$ meV at ambient pressure and at 286 MPa, respectively. It is clear that the phonons centered at about 4 meV become considerably sharper at 286 MPa, which is attributed to the reduced scattering by the orientational disorder. These experimental insights unambiguously indicate that the colossal barocaloric effects of NPG can be attributed to the suppression of the extensive orientational disorder by pressure.

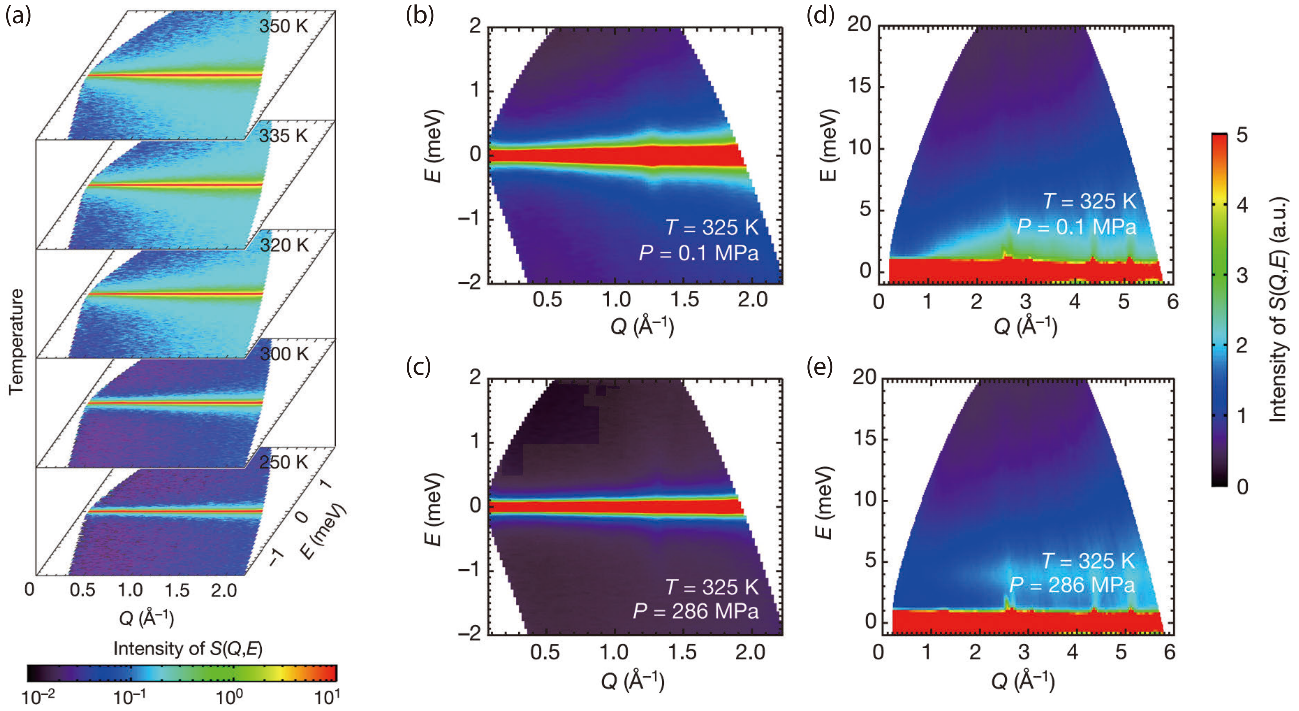

Figure 2. (a), Contour plots of $S(Q, E)$ at five temperatures around T_t, obtained with $E_i = 2.64$ meV at AMATERAS. (b), (c), QENS measurements at ambient pressure and 286 MPa obtained at 325 K with $E_i = 2.64$ meV. (d), (e), INS measurements at ambient pressure and 286 MPa obtained at 325 K with $E_i = 23.72$ meV. We note that the inelastic signals at about 1.3, 2.6, 4.4 and 5.1 Å^{-1} are contributed by phonons from Teflon.

4. Prospect

The core physical issue of caloric materials is the evolutions of atomic structures and interactions as a function of driving forces including pressure, magnetic fields, electric fields, stresses as well as light illumination in multiple spatial and temporal scales. State-of-the-art characterization techniques based on large-scale facilities such as the neutron scattering are highly desirable in this case due to the powerful experimental abilities and versatile complex sample environments. In other words, the experimental techniques based on large-scale facilities provide a great opportunity for caloric materials research and we hope that our present study would inspire both the neutron scattering and caloric materials communities.

References

[1] B. Li et. al., Nature, **567** 506 (2019).
[2] K. Nakajima, et. al., J. Phys. Soc. Jpn, **80** SB028 (2011).
[3] Y. Inamura et. al., J. Phys. Soc. Jpn **82** SA031 (2013).
[4] R. T. Azuah et. al., J. Res. Natl. Inst. Stand. Technol. **114** 341–358 (2009).
[5] T. Hattori et. al., Nucl. Instrum. Methods Phys. Res. A **780** 55–67 (2015).
[6] A. Dewaele et. al., Phys. Rev. B **85** 214105 (2012).

B. Li[1], Y. Kawakita[2], S. Ohira-Kawamura[2], T. Hattori[2], T. Kikuchi[2], Z. Zhang[1], Z. Zhang[1], W. J. Ren[1], Z. D. Zhang[1], and K. Nakajima[2]

[1]*Shenyang National Laboratory for Materials Science, Institute of Metal Research CAS;* [2]*Neutron Science Section, Materials and Life Science Division, J-PARC Center*

A New Method for Structural Analysis of a Specific Protein or Lipid Membrane in a Molecular-Crowding Environment Mimicking Living Cells

1. Introduction

The interior of the living cells is a molecular-crowding environment wherein numerous molecules coexist at about 30–40% v/v. The structural stability of proteins in aqueous solutions is well known to vary by the presence of co-solutes (osmolytes) such as sugars and polyols. Thus, the equilibrium states of biological macromolecular systems are affected by molecular-crowding environments unmatched by in vitro diluted environments. In particular, molecular-crowding environments affect the interaction energy between the water layers and proteins and alter the hydration structure and accessible volume depending on protein size via changes in chemical potential and activity. However, the theoretical interpretations of the molecular-crowding effect in living cells remain controversial, as it is difficult to predict with certainty the behavior of a specific molecule.

On the other hand, by the combination of neutron and synchrotron X-ray scattering methods, we clarified the effect of small or large molecular weight osmolytes (sugar, polyol, and synthetic neutral polymer) on protein structure and its hydration [1–3]. We also reported that the presence of those molecules affected the structural stability of proteins against chemical and thermal perturbations [4–6]. However, as various kinds of intermolecular interactions exist in the interior of living cells, clearly, previous experimental conditions for molecular-crowding do not reflect well the actual environment inside cells for affording an accurate understanding of the mechanisms of biological reactions. Hence, one of the current issues in life science is how to observe the biological reactions in an environment that closely mimics the interior of living cells.

Therefore, investigations into the nature of such an environment are essential to understand both the elaborate biological reactions and the maintenance of homeostasis occurring therein. However, the knowledge about crowding effects is still insufficient due to the lack of relevant experimental studies. Recent developments in the techniques of *in-cell* NMR and large-scale molecular dynamics simulation are providing new insights into the structure and dynamics of biological molecules inside the cells. We have demonstrated successfully a new experimental technique for observing the structure of a specific protein or membrane in the molecular-crowding environment mimicking actual living cells by using the inverse contrast matching method of neutron scattering [7].

2. Experimental

The protein measured in this study was myoglobin. The small uni-lamellar vesicles (SUVs) measured were the mixtures of monosialoganglioside (G_{M1}), cholesterol, and 1,2-dipalmitoyl-*sn*-glycero-3- phosphocholine (DPPC). These SUVs constitute a lipid raft membrane model. Gangliosides, major components of glycosphingolipid, are acidic lipids composed of a ceramide linked to an oligosaccharide chain containing one or more sialic acid residues; they are abundant in central nervous systems. Lipid rafts are dynamic assemblies of sphingolipids and cholesterol in lipid bilayers that function as platforms for membrane-associated events such as signal transduction, cell adhesion, and lipid/protein sorting. *E. coli* (strain BL21) cells were deuterated by the culture in a deuterated cell growth media. These deuterated cells were disrupted by an ultrasonic irradiation on ice cooling and used as the crowder for mimicking environment of living cells. Further in this text, we will call this crowder cell debris.

The small- and wide-angle neutron scattering (SWANS) measurements were carried out on a BL15 TAIKAN spectrometer at the pulsed-neutron source of the Materials and Life Science Experimental Facility (MLF) of the Japan Proton Accelerator Research Complex (J-PARC, Tokai, Japan).

3. Results and discussion

At first, we characterized the cell debris in solution using the dynamic light scattering method (DLS) and the solvent contrast variation method of neutron scattering (SCV). The average diameter of the cell debris was ~7.5 nm in number distribution and 1.4 μm in intensity distribution. The size distribution function indicated that the crowder solution was rather polydisperse. Comparing the number distribution function with that of scattering intensity, showed that the cell debris included large molecules, but still their major components were small molecules and fragments. From the small-angle neutron scattering (SANS) curves of the cell debris (2% w/v) in the different H_2O/D_2O mixed solvents (100, 75, 50, 25, and 0% v/v D_2O) at 25°C, the contrast matching point of the cell debris was determined by 97.6% D_2O. The Porod plot and the Orstein-Zernike plot of the SANS curve of the cell debris solution (15% w/v in H_2O, at 25°C) indicated that the cell debris solution has the feature of a diffusion-limited aggregate solution with a correlation length of ~265 Å. In addition, the cell-debris solutions did not exhibit any distinct scattering profile that might pose an obstacle for data correction. This is important for extracting structural information of a specific protein or liposome from the background scattering of the crowder solutions.

Based on the above characterization of the cell-debris solution, we carried out the SWANS measurements of the protein and the SUVs in cell debris solutions (in 97.6% D_2O). The protein concentration varied from 0.25% to 5.0% w/v in 15% w/v cell debris. The minimum protein ratio in concentration ([protein] / [cell debris]) was 1/60 w/w. In the case of SUVs, the lipid concentration was fixed by 0.5% w/v, and the cell debris concentration was varied from 7% to 21% w/v. After executing a background correction based on the method appropriate for the wide-angle scattering data [8], we managed to determine the structure of the specific protein or SUV up to the concentration ratio of [protein or SUV] / [cell debris] = ~1/60 or 1/40. Figure 1 shows the photos of the cell debris solutions and the SWANS curves of the protein in the cell debris solution (15% w/v) [7]. By comparing the observed SWANS curves of the protein with the theoretical ones obtained by fitting using CRYSON program [9], we have demonstrated that the protein structure is determinable even at the lowest concentration (0.25% w/v) in 15% w/v cell debris solution. The structures of the SUVs have been also determined successfully. It should be noticed that the cell-debris crowder used in this experiment can reproduce an environment that more closely mimics the interior of living cells than model crowders used previously such as polyols and synthetic polymers.

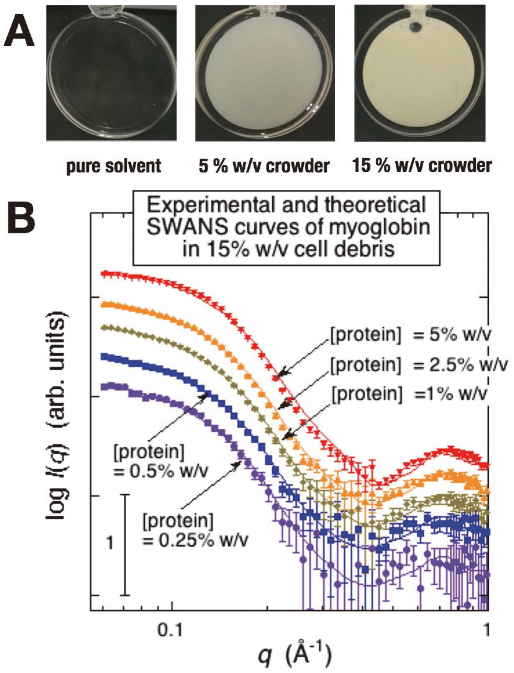

Figure 1. A, photos of the solutions composed of cell debris. B, comparison of the observed SWANS curves of myoglobin (0.25–5% w/v) in 15% w/v cell debris with theoretical ones obtained by fitting using CRYSON program.

4. Future plans

The present results clearly indicate that not only the *in-cell* NMR technique and *in silico* approaches, but also the inverse contrast matching method using the deuterated-cell debris provide a promising technique for studying the structure and dynamics of biological macromolecules in intracellular molecular-crowding environments that are essential in controlling biological systems. We are executing further experiments to clarify the specific interaction between a protein and lipid raft membrane.

References

[1] S. Ajito, et. al., Physica B: Condensed Matter, **551**, 249 (2018).
[2] M. Hirai, et. al., Biophysical J., **115** 313 (2018).
[3] M. Hirai, et. al., Physica B: Condensed Matter, **551**, 212 (2018).
[4] S. Ajito, et. al., J. Phys. Chem. B, **122**, 8685 (2018).
[5] M. Hirai, et. al., J. Phys. Chem. B, **122**, 9482 (2018).
[6] M. Hirai, et. al., J. Phys. Chem. B, **122**, 11962 (2018).
[7] M. Hirai, et. al., J. Phys. Chem. B, **123**, 3189 (2019).
[8] M. Hirai, et. al., Biochemistry, **43**, 9036 (2004).
[9] D. I. Svergun, et. al., J. Appl. Cryst., **28**, 768 (1995).

M. Hirai[1], S. Ajito[1], S. Arai[2], M. Adachi[2], R. Shimizu[2], S. Takata[3], and H. Iwase[4]
[1]*Graduate School of Science and Technology, Gunma University;* [2]*National Institute for Quantum and Radiological Science and Technology;*
[3]*Netron Science Section, Materials and Life Science Division, J-PARC Center;* [4]*Neutron Science and Technology Center, CROSS*

Directed Diffusion of Photovoltaic Active Layer Components into Porous ZnO-based Cathode Buffer Layers in Polymer Solar Cells

1. Introduction

Cathode buffer layers (CBLs) can successfully stretch further the efficiency of polymer solar cells (PSCs), after optimization of the active layer. Hidden between the active layer and the cathode of the inverted PSC device configuration is the critical yet often-unattended vertical diffusion of the active layer components across CBL. Here, we develop a novel methodology of contrast variation with neutron and anomalous X-ray reflectivity (NR and AXR) to map out the multi-component depth compositions of an inverted PSC, covering the area from the active layer surface down to the bottom of the ZnO-based CBL. Uniquely revealed for a high-performance model PSC are the often-overlooked porosity distribution of the ZnO-based CBL and the differential diffusions of the polymer PTB7-Th and fullerene-derivative $PC_{71}BM$ of the active layer into the CBL. Interface modification of the ZnO-based CBL with fullerene-derivative PCBE-OH for size-selective nanochannels can further selectively improve more the diffusion of PC71BM than that of the polymer. The deeper penetration of $PC_{71}BM$ establishes a gradient distribution of fullerene-derivatives over the ZnO/PCBE-OH CBL, resulting in markedly improved electron mobility and device efficiency of the inverted PSC. The result suggests a new CBL design concept of progressive matching of the conduction bands, via directed vertical diffusion of the active-layer fullerene-derivatives into porous, fullerene-decorated ZnO-CBLs.

2. New methodology and result

The new contrast methodology, which uses NR and AXR for revealing the interfacial structures of PSCs, is based on the changes of the scattering power of the metallic atoms in the metallic oxide of CBL, to neutrons and X-rays at energies away and close to the absorption edges of the metallic atoms [1–2]. With the rich and easy changes in the scattering contrast, the developed methodology opens a new channel to resolve increasingly complicated interfacial structures and depth-compositions of PSCs with multi-doped, metal-oxide cathode buffer layers. Here, we show an example that the new method can map successfully the multi-component depth compositions of a model PSC with ZnO-based cathode buffer layers.

The in-plane averaged density or scattering-length-density profile $\rho(z)$ of a stratified film through the film thickness can be reconstructed from an XR or NR profile measured as a function of the scattering vector q_z ($= 4\pi\lambda^{-1}\sin\theta$, with wavelength λ and incident angle θ) along the film normal [2]. A scattering-length-density (SLD) profile $\overline{\rho}(z)$ of the film then can be reconstructed from the data. For a n-component system, $\overline{\rho}(z) = \sum_{i=1}^{n} f_i(z)\rho_i$ is contributed by the n components of the corresponding scattering-length-density ρ_i, weighted by the depth-dependent volume fraction $f_i(z)$. Therefore, resolving the $f_i(z)$ profiles of the n-component system requires n sets of $\overline{\rho}(z)$ profiles reconstructed respectively from n sets of reflectivity profiles measured for the same film structure, with varied scattering contrasts. This can be achieved by NR and AXR measurements for a same film, with X-ray energy E tuned near and away the absorption K-edge of the selected metallic atoms of the film for varied $\overline{\rho_{E_i}}(z)$ values. Thus, the depth-dependent composition profiles of the film can be solved by the following relations arranged in a matrix form

$$\begin{bmatrix} \overline{\rho_{E_1}}(z) \\ \overline{\rho_{E_2}}(z) \\ \vdots \\ \overline{\rho_{E_n}}(z) \end{bmatrix} = \begin{bmatrix} \rho_{1,E_1} & \rho_{2,E_1} & \cdots & \rho_{n,E_1} \\ \rho_{1,E_2} & \rho_{2,E_2} & \cdots & \rho_{n,E_2} \\ \cdots & \cdots & \cdots & \cdots \\ \rho_{1,E_n} & \rho_{2,E_n} & \cdots & \rho_{n,E_n} \end{bmatrix} \begin{bmatrix} f_1(z) \\ f_2(z) \\ \vdots \\ f_N(z) \end{bmatrix} \tag{1}$$

where $\overline{\rho_{E_i}}(z)$ is individually deduced from the model fitting of corresponding anomalous XR data measured with X-ray energy E_i. For better resolution, NR is used as one of the relations in the matrix (1) for enhanced contrast variation. This is because fullerene-derivatives often used in PSCs have a markedly higher neutron scattering-density-density ρ_N than that of the conjugated polymers, thereby, providing a higher scattering contrast for increased sensitivity to fullerene distribution. In (1), ρ_n of each neat component can be calculated or measured from a neat film. We note that summation of $f_n(z)$ is less than 1 for a system with porosity [3].

We applied the above methodology to map the depth composition of a model PSC, comprising the active layer of conjugated polymer PTB7-Th and C_{70}-derivative $PC_{71}BM$ and a ZnO-based CBL selectively doped with a C_{60}-derivative PCBE-OH [4]. Three sets of anomalous XR profiles measured with the three X-ray energies of $E_1 = 9400$ eV, $E_2 = 9651$ eV, and $E_3 = 9656$ eV (near the absorption K-edge E_K of Zn in ZnO), complemented with one set of NR data, were used to solve the depth-dependent distributions of the four-component system from the surface of the PSC active layer down to the bottom of the CBL.

Shown in Fig. 1(a) are the NR and AXR data for an active layer of PTB7-Th:PC$_{71}$BM on a ZnO-C$_{60}$ CBL, spin-coated on Si substrate. These data are jointly fitted using the $\overline{\rho_x}$ (representatively shown for the E2 case) and $\overline{\rho_N}$ profiles shown in Fig. 1(b). With the obtained four SLD profiles, we then solved depth-by-depth the four volume fractions on the basis of (1) for the depth-dependent composition (volume fraction) profiles $f_i(z)$ of the active layers of PTB7-Th: PC71BM (1:1.5, w/w) on ZnO-C$_{60}$–doped ZnO CBL, as shown in Fig. 2(a). Reconstructed from the deduced composition profiles is the schematics shown in Fig. 2(b) for the vertical distributions of PTB7-Th and PC71BM of the active layers spin-coated on the ZnO-CBL doped with PCBE-OH.

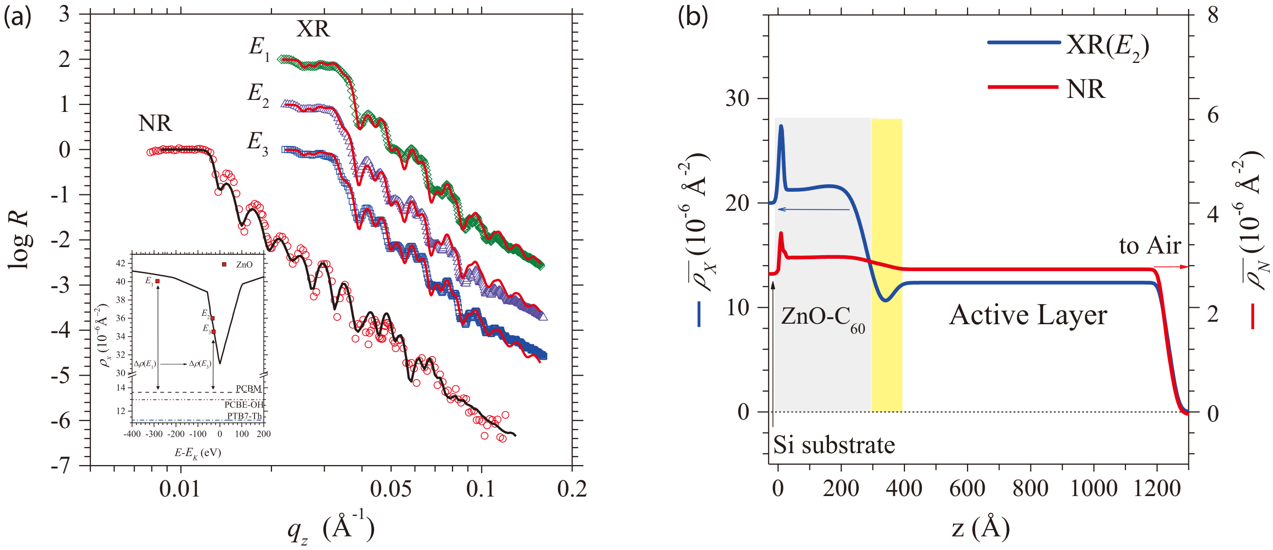

Figure 1. (a) Neutron and anomalous X-ray reflectivity data for an active layer of PTB7-Th:PC$_{71}$BM on a ZnO-C$_{60}$ CBL, spin-coated on Si substrate. Data are jointly fitted (solid curves) using (b) the $\overline{\rho_x}$ (representatively shown for the E2 case) and $\overline{\rho_N}$ profiles. For clarity, XR data with E_1 and E_2 are shifted vertically. The shaded zones in (b) are the transition zone and the ZnO-C$_{60}$ CBL sitting on Si substrate (z = 0).

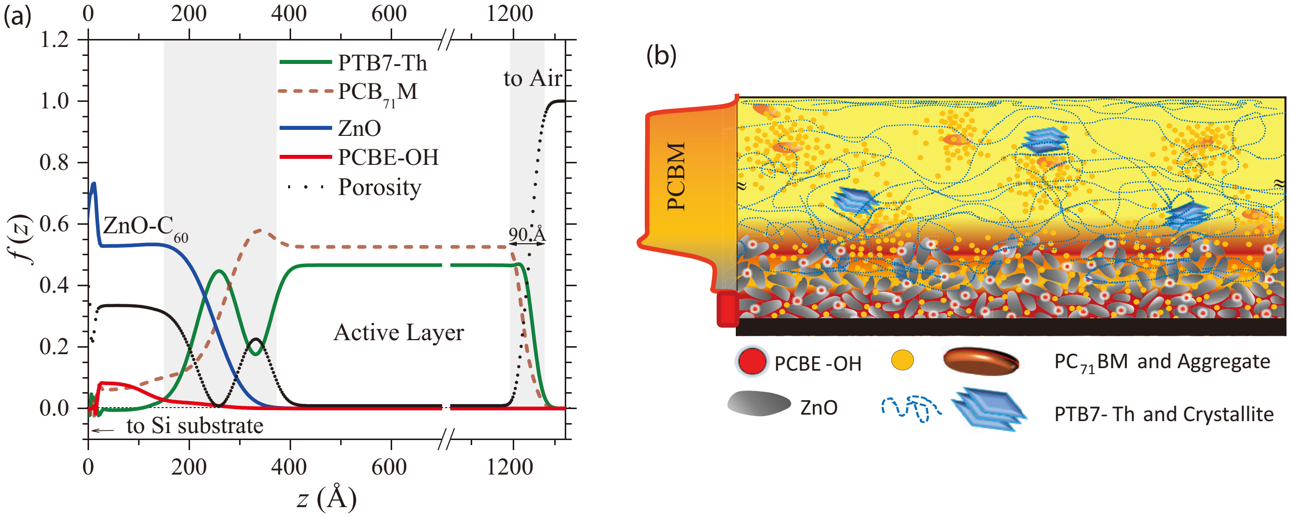

Figure 2. (a) Depth composition (volume fraction) profiles $f(z)$ for the active layers of PTB7-Th: PC71BM (1:1.5, w/w) on ZnO-C$_{60}$. Shaded areas highlight the surface and interface transition zones of distinct phase segregations. (b) Schematics for the vertical distributions of PTB7-Th and PC71BM of the active layer spin-coated on the ZnO-based CBLs, with the doped fullerene-derivative PCBE-OH enriched at the bottom part of the CBL (bridging the pathway for electrons).

3. Conclusion

We have developed a new methodology on the basis of contrast variation with neutron and anomalous X-ray reflectivity, which can map successfully the multi-component depth compositions of a model PSC with ZnO-based cathode buffer layers. The results reveal the differential vertical diffusion behaviors of the PSC components into the ZnO cathode buffer layer and the critical yet long-overlooked porosity distribution of the ZnO CBL. The advantages of doping ZnO CBLs with fullerene-derivatives are illustrated with the modified interfacial structures across the ZnO-fullerene CBL and the selectively enhanced vertical diffusion of the fullerene-derivatives from the active layer. The hence established depth-concentration gradient of fullerene-derivatives in the ZnO-C_{60} CBL is associated with the improved electron mobility and device performance; this positive correlation suggests a new CBL design concept with progressive matching of conduction bands in inverted PSCs. With neutron reflectivity and synchrotron anomalous X-ray reflectivity for rich scattering contrast variations, the developed methodology opens a new channel to resolve increasingly complicated interface structures and depth-compositions of PSCs with multi-doped, metal-oxide cathode buffer layers.

4. Instruments

Anomalous X-ray reflectivity measurements were carried out at Beamline 07 of the Taiwan Light Source (TLS) of the National Synchrotron Radiation Research Center (NSRRC), Hsinchu. Neutron reflectivity measurements were conducted at BL16 SOFIA neutron reflectometer in J-PARC MLF, Japan, with data collected in time-of-flight mode.

References

[1] J.-J. Kang, et al. Small **14**, 1704310 (2018).
[2] W.-R. Wu et al. Adv. Energy Mater. **7** 1601842 (2017).
[3] H.-J. Liu et al. Soft Matter, **7**, 9276 (2011).
[4] H. Liao, et al. Adv. Mater. **25**, 4766 (2013).

J.-J. Kang[1,2], T.-Y. Yang[3], Y.-K. Lan[4], W.-R. Wu[1], C.-J. Su[1], S.-C. Weng[1], N. L. Yamada[5,6], A.-C. Su[3], and U- Jeng[1,3]

[1]*National Synchrotron Radiation Research Center, Taiwan;* [2]*Physik-Department Technische Universität München, Germany;* [3]*Department of Chemical Engineering, National Tsing Hua University, Taiwan;* [4]*National Chung Shan Institute of Science and Technology, Taiwan;* [5]*Neutron Science Section, Materials and Life Science Division, J-PARC Center;* [6]*Institute of Materials Structure Science, KEK*

Probing a Unique Spin Texture of 4*f* Electron Magnet EuPtSi

1. Introduction

Magnetic skyrmions are particle-like, topologically non-trivial spin textures that have attracted interest because of their fundamental aspects as well as applications due to their potential as a low-power-consumption device. The magnetic skyrmion lattice can be represented by a triple-***q*** magnetic order in which three helical propagation vectors make an angle of 120° with each other in the plane normal to the applied field ***H***. Therefore, the six-fold magnetic pattern in the plane normal to ***H*** in the neutron diffraction is a crucial evidence for a formation of skyrmion lattice. This realization was first identified in a chiral magnet MnSi by the small angle neutron scattering [1]. This discovery has triggered an intensive search for compounds with similar crystal structures, leading to the discovery of their existence in FeGe [2] and the insulator Cu_2OSeO_3 [3]. Various characteristic properties have been unveiled as the number of skyrmion compounds has increased. Unlike this diversity, magnetic ions have been mostly limited to 3*d* transition metal elements.

Recently, high-quality single crystals of the 4*f* electron compound EuPtSi with a similar crystal structure have been grown. In EuPtSi, seven 4*f* electrons carry magnetism. This compound exhibits an antiferromagnetic transition at $T_N = 4$ K at a zero magnetic field [4]. Characteristic features emerged under magnetic fields, including a field-induced phase, *i.e.*, the *A*-phase, which appeared only at a finite temperature and a magnetic field, as shown in Fig. 1. This feature, common to the skyrmion phase of MnSi, implies the existence of a magnetic skyrmion in EuPtSi. To obtain microscopic insights into magnetic ordering phenomena in EuPtSi, single-crystal neutron diffraction experiments were carried out.

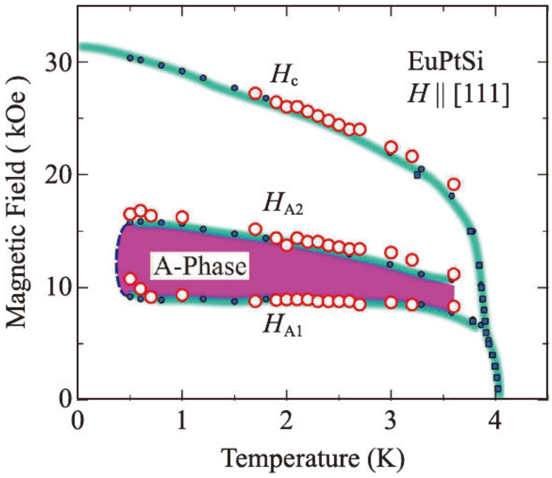

Figure 1. Magnetic phase diagram of EuPtSi for ***H*** || [111] [4]. The field-induced *A*-phase only exists at a finite temperature and magnetic field.

2. Experiment

Single crystals of EuPtSi were grown by the Bridgman method using naturally occurring Eu. Several crystals with typical sizes of $2 \times 2 \times 1$ mm^3 were used in the following experiments.

Single crystal neutron diffraction experiments at zero field were carried out on the time-of-flight Laue diffractometer SENJU at BL18 of MLF, J-PARC. A half-polarized neutron scattering experiment and single-crystal diffraction experiments under the magnetic field were carried out on the polarized triple-axis spectrometer HB-1 and the wide-angle neutron diffractometer WAND^2, respectively, both installed at the High Flux Isotope Reactor (HFIR), Oak Ridge National Laboratory (ORNL), U.S.A..

3. Magnetic structure at zero field

A neutron scattering intensity map of (*h*, *k*, 0) recorded at 0.3 K on SENJU is displayed in Fig. 2. In addition to a number of nuclear Bragg peaks with integer *h* and *k*, superlattice reflections with a rectangular pattern were identified around each nuclear peak [5]. The observed magnetic peaks are characterized by the ordering vector $\boldsymbol{q}_1 = (0.2, 0.3, 0)$. Note that there is no peak for $\boldsymbol{q} = (0.3, 0.2, 0)$ even with the cubic structure. The result reveals that the crystal structure is consistent with the symmetry $P2_13$ and the present sample consists of a single domain.

In order to get further insights into the magnetic structure with $\boldsymbol{q}_1$, the half-polarized neutron scattering experiments were performed. In case that incoming neutron spins are aligned parallel/antiparallel to the scattering vector *Q* (called *x* channel), the magnetic peak was observed only for the antiparallel configuration (I_x^-) as displayed in Fig. 3. A distinct difference between parallel (I_x^+) and antiparallel (I_x^-) configurations, and an intense peak only for I_x^- indicate that Eu magnetic moments form an anti-clockwise helix in the plane perpendicular to $\boldsymbol{q}_1$, namely, the magnetic structure in the ground state has a chirality [5].

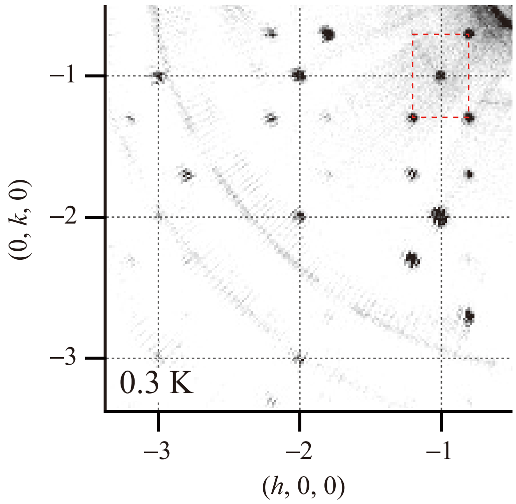

Figure 2. Neutron scattering intensity map of the (*h*, *k*, 0) plane at 0.3 K at zero field [5].

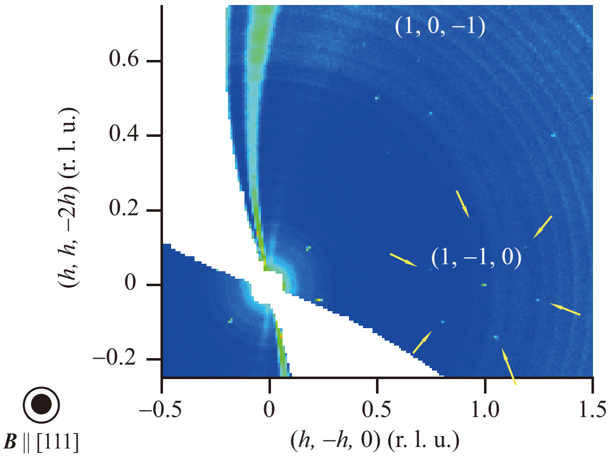

Figure 4. Neutron scattering intensity map of the plane normal to the applied field ***H***||[111] recorded in the A-phase [5].

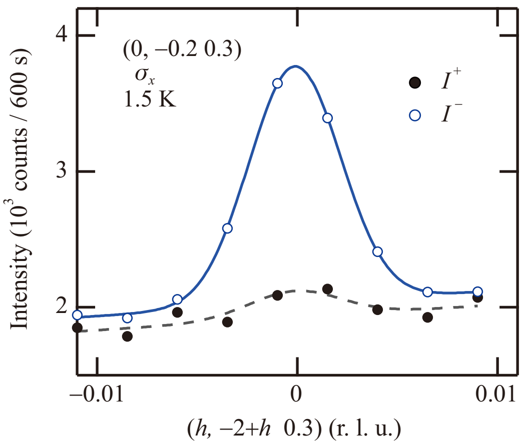

Figure 3. Half-polarized neutron scattering profile of the magnetic reflection (0, –0.2, 0.3) at 1.5 K [5].

4. Magnetic structure in the *A*-phase

As a next step, the magnetic structure in the field-induced *A*-phase was investigated by single-crystal neutron scattering experiments for the field applied along the [111] direction using the vertical field magnet. In this setup, the horizontal scattering plane is defined by the two orthogonal vectors (*H*, –*H*, 0) and (*H*, *H*, –2*H*). The magnetic peak of the helical structure $\boldsymbol{q}_1$ does not exist in this horizontal plane. By applying magnetic field of 12 kOe at 1.9 K to enter into the *A*-phase, the magnetic patterns exhibit substantial change; magnetic peaks emerge in the horizontal scattering plane and form a six-fold pattern around the nuclear magnetic peaks, as illustrated in Fig. 4 [5]. The observed hexagonal peak can be described by the peculiar, three ordering vectors of $\boldsymbol{q}_{A1}$ = (0.09, 0.20, –0.28), $\boldsymbol{q}_{A2}$ = (0.20, –0.28, 0.09) and $\boldsymbol{q}_{A3}$ = (–0.28, 0.09, 0.20). Note that these three ordering vectors are equivalent with cyclic permutation and make an angle of 120° with each other. And the periodic length of $\boldsymbol{q}_{\mathrm{A}}$ is the same as $\boldsymbol{q}_1$. These characteristic features, (i) the three ordering vectors make an angle of 120° in the plane normal to the applied field, (ii) the same periodicity as in the ground state helimagnetic structure, are common to the archetypical skyrmion compound MnSi. The present result, together with the emergence of huge topological Hall effect, demonstrates a formation of the skyrmion lattice in the *A*-phase of EuPtSi, a first example in the 4*f* electron magnets [5].

Contrary to the common features mentioned above, there are distinct differences between EuPtSi and MnSi. One of the examples is the periodic length. The periodicity in MnSi is quite long, requiring small-angle neutron scattering to separate magnetic and nuclear peaks, whereas the 'standard' diffraction is sufficient to reveal magnetic patterns of EuPtSi owing to its shorter periodic length: 18 versus 1.8 nm in MnSi and EuPtSi, respectively. In addition, the *A*-phase in EuPtSi was stabilized over a relatively wide temperature range, whereas that of MnSi exists over only a narrow region in close proximity to the transition temperature. Overall, the discovery of a magnetic skyrmion phase in 4*f* electron systems has provided a new direction to explore other compounds and has unveiled more characteristics of skyrmions.

References

[1] S. Mühlbauer, B. Binz, F. Jonietz, C. Pfleiderer, A. Rosch, A. Neubauer, R. Georgii, and P. Boni, Science **323**, 915 (2009).

[2] H. Wilhelm, M. Baenitz, M. Schmidt, U. K. Rößler, A. A. Leonov, and A. N. Bogdanov, Phys. Rev. Lett. **107**, 127203 (2011).

[3] S. Seki, X. Z. Yu, S. Ishiwata, and Y. Tokura, Science **336**, 198 (2012).

[4] M. Kakihana, D. Aoki, A. Nakamura, F. Honda, M. Nakashima, Y. Amako, S. Nakamura, T. Sakakibara, M. Hedo, T. Nakama, and Y. Ōnuki, J. Phys. Soc. Japan **87**, 023701 (2018).

[5] K. Kaneko, M. D. Frontzek, M. Matsuda, A. Nakao, K. Munakata, T. Ohhara, M. Kakihana, Y. Haga, M. Hedo, T. Nakama, and Y. Ōnuki, J. Phys. Soc. Japan **88**, 013702 (2019).

K. Kaneko[1,2], M. D. Frontzek[3], M. Matsuda[3], A. Nakao[4], K. Munakata[4], T. Ohhara[2], M. Kakihana[5], Y. Haga[6], M. Hedo[7], T. Nakama[7], and Y. Ōnuki[7]

[1]*Materials Sciences Research Center, JAEA;* [2]*Neutron Science Section, Materials and Life Science Division, J-PARC Center;* [3]*Neutron Scattering Division, Oak Ridge National Laboratory;* [4]*Neutron Science and Technology Center, CROSS;* [5]*Graduate School of Engineering and Science, University of the Ryukyus;* [6]*Advanced Science Research Center, JAEA;* [7]*Faculty of Science, University of the Ryukyus*

In Situ Neutron Diffraction on Phase Transformations for a 1.5Mn-1.5Si-0.2C Steel

1. Introduction

In the past, a steel sample was interruptedly cooled from an elevated temperature in order to freeze its microstructure and then observations were carried out at room temperature to monitor the microstructural evolution during heat treatment. In the case of low alloy steels, austenite phase at a high temperature transforms to martensite during quenching so that the high temperature microstructure is changed. Therefore, in situ observations of microstructural change during heat treatment have been attempted by using various techniques like confocal scanning laser microscopy, scanning electron microscopy (SEM)/electron back scatter diffraction (EBSD), X-ray diffraction and so on. It should be, however, noted that the surface layer of a specimen is easily damaged at elevated temperatures even in vacuum or inert gas atmosphere; oxidation, decarburization, *etc.* hinder the collection of real information. In this study, we employed dilatometry, SEM/EBSD observation, X-ray diffraction and in situ neutron diffraction to monitor phase transformations in situ during heating and cooling for a Mn-Si-C steel [1, 2].

2. Experimental procedures

The details concerning the specimen preparation were reported in refs. [1–3]. The chemical compositions of the steel used were 0.20C-1.50Mn-1.52Si-0.009P-0.001S in mass%. The starting microstructure was controlled to consist of ferrite, bainite and austenite. As a popular experimental method, dilatometry test was performed, where the specimen was heated with a speed of 0.05°C/s up to 950°C, held there for 600 s, and then cooled with –0.05°C/s down to 400°C. In situ SEM/EBSD and X-ray diffraction measurements were carried out using similar heat history but with step-wise control of the specimen temperature (the details are covered in refs. 1 and 2). For in situ neutron diffraction during heating and cooling, five steel sheets with 1.2 mm in thickness, 30 mm in length and 4–6 mm in width were stacked into nearly cylindrical shape, and set in a conventional dilatometer, which was installed into an engineering neutron diffractometer, BL19, Takumi at the Materials and Life Science Experimental Facility of the Japan Proton Accelerator Research Complex (MLF J-PARC) operated at 400 KW (the maximum designed power is 1 MW). A slit of 5 × 5 mm^2 for the incident beam and a 5 mm collimator for the diffraction beam were used in a medium intensity mode. The specimens were set in such a way that the angle between the incident beam and the longitudinal direction (rolling direction: RD) of a specimen was 45 degrees. The specimens were heated to 950°C and cooled with a heating or cooling speed of 0.05°C/s in vacuum. Using orthogonally installed two detector-banks, diffraction profiles with respect to RD and ND were recorded simultaneously. The data obtained for every 60 s were analyzed using the Z-Rietveld code [4].

3. Experimental results and discussion

The obtained dilatometry curve is shown in Fig. 1. During heating to 950°C and subsequent cooling, the change in the specimen's length with temperature was found to deviate from the thermal expansion or contraction line, indicating the occurrence of phase transformations. Here, the thermal expansion coefficients of ferrite (K^{α}) and austenite (K^{γ}) were determined to be 13.5 × 10^{-6}/°C and 21.0 × 10^{-6}/°C, respectively. This deviation was attributed to the expansive strain of austenite to ferrite transformation. On cooling, the ferrite transformation speed was higher in the beginning, then slowed down and accelerated again after point P, which is likely to indicate the onset of pearlite transformation.

Changes in austenite 111γ and ferrite 110α peaks obtained by in situ neutron diffraction during heating and cooling are shown in Fig. 2 together with the sample temperature as a function of elapsed time. Here,

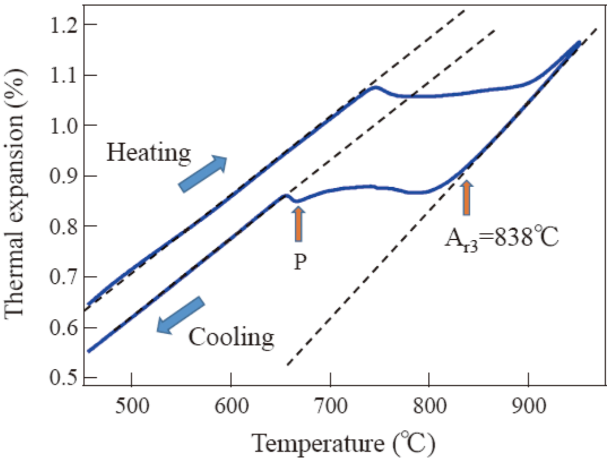

Figure 1. Result of dilatometry test for monitoring phase transformations [2].

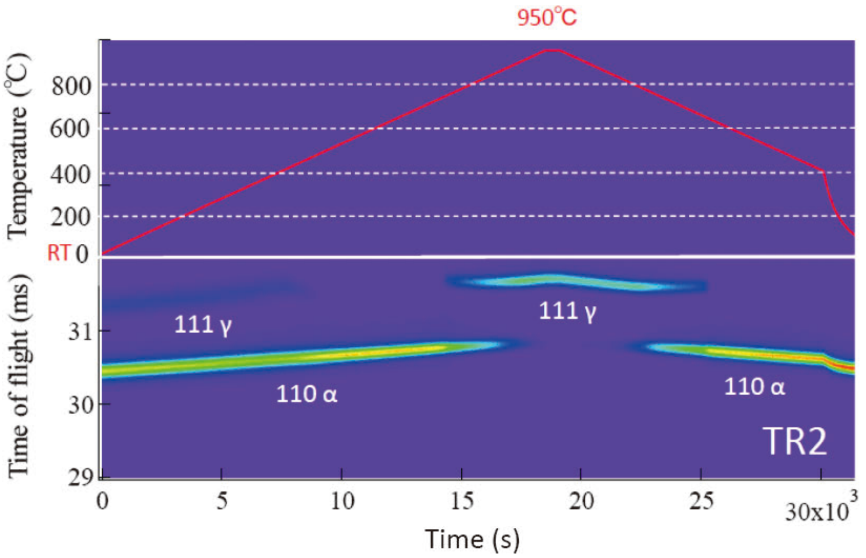

Figure 2. Changes in neutron diffraction intensities for 111 austenite (γ) and 110 ferrite (α) with heating and cooling obtained in the axial direction [1].

only the results of cooling [2] are discussed. As seen in Fig. 2, ferrite transformation started at about 850°C and finished at 620°C. The austenite volume fraction (f_γ) was determined using the Z-Rietveld software [4]. As seen in Fig. 3, the f_γ decreases rapidly in the beginning, then slows down before the arrowed point P and decreases rapidly again after the point P with the temperature reduction. The starting temperature of ferrite transformation shows a good agreement with the result of dilatometry. Contrary to these neutron results, the transformation temperatures determined either by SEM/EBSD or X-ray diffraction were much higher, because of the decrease in Mn and C concentrations near the surface at elevated temperatures. Only neutron diffraction enables us to monitor the bulky averaged information, which is hardly influenced by surface phenomena.

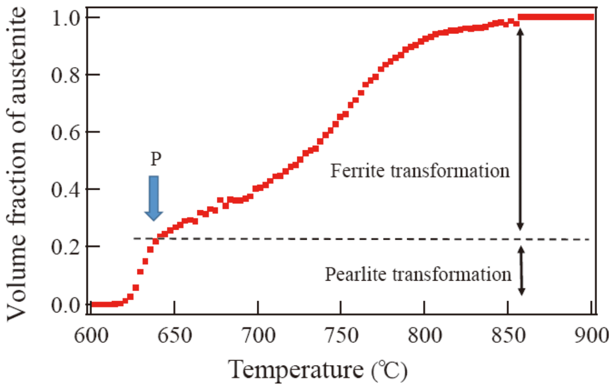

Figure 3. Change in austenite volume fraction during cooling determined by *in situ* neutron diffraction measurement [2].

Different from the dilatometry measurement, *in situ* neutron diffraction provides fruitful insights on microstructural change. For example, the lattice parameters of ferrite and austenite were determined using the Rietveld analysis and the obtained results are presented in Fig. 4. The austenite lattice parameter is believed to depend on temperature (T), carbon concentration ($C(mass\%)$) and elastic internal strain (ε), *i.e.*, $a^\gamma(T,C,\varepsilon)$. Similarly, the ferrite lattice parameter is, hereafter, described as $a^\alpha(T,C,\varepsilon)$ although the carbon content in ferrite is very small. Thermal expansion and contraction could be satisfactorily fitted by a linear function. For austenite, the data from 840 to 940°C were expressed by $a^\gamma(T,0.20,0) = (0.3580 \pm 0.0005) + (7.991 \pm 0.006) \times 10^{-6}\,T$ (nm) and those from 550 to 610°C for ferrite by $a^\alpha(T,0,0) = (0.2863 \pm 0.0009) + (4.479 \pm 0.008) \times 10^{-6}\,T$ (nm). Thermal expansion coefficient was calculated using the lattice parameter of 0.3646 nm at 820°C for K^γ and 0.2889 nm at 575°C for K^α and the obtained results were, $K^\gamma = 21.9 \times 10^{-6}$/°C and $K^\alpha = 15.5 \times 10^{-6}$/°C, respectively. These values show good agreement with those determined by dilatometry in Fig. 1.

It is clear in Fig. 4 that the ferrite lattice parameter deviates from its thermal contraction line. This suggests that compressive internal stress generated due to the transformation strain in ferrite phase. On the other hand, the austenite lattice parameter deviates towards the upper side. This must be due to the internal stresses balanced with those in ferrite. Another important origin for this deviation would be carbon enrichment. The deviation from the thermal expansion line is attributed

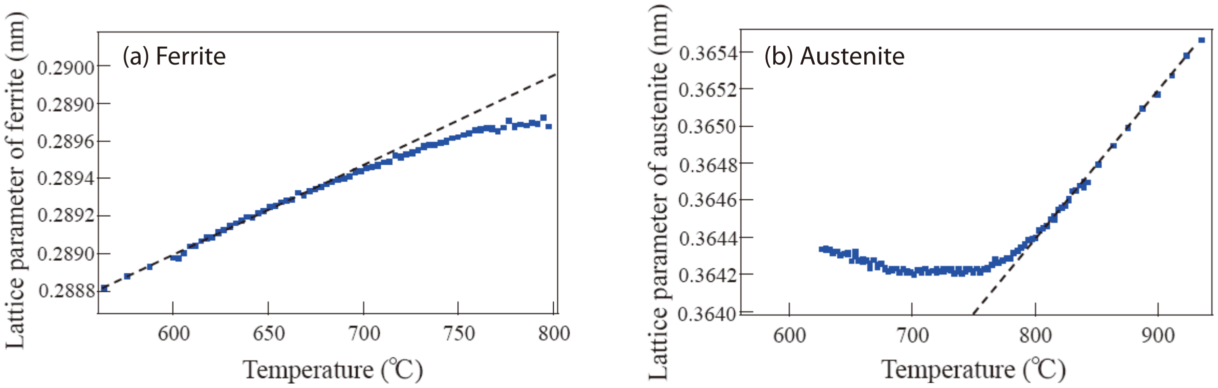

Figure 4. Changes in lattice parameters of ferrite (a) and austenite (b) with cooling determined by *in situ* neutron diffraction measurement [2].

to transformation strains, thermal misfit strains and carbon enrichment in austenite. The volume strain of austenite to ferrite transformation was estimated to be 0.981% [2]. Assuming isotropic expansion, transformation strains (ε_{ij}^{trans}) are described as $\varepsilon_{11}^{trans} = \varepsilon_{22}^{\mathrm{trans}} = \varepsilon_{33}^{\mathrm{trans}} =$ 0.327%. If one computed transformation strains using parameters at 0°C, ε_v would become 2.3% and then ε_{11}^{trans} = 0.767%. That is, the strain ε_v depends on transformation temperature. As it will be discussed later, ε_{ij}^{trans} is also influenced by the carbon concentration of austenite, which increases with ferrite transformation and lowers the value of ε_{ij}^{trans}. In an austenite-ferrite temperature region, thermal misfit strain ($\varepsilon_{ij}^{trans}(T)$) is generated due to the difference in thermal expansion coefficients between austenite and ferrite, which is -6.4×10^{-6} (/°C) estimated from the above results. The thermal history depends on the time after ferrite forms and could be calculated as reported in ref. [2]. Several empirical equations related to the effect of carbon concentration on austenite lattice parameter at RT have been proposed and the following relationship [5] is adopted in this study: $a^{\gamma}(RT,C,0) = a^{\gamma}(RT,0,0) + 0.0033C\ (mass\%) = 0.3573 + 0.0033C\ (mass\%)$. The estimated $a^{\gamma}(RT,C,0)$ of 0.35951 nm gave the carbon concentration of 0.667 mass% [2]. The pearlite volume fraction obtained by SEM microscopy was 26.2%. If the carbon concentration in ferrite and grain boundary segregation were neglected, the carbon concentration in austenite could be calculated as 0.20 mass% (bulk average) /0.26 = 0.763 mass%. Therefore, pearlite transformation is expected to start when the carbon concentration of austenite is enriched to become approximately 0.7 mass%. This seems to be reasonable in comparison with the point P in Fig. 3. If one estimated the austenite fraction at P by the so-called lever rule in Fig. 1 using the drawn thermal contraction lines for ferrite and austenite, it would be about 10 %, which is much smaller than those determined either by micrography or neutron diffraction. This is because the drawn line is for austenite with 0.2 mass% C not 0.7 mass% C.

The lattice parameter is influenced by the hydrostatic component of elastic strains. During ferrite transformation on continuous cooling, three kinds of eigen strains (ε_{ij}^{*}) appear as mentioned above. They include transformation strain (about 0.327%), thermal misfit strain (about 0.032%) and carbon enrichment in austenite (0–0.647%). The internal stresses are caused by ε_{ij}^{*}, but high local internal stresses must be relaxed by diffusion and/or dislocation motion at elevated temperatures. The plastic relaxation is too difficult to take into consideration quantitatively here because its mechanism is uncertain. However, the unrelaxed state could be evaluated using the Eshelby inclusion theory [2]. The long range internal stresses, *i.e.*, phase stresses caused by ε_{ij}^{*} can be written as $\sigma_{ij}^{\gamma} = -f_{\alpha}\, C_{ijkl}\, (S_{klmn} - I)\varepsilon_{mn}^{*}$ and $\sigma_{ij}^{\alpha} = (1 - f_{\alpha})C_{ijkl}\, (S_{klmn} - I)\varepsilon_{mn}^{*}$ where C_{ijkl} and I refer to elastic moduli and unit tensor. Assuming spherical grain and the Poisson ratio of 0.30, the Eshelby tensor, S_{ijkl}, are expressed as $S_{1111} = S_{2222} = S_{3333} = \frac{7-5\nu}{15(1-\nu)} = 0.524$, $S_{2233} = S_{3311} = S_{1122} = S_{3322} = S_{1133} = S_{2211} = \frac{5\nu-1}{15(1-\nu)} = 0.0476$, $S_{1212} = S_{2323} = S_{3131} = \frac{-(4-5\nu)}{15(1-\nu)} = -0.238$. Here, three kinds of origins for ε_{ij}^{*} can be regarded to have isotropic feature, $\varepsilon_{ij}^{*} = q$ when i = j and $\varepsilon_{ij}^{*} = 0$ when i ≠ j. Employing the general isotropic Hooke's equation for C_{ijkl}, $\sigma_{11}^{\gamma} = \sigma_{22}^{\gamma} = \sigma_{33}^{\gamma} = -f_{\alpha} \times (3.57Eq)$ can be obtained, where E stands for Young modulus. Needless to say, the sum of phase stresses is zero and then, $\sigma_{\mathrm{ij}}^{\gamma} \times \mathrm{f}_{\gamma} + \sigma_{\mathrm{ij}}^{\alpha} \times \mathrm{f}_{\alpha} = 0$. The elastic internal strain contributing to diffraction peak shift is described by $\beta_{11} = \frac{1-2\nu}{E}\sigma_{11}$ where $\beta_{11} = \beta_{22} = \beta_{33} = \beta$. Stress or strain condition is hydrostatic in the present case. Paying attention to austenite phase, tensile hydrostatic strain increases in the beginning of ferrite transformation caused by transformation strain and thermal misfit strain. In conclusion, the lattice parameter of austenite could be expressed by $a^{\gamma}(T,C,\varepsilon) = (a^{\gamma}(RT,0,0) + 0.0033C)(1 + K^{\gamma}T)(1 + \beta)$.

4. Conclusions

The ferrite and pearlite transformation kinetics showed excellent agreements between dilatometry and neutron diffraction, whereas the ferrite formation was observed to start at a much higher temperature in the X-ray diffraction measurement. Such discrepancy in transformation temperature is attributed to the change in chemical composition near the surface of a specimen heated to elevated temperatures; oxidation and changes in Mn and C concentrations were found at near surface layer after the measurement. *In situ* neutron diffraction measurement enables us to investigate the changes in lattice constants of ferrite and austenite, showing not only thermal contraction but also carbon enrichment in austenite and phase stresses. The transformation strains, thermal misfit strains, carbon enrichment in austenite and generation of phase stresses during ferrite transformation were discussed from the neutron diffraction data using the Eshelby inclusion theory. The carbon concentration for the onset of pearlite transformation was estimated and the diffraction profile line broadening caused by pearlite formation was presented.

Acknowledgements

This paper is based on the results obtained from a project commissioned by the New Energy and Industrial Technology Development Organization (NEDO). The neutron diffraction measurements were performed at J-PARC MLF under a user program 2015A0153.

References

[1] Y. Tomota, et al., ISIJ Int., **57** (2017), 2237.
[2] Y. Tomota, et al., ISIJ Int., **58** (2018), 2125.
[3] Y. Tomota, et al., Tetsu-to-Hagané, **103** (2017), 573.
[4] R. Oishi, et al., Nucl. Instrum. Meth. A, **600** (2009), 94.
[5] R. C. Ruhl and M. Cohen, Trans. Metall. Soc. AIME, **245** (1969), 241.

Y. Tomota[1,2], Y. X. Wang[1], T. Ohmura[1], N. Sekido[1,3], S. Harjo[4], T. Kawasaki[4], W. Gong[5], and A. Taniyama[6]

[1]*Research Center of Structure Materials, National Institute for Materials Science;* [2]*National Institute of Advanced Industrial Science and Technology;* [3]*Graduate School of Engineering, Tohoku University;* [4]*Neutron Science Section, Materials and Life Science Division, J-PARC Center, Japan Atomic Energy Agency;* [5]*Elements Strategy Initiative for Structural Materials, Kyoto University;* [6]*Advanced Technology Research Laboratories, Nippon Steel Co.*

Average and Local Structure Analysis of Mn-based Li-ion Cathode Materials by Neutron and Synchrotron X-ray Sources

1. Introduction

The lithium ion battery that is currently in use, was realized by using $LiCoO_2$ with a layered rock-salt type structure as a positive electrode material [1]. In recent years, the attention has focused on the layered type $LiMnO_2$ [2, 3] or xLi_2MnO_3-(1−x)$LiMO_2$ (M = Mn, Ni, Co) solid solution [4–8]. However, the layered rock-salt type $LiMnO_2$ was a metastable phase not synthesized by solid-state method [3, 9, 10]. The crystal structure has not been completely revealed [9]. In the average structure analysis such as Rietveld method, it is difficult to discuss the effects of substituted Ti distinctly from Mn or solid solution with disordered arrangements because the Mn and the substituted elements occupied the same crystallographic site. Therefore, we performed local structure analysis by using a supercell obtained by expanding the unit cell refined by diffraction study. We focused on the two Li-ion cathode materials: I. layered rock-salt $Li_xMn_{0.9}Ti_{0.1}O_2$ and II. $0.4Li_2MnO_3$-$0.6LiMn_{1/3}Ni_{1/3}Co_{1/3}O_2$.

2. Experimental

The $Li_xMn_{0.9}Ti_{0.1}O_2$ ($x < 0.7$) was synthesized by the Na/Li ion-exchange [9, 10]. The $0.4Li_2MnO_3$-$0.6LiMn_{1/3}Ni_{1/3}Co_{1/3}O_2$ was synthesized by co-precipitation method [4–8]. The crystalline phases were identified by XRD (X'pert pro, PANalytical) with Cu Kα radiation and by ICP-AES (ICPE-9000, Shimadzu, Ltd.). The high resolution XRD data were collected by synchrotron XRD at SPring-8 (BL19B2). The diffracted patterns were analyzed by Rietveld method. The X-ray absorption fine structures (XAFS) were measured at BL14B2, and their data were analyzed.

Neutron powder diffractions were taken using a time-of-flight diffractometry of iMATERIA (BL20) at the J-PARC. The structural refinements using neutron diffraction data were performed by Rietveld method using Z-Code [11, 12]. We also performed a high-energy X-ray diffraction experiment, i.e. total scattering, with an incident beam of 61.5 keV by BL04B2 at SPring-8 and corrected the obtained data by using a standard program [13]. Neutron total scatterings were collected at NOVA (BL21), J-PARC. The PDF analysis for total scattering data was performed by PDFgui [14].

The electrochemical cell was constructed using HS cell (Hohsen Ltd.). The cathode on the Al current collector consisted of the synthesized active material, SUPER C65 (IMERYS Co. Ltd.), polytetrafluoroethylene (PTFE). The anode, electrolyte and separator were used as metal Li, 1 mol/L $LiPF_6$-EC:DMC (1:2 vol. ratio) and polypropylene (Celgard #2400), respectively. A charge-discharge apparatus (HJ1010m SM8A, Hokuto Denko Corp.) was employed to conduct the charge/discharge cycle test at 60°C or 25°C.

3. Results and discussion

3-I. Na/Li ion exchanged $Li_xMn_{0.9}Ti_{0.1}O_2$

The layered rock-salt structure of $Li_xMn_{0.9}Ti_{0.1}O_2$ has not been refined for the broad and unknown peaks in XRD. We synthesized the material following the method outlined in the previous report. The electrochemical measurements of $Li_xMn_{0.9}Ti_{0.1}O_2$ were also confirmed to achieve a relatively high capacity of 215 mAh g^{-1} at first cycle and 160 mA h^{-1} at 50th cycle. Although the 4 V plateau in the charge and discharge curves indicated the transition to spinel structure, the slightly changed curves implied the suppression of the spinelization by Ti-substitution [9]. The average structure for $Li_xMn_{0.9}Ti_{0.1}O_2$ was analyzed by Rietveld method. The hexagonal with $R\bar{3}m$ space group was adapted to the original structure, where the Mn and Ti, the Li and Na, and the oxygen were located at $3a$, $3b$ and $6c$ sites, respectively. Figures 1(a) and 1(b) show the Rietveld analysis for $Li_xMn_{0.9}Ti_{0.1}O_2$ using synchrotron X-ray and neutron diffractions. The results for the $Li_xMn_{0.9}Ti_{0.1}O_2$ were better fitting, which included no secondary phase but unknown peaks [9]. The bond valence sum, BVS, of the oxygen showed almost two by the analysis using neutron diffraction data, which lead to the better fitting than synchrotron XRD partly because of the sensitivity in the neutron for the light elements, Li and O. However, it was inferred that the $Li_xMn_{0.9}Ti_{0.1}O_2$ was not completely attributed to the layered rock-salt structure and was considered a slightly different structure.

The local structure analysis for the $Li_xMn_{0.9}Ti_{0.1}O_2$ was performed by the pair distribution function (PDF) analysis, where the $G(r)$ obtained by the total X-ray and the neutron total scatterings were used. The two original models were created by the super cell which was constructed by the $3a \times 3b \times c$ super cell. One was the model A defined as the simple expanded cell from the average structure analysis. The other was model B, in which one of Mn was moved to vacant Li site, assuming similar coordination of spinel structure. Figures 1(c) and 1(d) represented the results for the synchrotron X-ray and neutron total scattering data of the $Li_xMn_{0.9}Ti_{0.1}O_2$ using model B, respectively. The refined structures are shown in Fig. 2. The final reliability factors, R_w, were 16.8% and 12.5% for model A and B, respectively. Due to improved analytical accuracy, it was interpreted that there must be a local structure similar to the spinel-type. Once the Rietveld analysis was performed based on the local structure model B, the goodness of fit, S^2, was improved from 2.437 to 2.425. The Rietveld refinement of occupancy for Mn in Li layer lead to the 0.010. Therefore, the occupation of Mn in the Li layer was supported even in the diffraction method. Based on the PDF analysis, calculating and averaging the distortion parameters [15], σ^2, of TiO_6 showed to be smaller than those of MnO_6 which were derived from the Jahn-Teller effect in the $Mn^{3+}O_6$ with $3d^4$ electric coordination. The substitution of Ti with Mn led to the relaxation in MO_6 octahedra and to an improved cycle performance.

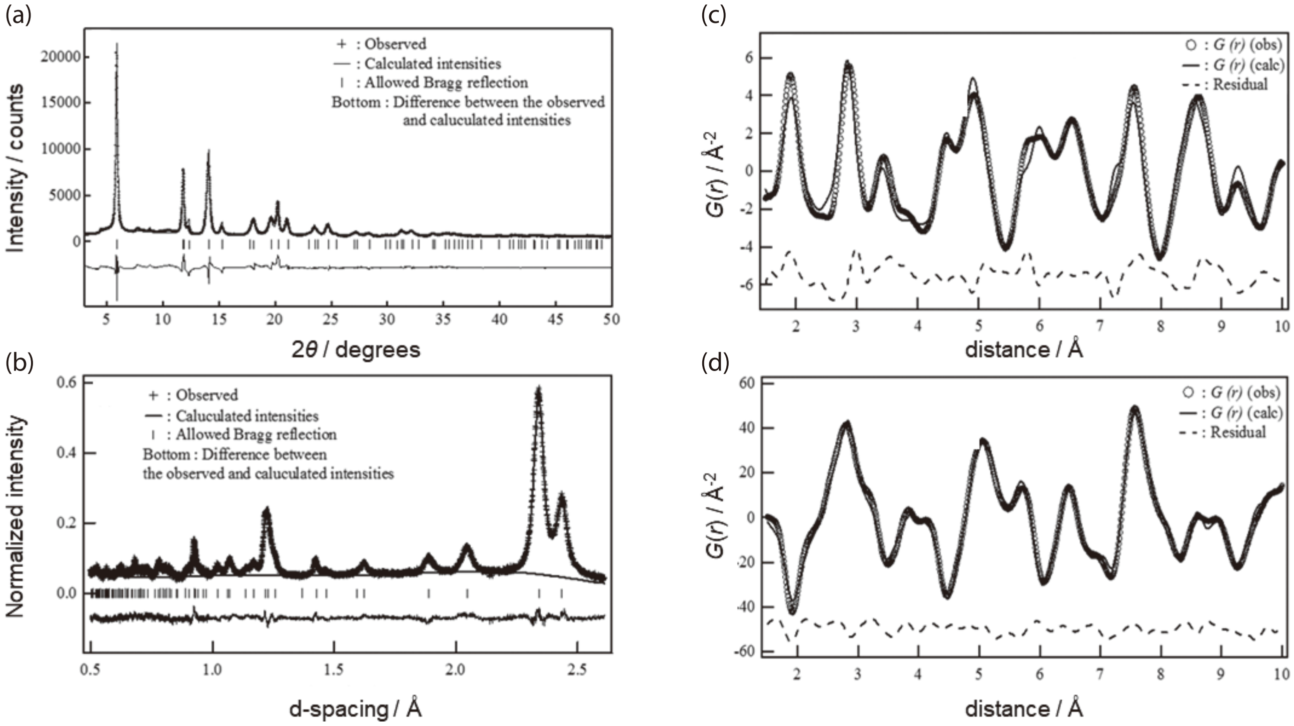

Figure 1. Rietveld analysis for (a) synchrotron XRD and (b) neutron diffraction patterns and PDF analysis for $G(r)$ derived from (c) synchrotron X-ray total scattering and (d) neutron total scattering data in $Li_xMn_{0.9}Ti_{0.1}O_2$.

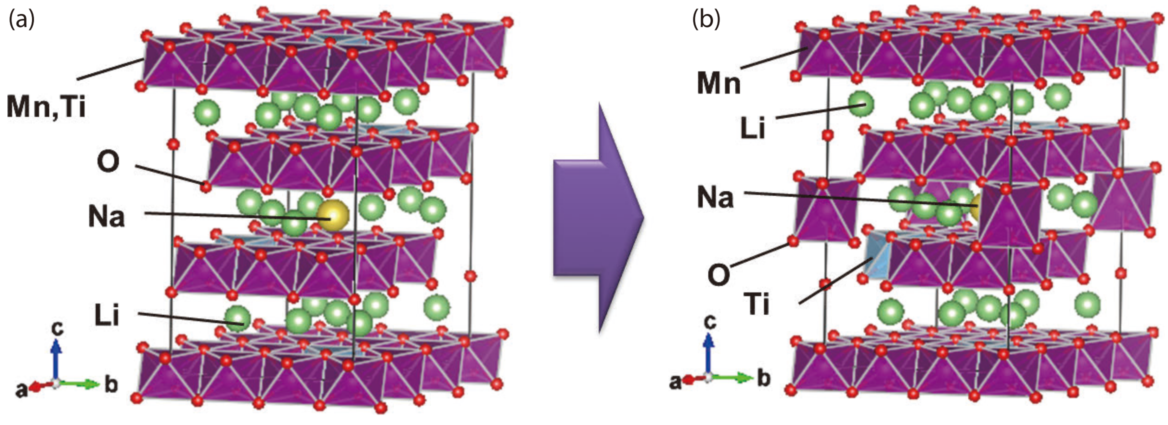

Figure 2. Refined local structures from super structure of (a) model A or (b) model B in $Li_xMn_{0.9}Ti_{0.1}O_2$.

3-II. $0.4Li_2MnO_3$-$0.6LiMn_{1/3}Ni_{1/3}Co_{1/3}O_2$

At high temperature (HT), the 4.5 V plateau increases derived from the loss of Li_2O or O_2, yielding a high initial discharge capacity of 280 mAh/g. As the cycle proceeded, the polarization became larger and the discharge potential and capacity decreased. We therefore conducted a local structural analysis using neutron and synchrotron X-ray total-scattering data to study detailed structural variations associated with the charge/discharge process. To study PDF data, we created a $3a \times 2b \times c$ supercell (yielding a total of 36 transition-metal atoms) for the initial structural model which followed a previous study [16]. For the pristine case, we performed a PDF analysis based on the $G(r)$ data obtained from neutron and synchrotron X-ray total-scattering measurements. Figures 3(a) and 3(b) show the fitting to neutron total-scattering data, the fitting to synchrotron X-ray total-scattering data, and 3(c) and 3(d) the structure obtained. The combined analysis yielded a good R_w of 8.69%. The results indicate a layered structure consisting exclusively of TM-O_6 octahedra interconnected in various directions.

Fitting the post-charging models to synchrotron X-ray total-scattering were performed for the room-temperature and high-temperature charge at 4.8 V. The R_w values were 7.64% and 12.33% for the room-temperature (RT) and HT charges, respectively. Because many Li and O atoms are lost in the HT post-charging, the local structural variations are complicated and thus it is more difficult to achieve good accuracy in the analysis, so that higher R_w values are obtained compared to the pristine. As a result, the structure contained some sites at which TM-O_6 octahedra failed to form due to Li and O loss; nonetheless, no spinel-derived tetrahedral structures were present.

Fitting the post-discharging models to synchrotron X-ray total-scattering data were also performed for the RT and HT discharge at 2.5 V. The R_w values were 7.96% and 8.85%, respectively. The insertion of Li and O atoms resulted in better fitting accuracy than the post-charging. The structures showed no spinel-derived tetrahedral structures.

In Table 1 we have separately computed distortion parameters for Ni-O_6 octahedra in TM layers and in Li layers. The results indicate that the distortion of Ni-O_6 octahedra that mix within the Li layer is particularly reduced at HT compared to RT. This means that the capacity is reversible even at HT, which we identify as one factor responsible for the increase in charging capacity. At both temperatures, the insertion of Li and O atoms upon discharge causes octahedra to form, yielding a state close to the pristine. Compared to the post-charging state, Mn becomes activated after discharge and was reduced from +4 to +3. Because the trivalent of Mn exhibits a Jahn-Teller distortion, this suggests that the distortion should increase. However, we found no evidence for such behavior; instead, the distortion decreased because of the layered structure resulting from the formation of octahedra due to Li and O insertion. Meanwhile, the valence of Co and Ni was reduced during the initial discharge from +4 to +3 and from +3 to +2, respectively, and that also contributed

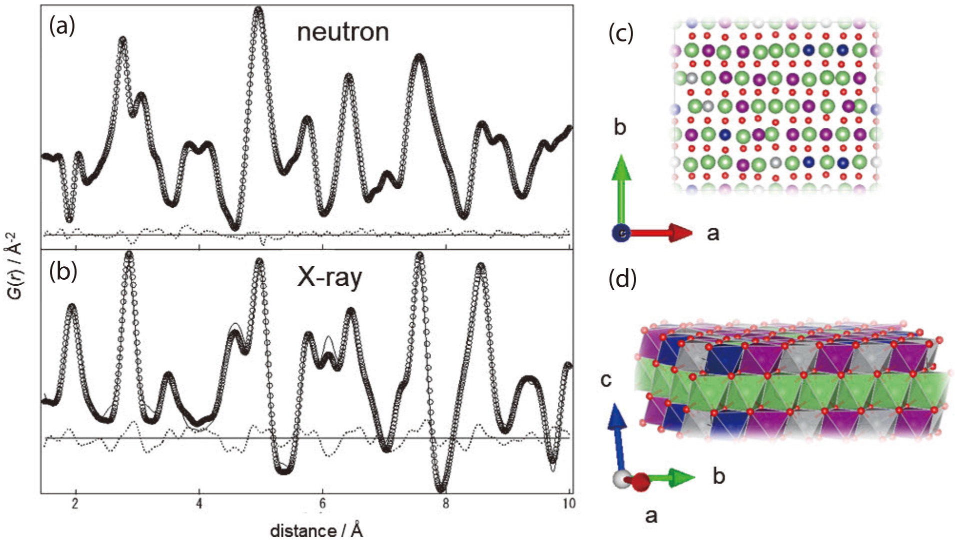

Figure 3. PDF analysis for (a) neutron and (b) synchrotron X-ray total scattering data in $0.4Li_2MnO_3$-$0.6LiMn_{1/3}Ni_{1/3}Co_{1/3}O_2$ and the local structures (c, d).

Table 1. Distortion parameters of NiO_6 octahedra located at TM or Li layer calculated by local structures from PDF fitting after charge/discharge at RT/HT.

	Charge (RT)		Discharge (RT)		Charge (HT)		Discharge (HT)	
Layer	TM	Li	TM	Li	TM	Li	TM	Li
λ	1.016	1.036	1.017	1.019	1.017	1.031	1.016	1.019
σ^2 / deg^2	45.72	93.53	36.54	40.04	34.46	64.19	32.67	39.51

to the reduced distortion. Because TM octahedra tend to exhibit less distortion at HT than at RT. Similarly to the post-charging case, the results indicate that the distortion of Ni-O_6 octahedra in both TM and Li layers was slightly reduced at HT. We attribute the fact that the structure is preserved at HT despite the loss of many Li, which yields a large reversible capacity and serves to stabilize the structure.

4. Conclusion

The improvement in cycle characteristics by Ti substitution was due to the existence of a coordination environment similar to the spinel type structure. The Mn occupied a part of the Li layer and the TiO_6 octahedral distortion was significantly smaller than the MnO_6 one. The influence of Ti substitution on the cathode property of $Li_xMn_{0.9}Ti_{0.1}O_2$ could be evaluated by the local structure analysis, which distinguished the partially substituted Ti with the Mn.

Refined distortion parameters of TM-O_6 in $0.4Li_2MnO_3$-$0.6LiMn_{1/3}Ni_{1/3}Co_{1/3}O_2$ revealed their distortions reduced at HT. The Ni-O_6 octahedra indicated that the mixing introduced less distortion at HT. This explains why the system retains its structure despite the loss of many Li at HT and shows the increased discharge capacity. Their details have been published in papers [17, 18].

References

[1] K. Mizushima, P.C. Jones, P.J. Wiseman, J.B. Goodenough, Mat. Res. Bull., **15**, 783–789 (1980).

[2] A.R. Armstrong et al., Nature, **381**, 499–500 (1996).

[3] A.R. Armstrong, A.J. Paterson, A.D. Robertson, P.G. Bruce, Chem. Mater., **14**, 710–719 (2002).

[4] N. Kumagai, J.-M. Kim, S. Tsuruta, Y. Kadoma, K. Ui, Electrochim. Acta, **53**, 5287–5293 (2008).

[5] N. Tran et al., Chem. Mater., **20**, 4815–4825 (2008).

[6] M.M. Thackeray et al., J. Mater. Chem., **15**, 2257–2267 (2005).

[7] T.A. Arunkumar, Y. Wu, A. Manthiram, Chem. Mater., **19**, 3067–3073 (2007).

[8] A. Ito, D. Li, Y. Ohsawa, Y. Sato, J. Power Sources, **183**, 344–346 (2008).

[9] N. Ishida, H. Hayakawa, H. Shibuya, J. Imaizumi, J. Akimoto, Chem. Lett., **41**, 1478–1480 (2012).

[10] N. Ishida et al., J. Power. Sources, **244**, 505–509 (2013).

[11] R. Oishi, T. Kamiyama et al., Nucl. Instrum. Methods Phys. Res., A**600**, 94–96 (2009).

[12] R. Oishi, T. Kamiyama et al., J. Appl. Crystallogr., **45**, 299–308 (2012).

[13] S. Kohara et al., J. Phys.: Condens. Matter, **19**, 506101–506115 (2007).

[14] C. Farrow et al., J. Phys. Condens. Matter., **19**, 335219–335225 (2007).

[15] K. Robinson, G.V. Gibbs, P.H. Ribbe, Science, **172**, 567–570 (1971).

[16] Y. Idemoto, Y. Sera, N. Ishida, N. Kitamura, Electrochem., **83**, 879–884 (2015).

[17] N. Ishida, K. Miyazawa, N. Kitamura, J. Akimoto, Y. Idemoto, Solid State Ionics, **325**, 209–213 (2018).

[18] Y. Idemoto, T. Hiranuma, N. Ishida, N. Kitamura, J. Power Sources, **378**, 198–208 (2018).

N. Ishida, N. Kitamura, and Y. Idemoto
Faculty of Science and Technology, Tokyo University of Science

Deformation Analysis of Reinforced Concrete Using Neutron Imaging Technique

1. Introduction

Reinforced concrete (RC), widely utilized for various architectural and civil engineering structures, is well known as a composite structure in which concrete with relatively low tensile strength and ductility is strengthened by reinforcements such as steel rods (rebars) with high tensile strength and ductility. The structural performance of RC is generally derived from the bond resistance between rebar and concrete, which can be assessed by measuring stress distribution along rebar using neutron diffraction [1]. In addition to that, it is also important to evaluate the deformation behavior of concrete around the rebar in order to discuss the mechanism of bond degradation between concrete and rebar. However, it is difficult to see internal deformation of concrete directly even if the neutron diffraction technique is employed, because neutron scattering from the hydrogen involved in concrete causes high background noise. Alternatively, image analysis techniques are typically utilized for evaluating deformation of concrete quantitatively. In this study, therefore, we aim to develop a novel method to observe internal deformation of concrete using the neutron transmission imaging technique.

2. Experimental procedure

In order to visualize the internal deformation of concrete, cement paste markers containing 34wt% Gd_2O_3 powder (hereafter called "Gd marker") were dispersed as a tracer around rebar in concrete two-dimensionally (Fig. 1). The Gd marker can make strong contrast to the concrete matrix due to high neutron cross-section of Gd. Therefore, the deformation of concrete can be detected by analyzing the displacement of the Gd markers in the neutron transmission image.

The neutron transmission images were taken by RADEN at BL22 in J-PARC MLF. The L/D ratio of the optical system of RADEN was set to 1000. The incident neutrons scattered and absorbed by the RC specimen were taken by a cooled CCD camera after being converted to visible light by a scintillator. The spatial resolution was approximately 0.2 mm. The position of the Gd marker in a neutron transmission image of the RC specimen was evaluated by an image analysis technique described below using an open source image processing program, ImageJ 1.51n [2].

3. Image Analysis

The flow of the image analysis is shown in Fig. 2. As shown in a neutron transmission image of the RC specimen in Fig. 2(a), the Gd markers in concrete can be recognized clearly. The dark area at the bottom of the center of the image represents the PVC pipe covering the rebar. In addition, the image contrast between concrete and the embedded rebar can be observed as well. The transmission image was normalized by the incident neutron flux and the shade image is depicted in Fig. 2(b). And then, the median filter was applied to a few transmission images taken at the same sample position or at the same loading, in order to remove white spot noise and to smooth the image. After applying the median filter, a Fourier transform was applied and the low frequencies in the transmission image were filtered by masking obtained by a 2D Fourier power spectrum less than 15 pixels in radius (Fig. 2(c)). After that, the spectrum obtained by excluding the low frequencies

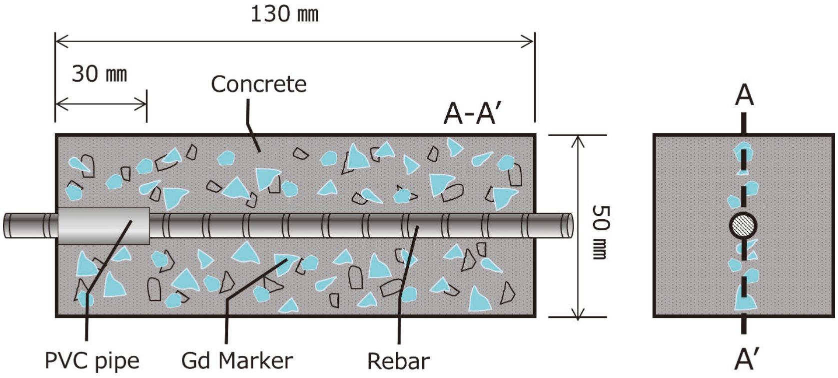

Figure 1. Schematic illustration of the RC specimen used in this study.

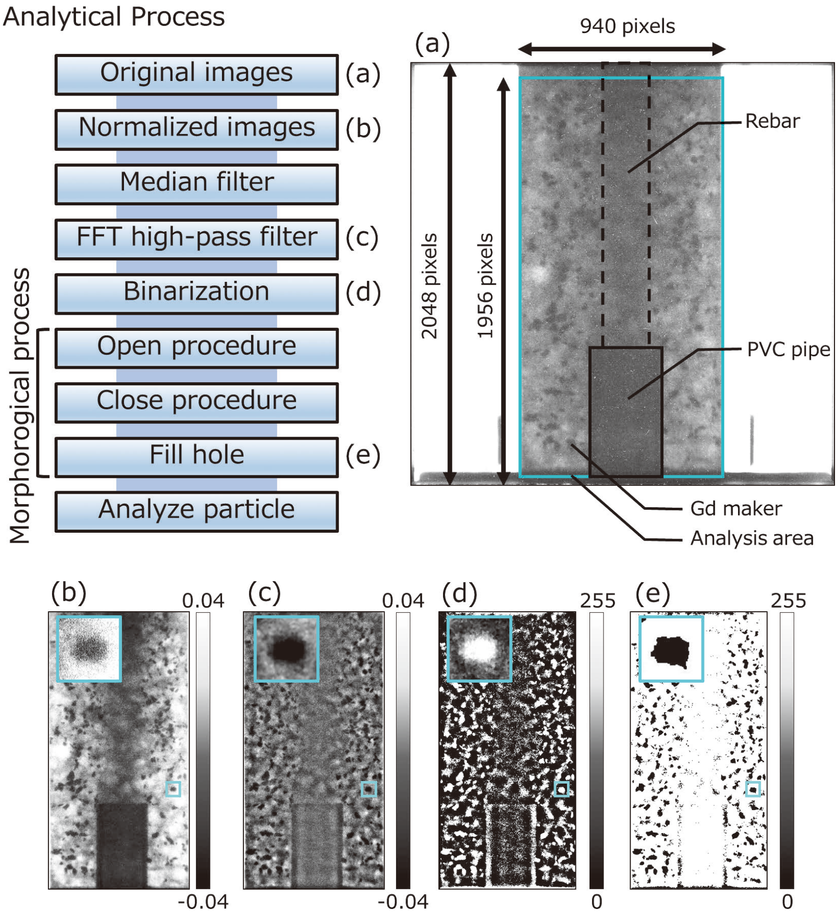

Figure 2. Transmission image of the RC specimen (a), and the images for each process, (b), (c), (d) and (e), in the analytical procedure.

was converted to the transmission image using an inverse Fourier transform procedure. This is known as a general high-pass filter, which can highlight the Gd marker images by reducing the background contrast variation representing the rebar and the PVC pipe. The transmission image obtained by the high-pass filter was binarized by defining an appropriate threshold (Fig. 2(d)). And then, using a morphological process, the spot noise on the obtained binary image was removed and the Gd marker images were shaped. Eventually, the Gd marker images were successfully extracted from the original transmission image as shown in Fig. 2(e). After extracting the Gd marker images, the center of mass (COM) for each marker was determined by analyzing particles using ImageJ. In the analysis, particles with less than 300 pixel^2 in size (equivalent to the area of a circle with a diameter of 1 mm) were omitted to distinguish from the noise. Furthermore, the particles obviously different from the Gd markers were also regarded as noise and were manually omitted as well.

4. Results and discussion

In order to confirm the spatial resolution of the proposed method, a displacement of the Gd marker image with respect to the sample stage displacement was verified at first. The displacement of each Gd marker image was evaluated by a change in the COM of each marker as a function of the travel distance of the vertical sample stage. As shown in Fig. 3, the average displacement was linearly plotted with approximately ±0.11 mm accuracy by image analysis for selected markers with higher contrast and higher circularity.

Secondary, the deformation of the RC specimen was measured under compressive deformation by analyzing the displacement of the Gd marker on the transmission image. As shown in Fig. 4, the Gd marker images move toward the loading direction proportionally to the applied loading. Furthermore, the displacement of the Gd marker images are always evaluated to be slightly smaller than the displacement of rebar measured by a displacement transducer, while their trends agree well within the error bars. This small difference might

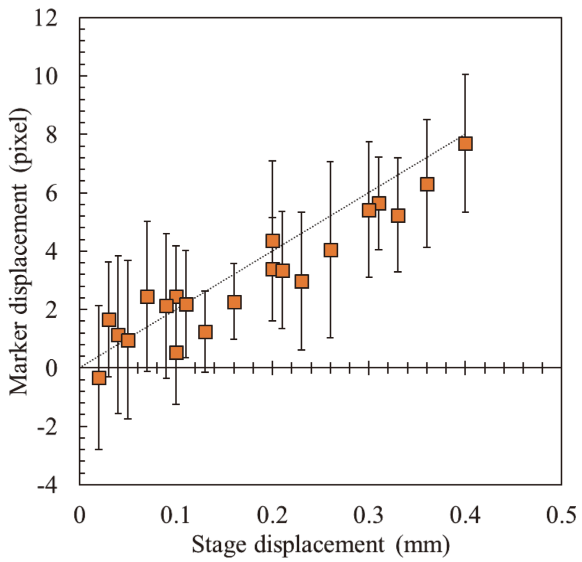

Figure 3. The relation between marker and stage displacements.

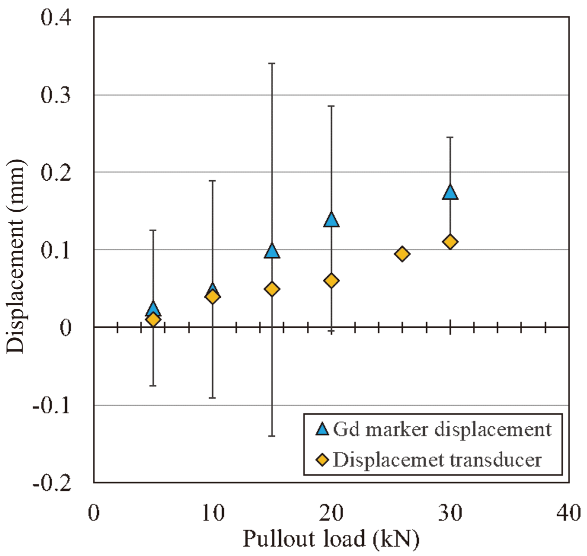

Figure 4. The relation between marker displacement and applied loading, compared with the displacement measured by a displacement transducer.

be caused by asymmetric distortion of the RC specimen under pullout loading. Selecting the appropriate Gd marker with higher contrast and circularity enables us to analyze deformation inside concrete accurately.

5. Summary

We have suggested a novel method to observe internal deformation of concrete by the neutron transmission imaging technique with image analysis. The measurement accuracy of the Gd marker displacement can be improved by choosing a spherical shaped Gd marker, by increasing the contrast of the Gd marker and also by increasing statistics accuracy. This method is expected to be utilized for clarifying the bond mechanism between concrete and rebar by observing concrete deformation around rebar combined with the bond stress distribution measured by the neutron diffraction technique.

References

[1] H. Suzuki, et al., Meas. Sci. Technol., **25** (2014) 025602.

[2] C.A. Schneider, W.S. Rasband and K.W. Eliceiri, Nature methods **9** (2012) 671–675.

H. Suzuki[1], T. Koyama[2], K. Ueno[2], and M. Kanematsu[3]

[1]*Material Sciences Research Center, JAEA;* [2]*Graduate School of Science and Technology, Tokyo University of Science;* [3]*Faculty of Science and Technology, Tokyo University of Science*

Muon May Reveal the True Worth of “Fool’s Gold”

1. Introduction

Hydrogen is the most ubiquitous element in nature, and occasionally yields an unintended effect on matter. In today’s electronics industry, hydrogen impurities in semiconductors are known to drastically change their electrical activity and characteristic of electronic devices. Hydrogen is the lightest and smallest of all the elements, therefore it is extremely difficult to discern its states and effect on host materials, especially in low concentrations. To understand how hydrogen behaves in the semiconductor FeS_2, we employed muon-spin rotation (μSR) experiments at J-PARC MLF and TRIUMF, a particle accelerator lab in Canada [1].

2. Pyrite—fool’s gold

Iron disulfide (FeS_2), also known as the mineral pyrite or fool’s gold, has created significant scientific interest and technological applications. It is a promising optoelectronic material due to its suitable indirect band gap and high absorption coefficient, which opens up great potential for emerging renewable energy applications, including photovoltaics, photodetectors, and photoelectrochemical cells [2, 3]. The interest in pyrite has also been revived due to its low toxicity, virtually infinite elemental abundance, and low raw material cost [4].

The main obstacle to the development of FeS_2 as an optoelectronic material is its low open-circuit photovoltage probably due to unintentional *n*-type conductivity. Meanwhile, it has been known for decades that natural pyrites often exhibit *n*-type conductivity which seems to be associated with hydrogen’s defects [5]. So, one may naturally suspect that hydrogen is the cause of these mysterious electrical activities in FeS_2. We cut a block of natural pyrite into slabs (see Fig. 1) and irradiated them with muon beam to implant muons into FeS_2.

3. Muogen—pseudo hydrogen

A positive muon (μ^+) implanted into matter can be regarded as a light proton isotope in the sense that the local structure of a muon-electron system is virtually equivalent with that of hydrogen. While the light mass of a muon (one-ninth that of a proton) often leads to the isotope effect, which is particularly distinctive in diffusion at low temperatures, where the quantum tunneling process becomes dominant, a muon also simulates hydrogen diffusion via classical over barrier jump at high temperatures [6]. Thus, muon in matter can be regarded as pseudohydrogen. We propose the designation “muogen” (Mu) as the appropriate elemental name analogous to hydrogen (see Fig. 2). The electronic state of Mu can be spectroscopically identified via muon-electron hyperfine parameters using μSR technique with utmost sensitivity.

4. Local electronic structure of H in pyrite

According to the μSR experiment, implanted-muons indicate that there are four electronically inequivalent Mu states in FeS_2, i.e., two paramagnetic centers labeled Mu_p and Mu^*_p and two diamagnetic centers labeled Mu_d and Mu^*_d. The magnitude of the hyperfine parameter [$\omega_{hf}/2\pi \approx 411(40)$ MHz for Mu_p and $\omega_{hf} = 0$ for Mu_d], combined with the Hartree potential calculation, suggests that Mu_p occupies an Fe-tetrahedron center corresponding to the S-S antibonding site (see Fig. 3).

It is inferred from time-dependent muon polarization that Mu_p exhibits fast conversion to a diamagnetic state Mu^*_d ($\omega_{hf} = 0$, exhibiting depolarization due to spin/charge exchange interaction), which suggests the possibility of diffusion-limited trapping of Mu_p by defects/impurities to form complex states. Mu_d is tentatively attributed to an effective-mass-like shallow

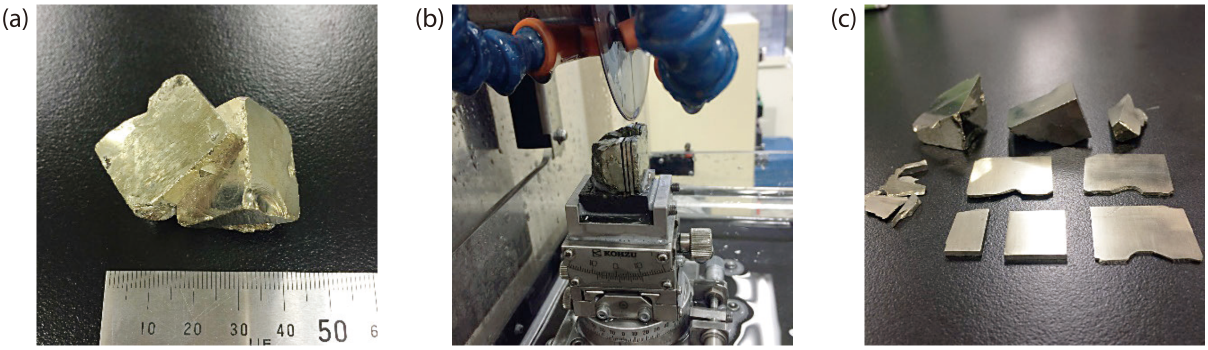

Figure 1. (a) Single-crystalline ingot of natural pyrite used in this experiment (unknown origin). (b) Cutting process at the CROSS user laboratory. (c) Pyrite slabs in the (100) crystal face orientation.

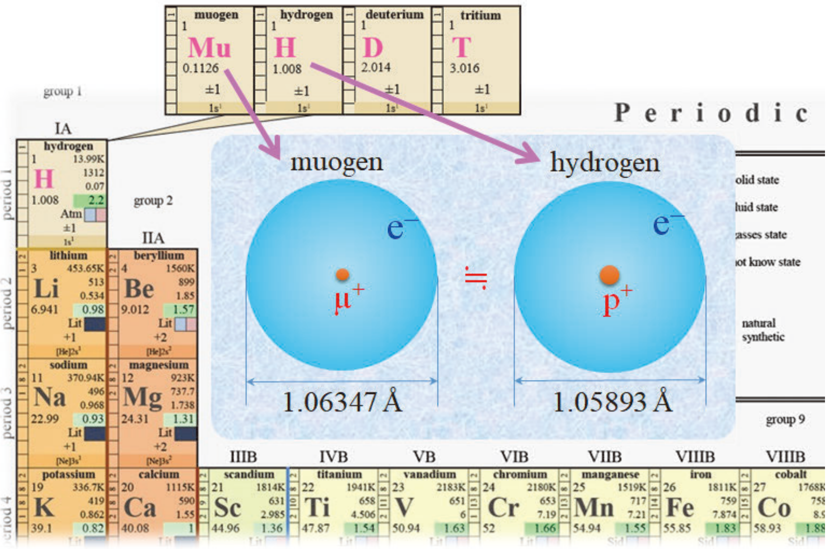

Figure 2. Modified periodic table. Muogen (Mu) is a light pseudo-isotope of hydrogen (H).

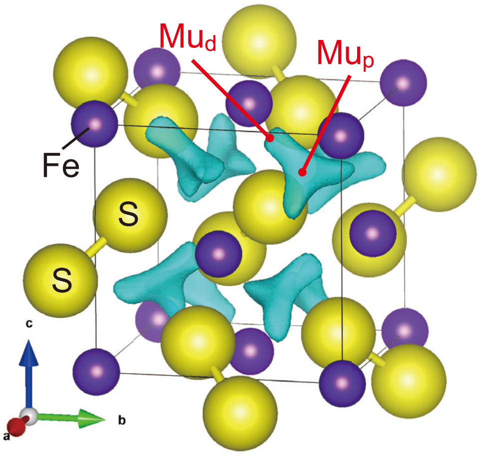

Figure 3. Atomic configuration of FeS_2 and possible candidate sites for two Mu states (Mu_p and Mu_d), where isosurfaces of the Hartree potential are displayed by blue hatched areas.

donor/acceptor state or a sulfhydryl-like SMu^- complex that serves as the donor by releasing an electron upon formation via the following process: $S_2^{2-} + Mu \rightarrow S^{2-} + SMu^- + e^-$.

The small ionization energy ($E_p \approx 10$ meV for Mu_p and $E_d \approx 1$ meV for Mu_d) indicates that the electronic levels associated with these Mu centers are situated near (or merged to) the band edge. Meanwhile, the electronic state of Mu^*_p inferred from a positive frequency shift under a high transverse field is interpreted as Mu_p undergoing strong dynamical modulation of ω_{hf}, probably due to fast diffusion. These observations suggest that interstitial hydrogen also serves as an electronically active impurity in FeS_2.

Comparing predictions from such an analysis with the results of this experiment could help us uncover the true worth of fool's gold.

Acknowledgements

This work was partially supported by the KEK-MSL Inter-University Research Program (Proposal No. 2016B0011) and by the MEXT Elements Strategy Initiative to Form Core Research Center for Electron Materials. We acknowledge CROSS-Tokai for the use of apparatus in their user laboratories and H. Lee for VASP calculations under the support of KEK Large Scale Simulation Program No. 16–17.

References

[1] H. Okabe, M. Hiraishi, S. Takeshita, A. Koda, K. M. Kojima and R. Kadono, Phys. Rev. B **98**, 075210 (2018).
[2] J. Puthussery, S. Seefeld, N. Berry, M. Gibbs, and M. Law, J. Am. Chem. Soc. **133**, 716 (2011).
[3] D.-Y. Wang, Y.-T. Jiang, C.-C. Lin, S.-S. Li, Y.-T. Wang, C.-C. Chen, and C.-W. Chen, Adv. Mater. **24**, 3415 (2012).
[4] C. Wadia, A. P. Alivisatos, and D. M. Kammene, Environ. Sci. Technol. **43**, 2072 (2009).
[5] R. Schieck, A. Hartmann, S. Fiechter, R. Könenkamp, and H. Wetzel, J. Mater. Res. **5**, 1567 (1990).
[6] H. Graf, G. Balzer, E. Recknagel, A. Weidinger, and R. I. Grynszpan, Phys. Rev. Lett. **44**, 1333 (1980).

H. Okabe[1,2], M. Hiraishi[1,2], S. Takeshita[1,2], A. Koda[1,2], K. M. Kojima[3], and R. Kadono[1,2]
[1]*Institute of Materials Structure Science, KEK;* [2]*Muon Science Section, Materials and Life Science Division, J-PARC Center;* [3]*Centre for Molecular and Materials Science, TRIUMF*

Renormalization of the Spin Excitations in Hexagonal HoMnO$_3$ by Magnon-Phonon Coupling

1. Introduction

Quasiparticles in condensed matter physics are a fundamental concept to understand the excited state of the system. These particles sometimes interact with themselves or others. The interactions are usually too weak to observe, however, the studies about the observation of the strong quasiparticle interaction have been highlighted [1–3]. To understand the physics easily, it is required to investigate the materials which have a concise structure.

Hexagonal HoMnO$_3$ is a perfect platform to investigate this kind of quasiparticle interactions. The Mn and Ho planes are well separated and the magnetism is usually dominant by Mn spin. In addition, Mn atoms form an ideal triangular plane and its magnetic structure is a non-collinear 120° spin ordered structure. Because the three-magnon interaction terms are non-zero in non-collinear magnets, we could expect the magnon-magnon interaction. Furthermore, the hexagonal rare-earth manganite usually has large magneto-elastic coupling and anomalous features in Raman spectra, ultrasonic wave velocity, inelastic neutron scattering (INS) measurements [4–6]. These indicate that the strong interaction between spin and lattice degrees of freedom is highly expected in HoMnO$_3$.

In this study [7], we focus on the magnon-magnon interaction and magnon-phonon interaction in HoMnO$_3$. We carried out an INS experiment at J-PARC, 4SEASONS beamline and analyzed the results using three different calculations, which will be discussed later.

2. Experimental results and discussions

Figure 1 presents the measured spin-wave dispersion along high symmetric momentum points in the 1st Brillouin zone. Most of the features can be explained by a conventional 3-sublattice Heisenberg model in a triangular lattice. We considered a nearest-neighbor exchange interaction J and a single-ion anisotropy D and found that the best fit is $J = 2.44$, $D = 0.38$ meV, which is consistent with the previous study [8].

However, there are several features that cannot be captured by the above model. First, the low-energy magnon dispersion curve located at 11 meV is shifted downward in comparison with the Heisenberg model. Second, there is a negative slope of the dispersion along the *AB* direction, which is not reproduced by any long-range interactions or exchange anisotropy within the linear spin-wave theory. Third, the diffusive signals located at 20 meV are present in the data and they are not expected in the Heisenberg model.

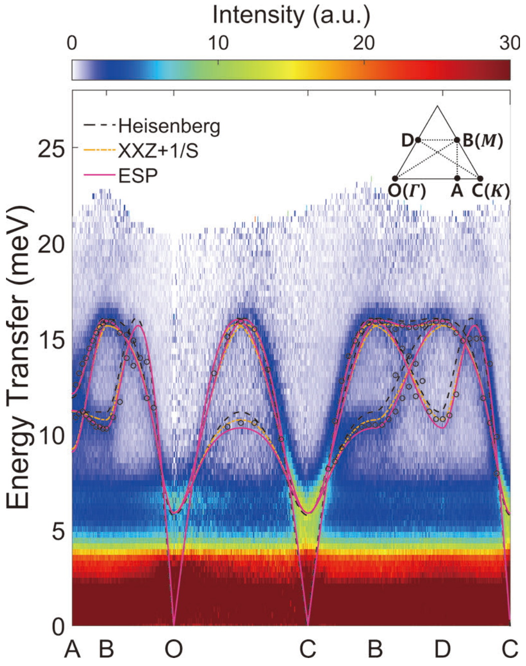

Figure 1. Spin-wave dispersion of HoMnO$_3$. Three different calculated dispersion curves are plotted together (See the legend) Adapted from the ref. [6].

We tried to explain the anomalies using two different models, which include the magnon-magnon interaction and the magnon-phonon interaction. For the magnon-magnon interaction, we used the XXZ model with 1/*S* expansion [9], which can be described as

$$H_{XXZ} = J\sum_{<ij>}[S_i^x S_j^x + S_i^y S_j^y + \Delta S_i^z S_j^z] + O(S^{-1}) \quad (1)$$

To include the magnon-phonon coupling, we also used an Einstein Site Phonon (ESP) model [10], which is explained by the equation below,

$$H_{ESP} = J\left[\sum_{<ij>}\vec{S}_i \cdot \vec{S}_j - cS^{-2}\sum_i\left(\sum_{j\in i}\hat{e}O_{ij}\,(\vec{S}_i \cdot \vec{S}_j)\right)^2\right] + D\sum_i (S_i^z)^2 \quad (2)$$

Here, the constant *c* indicates the coupling strength between the magnon and phonon.

As already shown in the Fig. 1, both the downward shift of the magnon energy and the negative slope along the *AB* direction are explained by the two models. Using the XXZ model with 1/S expansion, we got the best fit parameters with J = 2.7 meV and $\varDelta$ = 0.88.

For the ESP model, we could obtain the Hamiltonian parameters as $J = 2.53$ and $D = 0.38$ meV. Both parameters explain reasonably the observations.

Although both the XXZ model with $1/S$ expansion and the ESP model describe the same magnon dispersion curves, a critical difference appears in the intensity. Figure 2 shows the detailed INS data and the intensity profile of the experimental data and three different calculation models along the *AB* direction. As shown in Fig. 2(b), the intensity calculated from the ESP model is in good agreement with the experimental results. Especially, the peak ratio located at 11 and 16 meV is only reproduced by the ESP model. And the diffusive signals located at around 20 meV is highly expected as the magneto-elastic excitations, which comes from the hybridization of the magnon and phonon as observed in $(Y,Lu)MnO_3$ [6]. So, we could conclude that the magnon-phonon coupling was the dominant mechanism to explain the observed anomalies in $HoMnO_3$.

Furthermore, the two-magnon continuum from the decay of one-magnon appears to be weak in the data, which indicate that the magnon-magnon interaction is suppressed in $HoMnO_3$. This is also consistent with the theoretical estimation. The previous study on the triangular lattice [9] predicted that if the two-ion anisotropy $1\text{-}\Delta$ in the XXZ model is larger than 0.08, the one-magnon decay is not allowed. Based on our data and the fit, the $1\text{-}\Delta$ in $HoMnO_3$ was found to be 0.12, which was larger than 0.08. So, we could conclude that the magnon-magnon interaction was not the dominant mechanism for the energy renormalization in $HoMnO_3$.

3. Summary

We studied the INS spectra of $HoMnO_3$, which was the ideal platform to investigate the 2-dimensional triangular lattice antiferromagnets. We analyzed the data using three different calculation models, the simple Heisenberg with the single-ion anisotropy, the XXZ model with $1/S$ expansion, and the ESP model, to explain all the features. Both the XXZ model and the ESP model explain the anomalies, but the ESP model explains only the intensity ratio at the B point. Because of the weak two-magnon continuum and the diffusive signals at 20 meV expected as the magneto-elastic excitation, we could conclude that the magnon-phonon coupling was the dominant mechanism for the unconventional spin-wave dispersion in $HoMnO_3$. The magnon-magnon interaction is suppressed in $HoMnO_3$ due to the large two-ion anisotropy.

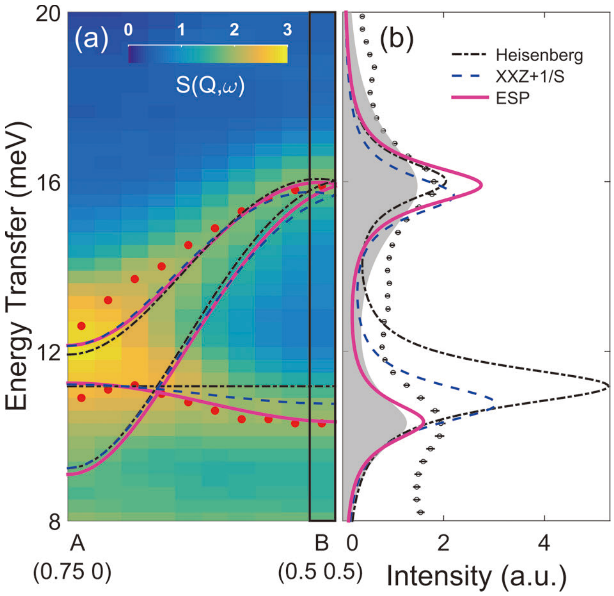

Figure 2. (a) INS data along the *AB* direction and the three different calculated types of dispersion. (b) The intensity profile at the B point. Adapted from the ref. [6].

References

[1] K. W. Plumb, et al., Nat. Phys. **12**, 224 (2016).
[2] S. Ito, et al., Nat. Commun. **8**, 235 (2017).
[3] T. Kim, et al., J. Phys. Soc. Jpn. **88**, 081003 (2019).
[4] A. P. Litvinchuk, et al., J. Phys.: Condens. Matter **16**, 809 (2004).
[5] M. Poirier, et al., Phys. Rev. B **83**, 054418 (2011).
[6] J. Oh, et al., Phys. Rev. Lett. **111**, 257202 (2013).
[7] T. Kim, et al., Phys. Rev. B **97**, 201113(R) (2018).
[8] O. P. Vajk, et al., Phys. Rev. Lett. **94**, 087601 (2005).
[9] A. L. Chernyshev, et al, Phys. Rev. Lett. **97**, 207202 (2006).
[10] F. Wang, et al., Phys. Rev. Lett. **100**, 077201 (2008).

T. Kim[1,2], J. C. Leiner[1,2], K. Park[1,2], J. Oh[1,2], H. Sim[1,2], K. Iida[3], K. Kamazawa[3], and J.-G. Park[1,2]
[1]*Center for Correlated Electron Systems, Institute for Basic Science, Seoul 08826, Korea;* [2]*Department of Physics and Astronomy, Seoul National University, Seoul 08826, Korea;* [3]*Neutron Science and Technology Center, CROSS*

Structure and Dynamics of Glycine Solution in Mesoporous Silica

1. Introduction

The separation and purification techniques that use mesopores for organic molecules are indispensable in the field of analytical chemistry, pharmacy and engineering [1]. Although the separation mechanism of solutes is very complex, its key factors can be attributed to the interaction between a solute and column wall and the confinement effect on an eluent. The interactions between bioorganic molecules and inorganic surfaces have drawn a wide interest due to their significant role in various fields, including biomineralization [2] and biosensors [3]. With the progress of microanalysis technology, a technique for immobilizing biomolecules to solid surface [4] has attracted attention. Therefore, it is very important to determine the behaviors of solute and water molecules confined in nano-space.

Glycine, the simplest molecule among amino acids, is a zwitterion to form $–NH_2/–NH_3^+$ and $–COOH/–COO^-$ with a pH change of the solution (the isoelectric point of glycine is 5.47). When observing the change in the charge state of glycine, the mechanism of interaction between glycine and silica surface and the hydration structure of glycine in a confined environment are still unknown. In the present study, the thermal, structural, and dynamical properties of the glycine solution in micelle-templated mesoporous silica MCM-41 were investigated at pH = 5 (neutral) and 2 (acidic) [5].

2. Sample preparation

Mesoporous silica, MCM-41, was synthesized by Beck's method. The pore size, the specific surface area, and pore volume of MCM-41 were estimated as 31.3 Å, 723 m^2/g, and 0.795 cm^3/g by the BJH and BET methods, respectively. The pH of glycine solution is 5 without pH adjustment. By adding hydrochloride solution, pH of the solution was adjusted to pH = 2. A required amount of the glycine solution and the MCM-41 powder were mixed in an Eppendorf tube. The tube was vibrated with a vortex mixer for 1 h. The loading ratios (h = mass of glycine solutions/mass of dry MCM-41) of glycine solution to MCM-41 powder were 0.6 and 0.8. It was ensured that no exothermic and endothermic peaks due to freezing and melting of a bulk solution appear in the cooling and heating process of DSC measurements, respectively.

3. Thermal and structural properties

Only one peak in the DSC results of confined glycine solution was found, and the melting and freezing temperatures did not change against the concentration of glycine. This result indicates that confined glycine solutions at the concentrations measured form eutectic as well as the bulk. The endo- and exothermic peaks of confined glycine solutions were broader than those of confined pure water due to the two-phase coexistence extending down to the eutectic temperature. The melting and freezing temperatures of confined glycine solutions were lower by ~10 K than those of confined water. This finding implies that water structure is disordered by the hydration of glycine. The enthalpy of fusion of confined glycine solution at pH = 2 was larger than that at pH = 5, regardless of the glycine concentration and h. This implies that the charge state of glycine dominantly affects the water structure in MCM-41.

By subtracting the X-ray diffraction intensity of dry MCM-41 from that of glycine solution loaded MCM-41, the radial distribution function (RDF) of glycine solution in MCM-41 was obtained. Compared with RDF at $h = 0.8$, a shoulder at 2.8 Å in the RDF is seen more clearly at $h = 0.6$. At the lower loading ratio, the pores of MCM-41 are partially filled with the solution, and the confined solution would be distributed near the pore wall. Compared with the RDFs at pH = 2, the small peaks were observed at 2.65 Å, 3.9 Å, and 5.2 Å in the RDFs at pH = 5. Since the silanol group of MCM-41 is charged negatively at pH = 5, the amino group ($–NH_3^+$) of glycine could interact with the silanol group of MCM-41. The NMR results of the glycine solution confined in mesoporous silica indicate that the $–NH_3^+ \cdots O\text{-}Si$ bonding could be formed [6]. Therefore, these peaks could be assigned to N (amino group) – O (silanol group), N (amino group) – Si, and C (carbonyl group) – Si interactions, respectively. This indicates that glycine molecules are present near the pore wall of MCM-41 at pH = 5. On the other hand, since no such peaks were seen in the RDFs at pH = 2, glycine molecules could be relatively hydrated by confined water. Thus, the liquid structure of the glycine solution in MCM-41 at pH = 5 and 2 is illustrated in Fig. 1. To verify the surmise, the dynamics of glycine and water is investigated.

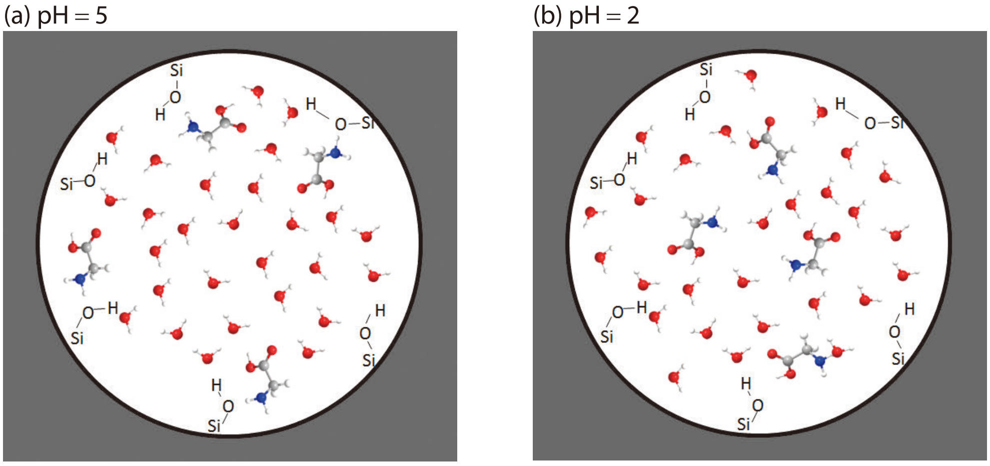
(a) pH = 5

(b) pH = 2

Figure 1. Illustrations of the liquid structure of glycine solution in MCM-41 at (a) pH = 5 and (b) 2.

4. Dynamics of glycine and water in MCM-41

Two kinds of glycine solutions (deuterated glycine/H_2O and glycine/D_2O) were prepared; these are abbreviated to D-Gly/H_2O and H-Gly/D_2O. The powder samples were wrapped with a sheet of aluminum foil (20 μm thick). Then, it was bent cylindrically and inserted into a cylindrical aluminum cell of 14.0 mm in inner diameter, 0.25 mm in thickness, and 50 mm in height. The QENS measurements were carried out using a time-of-flight near backscattering spectrometer DNA (BL02), and the energy transfer of neutrons by scattering, ω, varied within −20~+100 μeV. The QENS measurements of the samples were performed at 245–305 K. The sample was measured at 100 K to estimate the instrumental resolution.

QENS spectra, $S(Q,\omega)$, reflect translational and rotational motions. In the present experiment, since the spectra which arise from the rotational motion are much wider, compared with the observable energy range of the spectrometer, the contribution from the molecular rotation is included in a background term. Therefore, $S(Q,\omega)$ was analyzed by a model of translational diffusions of water and glycine molecules as follows:

$$S(Q,\omega) = \left\{ C(Q)\cdot\delta(\omega) + D(Q)\frac{1}{\pi}\,\frac{\Gamma(Q)}{(\omega^2+\Gamma(Q)^2)} \right\} \otimes R(Q,\omega) + BG\,, \qquad (1)$$

where $C(Q)$ and $D(Q)$ are intensities of elastic and QENS components, respectively. $\Gamma(Q)$ is the half-width at half-maximum of Lorentzian function, reflecting the translational diffusion of water and glycine molecules. BG is the background, and $R(Q,\omega)$ is the resolution function.

Since the incoherent scattering cross-section of protons is larger by a factor of ~40 than those of the other atoms, the dynamics of glycine molecule would be obtained from the result of H-Gly/D_2O solution, whereas the dynamics of water molecule would be derived from the result of the D-Gly/H_2O solution.

Figure 2 shows the Q dependence of $\Gamma(Q)$ of confined H-Gly/D_2O at pH = 5. Since the translational motion is faster at a higher temperature, the Lorentzian component in the spectrum becomes wider. Hence, the fitting of the model became difficult under the increasing temperature. Moreover, the QENS spectra at $Q^2 > 2$ Å^{-2} were not analyzed since the elastic peak due to the scattering of MCM-41 was not negligible in the Q-range. The activation energy of the diffusion constant was calculated from the Arrhenius plot of diffusion constants (Fig. 3). The activation energies of the water molecule at pH = 5 and 2 are 20.9 ± 1.2 and 21.8 ± 1.5 kJ/mol, respectively. The activation energy of the translational motion of water in confined glycine solutions is comparable to that of pure water confined in MCM-41 (21.6 kJ/mol) [7] but is larger than that of bulk

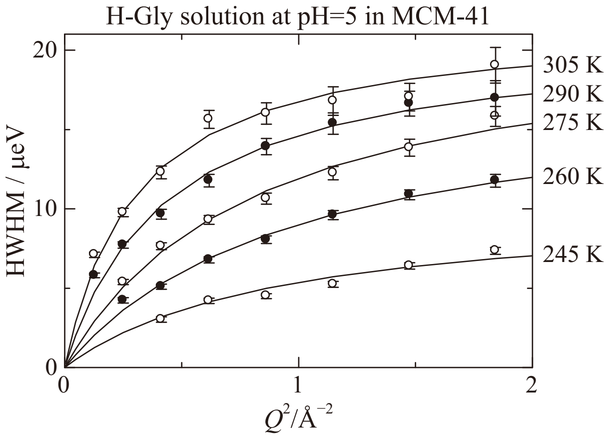

Figure 2. Q dependence of the width of a Lorentzian function of H-Gly/D_2O at pH = 5 in MCM-41. The solid line shows the results according to the jump diffusion model.

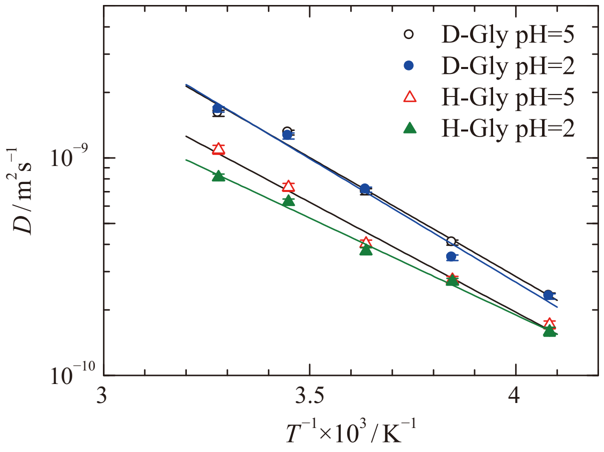

Figure 3. Arrhenius plot of diffusion constants of glycine and water molecules in confined solutions at pH = 5 and 2.

water (17.9 ± 0.9 kJ/mol) [8]. This would be due to the attractive interaction between water and silanol group of the MCM-41 wall. On the other hand, the activation energies of the translational motion of glycine at pH = 5 and 2 are 19.3 ± 1.1 and 17.0 ± 0.8 kJ/mol, respectively. The activation energy of translational motion of glycine at pH = 5 is larger than that at pH = 2. These results can be explained by the attractive interaction of glycine molecules with the silica wall of MCM-41, as seen in the RDF of glycine solution in MCM-41 at pH = 5.

NMR results of a glycine solution confined in mesoporous silica indicate that the $-NH_3^+\cdots$O-Si bonding could be formed [6]. However, some DFT calculations of the system of glycine, water, and silica revealed that the direct hydrogen bonds of $-CO^-\cdots$HO-Si are formed, and that $-NH_3^+$ interacts with O-Si via a water molecule [9]. The RDFs in the present study could not rule out the possibility of forming the direct hydrogen bonds of $-CO^-\cdots$HO-Si.

Further work, such as neutrons diffraction with ^{14}N/^{15}N isotope substitution is needed to clarify this issue. The silanol group of MCM-41 is charged positively at pH = 2 [10], and a glycine molecule also has a positive charge at pH = 2 which is lower than the isoelectric point. Under this situation, the repulsive interaction between the glycine molecule and silanol group would keep glycine molecules away from the wall of MCM-41. Consequently, water molecules will be adsorbed on the wall of MCM-41 instead of glycine molecules. The present results are expected to give essential knowledge about the interaction between bioorganic molecules and inorganic surfaces and to improve technique for immobilizing biomolecules to microchannels.

5. Future perspectives

The present result demonstrated that quasi-elastic neutron scattering with H/D substitution could clarify the dynamical behavior of solute and water in confined nano-space. For further applications, the analysis of dynamical behavior in mesoporous silica nanoparticle (MSN) will continue. Since MSN has the size of few tens of nm and biocompatibility, MSN can penetrate the living cell [11]. The application of the loading of small molecules as well as macromolecules such as proteins, siRNA is being developed. Thus, MSN is attracting attention as a material for elucidating cell dynamics. Neutron beams can become strong tools to uncover life phenomena from the perspective of physical science.

References

[1] S. Ahuja et al., Handbook of Pharmaceutical Analysis by HPLC (Academic Press, 2005).
[2] S. Mann, Biomineralization: Principles and Concepts in Bioinorganic Materials Chemistry (Oxford University, New York, 2001).
[3] K.Besteman et al., Nano Lett. **3**, 727–730 (2003).
[4] K. Nakanishi et al., J. Biosci. Bioeng. **91**, 233–244 (2001).
[5] K. Yoshida et al., J. Chem. Phys. **149**, 124502 (2018).
[6] I. B. Shir et al., J. Phys. Chem. C **116**, 9691–9702 (2012)
[7] T. Yamada et al., J. Phys. Chem. B **115**, 13563–13569 (2011).
[8] S. Takahara et al., J. Phys. Chem. B **103**, 5814–5819 (1999).
[9] A. Costa et al., Phys. Chem. Chem. Phys. **10**, 6360–6368 (2008).
[10] G. E. Musso, et al., Phys. Chem. Chem. Phys., **17**, 13882-94 (2015).
[11] R. Narayan et al., Pharmaceutics **10**(3), 118 (2018).

K. Yoshida[1], T. Inoue[1], M. Torigoe[1], T. Yamada[2], K. Shibata[3], and T. Yamaguchi[1]
[1]*Fukuoka University;* [2]*Neutron Science and Technology Center, CROSS;* [3]*Neutron Science Section, Materials and Life Science Division, J-PARC Center*

Topological Transitions among Skyrmion- and Hedgehog-Lattice States in Cubic Chiral Magnets

1. Introduction

Topological spin textures such as skyrmions and spin hedgehogs (Fig. 1) give rise to novel emergent properties, which can be exploited for spintronic functionalities [1]. Whereas the formation or deletion process of them has been intensively studied, switching of spin textures among different topological orders remain largely unexplored.

We have investigated the topological transitions among skyrmion lattice (SkL) and hedgehog lattice (HL) in new chiral magnets MnSi$_{1-x}$Ge$_x$. By changing chemical pressure through substitution between Si and Ge, we have discovered that the SkL in MnSi undergoes two-step transitions to the cubic-3***q*** HL in MnGe (Fig. 2). In the intermediate composition range (x = 0.3 – 0.6), we have unveiled a new topological spin texture characterized four wavevectors (***q***-vectors), *i.e.*, tetrahedral-4***q*** state (Fig. 1(b)).

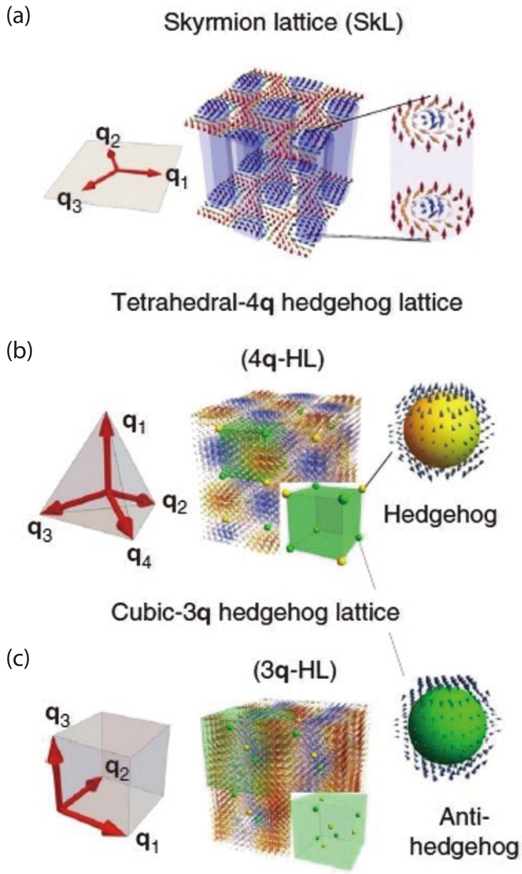

Figure 1. Schematics of topological multiple-***q*** spin textures. The tetrahedral-4***q*** HL is a new topological spin texture which has been identified in our work.

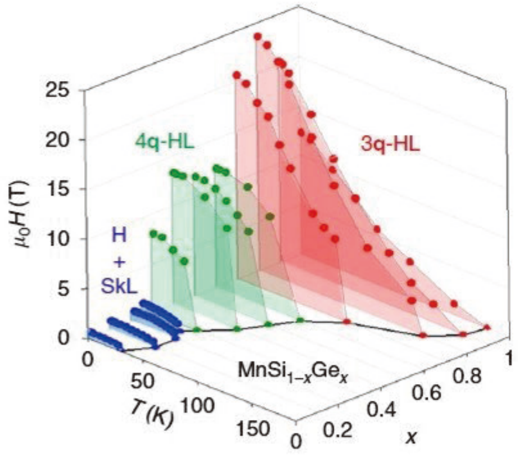

Figure 2. Variation of magnetic phase diagram in MnSi$_{1-x}$Ge$_x$. The drawn phase boundary line for each x represent the ferromagnetic transition.

2. Experiment

Neutron scattering experiments were performed at small- and wide-angle neutron scattering instrument (TAIKAN) built at BL15 of MLF. A powder sample of polycrystalline MnSi$_{1-x}$Ge$_x$, synthesized by high-pressure technique, was packed in an aluminum container filled by He gas and installed in a cryomagnet. Magnetic field was applied perpendicular to the incident neutron beam. The diffracted neutron beam with the wavelength of $0.5 < \lambda < 7.8$ Å was collected by four detector banks of small-, middle-, and high-angle and backward detector banks, and analysed by using time-of-flight (TOF) method.

3. Result

In order to clarify the variation of magnetic period (λ) and direction of ***q***-vectors in MnSi$_{1-x}$Ge$_x$, small- and wide-angle neutron scattering experiments were performed at zero magnetic field. Figure 3(a), (b) show the small-angle neutron scattering (SANS) intensity patterns of $x = 0.6$ and 0.8 after zero field cooling from room temperature. The observed Debye-ring-like patterns indicate the formation of periodically modulated magnetic structures. Their modulation periods are determined from the radius (q) of the diffracted ring pattern as $\lambda = 2\pi/q$, which we will be discussed in the later section.

The q-vectors, which are fixed along specific crystal-axes due to magnetic anisotropy, were identified by wide-angle neutron scattering. Figure 3(c), (d) show the

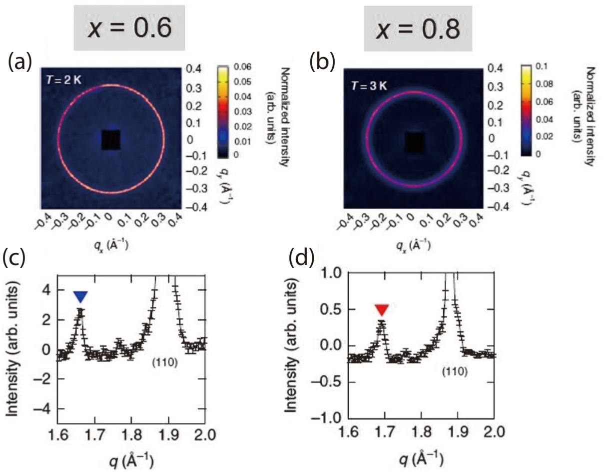

Figure 3. The SANS intensity patterns ((a), (b)) and powder neutron diffraction patterns around (100) nuclear reflection ((c), (d)) after zero-field cooling.

wide-angle neutron diffraction profiles around (110) nuclear reflection. Because magnetic reflections generally appear as satellite peaks at the wavenumber of $|\boldsymbol{q}_\mathrm{n} \pm \boldsymbol{q}|$ in a powder neutron diffraction, we can determine the $\boldsymbol{q}$-direction from the satellite peak position once we identify the magnitude of $\boldsymbol{q}$ by SANS. Here, $\boldsymbol{q}_\mathrm{n}$ is the reciprocal lattice vector. Each satellite peak observed in $x = 0.6$ and 0.8 (indicated by blue and red triangles in Fig. 3(c), (d)) can be indexed as $(2\pi/a - q/\sqrt{3}, 2\pi/a - q/\sqrt{3}, \pm q/\sqrt{3})$ and $(2\pi/a - q, 2\pi/a, 0)$, respectively (a is lattice constant). Namely, the $\boldsymbol{q}$-vector directions are along <111> crystal axes for $x = 0.6$, and <100> crystal axes for $x = 0.8$.

Next, we investigated the magnetic structures under magnetic field by SANS in $x = 0.2$, 0.6, 0.8. Magnetic field (H) is applied perpendicular to the incident neutron beam. As shown in Fig. 4(a), the SANS pattern of $x = 0.2$ exhibits intensity peaks parallel ($\varphi = 0°, 180°$) and perpendicular ($\varphi = \pm 90°$) to H, which indicates the conical state modulating along H coexists with SkL. We also confirmed that the peaks at $\varphi = \pm 90°$ only emerge in the SkL phase identified by the magnetization measurements.

In $x = 0.6$ and 0.8, we also detect characteristic SANS patterns under H: In addition to the intensity peaks at $\varphi = 0°, 180°$, there appears peaks at $\varphi = \pm 70°, \pm 110°$ for $x = 0.6$ and at $\varphi = \pm 90°$ for $x = 0.8$. We interpret these SANS patterns in terms of multiple-$\boldsymbol{q}$ structures. As for $x = 0.6$, Fig. 4(b) illustrates the possible multiple-$\boldsymbol{q}$ structure explaining the SANS result, *i.e.*, the tetrahedral-4$\boldsymbol{q}$ state. As for $x = 0.8$, the observed intensity pattern is identical to that of MnGe where the cubic-3q HL is realized (Fig. 4(c)) [2, 3].

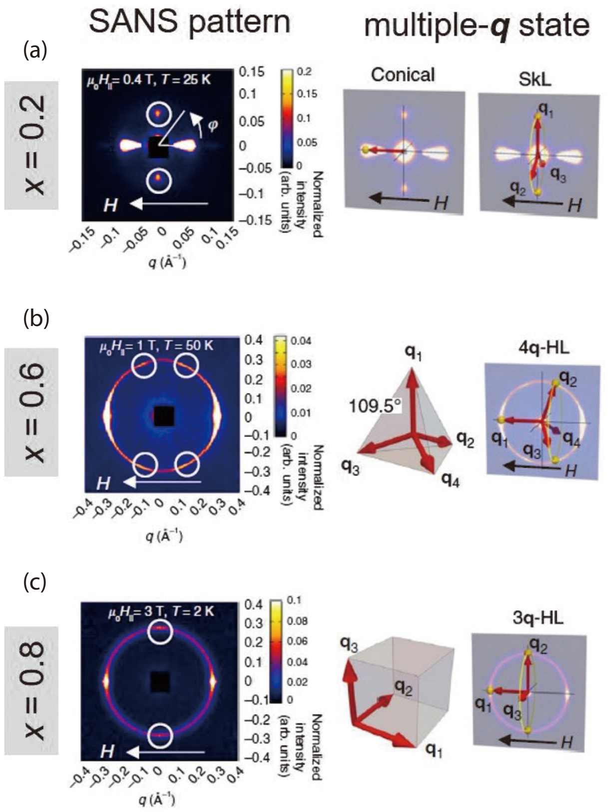

Figure 4. The SANS intensity patterns under magnetic field and the candidate multiple-$\boldsymbol{q}$ states explaining the results.

We note that we cannot exclude a possibility of multi-domain state of the single-$\boldsymbol{q}$ helical structure on the basis of the SANS results alone. However, such a scenario is incompatible with the observation of large topological Hall effect (THE), which is the hallmark of the formation of non-coplanar spin textures endowed with scalar spin chirality (data not shown). Indeed, we observed THE with distinct features unique to each topological phase realized in $\mathrm{MnSi}_{1-x}\mathrm{Ge}_x$.

4. Discussion

We have unveiled the transitions among distinct topological spin textures, namely SkL and two classes of HLs in cubic chiral magnets $\mathrm{MnSi}_{1-x}\mathrm{Ge}_x$. It is noteworthy that the observed topological transitions can be driven essentially by the lattice constant change. One important indication we obtain is that the dominant magnetic interactions for HL may differ from those for SkL where the competition between ferromagnetic exchange interaction (EXI) ($J\boldsymbol{S}_i \cdot \boldsymbol{S}_j$) and Dzyaloshinskii-Moriya interaction (DMI) ($\boldsymbol{D} \cdot (\boldsymbol{S}_i \times \boldsymbol{S}_j)$) determines the magnetic period as $\lambda \sim a \cdot J/D$. In the conventional SkL materials, the magnetic ground state is a long-period helical structure ($\lambda = 10$–100 nm) since the energy scale

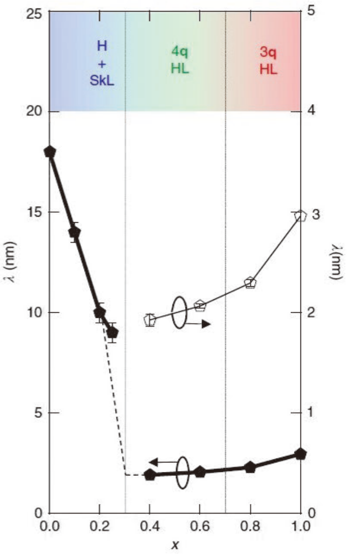

Figure 5. Variation of magnetic period (λ) in $MnSi_{1-x}Ge_x$. The extremely short in $x = 0.4–1$ is beyond the understanding of conventional paradigm based on Dzyaloshinskii-Moriya interaction.

is well-separated as $J \gg D$. If the same model could be applied, the extremely short λ (1.94–2.80 nm) observed in $MnSi_{1-x}Ge_x$ ($x = 0.4–1$) (Fig. 5) would require much larger DMI even exceeding EXI, which is not consistent with our first-principles calculation.

Thus, DMI may not be the primary origin of the short-period helical structure in HL. Instead, the magnetic frustration or Ruderman-Kittel-Kasuya-Yoshida (RKKY) interaction causing competing ferromagnetic and anti-ferromagnetic EXIs can be a possible mechanism.

References

[1] N. Nagaosa and Y. Tokura, *Nat. Nanotech.* **8**, 899 (2013).

[2] N. Kanazawa *et al.*, *Phys. Rev. Lett.* **106**, 156603 (2011).

[3] N. Kanazawa et al., *Phys. Rev. B* **86**, 134425 (2012).

Y. Fujishiro[1], N. Kanazawa[1], T. Nakajima[2], X. Z. Yu[2], K. Oishi[3], Y. Kawamura[3], K. Kakurai[2,3], T. Arima[2,4], H. Mitamura[5], A. Miyake[5], K. Akiba[5], M. Tokunaga[5], A. Matsuo[5], K. Kindo[5], T. Koretsune[6], R. Arita[1,2], and Y. Tokura[1,2]

[1]Department of Applied Physics, The University of Tokyo; [2]RIKEN, CEMS; [3]Neutron Science and Technology Center, CROSS; [4]Department of Advanced Materials Science, The University of Tokyo; [5]ISSP, The University of Tokyo; [6]Department of Physics, Tohoku University

2D Bragg-Edge Elastic Strain Tomography

Background

The rapid development of pixelated time-of-flight neutron detectors has given prominence to Bragg-edge transmission geometry as an excellent approach for elastic strain measurement in polycrystalline materials (see Fig. 1(a)). Bragg-edges refer to abrupt increases in the transmission rate in polycrystalline samples at wavelengths corresponding to back scattered neutrons. Relative shifts in the location of these edges can provide a measure of elastic strain in much the same way as traditional diffraction techniques. Along with the development of pixelated time-of-flight detectors, significant interest in strain imaging techniques and the associated 'rich' tomography problem has been generated. The state-of-the-art due to Tremsin is now capable of two-dimensional strain imaging with spatial resolution down to 55 μm (e.g. [1]).

Several attempts have been made at solving the associated tomographic reconstruction problem over the past decade. As opposed to conventional tomographic imaging, this problem focuses on the reconstruction of a tensor field, which is a significantly more complex problem.

Bragg-edge strain tomography has the potential to transform the way in which experimental mechanics is carried out. In much the same way that regular CT transformed medicine and other sciences, a full-field approach to measuring strain distributions within engineering materials may have an impact across a range of areas. One obvious example is in the development of novel manufacturing processes such as 3D printing. Residual stress locked in by the printing process has a critical impact on the strength of the resulting parts; this must be understood in order to advance the technology. In contrast to X-ray and pointwise neutron diffraction techniques, Bragg-edge strain tomography promises to reveal the full three-dimensional distribution of strain throughout printed engineering parts over the scale of centimeters.

A recent paper by Lionheart and Withers [2], and prior work by Sharafutdinov [3], clearly demonstrated that the problem was mathematically ill-posed. The issue revolves around the fact that multiple strain fields can project to the same set of strain images; solutions to the tomography problem are not unique. This does not prohibit reconstruction in general, however it does mean that additional information is required. Historically, this information has taken the form of assumptions (i.e. special cases). As an example, much of the initial work in this area was limited to assumptions of axial symmetry (e.g. [4]). A reconstruction algorithm for the special case of strain fields resulting strictly from *in situ* applied loads has also been developed and demonstrated experimentally [6, 7].

Recent work by the authors has provided a path to general reconstruction through consideration of known physical constraints, such as equilibrium. Through this approach, we have been able to demonstrate tomographic reconstruction of two-dimensional residual strain fields (plane-stress) in simulation, and, as outlined in this paper, from experimental measurements.

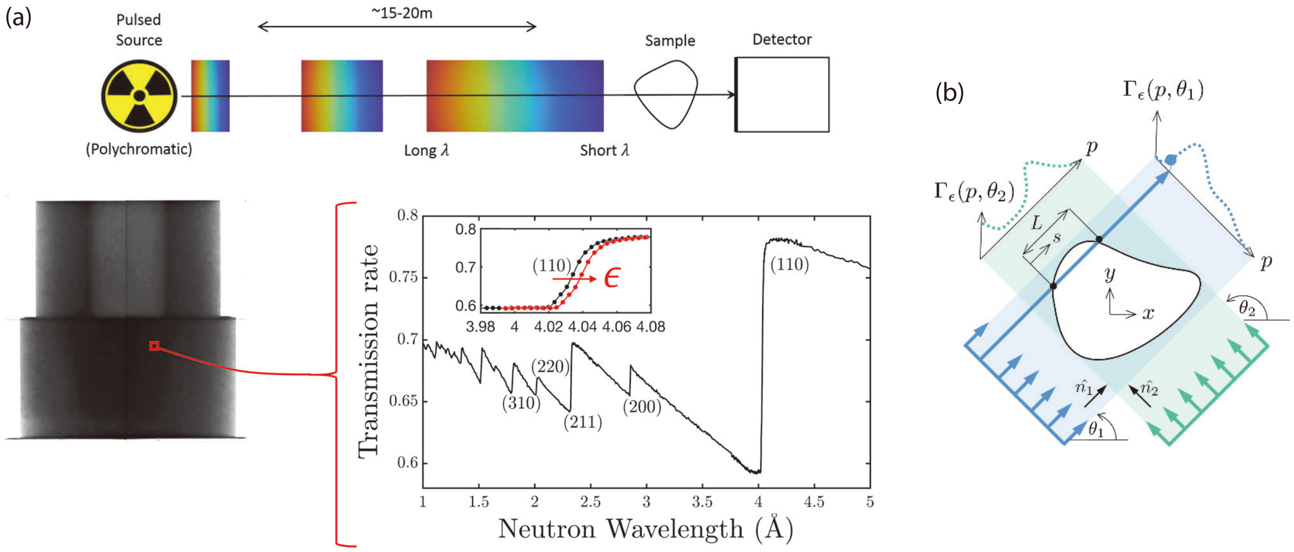

Figure 1 (a) Bragg-edge imaging on a pulsed neutron source. (b) Transmission geometry and coordinate system.

Reconstruction

Mathematically, Bragg-edge strain measurement is described by a generalization of the well-known Radon transform known as the Longitudinal Ray Transform (LRT);

$$\Gamma_\epsilon(p,\theta) = \frac{1}{L}\int_0^L \epsilon_{ij}(x_0 + s\hat{n})\hat{n}_i\hat{n}_j ds$$

where, with reference to Fig. 1(b), ϵ is the strain field within the sample, $\hat{n} = [\cos\theta \; \sin\theta]^T$ is a unit vector in the direction of the beam, x_o is the point of entry into the sample, and s is measured along the path of length L through the sample.

As discussed earlier, the LRT has a non-trivial null-space which prohibits its direct inversion. Additional information is required, and, in our work, this takes the form of an assumption of mechanical equilibrium. This is implemented through the concept of stress functions from which the unknown stress is defined in a way that automatically satisfies the well-known equations of equilibrium. In 2D (i.e. plane stress or plane strain), Airy stress functions provide a good example whereby the unknown components of stress can be defined as;

$$\sigma_{ij} = \frac{\partial^2\varphi}{\partial_i\partial_j}$$

for an arbitrary (unknown) Airy stress function φ.

Together with Hooke's law to relate stress and strain, we can tomographically reconstruct φ from the observed strain images in order to establish the unknown strain field. Practically, this can be achieved through a number of techniques; our approach has involved the implementation of Gaussian Process (GP) regression. Through the GP approach we have also been able to include other known constraints such as, in the case of residual stress samples, the absence of externally applied loads. A full description can be found in [11].

Experimental Demonstration

An experimental demonstration of this technique has been carried out using a set of strain images measured on the RADEN (Energy Resolved Neutron Imaging) instrument at J-PARC. This experiment focused on two samples (see Fig. 2(a)); 1. A crushed steel ring, and 2. An offset steel ring-and-plug. All details of the sample design, experiment set-up, and strain measurement can be found in [9]. For context, we provide the following summary.

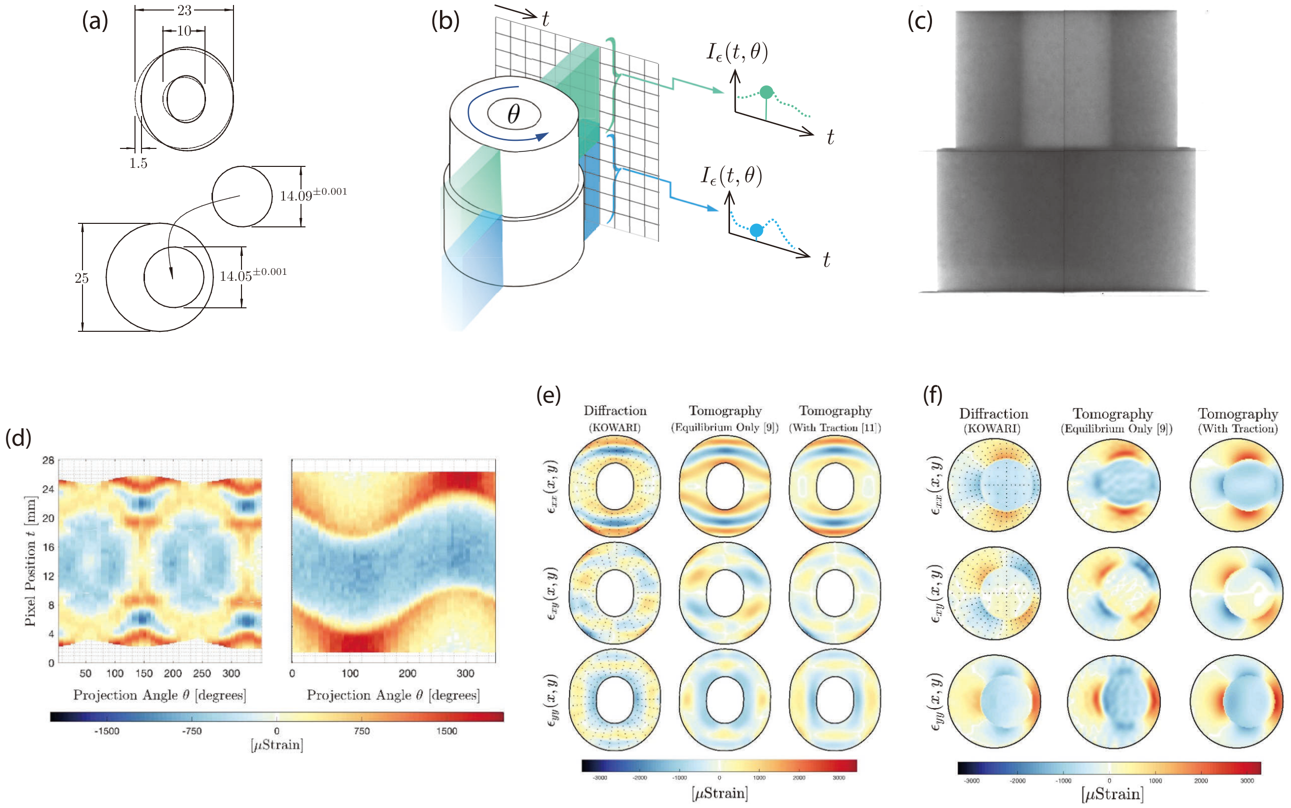

Figure 2 (a) Sample geometry; upper - crushed ring, lower - asymmetric ring-and-plug. (b) and (c) Transmission strain profiles were measured from the two samples simultaneously on RADEN. (d) The resulting strain-sinograms; left - crushed ring, right - asymmetric ring-and-plug. (e) and (f) Reconstructions compared to constant wavelength strain scans from KOWARI (measurement locations indicated by data points).

The two samples were constructed from the same bar of EN26 low-carbon/high alloy steel. The first sample was plastically defomed by 1.5 mm on the diameter to create a residual strain field, the second contained a residual stress field resulting from interference between the ring and a plug using a shrink-fit assembly process. Both samples were 14 mm thick, allowing them to be stacked within the field of view of a 10B MCP pixelated ToF detector [1] (see Figs. 2(b) and 2(c)). A set of 50 strain images was measured over golden angle increments of rotation. Measurements were performed over columns of pixels spanning the thickness of the sample to provide one-dimensional projections of the two-dimensional strain field. In total, 20,664 individual measurements were collected over the 50 projections, each with a measurement uncertainty around 10^{-4}.

The resulting strain-sinograms are shown in Fig. 2(d), from which we were able to reconstruct the strain fields shown in Figs. 2(e) and 2(f). These reconstructions are shown in comparison to detailed strain scans carried out on the KOWARI strain diffractometer at the Australian Centre for Neutron Scattering within ANSTO (0.5 × 0.5 × 14 mm gauge volume). Two separate reconstructions are shown; 1. A reconstruction constrained only by equilibrium, and 2. A reconstruction constrained by both equilibrium and an absence of surface traction. Both reconstructions agree well with the traditional strain scan, however the second one shows much greater fidelity.

Conclusions

Bragg-edge elastic strain tomography for general strain fields has been successfully demonstrated using the RADEN energy resolved imaging instrument within J-PARC. The approach we have developed has a natural extension to three dimensions (i.e. triaxial strain fields) and our current work is focused on achieving this goal.

References

[1] AS Tremsin et al. "High-resolution strain mapping through time-of-flight neutron transmission diffraction with a microchannel plate neutron counting detector", *Strain*, **48**:296–305, 2012.

[2] WRB Lionheart and PJ Withers. "Diffraction tomography of strain", *Inverse Problems*, **31**:045005, 2015.

[3] VA Sharafutdinov. "Integral geometry of tensor fields" VSP, The Netherlands, 1994.

[4] HJ Kirkwood et al. "Neutron strain tomography using the radon transform", *Mat. Today: Proc.*, **2**:S414-S423, 2015.

[5] CM Wensrich et al. "Neutron transmission strain tomography in granular systems" *Strain,* **52**:80–87 2016.

[6] CM Wensrich et al. "Bragg-edge neutron transmission strain tomography for in situ loadings", *Nucl. Inst. & Meth. in Phys. Res. B*, **383**:52–58, 2016.

[7] JN Hendriks et al. "Bragg-edge elastic strain tomography for in situ systems from energy-resolved neutron transmission imaging", *Phys. Rev. Mat.* **1**:053802, 2017.

[8] AWT Gregg et al. "Tomographic reconstruction of residual strain in axisymmetric systems from Bragg-edge neutron imaging", *Mech. Res. Comm.* **85**:96–103, 2017.

[9] AWT Gregg et al. "Tomographic reconstruction of two-dimensional residual strain fields from Bragg-edge neutron imaging", *Phys. Rev. App*. **10**:064034, 2018.

[10] C Jidling et al. "Probabilistic modelling and reconstruction of strain", *Nucl. Inst. & Meth. in Phys. Res. B.* **436**:141–155, 2018.

[11] JN Hendriks et al. "Implementation of traction constraints in Bragg-edge neutron transmission strain tomography", *Strain* (arXiv:1805.09760v2), 2018 (in Press).

C. M. Wensrich[1], A. W. T. Gregg[1], J. N. Hendriks[1], A. S. Tremsin[2], T. Shinohara[3], V. Luzin[1,4], A. Wills[1], O. Kirstein[1,5], M. H. Meylan[6], and E. H. Kisi[1]

[1]*School of Engineering, The University of Newcastle;* [2]*Space Sciences Laboratory, University of California;* [3]*Neutron Science Section, Materials and Life Science Division, J-PARC Center;* [4]*Australian Centre for Neutron Scattering, ANSTO;* [5]*European Spallation Source;* [6]*School of Mathematical and Physical Sciences, The University of Newcastle*

Crystalline Electric Field Level Scheme of the Non-Centrosymmetric CePtSi$_3$

Introduction

The study of new phenomena that appear due to a lack of inversion symmetry, such as spin Hall effect, multiferroics, topological insulators, and parity-mixing superconductors, has become one of the trends in modern physics. Especially, interesting phenomena such as unconventional pressure-induced superconductivity and multiple metamagnetic transitions have been reported in the CeTSi$_3$ system with a non-centrosymmetry (T = transition metals) [1, 2]. As a starting point of research on the CeTSi$_3$ system, we chose CePdSi$_3$ which has not been reported as superconductive by polycrystalline studies. We grew a single crystalline sample and measured the specific heat and magnetization to estimate the crystalline electric field (CEF) level scheme [2]. These results were in good agreement with the results of inelastic neutron scattering (INS) experiments reported in previous researches [3] and revealed that the wave function of the ground state of CePdSi$_3$ was Γ_6. Knowing the CEF levels in the CeTSi$_3$ systems, we noticed that the previous study on CePtSi$_3$ claimed that the CEF level lies at anomalously high energy [4]. Therefore, in the present study, we examined the CEF excitations in CePtSi$_3$ by INS experiment with a polycrystalline sample.

Experimental procedure

The constituent elements (Ce, 3N; La, 3N; Pt, 3N; Si, 6N) of Ce: Pt: Si = 1: 1: 3 were melted on a water-cooled copper hearth in an arc furnace to obtain a polycrystalline sample. The obtained sample was enhanced by annealing at 1050°C for 1 week.

INS experiments were carried out on polycrystalline samples of CePtSi$_3$ and LaPtSi$_3$ using the High Resolution Chopper (HRC) spectrometer installed at BL12 in J-PARC MLF. Nonmagnetic and isostructural LaPtSi$_3$ was used to estimate the phonon contribution to the scattering. Samples were cooled to 2.8 K, and INS spectra were acquired with three incident energies E_i = 11, 50, and 258 meV.

Results and discussion

Color-coded $|Q|$-E plots of the INS intensities of CePtSi$_3$ are shown in Figs. 1(a) and 1(b) [5]. Figure 1(a) shows the data at E_i = 258 meV, and no excitation was observed around 86 meV at which the previous magnetic susceptibility analysis suggested one of the CEF excitations [4]. By contrast, CePtSi$_3$ clearly shows the magnetic scattering below 20 meV as seen in Fig. 1(b) which was obtained by E_i = 50 meV. Here, we subtracted the phonon contribution of CePtSi$_3$ which was evaluated from the observed phonon spectrum in LaPtSi$_3$. The CEF excitations have been observed at approximately 5.3 and 17.5 meV, as indicated by the black arrows in Figs. 1(b) and 1(c). To see the CEF excitation peaks more clearly, the 1D-cut of Fig. 1(b) was constructed by integrating the intensity at $|Q|$ = 3 Å^{-1} over the width of ±0.1 Å^{-1} and shown in Fig. 1(c). The inset shows the expanded profile observed with E_i = 11 meV to better resolve the lower

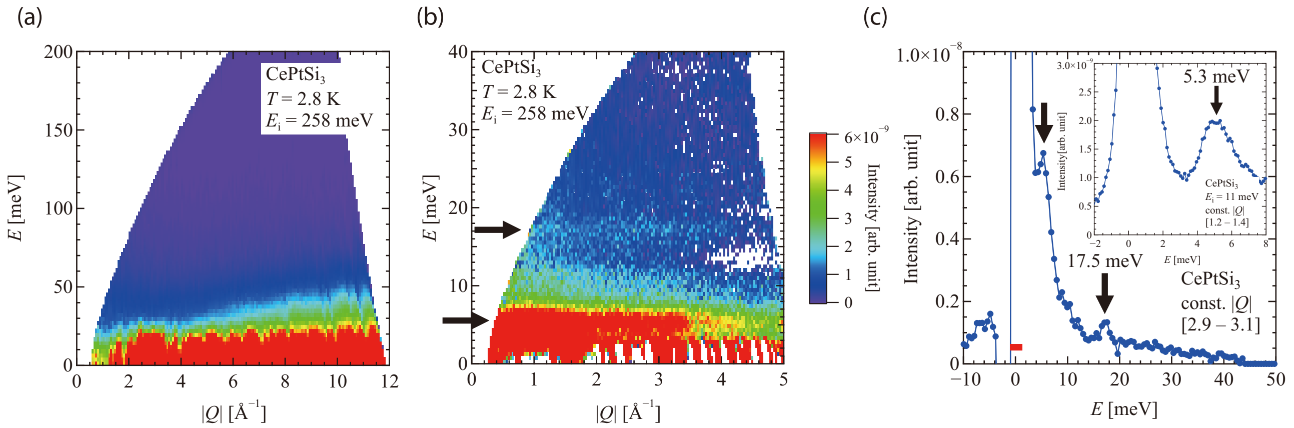

Figure 1. Color-coded plots of the INS intensity (a) with E_i = 258 meV and (b) magnetic scattering with E_i = 50 meV of CePtSi$_3$ at 2.8 K. (c) is a cut of magnetic scattering integrated over $|Q|$ from 2.9 to 3.1 Å^{-1}, and the inset shows the cut integrated from 1.2 to 1.4 Å^{-1} measured with E_i = 11 meV. The black arrows indicate the positions of the two CEF excitations at approximately 5.3 and 17.5 meV [5].

peak at 5.3 meV. The result of the CEF model calculation, which takes into account the observed CEF excitations, explains well the behavior of the specific heat and the magnetization, and we established that the wave function of the ground state of $CePtSi_3$ is Γ_6. The level scheme of $CePtSi_3$ is in qualitatively good agreement with the result of $CePdSi_3$ [2, 3]. We note that although the wave function of the ground state of pressure-induced superconductors $CeRhSi_3$ and $CeIrSi_3$ is Γ_7, the ground state of $CePdSi_3$ and $CePtSi_3$ with the multiple metamagnetic transitions is Γ_6. In the $CeTSi_3$ system, the differences in the physical properties such as superconductivity and multiple metamagnetic transitions may be classified by the wave function of the ground state.

References

[1] N. Kimura, K. Ito, H. Aoki, S. Uji, and T. Terashima, Phys. Rev. Lett. **95**, 247004 (2005) etc.

[2] D. Ueta, Y. Ikeda, and H. Yoshizawa, J. Phys. Soc. Jpn. **85**, 1014703 (2016).

[3] M. Smidman, Ph.D. thesis, The University of Warwick (2014).

[4] T. Kawai, Y. Okuda, H. Shishido, A. Thamizhavel, T. D. Matsuda, Y. Haga, M. Nakashima, T. Takeuchi, M. Hedo, Y. Uwatoko, R. Settai, Y. Ōnuki, J. Phys. Soc. Jpn. **76**, 014710 (2007).

[5] D. Ueta, T. Kobuke, M. Yoshida, H. Yoshizawa, Y. Ikeda, S. Itoh, T. Yokoo, Physica B **536**, 21 (2018).

D. Ueta[1,2], T. Kobuke[1], M. Yoshida[1], H. Yoshizawa[1], Y. Ikeda[3], S. Itoh[4,5], and T. Yokoo[4,5]

[1]*Institute for Solid State Physics, University of Tokyo;* [2]*Okinawa Institute of Science and Technology Graduate University;* [3]*Institute for Materials Research, Tohoku University;* [4]*Neutron Science Section, Materials and Life Science Division, J-PARC Center;* [5]*Institute of Materials Structure Science, KEK*

Observation of Temperature-Induced Structural Transition of Ceria via Solid-Gas Reaction

1. Introduction

Monitoring solid-gas chemical reactions is important not only in general chemistry but also in industrial applications. In the three-way catalysis (TWC) used in the automotive industry, the catalysts undergo a crystal structure change at high temperatures in a gas atmosphere.

Cerium dioxide (ceria or CeO_2) plays an extremely important role in TWC. This is attributed to the high oxygen storage capacity of CeO_2 resulting from the spontaneous redox reaction of cerium ($Ce^{IV} \leftrightarrow Ce^{III}$) [1]. Under hydrogen atmosphere, CeO_2 forms complex oxygen-deficient structures with a stoichiometric composition or non-stoichiometric compositions [2–4]. On the other hand, the diverse structure, which is the hydrogen-containing ceria (H_yCeO_2), was predicted by a calculation [5]. Although experimental and simulation studies showed that hydroxyls are formed by hydrogen [6–8], the chemical reaction and the crystal structure have not been experimentally observed yet.

In general, the reduction is explained by the reaction kinetics, which depends on temperature. To elucidate the structural changes in ceria under hydrogen, the investigation of the isothermal holding time and the crystal structure after thermal treatment is important. Herein, we investigated the crystal structure of ceria depending on the isothermal holding time at high temperature and various temperatures under hydrogen by using *in situ* neutron powder diffraction (NPD).

2. Experimental

We performed *in situ* NPD measurements of ceria, which were carried out using iMATERIA(BL20) [9, 10]. The reduction of ceria at 800°C under hydrogen gas (3% H_2 in N_2) was investigated using an infrared gas furnace. The oxygen pressure was less than 10^{-22} atm. The ceria pellets were placed in a quartz cell in the gas furnace. After evacuating the air from the furnace, hydrogen was injected at a gas flow rate of 50 ml/min. The heating/cooling rate was 10°C/min. The gas furnace was placed in an outer vacuum chamber and installed in the iMATERIA. *In situ* NPD measurements were performed at isothermal holding time of 30 min. or 20 h between 800°C and 25°C. The crystal structure was analyzed using Rietveld refinement (Z-Rietveld: Ver. 1.0.2) [11, 12].

3. Results and discussion

A: Crystal structure analysis of the short holding time ceria

During the cooling process form 800°C to 25°C, the new defined peaks of the sub-phase appeared around the peaks of the main phase below 500°C. In the results of Rietveld refinement at 25°C, the structure of the sub-phase was refined as the cubic oxyhydroxide CeO_2H (Ce^{III}) structure, as shown in Fig. 1. The H atoms condensed around the O atoms, and the occupancy was 0.125 (32*f* site). The final result provided the following crystallographic parameters for the cubic structure (space group *Fm-3m*), for the main phase: $a = 5.448319(8)$ Å, and for the sub-phase: $a = 5.51801(8)$ Å. The mass fraction of the main phase and the sub-phase were 93.1% and 6.9%, respectively. The lattice constant of the CeO_2H crystal increased up to approximately 1.3% compared with that of the main phase. The expansion behavior correlated with the change in the ionic radius of Ce and also the incorporation of numerous H atoms into the lattice.

B: Crystal structure analysis of the long holding time ceria

To evaluate the holding time dependence of the crystal structural changes of ceria over 20 h at 800°C, we sliced the isothermal holding time diffraction to the hourly measurement data, as shown in Fig. 2 (a). These diffraction peaks clearly showed that the *d*-spacing shifting consists of high region for increasing the holding time. Figure 2 (b) shows the holding time dependence of the lattice constant for a holding time of 20 h.

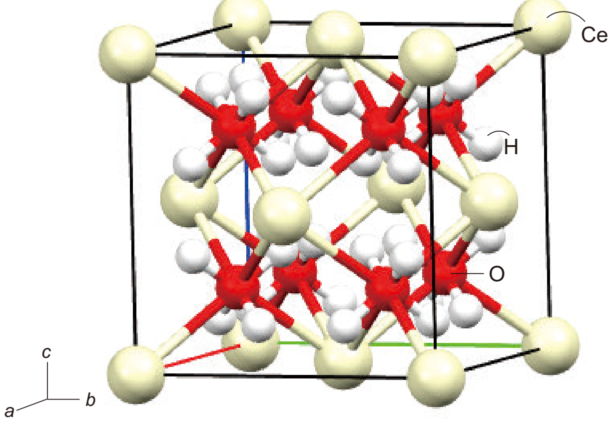

Figure 1. Packing arrangement of the cubic CeO_2H crystal.

The lattice constant continuously increased when the holding time was increased, because the extent of Ce reduction tended to increase with the progress of oxygen vacancy (the inset in Fig. 2 (b)). The 20 h data were refined to a cubic oxygen-deficient structure. The oxygen occupancy was estimated to be 0.9547(7), and the corresponding composition was $CeO_{1.909(1)}$. Ceria assumed an oxygen-deficient structure after 3 h, and the oxygen deficiency continually increased until a holding time of 20 h.

The temperature dependence of ceria during the cooling process between 800°C and 25°C is shown in Fig. 3 (a). Additional peaks (sub-phase) with a low *d*-spacing were seen as compared with the pattern of the main phase at 500°C. Moreover, below 400°C, the main phase of ceria changed substantially to a completely different structure. At 500°C, the structures of both the main phase and sub-phase were refined as cubic $CeO_{1.892(1)}$ and cubic $CeO_{1.94(2)}$, respectively. The refinement of the data at 25°C revealed that the main phase of ceria underwent a structural transition to the triclinic oxygen-deficient structure $Ce_{11}O_{20}$ (*i.e.*, $CeO_{1.83}$) as shown in Fig. 3 (b). Indeed, the structure of the sub-phase was entirely restored to CeO_2. The final results provided the following crystallographic parameters: (1) a main phase ($Ce_{11}O_{20}$), belonging to space group *P*-1; (2) a sub-phase (CeO_2), belonging to space group *Fm*-3*m*.

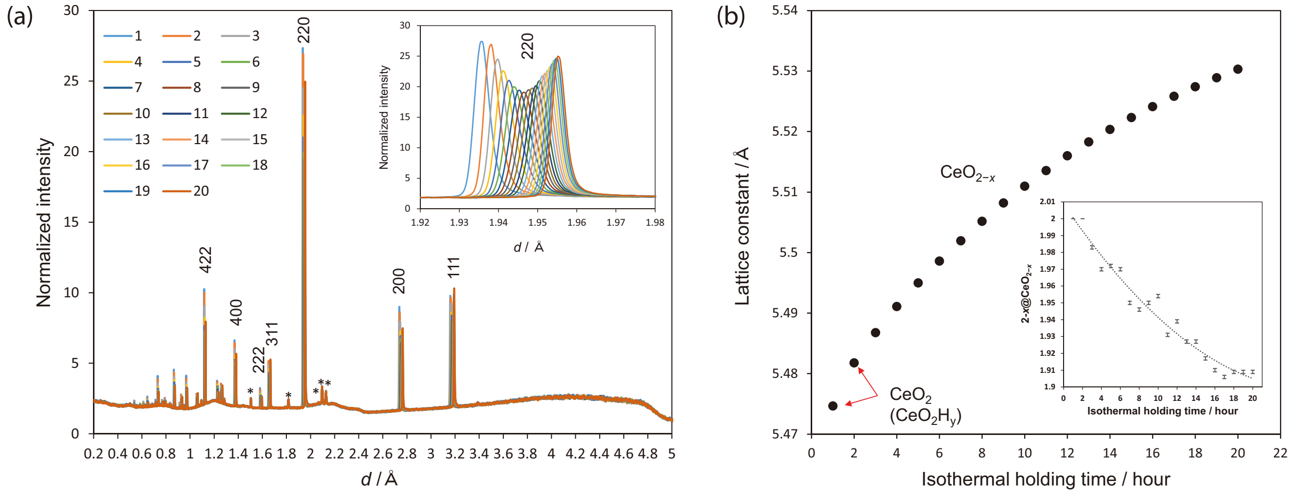

Figure 2. (a) Time sliced *in situ* NPD patterns of ceria crystal during 20 h at 800°C. The diffraction of isothermal holding time at 20 h was sliced to the 20 hourly measurement data (unit: h). Inset shows the diffracted patterns on 220. The asterisk denotes the peaks of the thermocouple. (b) Isothermal holding time dependence of the lattice constants of ceria at 800°C. Inset: time profiles of the 2−*x* value in CeO_{2-x} during 20 h holding at 800°C.

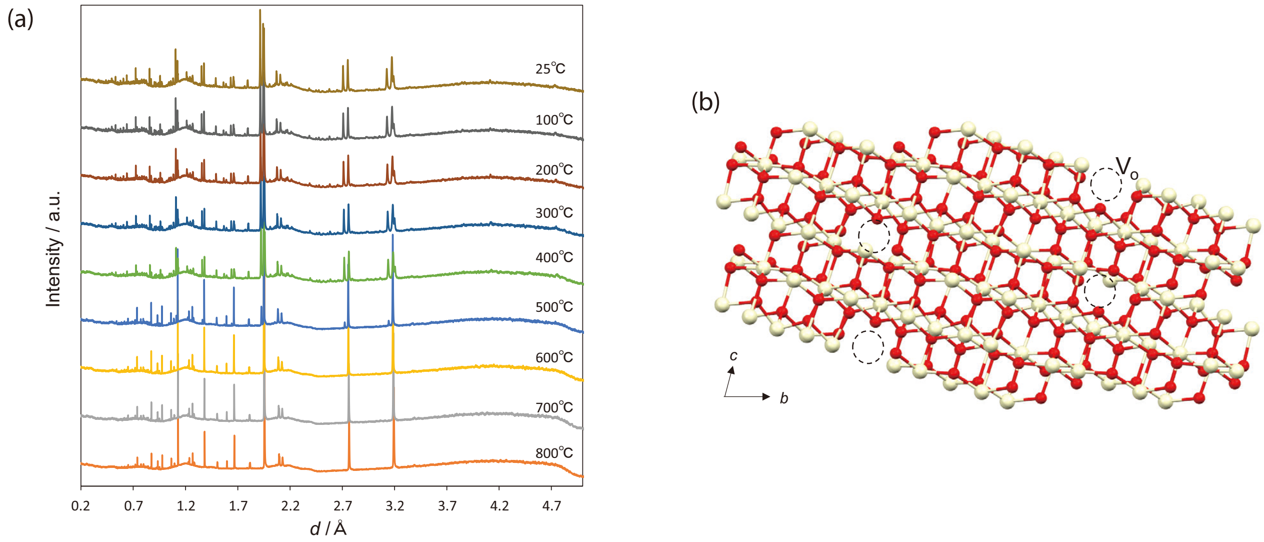

Figure 3. (a) NPD patterns of ceria crystal in the temperature range 25°C to 800°C. (b) Packing arrangement of the triclinic $Ce_{11}O_{20}$ crystal viewed perpendicular to the *a* axis. The black dot circle shows the oxygen vacancy (V_o) site.

C: Crystal transitions of ceria

At 800°C, the thermal diffusion and hydrogen incorporation into the lattice of ceria particle occur easily. CeO_{2-x} was created by the desorption of water molecules from CeO_2H. As cooling proceeded below 500°C, the thermal was not propagated in the ceria lattice, and the incorporation of hydrogen might be difficult. In particular, the "center" of the reduced ceria particles was unstable, because of absence of reducing conditions. In order to oxidize from CeO_{2-x} phase to CeO_2 phase, the CeO_{2-x} phase at the center/core of the ceria particles underwent oxidation into CeO_2 by accepting oxygen from the outer region (outside) of the particles. The CeO_2 phase was concentrated at the center of the ceria particle during cooling ($Ce^{III} \rightarrow Ce^{IV}$). On the other hand, reduction of the outer phase of the ceria particles was more pronounced in the bulk by desorption of the O atoms from the particle. Strained Ce and O atoms of the oxygen-deficient $Ce_{11}O_{20}$ structure were formed by rapid breakage of covalent bonds at low temperature.

3. Conclusions

We investigated the crystal structure of ceria depending on the isothermal holding time at high temperature and various temperatures under hydrogen by using *in situ* NPD measurements. In the case of short holding time, the cubic oxyhydroxide (CeO_2H) was formed by the interaction of hydrogen interaction with ceria during the cooling process from 800°C. On the other hand, the oxygen vacancies of ceria were kinetically progressed during a long holding time at 800°C. Below 400°C, the main phase of CeO_{2-x} changed to a triclinic oxygen-deficient structure $Ce_{11}O_{20}$. The solid-gas reaction of ceria occurred with strong dependence on the isothermal holding time and the temperature.

References

[1] Z. Hu, *et al*., ACS Catal., **6**, (2016) 2265.

[2] S. P. Ray, *et al*., J. Solid State Chem., **15**, (1975) 344.

[3] O. T. Sorensen, J. Solid State Chem., **18**, (1976) 217.

[4] S. Bernal, *et al*., J. Chem. Soc. Faraday Trans., **89**, (1993) 3499.

[5] K. Sohlberg, *et al*., J. Am. Chem. Soc., **123**, (2001) 6609.

[6] B. Chen, *et al*., J. Phys. Chem. C, **117**, (2013) 5800.

[7] X.-P. Wu, *et al*., Phys. Chem. Chem. Phys., **17**, (2015) 3544.

[8] K. Werner, *et al*., J. Am. Chem. Soc., **139**, (2017) 17608.

[9] T. Ishigaki, *et al*., Physica B, **385–386**, (2006) 1022.

[10] T. Ishigaki, *et al*., Nucl. Instrum. Meth. A, **600**, (2009) 189.

[11] R. Oishi, *et al*., Nucl. Instrum. Methods Phys. Res., Sec. A, **600**, (2009) 94.

[12] R. Oishi-Tomiyasu, *et al*., J. Appl. Crystallogr., **45**, (2012) 299.

T. Matsukawa, A. Hoshikawa, and T. Ishigaki
Frontier Research Center for Applied Atomic Sciences, Ibaraki University

Nuclear Magnetic Field Detected with $\mu^{\pm}$SR

1. Introduction

Positive muon spin rotation and relaxation (μ^+SR) is a unique technique to detect a nuclear magnetic field in solids regardless of the presence of magnetic ions [1, 2]. It provides a great advantage over NMR, particularly for studying ion diffusion in cathode materials for a Li-ion battery, because such materials always include magnetic ions. Here, the implanted μ^+ sits at the interstitial site, where the electrostatic potential is minimal. However, at high temperatures, such μ^+ starts to diffuse, while one cannot predict the temperature above which μ^+ becomes mobile. Therefore, the μ^+SR result obtained at high temperatures unavoidably includes an ambiguity. We have therefore started a new project for detecting a nuclear magnetic field in solids with μ^-SR, since the implanted μ^- is captured on a nucleus, leading to the formation of a muonic atom, which is stable even at high temperatures.

Before measuring Li diffusion with μ^-SR, we have attempted to measure the μ^-SR spectrum on MgH_2 (Fig. 1), which was investigated extensively as a candidate of the hydrogen storage material, for detecting a nuclear magnetic field. This is because, since the μ^- captured on H in MgH_2 is quickly transferred to Mg nuclei, the μ^-SR spectrum is expected to be analyzed easily.

2. Experimental

The internal magnetic field in MgH_2 was studied with both μ^+SR and μ^-SR. During μ^+SR measurements at temperatures between 300 and 800 K, the pressure in the sample cell was monitored to know the change in the μ^+SR parameters at the desorption temperature, that is, we have developed an *in-situ* μ^+SR technique [3].

The μ^-SR experiment on MgH_2 was performed only at room temperature in order to confirm the observation of a nuclear magnetic field. The experimental details for both measurements are described elsewhere [3, 4].

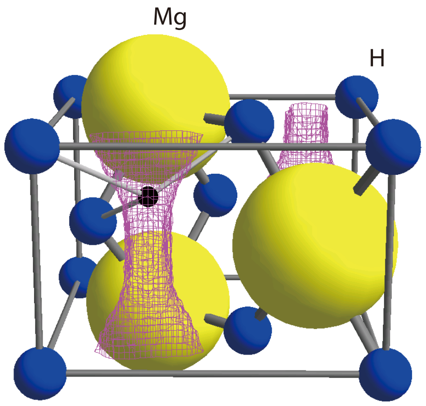

Figure 1. The crystal structure of MgH_2 in tetragonal symmetry with the space group $P4_2/mnm$ together with the μ^+ sites predicted by DFT calculations [3]. The implanted μ^+ distributes in a pinkish one-dimensional channel along the *c*-axs. On the other hand, μ^- locates at the Mg position. Reproduced from Ref. [3] with permission from The Royal Society of Chemistry.

3. Results

Figure 2 shows the temperature dependences of the field distribution width (Δ) and field fluctuation rate (ν) in MgH_2 estimated with μ^+SR together with the

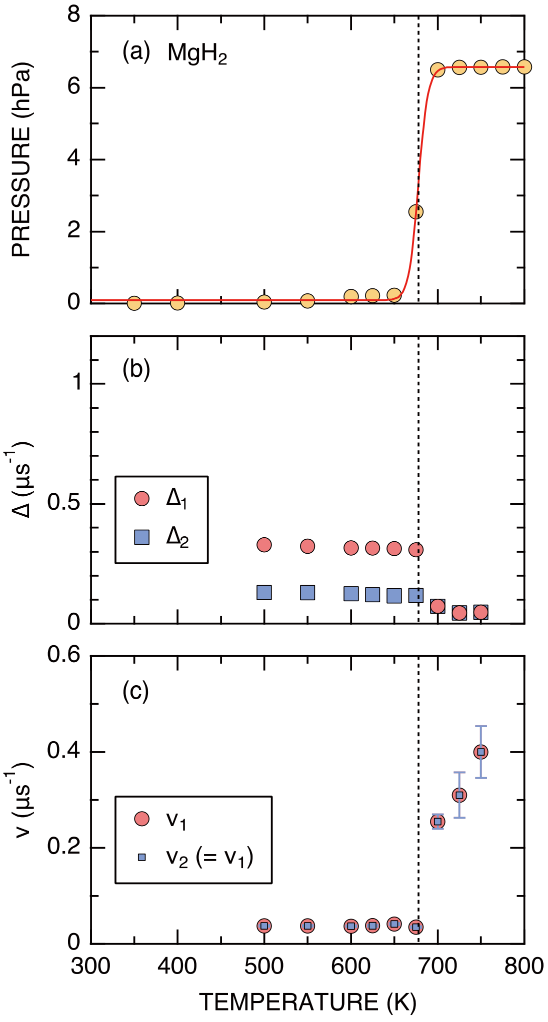

Figure 2. The temperature dependences of the gas pressure and μ^+SR parameters for MgH_2 [3]: (a) gas pressure in the cell; (b) the field distribution widths (Δ_1 and Δ_2); (c) the field fluctuation rates (ν_1 and ν_2). Dipole field calculations provide that Δ^{calc} ranges 0.629 and 0.664 μs^{-1}. Dotted lines show the desorption temperature determined from the $p(T)$ curve. Reproduced from Ref. [3] with permission from The Royal Society of Chemistry.

pressure (*p*) in the sample cell. Both Δ and ν are found to be temperature independent below the vicinity of the desorption temperature (T_d = 680 K), around which *p* increases very rapidly. Although μ^+SR shows a static behavior up to 680 K, the magnitude of Δ is about 1/2 of the value predicted with dipole field calculations. This implies the μ^+ diffusion in MgH_2 above 300 K.

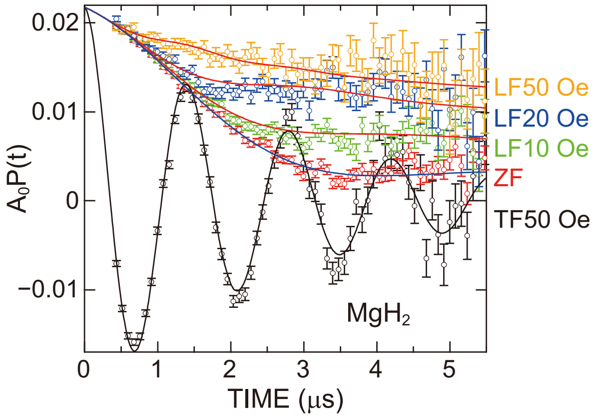

Figure 3. The TF-, ZF-, and LF-μ^-SR asymmetry spectra for MgH_2 recorded at room temperature. The fit provides that Δ = 0.520(7) μs^{-1} [equivalent to a field distribution width of 6.11(8) Oe], while dipole field calculations predict Δ^{calc} = 0.5807 μs^{-1} [6.819 Oe] at the Mg site. Copyright 2018 American Physical Society.

On the contrary, μ^-SR provides a reasonable Δ for the Mg site at room temperature (Fig. 3), as expected. This demonstrates the unique power of μ^-SR for detecting an internal magnetic field in solids at high temperatures.

4. Future plans

The nuclear magnetic field in MgH_2 was successfully detected with μ^-SR from a fixed Mg position. Based on this result, we wish to propose a combination of μ^+SR and μ^-SR to obtain reliable information on the dynamic behavior in the nuclear magnetic field in solids. Such combined work should be useful specifically for measuring ion diffusion in battery materials and we are working in that field.

References

[1] J. Sugiyama et al., Phys. Rev. Lett., **103**, 147601-1-4 (2009).
[2] J. Sugiyama et al., Phys. Chem. Chem. Phys. **15**, 10402–10412 (2013).
[3] J. Sugiyama et al., Sustainable Energy Fuels **3**, 956–964 (2019).
[4] J. Sugiyama et al., Phys. Rev. Lett., **121**, 087202-1-5 (2018).

J. Sugiyama[1,2], I. Umegaki[2], S. Takeshita[3,4], A. Koda[3,4], K. Shimomura[3,4], and W. Higemoto[3]
[1]Neutron Science and Technology Center, CROSS; [2]Toyota Central Research & Development Labs., Inc; [3]Muon Science Section, Materials and Life Science Division, J-PARC Center; [4]Institute of Materials Structure Science, KEK

Neutron Source

Progress of the Neutron Source Section

Fiscal year 2018 started with a beam operation of 500 kW, which had been recognized as an important milestone to reach the final goal of 1 MW. Since two targets failed consecutively during the 500-kW beam operation in 2015, considerable efforts were put into improving the design of the next mercury target, target #8, to make it more robust and reliable in a high-power operation. Target #8 had been used at 300 kW and 400 kW since the last fiscal year and completed its user beam operation successfully on June 30, 2018 after a 3-months operation at 500 kW, which demonstrated the validity of the design improvement. Additionally, target #8 was operated with a 935-kW power for one hour at the high-power beam study held on July 3. Reaching almost 1 MW was a great achievement for J-PARC.

Gas-micro-bubbles injection into mercury and the high-speed mercury flow in a narrow channel formed by the double walled structure, shown schematically in Fig. 1, are the key measures to mitigate the pitting damage at the beam window located at the front end of the target vessel. At the high-power beam study, the vibration of the target vessel under the beam operation condition of 25 Hz was measured at almost 1 MW for the first time, as shown in Fig. 2. The displacement velocity on the top side of the target vessel at 935 kW remained on the same trend line with those measured at a lower beam power. It shows the efficacy of gas-micro-bubble injection to reduce the displacement velocity at a 1-MW operation.

The specimens were taken out of the used target #8 and the maximum depth of pitting damage on the inner side of the beam window was 18 μm, which was less than predicted. This fact demonstrated the effectiveness of the present measures to mitigate pitting damage. Then, target #8 was replaced with target #9, which has the same structure as target #8. The beam operation of target #9 had continued well at 500 kW with the high average availability of 93.2% as of the end of fiscal year 2018.

An important event was the transportation of the used target vessel from the MLF (Materials and Life Science Experimental Facility) to the RAM (Radio Activated Materials) building to save the limited space of the used components storage room in the MLF. A shielding container, 200 mm in wall thickness and 44 tons in total weight, was fabricated and used in combination with the shipping container fabricated in 2017. The preparation and rehearsal took almost a month and the used target vessel was transported successfully to the RAM building for the first time on January 16, 2019. The transportation is going to be held every year.

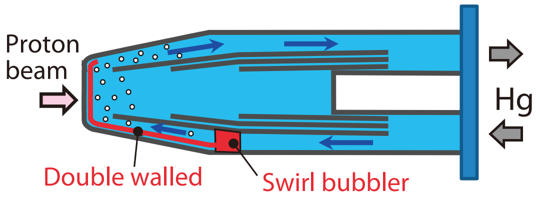

Figure 1. Measures to mitigate pitting damage applied in target #8.

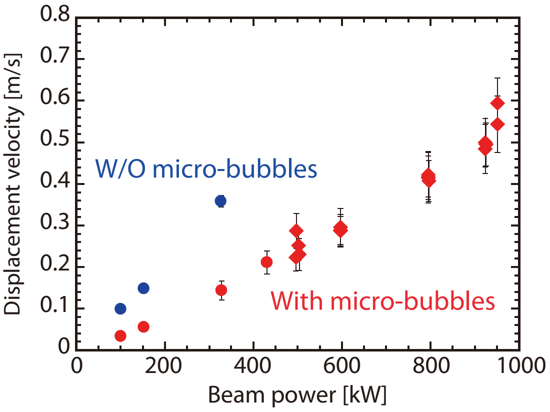

Figure 2. Displacement velocity at the top side of target vessel #8 at beam study.

Figure 3. Transportation of a used target vessel.

K. Haga
Neutron Source Section, Materials and Life Science Division, J-PARC Center

Operation Status and Design Improvement for the Mercury Target Vessel

1. Introduction

In a mercury target for the J-PARC neutron source, reduction of the pressure waves caused by rapid thermal expansion of liquid mercury due to the high-intense pulsed 3 GeV proton beam injection at 25 Hz is a key to achieve high-power stable operation. The pressure waves induce not only fatigue but also severe cavitation erosion on the mercury enclosure vessel [1]. To reduce the pressure waves, the mercury target system has been operated with helium microbubbles injection into mercury by using cushion effect of the microbubbles [2].

Here, the operational result of target vessel No. 8 is reported, which was operated under gas microbubbles injection into liquid mercury to reduce the pressure waves. Furthermore, an improved target vessel design to reduce thermal stress for the high-power operation is also introduced.

2. Gas microbubble injection

In the original operation, helium gas, pressurized by a compressor, was supplied to the bubble generator which made a crowd of gas into microbubbles. Since December 2017, the gas has been supplied to the bubble generator without an operating compressor because of the possibility that the activated gas could spill into the environment in the case of compressor failure under the high pressure of 300 kPa.

To avoid high pressure in the gas-supplying line during operation, the configuration of the bubble generator was improved to create negative pressure at the bubbler and bring in an amount of gas comparable to the one delivered when the compressor was still used. During the operation, the vibration of the target vessel due to the pressure waves was monitored by a Laser Doppler Vibrometer to understand the reduction behavior of the pressure waves changed by gas microbubbles injection.

Figure 1 shows the time histories of the peak amplitude of vibration (displacement velocity) on target vessel No. 8 and the beam power. As the beam power was ramped up from 300 kW to 400 kW, the velocity increased from 0.13 m/s to 0.17 m/s. The estimated displacement velocity without microbubbles [1] is also shown in Fig. 1. The ratio of the measured displacement velocity to the estimated one without microbubble is approximately 0.3, which is independent of both the beam power and the operation with or without compressor. In short, the amount of microbubble injection for improved bubble generator without compressor was as much as with the operating compressor.

3. Effect of the gas microbubble injection on cavitation damage

The beam window portion of the used target vessel No. 8, which operated at up to 1812 MWh and 434 kW in average power, was cut using an annular cutter aiming to investigate the effect of a gas microbubble injection into the mercury. Figure 2 shows the photographs of the interior surface cutout from the used target vessel. It can be seen that the localized deep pits are recognized on the inner wall surface facing the bubbly mercury, whereas the pits with lesser damage are recognized on the outer wall surface facing the narrow channel. The cavitation damage on the narrow channel surface was slightly less than that of the damage observed in target vessel No. 5 that was operated under the average beam power of 400 kW. The max. damage depth of the inner wall surface was estimated to be 286 μm. It was found that the estimated damage depth faced with bubbly mercury was corresponded to the damage formed at approximately 30% of the beam power without injecting gas microbubbles [2, 3].

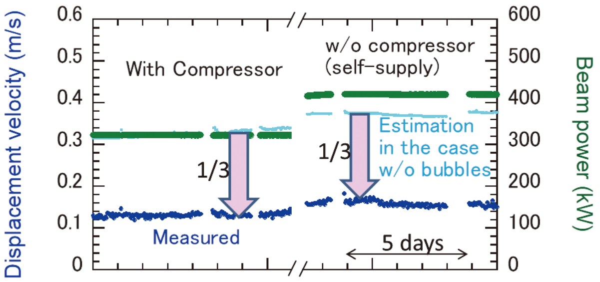

Figure 1. Time history of displacement velocity on target vessel No.8 and the beam power.

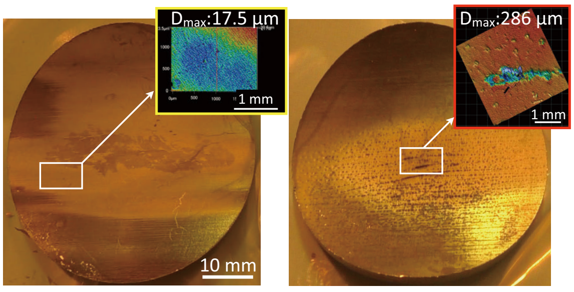

Outer wall Inner wall

Figure 2. Cutout surfaces of target vessel No. 8.

4. New target vessel, constraint free type, design and fabrication

Figure 3 shows a schematic cross-sectional view of an improved mercury target vessel. A mercury vessel is covered by a water shroud to prevent spills of mercury in a case of its failure. The original design of the mercury target vessel had a constraint structure between the water shroud and the mercury vessel with monolithic structure to maintain the robustness as shown in Fig. 4(a) [4–5]. The structure of the vessels has been greatly improved from target vessel No. 10. In particular, the constrain free structure between the mercury vessel and the water shroud was adopted to reduce the thermal stress during high-power operation in addition to improve the location of welding line and fabrication process (Fig. 4(b)) [6]. As seen in the figure, the mercury vessel and the water shroud is fixed at the end of the mercury vessel through a support plate by TIG welding. The main design conditions of the target vessels are shown in Table 1. In the constraint free type design, it is expected to reduce the thermal stress due to the difference of thermal expansion between the mercury vessel and the water shroud, whereas the deformation of water shroud by the gas pressure in the helium layer is increased. Therefore, it was necessary to modify some designs for the fabrication technique and processes, such as water channels, support plate structures, and welding technology using electron beam welding.

Table 1. Design condition of mercury target vessel.

	Design Pressure (MPa)	Temperature of inlet (°C)
Hg (Layer)	0.5	50
He (Layer)	0.2	25
H_2O (Layer)	*0.2 or 0.5	25

*0.5 MPa for #11, and #12, 0.2 MPa for #8, #9, and #10

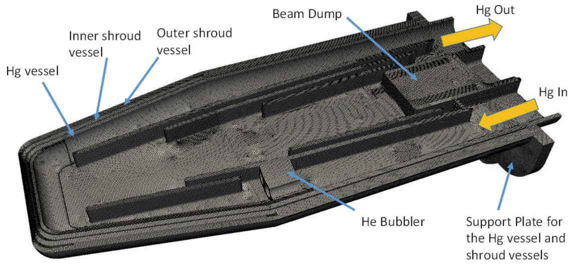

Figure 3. A cross section view of mercury target vessel. The support plate is shown in the left-hand side.

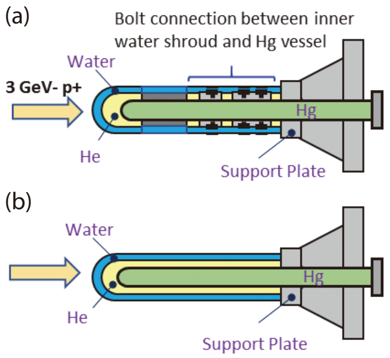

Figure 4. Schematic cross-sectional images of (a) a constraint structure and (b) a constraint free structure between mercury vessel and water shroud.

The calculated thermal stress decreased and was improved in comparison with the previous type. The new type has been fabricated, and it will be operated from December 2019.

5. Summary

1) The peak vibration (displacement velocity) on target vessel No. 8 was evaluated under the beam power of 300 and 400 kW. The ratio of the measured velocity to the estimated one without microbubble was approximately 0.3, which was independent of both of the beam power and the compressor operation.
2) The beam window portion of the used No. 8 was cut to investigate the effect of the gas microbubble injection into the liquid mercury. The cavitation damage on the narrow channel surface was slightly less than that of No. 5, and the max. damage depth of the inner wall surface was 286 μm.
3) New target vessel with constraint free type was designed and fabricated.

References

[1] T. Naoe, et al., Cavitation damage prediction for the JSNS mercury target vessel, J. Nucl. Mater. **468** (2016) 313–320.
[2] H. Kogawa, et al., J. Nucl. Sci. & Tech., **54** (2017) 733–741.
[3] H. Kogawa, et al., J. Nucl. Sci. & Tech., **52** (2015) 1461–1469.
[4] T. Wakui, et al., J. Nucl. Mater. **506** (2018) 3–11.
[5] T. Wakui, et al., presented in IWSMT14, in Iwaki, Japan (Nov. 2018).
[6] E. Wakai, et al., Proceedings of the 15th annual meeting of Particle Accelerator Society of Japan, (2018) 181–184.

E. Wakai[1], H. Kogawa[2], T. Naoe[2], and T. Wakui[2]
[1]*Materials and Life Science Division, J-PARC Center;* [2]*Neutron Source Section, Materials and Life Science Division, J-PARC Center*

Quadrupole Magnet (QC12) Trouble in 3NBT

1. Introduction

The 3-GeV proton beam transport facility (3NBT) transports the beam from the 3-GeV Rapid Cycling Synchrotron (RCS) to the Material and Life Science Experimental Facility (MLF) in J-PARC. In the 3NBT, the 300-meter long beamline has many electric magnets such as 9 bending, 54 quadrupole, 48 steering, and 2 octupole magnets. Here we report a failure of a quadrupole magnet (QC12, see Fig. 1) that happened on May 17, 2018.

2. Failure of the magnet

At 4 AM on May 17, 2018, a layer short occurred at the coil of quadrupole magnet QC12. The layer short caused an unbalanced quadrupole magnetic field. Along the downstream of the QC12, the beam position moved into the horizontal and vertical directions. By the beam orbit confirmation, the beam was kicked at the QC12 with an angle of about 7 mrad for both directions. This angle was created by the offset of the centerfield ~7 mm to the magnet. When the layer short happened, the beam position shifted about 40 mm in the vertical direction at the beam monitor placed at the proton beam window (PBW). The beam shift led to an abnormal temperature increase, which was observed by the beam halo monitor placed at the PBW. Eventually, the machine protection system (MPS) of the beam halo monitor stopped the beam.

The quadrupole magnet is driven by the given current to control the field. Due to the layer short, the supplied voltage dropped from 77 to 71 V. Several hours after the event, the supplied voltage was stable, which implied conserving the status. Therefore, we decided to continue the beam operation by using steering magnets to centralize the beam position. As a countermeasure against further layer short, we added the interlock for the beam position and the current density of the beam monitors placed at the PBW. Also, the interlock was added for the supplied voltage of QC12. After beam tuning and additional interlock, the beam operation resumed successfully 13 hours later at 5:15 PM.

3. Research of the layer short

Figure 2 shows a cross-sectional view of the QC12 coil. Each coil has 129 turns of a hollow conductor made of dioxide copper. Due to the flow of the cooling water with the temperature kept less than 60°C to prevent erosion, the coil was divided into three zones

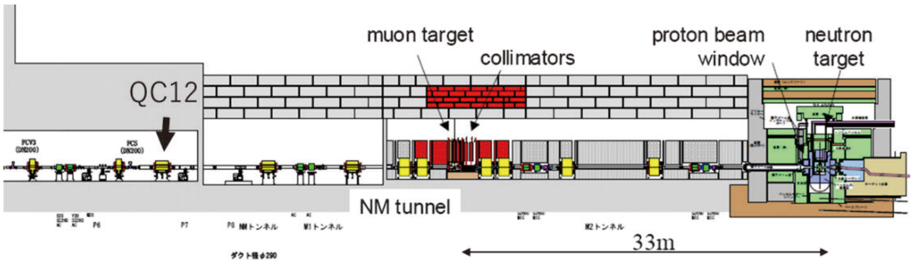

Figure 1. Segment of the 3NBT proton beamline from around QC12 to the neutron target.

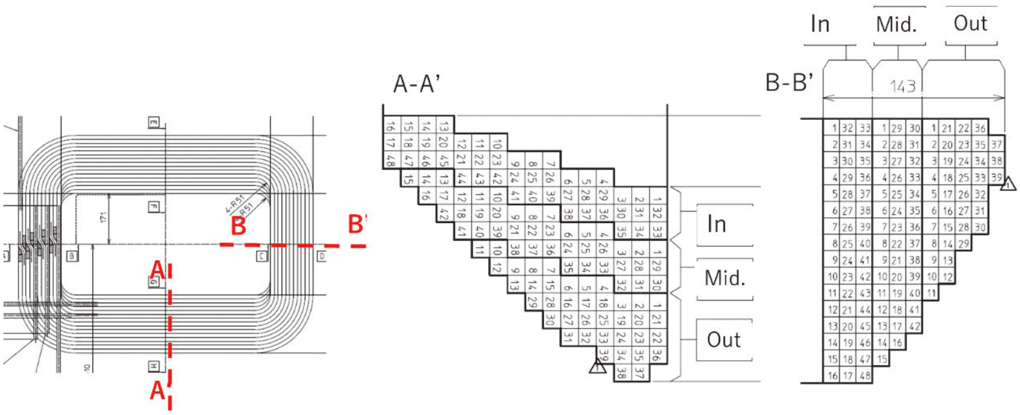

Figure 2. Overview of the QC12 coil (left) and cross-section of the A-A' and B-B' position.

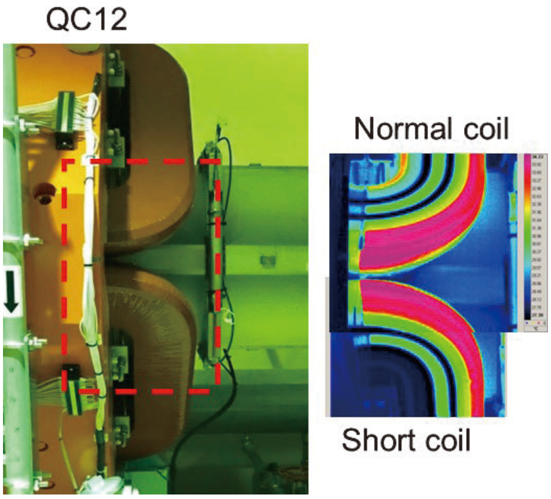

Figure 3. Photo (on the left) and infrared image (on the right) of the QC12. The infrared image shows a normal coil and a coil with short circuit.

called inner, middle, and outer coil. The reactance and inductance of the coil were measured for each zone. The inductance of the inner coil and middle coil was found to be about one-tenth of the others. It was concluded that the layer short occurred between the inner and middle coil. In order to find the anomaly coil, we observed the temperature distribution of the coil with an exciting magnetic field. Figure 3 shows the infra-red image of the QC12. It was found that the coil placed at the lower part showed lower temperatures than other ones, which did not have layer short. The infra-red view also suggested that the layer short happened between the inner and middle coil, even though it was difficult to pinpoint the exact place of the short circuit.

4. Subsequent actions

There was a possibility for the layer short to worsen over a longer time period. Although we had a spare coil, the exchange of the coil for the QC12 was expected to take long, about one month. In order to replace the coil, we had to take an unscheduled beam stop. Therefore, we tried to find the solution without the usage of the QC12. After beam study, we found a solution of the beam optics that excluded the affected magnet but prevented significant beam loss. Without the use of the QC12, the beam operation continued until the summer outage period. It should be mentioned that the demonstration with a 1-MW beam power was made without the use of the QC12. Since the beam quality of the Rapid Cycling Synchrotron (RCS) was better than designed, a high-intensity beam operation was completed without the QC12 successfully without beam loss.

Although the cause of the layer short has not been determined yet, it was probably related to a water leak event in the early days of the QC12 magnet. The water leak may cause corrosion with the radiation leading to the layer short. Since another quadrupole magnet had leaked water in the past, it was decided to exchange the coil in the next year as a precaution against layer short. Furthermore, in order to apply quick recovery against more layer shorts in the future, a study without the usage of another quadrupole magnet will be performed later.

It should be noted that the method of deactivating the magnet can be applied for the quadrupole. For the bending magnet failure, the coil must be exchanged. In 2019, the bending magnet for the beam transport from the RCS to the 30-GeV synchrotron (MR) failed. The lack of a spare coil for the failed magnet halted the beam operation of the MR for a long time. All of magnet failure events were somewhat related to the corrosion of the coil. To avoid the corrosion, the purification system of the cooling water will be improved. Also, the failure event showed the importance of having a spare coil. Therefore, we will increase the number of spare coils to handle effectively the failures of the magnet.

M. Ooi and S. Meigo
Neutron Source Section, Materials and Life Science Division, J-PARC Center

Neutron Science

Neutron Science Section

1. User program

In the beginning of JFY2018, the target was operated at 400 kW and from April 19, the power was increased up to 500 kW.

For the general-proposal round for 2018A, 175 general proposals and 5 new user promotion (NUP) proposals were approved from 260 submissions. 174 approved experiments and 9 reserved ones were executed among them. For 2018B, 190 general proposals and 8 NUP proposals were approved from 285 submissions. 178 approved experiments and 13 reserved ones were executed among them. Additionally, 4 newly approved long-term proposals became the beginning of a 3-years project from 2018B term. Fast Track Proposal, which is a mail-in program, has just started from the end of JFY2017 for Super HRPD at BL08 and NOVA at BL21. In 2018, 3 experiments were executed at BL08 and 2 experiments were done at BL21.

2. Instruments

The layout of the neutron instruments at the MLF, as of the end of JFY2018, is shown in Fig. 1.

This year, the MLF was stably operated with beam power of 500 kW . On July 3, a test operation with 1 MW was performed for 1 hour. The high beam power was experienced in each beam line. For example, on the chopper spectrometers AMATERAS at BL14 and 4SEASONS at BL01, inelastic neutron scattering from $S = 1/2$ one-dimensional antiferromagnets were measured. The dispersion relation of the spin excitations could be identified in the measurement for a few minutes, and well-analyzable data were obtained even within 1 hour.

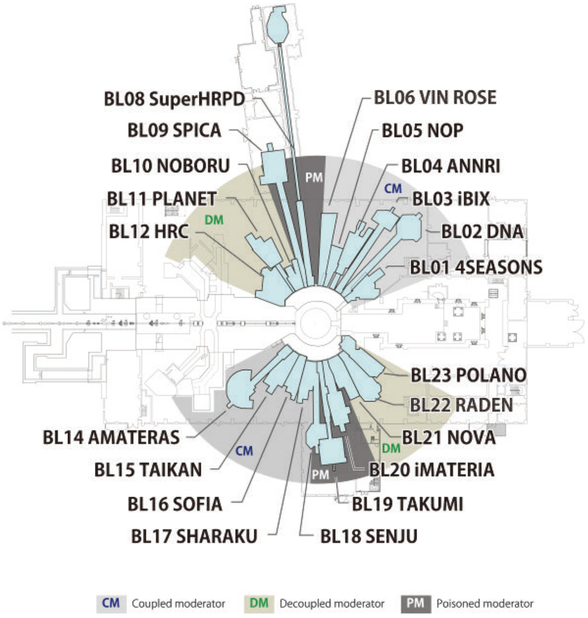

Figure 1. Layout of the neutron instruments at MLF as of JFY2018. BL23 was in the commissioning phase.

Since the start of the user program in the MIEZE part of the neutron spin-echo suit VIN ROSE at BL06 in 2018, scientific outcomes are starting to appear. An experiment was performed in MnSi, where various spin structures, such as helical spin structure, conical spin structure, and skyrmions, are expected below the transition temperature. Clear spin relaxation was successfully observed just above the transition temperature.

POLANO (Polarized Neutron Spectrometer) at BL23 is still under commissioning. On-beam commissioning using actual samples was performed with an unpolarized neutron beam. Magnetic excitations in a single-crystalline sample of one-dimensional antiferromagnet $CsVCl_3$, whose excitation energies spread up to 80 meV, were successfully observed. Also, excitations in ZrH_2 were observed. In ZrH_2, the motion of a hydrogen atom can be approximated to be a quantum harmonic oscillator, and energy levels with an equal interval can be observed. Using the detector system covering scattering angles up to 130°, the entire $S(Q, \omega)$ of the harmonic oscillator was clearly observed. These results indicate that POLANO is useful not only for studies of spin systems but also for studies of hydrogens. POLANO will open for user program from 2019A with unpolarized neutrons.

3. Event, meetings, and other activities

The 3rd Neutron and Muon School was held in November 20–24. 35 young researchers and graduate students from China (8), India (5), Korea (1), Thailand (1), Russian Federation (1), United Kingdom (1), as well as Japan (17) participated in the school. From the neutron group, 9 neutron instruments (4SEASONS, DNA, iBIX, PLANET, TAKUMI, iMATERA, TAIKAN, SHARAKU) were contributed to hands-on experiments (Figs. 2 and 3).

J-PARC Center and CROSS hosted the J-PARC Workshop “Deuterium Labeling Study for Neutron Science” on January 15 and 16, 2019. We invited Dr. T. A. Darwith from ANSTO and the 20 participating scientists discussed neutron studies on material and life siences by utlizing deuterium labeling.

The neutron science group hosted user group meetings of individual intruments. DIRECTION 2019 (MLF spectroscopy group user meeting) was held on

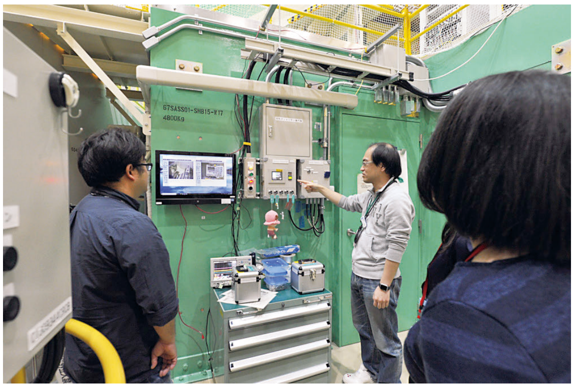

Figure 2. Dr. Kosuke Hiroi explaining the operation of the shutter control pannel at TAIKAN at the 3rd Neutron and Muon School hands-on experiment.

Figure 3. Dr. Shinichi Takata explaining instruments in the experimental hall of MLF to students of the 3rd Neutron and Muon School.

October 11 at Ibaraki Quantum Beam Research Center (IQBRC). We had 54 participants. User group meeting of DNA was held on October 12 at IQBRC and 18 particpants joined. We also had user group meeting of RADN (October 10) and PLANET (October 11). At these meeting, latest information of instruments and recent outcomes from experiments by users were presented and the users provided feedback to the instrumental scientists.

In the frame work of the young research fellowship program orgnaized by the Asia-Oceania Neutron Scattering Association (AONSA), we accepted as a research fellow Dr. Xingxing Zhang (Institute of Metal Research, Chinese Academy of Sciences). Dr. Zhang joined TAKUMI group from November 1 to December 27 and he enjoyed his research on Al-based composit materilas.

4. Resultant outcomes

The research activities in neutron science at the MLF resulted in more than 180 papers and 10 press releases. The number of papers includes articles in influential journals such as Nature Physics (1), Nature Materials (1) and Scientific Reports (6). Press releases included two detector developments, such as a high-resolution (~11 nm) emulsion type detector and a high-speed neutron imaging detector via a solid-state superconducting detector.

Dr. Takuro Kawasaki won the 16th Young Researchers Prize of the Japanese Society for Neutron Science for the development of stroboscopic measurements and leading research with the technique on SENJYU (BL18) and TAKUMI (BL19).

The RADEN (BL22) group won JAEA President's Award for the development of energy-resolved neutron imaging and leading researches on RADEN.

Figure 4. Dr. Takuro Kawasaki recieving certification from Prof. Y. Kiyanagi, the president of the Japanese Society for Neutron Science.

K. Nakajima[1], Y. Kawakita[1], S. Itoh[1,2], and T. Otomo[1,2]

[1]*Neutron Science Section, Materials and Life Science Division, J-PARC Center;* [2]*Institute of Materials Structure Science, High Energy Accelerator Research Organization, KEK*

BL01: 4D-Space Access Neutron Spectrometer 4SEASONS

1. Introduction and statistics

4SEASONS is a direct-geometry time-of-flight neutron spectrometer for thermal neutrons, and one of the Public Beamlines in MLF [1]. The momentum-energy region for this spectrometer occupies the middle of the momentum-energy space covered by all the MLF spectrometers [2, 3]. In 2018, 23 General Use (short-term) proposals, 1 Project Use proposal, and 1 Instrument Group Use proposal, were approved for 4SEASONS. In addition, 1 reserved (short-term) proposal was given beamtime. About 80% of the proposals were submitted for the fields of magnetism and strongly correlated electron systems. 2/3 of the proposals targeted magnetic excitations, while 1/3 of the proposals were for measurements of phonons. As for the outcomes from using the instrument, 15 peer-reviewed papers were published in 2018. 12 were papers for material science, while 3 papers were related to the instrumentation.

2. Instrument upgrade

Detectors: 4SEASONS is equipped with a number of ϕ3/4 inch × 2.5 m ^{3}He position sensitive detectors. We have been increasing the number of detectors since the start of the instrument's operation. In 2018, we installed 37 detectors. As a result, the maximum scattering angle in the horizontal plane reached 127 degrees.

Fermi chopper: We have been developing a Fermi chopper with supermirror-coated slits, which is expected to provide higher transmission at low energies. In 2014, we conducted a performance test of a prototype, which this year was finally followed by a performance test of a real model. We expected the real model to perform better than the prototype, because the supermirrors used in the real model have higher reflectivity. We found that the real model showed higher transmission at a high-energy region. Unexpectedly, however, the transmission at low energies was lower than that with the prototype. We suspect the supermirror does not work as expected, but the true cause is still unclear.

Sample environment: There are difficulties in the use of the high-field magnetic device at 4SEASONS, because the instrument consists of many iron components. Because of that, we have investigated whether the superconducting magnet of the MLF Sample Environment Group can be used at our instrument [4]. Based on the results of an investigation of the stray magnetic fields by calculation and an operation test without neutron beam, we performed an on-beam demonstration of the magnet this year [5]. For this demonstration measurement, we employed a single crystal of TbB_2C_2. A previous inelastic neutron scattering study using a powder sample of TbB_2C_2 reported that magnetic excitation appears around 3.5 meV at low temperatures, and it shifts toward higher energies under applied magnetic field (H) of the order of 1 T [6]. Figure 1 shows the magnetic excitation spectra measured under $H \leq 3$ T. The data were powder-averaged and sliced in the range of $Q = 1.5–2$ Å^{-1}. At $H = 0$ T, we observed a broad excitation peak around 3 meV. As H increased, the peak sharpened and changed its position toward higher energies. These observations reproduce well the results in Ref. [6].

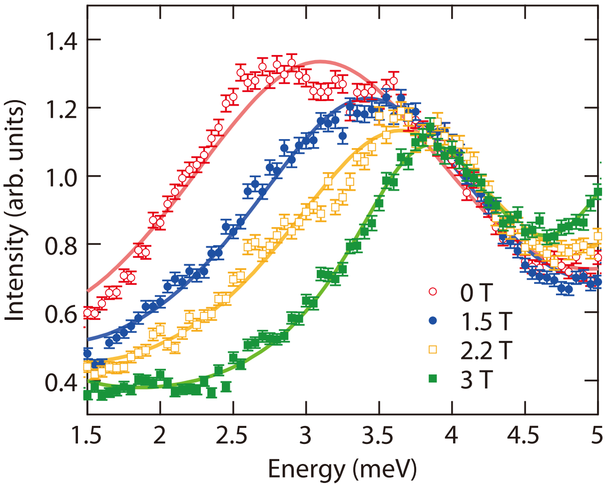

Figure 1. Powder-averaged inelastic neutron scattering profiles of $Tb^{11}B_2C_2$ at 4 K as a function of energy transfer. Open circles, closed circles, open squares, and closed squares denote the data measured under 0, 1.5, 2.2, and 3 T, respectively. The solid lines are guides to the eye [5].

Acknowledgements

We thank H. Kira, K. Kaneko, S. Ohira-Kawamura, R. Takahashi, K. Aoyama, and W. Kambara for their support and advice. The instrumentation works described here were supported by the engineers of the Neutron Science Section and the Technology Development Section of MLF.

References

[1] R. Kajimoto et al., J. Phys. Soc. Jpn. **80**, SB025 (2011).

[2] H. Seto et al., Biochim. Biophys. Acta, Gen. Subj. **1861**, 3651 (2017).

[3] R. Kajimoto et al., Physica B **562**,148 (2019).

[4] R. Kajimoto et al., J. Phys.: Conf. Ser. **1021**, 012030 (2018).

[5] R. Kajimoto et al., Physica B **556**, 26 (2019).

[6] A. M. Mulders et al., Physica B **359–361**, 1231 (2005).

R. Kajimoto[1], M. Nakamura[1], K. Kamazawa[2], Y. Inamura[1], K. Ikeuchi[2], K. Iida[2], M. Ishikado[2], and N. Murai[1]
[1]*Neutron Science Section, Materials and Life Science Division, J-PARC Center;* [2]*Neutron Science and Technology Center, CROSS*

Current Status of BL02 DNA in 2018

1. Introduction

DNA is a TOF backscattering spectrometer designed to elucidate atomic and molecular dynamics [1]. DNA can provide micro-eV energy resolution measurements over a broad energy range of $-500\ \mu\text{eV} < E < 1500\ \mu\text{eV}$, thanks to the near-backscattering geometry of the instrument and its pulse-shaping options. In addition, back-coated Si analyzers with Gd or Gd_2O_3 neutron absorber give extra high signal-to-noise ratio of around 10^5, which enables to detect small scattering amplitudes or signals from small quantities of samples. The accessible momentum transfer range is from 0.08 to 1.86 Å^{-1} by using Si111 analyzer mirrors.

The number of peer-reviewed papers from DNA was 9 in 2018 almost the same number (8) as in 2017 [2].

2. User Program in the periods 2018A and 2018B

11 General Proposals (GP) including 1 New User Promotion (NUP) proposal, and 10 GPs including 2 NUP were approved for 2018A and 2018B, respectively. The portion of approved beamtime from all requested beamtime was 63% for 2018A and 40% for 2018B. The competition rate of 2018B, 2.3, was much higher than 1.2 for 2018A. Additionally, two reserved proposals were also conducted in 2018B.

Also, on the General Proposal (Long Term) (hereafter LTP) Program, two proposals have been newly adopted from 2018B. In total, three LTP's run at BL02.

The 3rd Neutron and Muon School was held in November. We accepted 4 students. They enjoyed hands-on experiment on molecular dynamics of water in Nafion membranes at DNA.

3. Beamline activities

Beamline

The fast disk choppers used in DNA showed vibration at high speeds, which limited the maximum available speeds to 225 Hz. In January 2019, improved disks were installed, which made it possible to achieve the design speed of 300 Hz. We found that the best energy resolution using 10 mm slit with 300 Hz was 1.4 μeV for 10 mm tall sample, which confirmed the design value of DNA (Fig. 1(a)). The improvement was also remarkable for the 30 mm slit, the most frequently used condition in entire Q-region, as shown in Fig. 1(b).

On July 3, 2018, MLF succeeded in operating continuously for one hour at a beam power of approximately 1 MW. Test measurements were performed to demonstrate the performance of DNA at 1 MW. Figure 2(a) shows the temperature dependence of the elastic intensity of starch with water. Clear drops at 0°C were observed for all data, whereas the drop at 60°C appears only for the first heating data due to gelatinization, which confirms the change obtained by differential thermal analysis with the same heating/cooling speed of 1°C/min. Figure 2(b) shows QENS spectrum with a measurement time of 2 minutes at 50°C during the heating process. The quality of the spectra was enough for quantitative QENS analysis. Thus, a beam power of 1 MW enables the study of dynamics in conditions nearly identical to those of a typical thermal analysis. Conventional QENS measurements have been limited to thermally-equilibrated systems. High-intensity neutron beams will open a new area of innovative application of QENS to the non-equilibrium phenomena, such as the starch gelatinization.

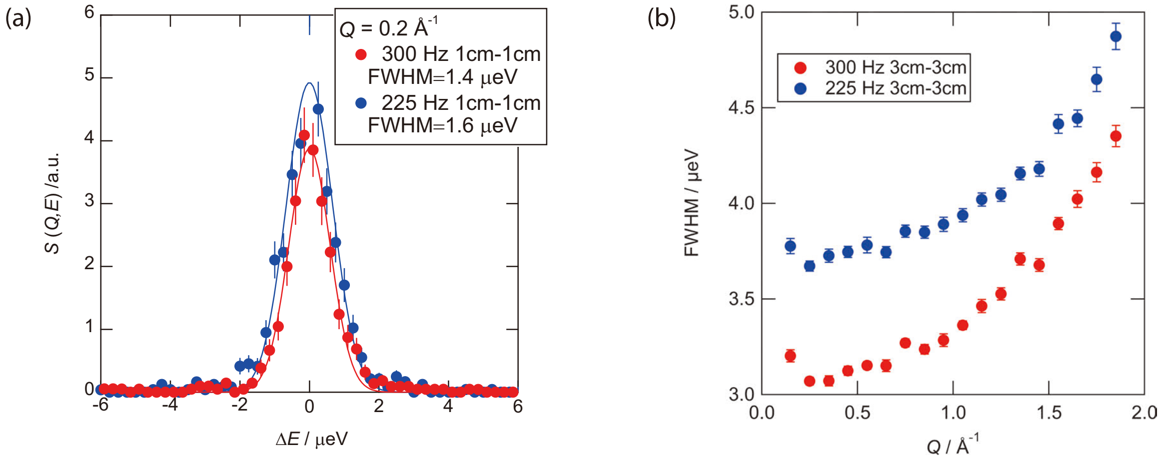

Figure 1. (a) Best energy resolution before (225 Hz) and after (300 Hz) installation of the new fast chopper disk with 1 cm-1 cm slit. (b) Q-dependence of the energy resolution with 3 cm-3 cm slit.

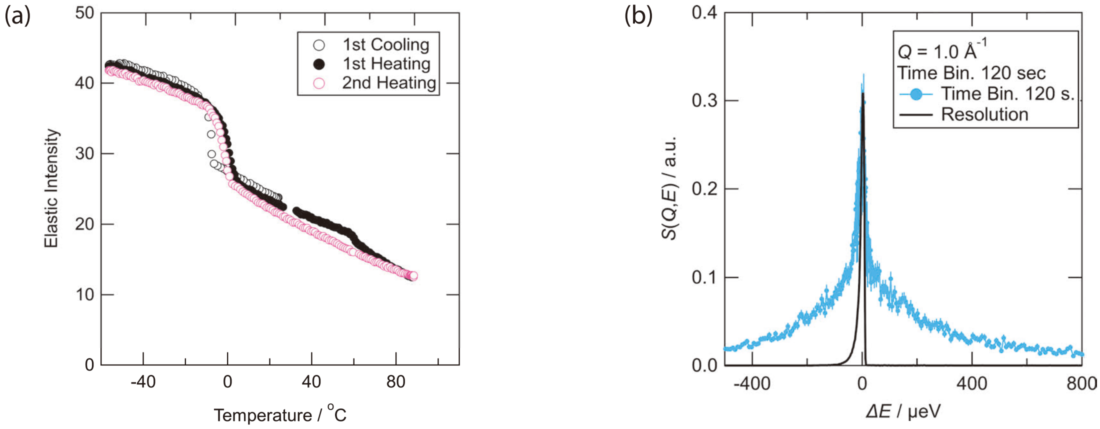

Figure 2. (a) Temperature dependence of the elastic intensity of starch with water measured at a beam power of approximately 1 MW with heating and cooling rate of 1 degree/min. (b) QENS spectrum at Q = 1.0 Å^{-1} with time bin of 120 seconds at 50 degrees.

Eight years have passed since starting the operation of DNA, and now we found problem of the beam monitor caused by aging. The intensity of the beam monitor was gradually reduced by a half between 2013 and 2017. Therefore, we replaced the monitor to a fresh monitor in January 2019. Since, in DNA, we normalize the scattered intensity by spectra of the beam monitor installed before the sample, the stability of the beam monitor is crucial. We plan to refresh the converter gas for the old monitor.

Sample environment

Owing to the variety of samples measured at DNA, experiments using special sample environments, such as dilution refrigerator, magnet, high-pressure cell, sample changer, and vapor-controlled system, have increased in number at DNA. To meet their requirements, we have installed distribution boards of electricity, cooling water, and He gas on the roof shield of DNA. In addition, a part of the fence surrounding the roof was changed to a sliding type to easily bring apparatus from the ground level onto the roof shield.

Software

The software package Utsusemi has been customized to reduce and visualize data from DNA. On the other hand, such customization prevents us from keeping up with the modification of Utsusemi. We have incorporated DNA's special code into the latest Utsusemi.

4. Future plans

Si311 analyzer mirrors extending the momentum transfer range to 3.8 Å^{-1} with 12 micro eV resolution with 10 mm slit will be installed in 2019–2020.

5. Others

In 2018, DNA joined the user group meeting on the MLF spectrometers "DIRECTION 2018" held on October 11 in Tokai. 54 attendees discussed new science and methods obtained from the MLF spectrometers. After "DIRECTION 2018", we had the first user group meeting for DNA on October 12 with 18 attendees. The current status and future plans of DNA, including the development of sample changer, auto gas-exchanger, fitting program (QENS fit), and data correction, were shown by the instrument team of DNA. In addition, we had extensive discussions on the future plans for neutron studies in biology, the current status of software development at MLF, and requests from users.

We had a guest, Mr. Shun Asano as an intern-student from Tohoku University in January of 2018. He studied measurement and analysis of quasi-elastic scattering at DNA. He also participated in the commissioning of the improved fast disk chopper.

References

[1] Kaoru SHIBATA et. al., JPS Conference Proceedings, **8** (2015), 036022.

[2] Ryoichi Kajimoto et. al., Physica B: Condensed Matter, **562** (2019) 148.

Y. Kawakita[1], M. Matsuura[2], T. Yamada[2], T. Tominaga[2], M. Kobayashi[2], and H. Nakagawa[1,3]

[1]*Neutron Science Section, Materials and Life Science Division, J-PARC Center;* [2]*Neutron Science and Technology Center, CROSS;* [3]*Materials Sciences Research Center, JAEA*

IBARAKI Biological Crystal Diffractometer iBIX

1. Introduction

The IBARAKI biological crystal diffractometer iBIX was constructed to perform high throughput single-crystal neutron structure analysis, mainly for biological macromolecules in various life processes at BL03, MLF (2008) [1]. To achieve high performance, we developed successfully, in cooperation with JAEA, a new photon-counting two-dimensional detector system using scintillator sheets and wavelength-shifting (WLS) fiber arrays for the X/Y axes. In 2012, the installation of 30 detectors on the iBIX diffractometer was completed [2]. By the end of 2012, iBIX became available for user experiments on biological macromolecules, supported by the Frontier Research Center of Applied Atomic Sciences, Ibaraki University. The final specifications of iBIX are shown in Table 1.

Table 1. Specifications of iBIX.

Moderator	Coupled
Wavelength of incident neutron (Å)	0.7 ~ 4.0 (1st frame) 4.0 ~ 8.0 (2nd frame)
Neutron intensity (n/s/mm^2) (@1 MW)	0.7×10^6
L_1 (m)	40
L_2 (mm)	491
Solid angle of detectors (% for 4π)	22.0
Detector covered region (deg.)	15.5 ~ 168.5
Detector size (mm^2)	133 × 133
Detectors pixel size (mm^2)	0.52 × 0.52
No. of detectors	34

2. Current status

In 2016, we carried out neutron structure analysis of Mn Catarase with the largest unit cell in the neutron diffraction experiment by using iBIX to estimate its own performance. The results showed that iBIX was able to achieve the maximum cell dimension of the design specifications without any peak de-convolution procedure. And then, it was confirmed that iBIX achieved all design target values (maximum cell dimension, resolution, measurement efficiency, etc.). In 2017, we assembled by ourselves the four newly added detectors. They have already been installed on the iBIX diffractometer (Fig. 1). The measurement efficiency with 34 detectors will increase 1.13 times over that of the previous 30 detectors. Commissioning the without/with neutron beam has already finished. By using the four newly added detectors, we could obtain the TOF diffraction data with the same accuracy as with the current detectors. The new detectors are available for users experiments.

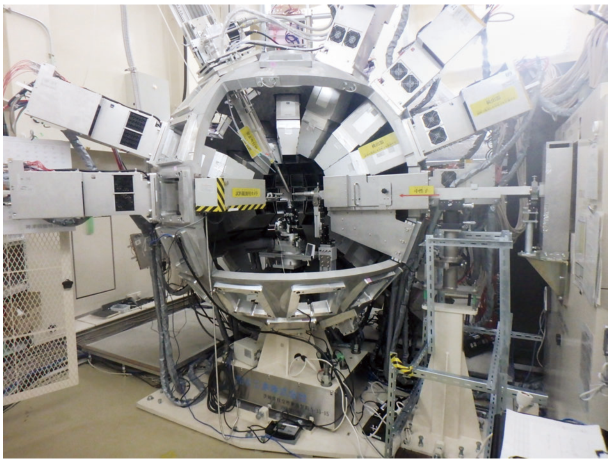

Figure 1. The current diffractometer iBIX.

In 2018, J-PARC was operated regularly at accelerator power of 500 kW. The results from the experiments on the full data set of biological macromolecules for neutron structure analysis by using iBIX were as follows. We were able to collect a full data set of biological macromolecules for neutron structure analysis with around 2.0 Å resolution in about 8 days by using iBIX at accelerator power of 500 kW. The average volume of the sample measured by iBIX was about 1.5 mm^3. If the accelerator power reaches 1 MW, the total measurement time of the sample size will be reduced to a half of the previously necessary time or the sample size can be reduced by a half with the same measurement time.

We prepared a users' manual and a distribution package of the data reduction software "STARGazer", which would allow the iBIX users to perform personally data reduction in their laboratory [3]. STARGazer works on Linux and on Windows and OS X with virtual box. We continue to develop the data reduction software in order to improve its usability.

3. Future plans

We assumed that a full data set of a 2-mm^3 protein sample could be obtained by iBIX in about 2 to 4 days under the 1-MW operation. The assumption implied that iBIX was capable of achieving the designed target value. However, the sample size was still large, and the measurement time was still long, especially for the users. We would like to reduce the difficulties of sample preparation as much as possible. In other words, it is necessary to further improve the measurement efficiency of iBIX by developing the beam line instrument.

As a simple and effective way to improve the measurement efficiency, we carried out the installation of the newly added detectors. A maximum of 60 detectors can be installed on the support frame of the iBIX diffractometer without any design changes. We will try to get a construction budget to install the additional detectors. Currently, we also consider other possibilities to improve the measurement efficiency. For example, increasing the beam divergence by the insertion of a super mirror, changing the distance between the sample and the detector surface, improving the chopper instrument, and so on. We will continue to develop both the data reduction software and the beam line instruments to improve the measurement efficiency and the accuracy of the intensity data obtained from smaller protein samples in order to build a single-crystal neutron diffractometer for biomacromolecules with one of the highest levels of performance in the world.

References

[1] I. Tanaka, K. Kusaka, T. Hosoya, N. Niimura, T. Ohhara, K. Kurihara, T. Yamada, Y. Ohnishi, K. Tomoyori and T. Yokoyama, Acta Cryst. D**66** (2010) 1194–1197.

[2] K. Kusaka, T. Hosoya, T. Yamada, K. Tomoyori, T. Ohhara, M. Katagiri, K. Kurihara, I. Tanaka and N. Niimura, J. Synchrotron Rad. **20** (2013) 994–998.

[3] N. Yano, T. Yamada, T. Hosoya, T. Ohhara, I. Tanaka N. Niimura and K. Kusaka, Acta Cryst. D**74** (2018) 1041–105.

K. Kusaka[1], T. Yamada[1], N. Yano[1], T. Hosoya[1], I. Tanaka[1], and T. Ohhara[2]

[1]*Frontier Research Center for Applied Atomic Sciences, Ibaraki University;* [2]*Neutron Science Section, Materials and Life Science Division, J-PARC Center*

Neutron Total Cross Section Measurement at ANNRI (BL04)

1. Introduction

Accurate data of neutron-capture cross sections are important in detailed engineering designs and safety evaluations of innovative nuclear reactor systems. Especially, nuclear data for minor actinides (MAs) and long-lived fission products (LLFPs) are necessary for burn-up analyses of nuclear fuels, improving the design and performance of advanced nuclear reactors and the nuclear transmutation [1]. However, accurate measurements of these cross sections are very difficult to obtain due to the high radioactivity of these samples.

To satisfy these demands, a time-of flight experimental instrument named "Accurate Neutron-Nucleus Reaction measurement Instrument (ANNRI)" has been constructed by the collaboration of Hokkaido University, Tokyo Institute of Technology, and Japan Atomic Energy Agency. Measurements of neutron-capture cross sections of MAs, LLFPs and some stable isotopes with high intensity pulsed neutrons have been started in 2008 [2]. In recent years, a measurement system for neutron total cross section has been developed and the first results of the total cross sections were reported.

2. Detectors and DAQ

For neutron total cross section measurements, two types of Li-glass scintillation detectors have been installed in ANNRI. The set-up of the detectors is shown in Fig. 1. A ^{6}Li-glass detector (PMT:H7195) manufactured by OKEN has been installed at flight length of 28.7 m to obtain transmission neutron TOF spectra. The scintillator of the detector is GS-20 manufactured by Saint Gobain with dimensions of 50 mm × 50 mm and a thickness of 1 mm using enriched ^{6}Li (^{6}Li enrichment higher than 95%). Neutrons passing through the samples are detected by the ^{6}Li-glass detector via the $^{6}\mathrm{Li}(\mathrm{n},\alpha)^{3}\mathrm{H}$ reactions.

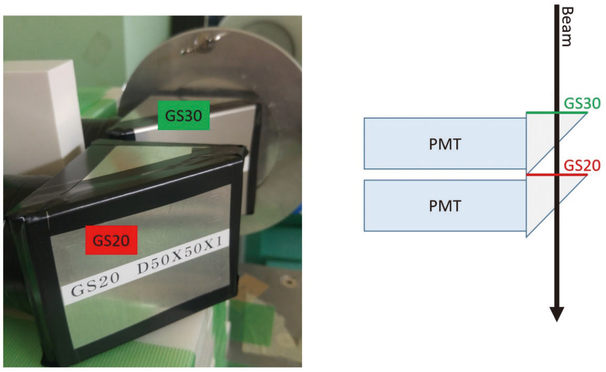

Figure 1. The photo and the schematic view of the Li-glass detectors for total-neutron cross section measurement.

Additionally, to determine the background caused by high-intensity gamma-rays, a ^{7}Li-glass detector (depleted in ^{6}Li) has also been installed. The scintillator of the ^{7}Li-glass detector was GS-30 (^{7}Li enrichment higher than 99.99%) manufactured by Saint Gobain with the same size and chemical component of the ^{6}Li-glass scintillator. The ^{7}Li-glass detector is set on the upstream side of the ^{6}Li-glass detector. The signals from the photomultipliers (HAMAMATSU:H7195) are analyzed using CAEN V1720 (12-bit 250 MHz) module with digital pulse processing software, DPP-CI. The module records a pulse height and a time of flight in "event-by-event" mode.

3. Neutron total cross section measurement of ^{241}Am

In recent years, total cross sections of ^{241}Am and ^{243}Am were measured in ANNRI [3, 4]. As an example of the measurements, the neutron total cross section measurement of ^{243}Am are reported.

For the experiment, a ^{243}Am sample with nominal activities of 240 MBq was prepared. The sample was encapsulated in Al containers with diameter of 22 mm and thickness of 0.1 mm. Similarly, a "dummy sample" without Am sample was prepared. The ^{243}Am sample and the dummy sample were set on the neutron beam line at the flight length of 24.5 m. Transmission neutrons were detected with the Li-glass detectors. The total measuring time was about 16 hours for the ^{243}Am sample and about 8 hours for the dummy sample.

The TOF spectra of the ^{243}Am sample and the dummy sample with the Li-glass detectors are shown in Fig. 2. Dead-time correction and background subtraction were applied. The transmission ratio of the ^{243}Am sample was obtained.

The deduced total cross section of ^{243}Am is shown in Fig. 3. The cross section was derived using the transmission ratio of the sample and the areal density of the ^{243}Am sample.

Using our new detectors and DAQ, total cross section of ^{243}Am was derived in the neutron energy range from 4 meV to 100 eV.

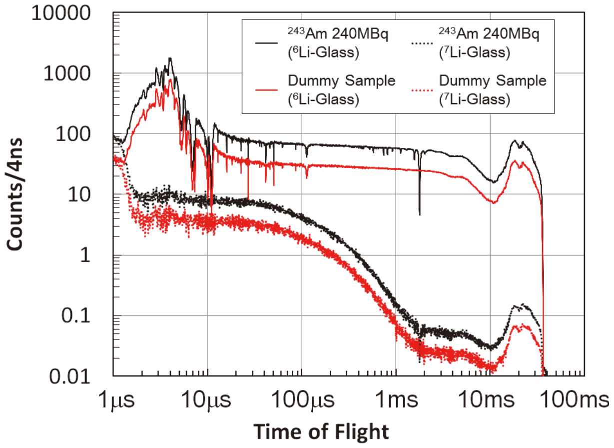

Figure 2. TOF spectra of the ^{243}Am sample and the dummy sample with the Li-glass scintillation detectors [4].

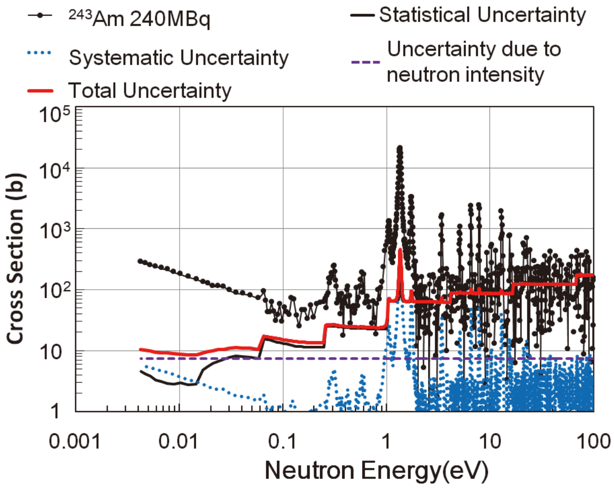

Figure 3. Derived total cross section of ^{243}Am, and uncertainties of the cross sections (total, statistical uncertainty, systematic uncertainty, uncertainty due to neutron intensity, and uncertainty due to impurity subtraction) [4].

References

[1] M. Salvatore, R. Jacqmin, "Uncertainty And Target Accuracy Assessment for Innovative Systems using Recent Covariance Data Evaluations." WPEC-26, OECD NEA, (2008).

[2] H. Harada, et al., J. Korean Phys. Soc. **59**, (2011) 1547.

[3] K. Terada, et. al., Journal of Nuclear Science and Technology, (2018), https://doi.org/10.1080/00223131.2018.1485519

[4] A. Kimura, et. al., Journal of Nuclear Science and Technology, (2018), https://doi.org/10.1080/00223131.2019.1598508

A. Kimura and S. Nakamura
Nuclear Data and Reactor Engineering Division, Nuclear Science and Engineering Center, Japan Atomic Energy Agency

Status of Fundamental Physics Beamline BL05 (NOP) in 2018

1. Introduction

“Neutron Optics and Physics (NOP/BL05)” at MLF in J-PARC is a beamline for studies in the field of fundamental physics. The beamline is divided at the upstream into three branches, the so-called Polarized, Unpolarized, and Low-Divergence branches, used in different experiments in a parallel way [1–2].

A neutron lifetime measurement is conducted at the Polarized beam branch with a spin flip chopper. Pulsed ultra-cold neutrons (UCNs) by a Doppler shifter are available at the Unpolarized beam branch. At the Low-Divergence beam branch, the search for an unknown intermediate force is performed by measuring neutron scattering with rare gases. The beamline is used also for R&D of optical elements and detectors [3].

2. Measurement of the neutron lifetime

A neutron decays into a proton, an electron, and an antineutrino. The decay lifetime is an important parameter for the unitarity of the CKM matrix and also for the primordial big bang nucleosynthesis. However, recently reported values for the neutron lifetime deviate significantly from the systematic uncertainties. An experiment to measure the neutron lifetime with a pulsed beam is ongoing at BL05 (NOP). The lifetime is measured as a ratio of the electron events of the neutron decay to the $^3He(n,p)^3H$ events caused by ^3He gas precisely doped in a time-projection chamber (TPC). By analyzing the data, we obtained our first preliminary result of the neutron lifetime as $\tau_n = 896 \pm 10$ (stat.) $^{+14}_{-10}$ (sys.) [4].

3. Development of a sub-micrometer position sensitive neutron detector using nuclear emulsion

Nuclear emulsion, which is a kind of photographic film, is used as a high-sensitivity position tracking detector for particle and nuclear physics. An ionizing particle passing though the emulsion makes fine grains along its track. Observing the grains by a microscope, the track can be reconstructed very precisely.

We applied the nuclear emulsion to neutron detection with sub-micrometer spatial resolution [5]. The detector consists of ^{10}B and cover layers on Si substrate. Nuclear emulsion of 10 μm thickness was coated on it (Fig. 2 Left). Neutron that makes $^{10}B(n,\alpha)^7Li$ reaction at the ^{10}B layer emits either an α particle or ^7Li-ion into the

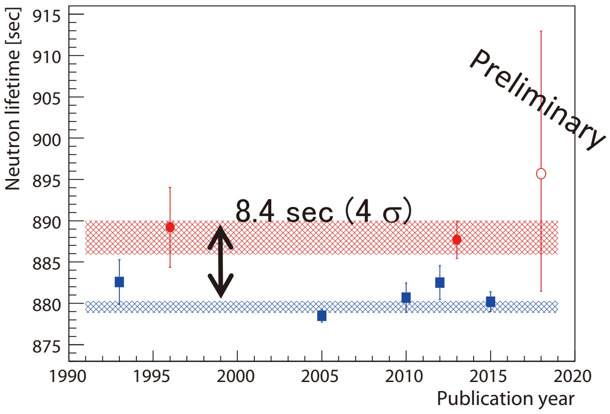

Figure 1. The neutron lifetime measurements in the 2017 PDG [1], the storage methods are denoted as blue squares, the proton counting is shown as closed red circles. The J-PARC preliminary result is shown as a red open circle [3].

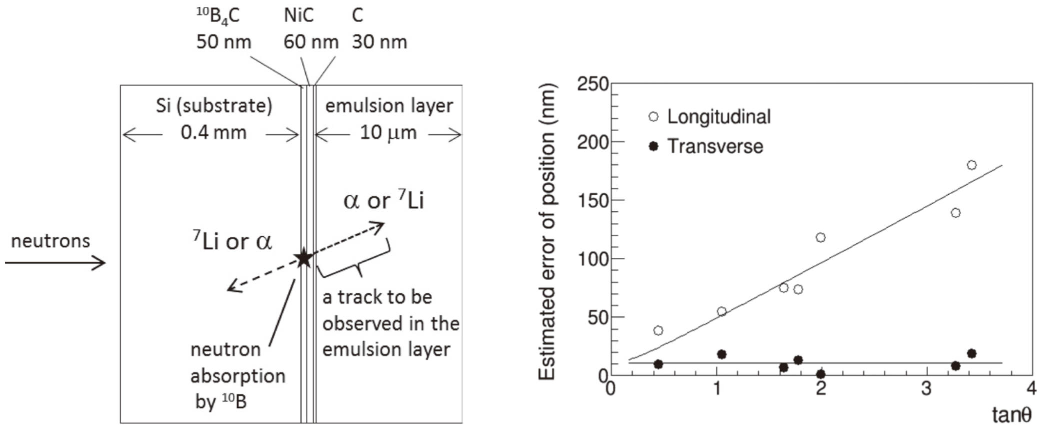

Figure 2. (Left)A schematic view of the detector. (Right) Position errors of detected tracks in longitudinal and transverse directions with the track angles (tanθ).

emulsion layer, whose track lengths are 5.1 and 2.6 μm, respectively. Reconstruction analysis of the grains by the track can determine the starting position of the track where the neutron was captured by ^{10}B. The error of the starting position depends on the track angle to the substrate, θ. If we select $\tan(\theta) < 1.9$, which corresponds to acceptance efficiency of 34%, the spacial resolution to the longitudinal direction is estimated to be 11–99 nm. The resolution to the transverse direction was estimated as 11 nm independently in the track angle (Fig. 2 Right). This unprecedented spatial resolution detector can be applied for various experiments involving neutron quantum effects or sub-micro neutron imaging.

References

[1] K. Mishima et al., "Design of neutron beamline for fundamental physics at J-PARC BL05," *Nucl. Instruments Methods Phys. Res. Sect. A*, vol. **600**, no. 1, pp. 342–345, 2009.

[2] K. Mishima, "J-PARC Neutron fundamental physics beamline (BL05/NOP)," *Hamon Neutron Netw. news*, vol. **25**, no. 2, pp.156–160, 2015.

[3] K. Mishima et al., Fundamental physics activities with pulsed neutron at J-PARC (BL05). Proceedings of International Conference on Neutron Optics (NOP2017) JPS Conference Proceedings, Vol. **22** (2018) 11033. (arXiv:1712.06351, 2017)

[4] N. Nagakura et al., PPNS2018, Grenoble, France.

[5] N. Naganawa et al., "A Cold/Ultracold Neutron Detector using Fine-grained Nuclear Emulsion with Spatial Resolution less than 100 nm", European Physical Journal C (2018) **78**: 959.

K. Mishima[1,2] on behalf of NOP collaboration

[1] *Neutron Science Section, Materials and Life Science Division, J-PARC Center;* [2] *Institute of Materials Structure Science, KEK*

BL06: Commissioning Status of VIllage of Neutron ResOnance Spin Echo Spectrometers (VIN ROSE)

1. Introduction

Neutron spin echo (NSE) is a variety of neutron spectrometry for high-resolution inelastic and quasi-elastic neutron scattering methods [1]. Because the energy resolution of the energy transfer measurement is not limited by the energy spectrum of the incoming neutrons in the NSE technique, a moderately (10–15% FWHM) mono-chromatic neutron beam is acceptable. In addition, the intermediate scattering function can be directly derived by NSE, so that the method is suitable for studying slow relaxation dynamics in condensed matter, and high-intensity and high-energy-resolution NSE spectrometers have been developed and built [2].

Since 2011, Kyoto University and The High Energy Accelerator Research Organization (KEK) have been jointly constructing beamline 6 (BL06), which consists of two types of NSE spectrometers with neutron resonance spin flippers (RSFs), that is, a neutron resonance spin echo (NRSE) instrument and a modulated intensity by zero effort (MIEZE) instrument, at Materials and Life Science Experimental Facility (MLF), Japan Proton Accelerator Research Complex (J-PARC) [3]. The spectrometers use RSFs, which can replace large magnetic precession fields with low guide fields, therefore downsizing and adjacence of the spectrometers become possible [4].

In this report, the status of the MIEZE and NRSE spectrometers at BL06 in FY2018 is summarized.

2. Commissioning status at BL06 in FY2018

Time-of-flight neutron spectroscopy and MIEZE (TOF-MIEZE) is a novel approach. We have verified quantitatively fundamental characteristics of TOF-MIEZE [5]. Since the 2017B proposal round, the user program has been partially started with the MIEZE spectrometer, which will be described in the following section in detail.

At the NRSE spectrometer, used for high-energy resolution, commissioning of the devices such as RSFs and two-dimensional ellipsoidal neutron-focusing mirrors were intensively conducted. The 5Q_c NiC/Ti two-dimensional ellipsoidal neutron-focusing supermirrors, where xQ_c means that the critical angle is x times larger, were developed in close collaboration with the RIKEN center for advanced photonics [6]. The optical design includes 1250 mm semi-major axis and 65.4 mm semi-minor axis with 900 mm length, as shown in Fig. 1. By using the mirrors, the characteristics of the spectrometer were evaluated quantitatively. The achieved findings will be applied to the further developments of the NRSE spectrometer.

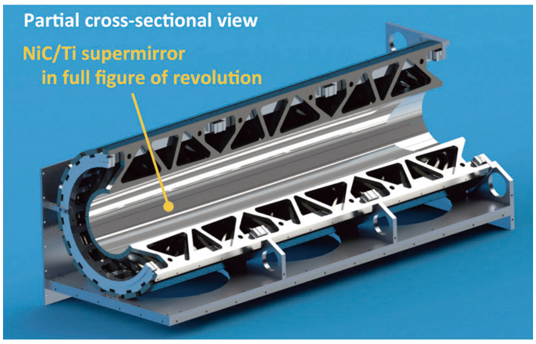

Figure 1. Partial cross-sectional view of the ellipsoidal neutron-focusing mirror (see ref. [6]).

3. User Program

The great advantages of the MIEZE spectrometer is that relatively strong magnetic field in any direction can be added in the sample position. This characteristic is very appropriate for studies of slow-spin dynamics on magnetic properties, such as the Skyrmion phase observed in magnetic substances [8]. In order to execute such kind of investigations, a 4K GM cryostat and a very compact magnet, which can add maximum 0.2 T at the

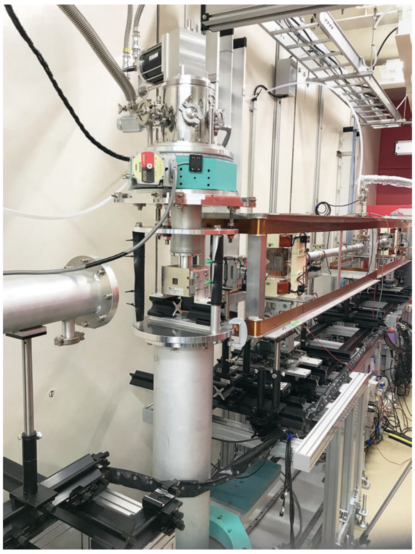

Figure 2. The sample stage of the MIEZE spectrometer, where a 4K GM cryostat and a 0.2 T permanent magnet at the sample position are installed.

sample position, have been installed to the instrument. Figure 2 shows the cryostat and the magnet at the sample stage, where the magnetic field is parallel to the beam propagation direction, which is normally impossible for generic "Mezei type" spin echo spectrometers. We have been able to observe 200 kHz MIEZE signals (corresponding to maximum 2 ns Fourier time) clearly with this geometry. Five user programs in total were carried out with the MIEZE spectrometer in FY2018 in addition to internal studies, in which three topics were related to magnetism.

4. Summary

The current status of BL06 VIN ROSE in FY2018 was briefly reported. The public use has been started partially with the MIEZE spectrometer. A 4K GM cryostat and a compact maximum 0.2 T permanent magnet are available as sample environments. At the NRSE spectrometer, the two-dimensional ellipsoidal neutron-focusing supermirrors with 5Qc were tested, which was essential for the development of NRSE with high-energy resolution.

Acknowledgments

We thank Dr. T. Hosobata and Dr. Y. Yamagata at RIKEN Center for Advanced Photonics for providing the substrates of the two-dimensional ellipsoidal supermirrors.

References

[1] F. Mezei ed., Neutron Spin Echo, Lecture Notes in Physics, (Springer, Berlin) **128**, (1982).

[2] D. Richter, M. Monkenbusch, A. Arbe, J. Colmenero, *Adv. Polym. Sci.* **174**, (2005) 1–221.

[3] M. Hino, T. Oda, M. Kitaguch, N.L. Yamada, H. Sagehashi, Y. Kawabata, H. Seto, *Physics Procedia* **42**, (2013) 136.

[4] R. Gähler and R. Golub, *J. Phys. France,* **49**, (1988) 1195–1202.

[5] T. Oda, M. Hino, H. Endo, N.L. Yamada, Y. Kawabata, H. Seto, *JPS Conf. Proc.* **22**, (2018) 011010.

[6] T. Hosobata, M. Hino, H. Yoshinaga, T. Kawai, H. Endo, Y. Yamagata, N. L. Yamada, S. Takeda, *JPS Conf. Proc.* **22**, (2018) 011010.

[7] H. Endo, T. Oda, M. Hino, T. Hosobata, *Physica B* **564**, (2019) 91.

[8] S. Mühlbauer, B. Binz, F. Jonietz, C. Pfleiderer, A. Rosch, A. Neubauer, R. Georgii, P. Böni, *Science*, **323**, (2009) 915.

H. Endo[1,2], M. Hino[3], T. Oda[3], N. L. Yamada[1,2], H. Seto[1,2], and Y. Kawabata[3]

[1]*Neutron Science Division, Institute of Materials Structure Science, KEK;* [2]*Neutron Science Section, Materials and Life Science Division, J-PARC Center;* [3]*Institute for Integrated Radiation and Nuclear Science, Kyoto University*

Current Status of BL08 SuperHRPD in 2018

1. Introduction

Super High-Resolution Powder Diffractometer (SuperHRPD) is a neutron powder diffractometer with super high resolution, which in 2008 achieved the world's best resolution ($\Delta d/d = 0.035\%$) among similar diffractometers [1]. SuperHRPD is one of the day-one instruments and has been in operation for 10 years. The construction of the instrument has been completed and its main task is to perform general user programs. However, the expansion of the instrument's capabilities is gradually progressing to make it more useful in the development of advanced science.

2. A breakdown of the total beam time in FY2018

In FY2018, SuperHRPD performed 911 measurements, and all 12 proposed general user programs could be carried out. SuperHRPD has several instruments for sample environment and the breakdown of usage in FY2018 is shown in Fig. 1. About half of the total measurement time was occupied by low-temperature experiments using a cryostat, 20% was room temperature measurement by auto sample changer, 10% was high-temperature measurement by vanadium furnace, and the remaining 17% as commissioning the 14-Tesla magnet. Two of the cryostats we own are older models that have been in use for 20 years since the KENS era, and it is hoped that they will be upgraded to new equipment with improved performance. Considering the environment for low-temperature experiments, the introduction of more advanced cryo-furnace that can continuously measure from low to high temperatures is in progress.

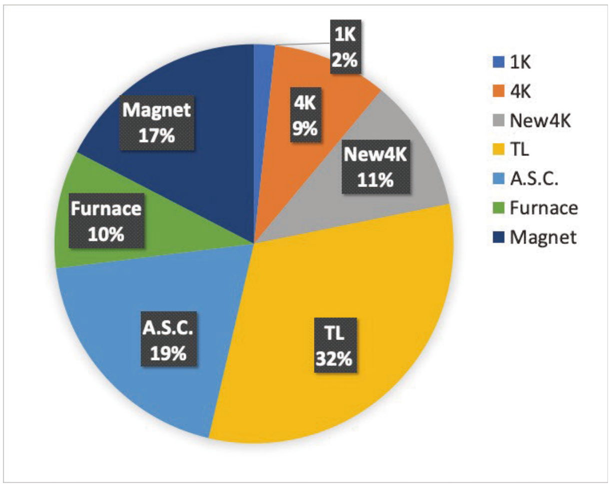

Figure 1. Operating ratio of the sample environment in total measurement time in FY2018. The total measurement time in 2018 was about 4000 hours, and 911 measurement data could be obtained. Of the graph legends, 1K, 4K, New4K, and TL are low-temperature devices, and TL is a Top-Loading type. A.S.C. indicates an Auto Sample Changer used for room temperature measurement.

3. Official start of a Fast Track Proposal

The three beamlines, SuperHRPD, NOVA and PLANET, have officially started a Fast Track Proposal (mail-in program). In FTP, the user sends their samples to the MLF, and the MLF staff performs the experiment on behalf of the user and sends them the data. Currently, there is a limit of 24 hours per one proposal, but within that time, room temperature measurement using an auto sample changer and low temperature measurement using a cryostat can be performed. SuperHRPD has conducted this proposal on a trial basis in advance and has completed seven proposals by the end of FY2018. FTP is useful for beamline groups with limited manpower like ours, and is a useful system for effective beam usage, like taking advantage of beam time that is vacant on the weekends and time adjustments to avoid user change at midnight.

4. Installation and commissioning of several devices

An electric 4-quadrant slit system (Fig. 2) was installed at incident side of the sample vacuum chamber of SuperHRPD. Until now, a simple manual incident beam slit using a sintered B_4C plate was used, but this motorization is expected to shorten the time of

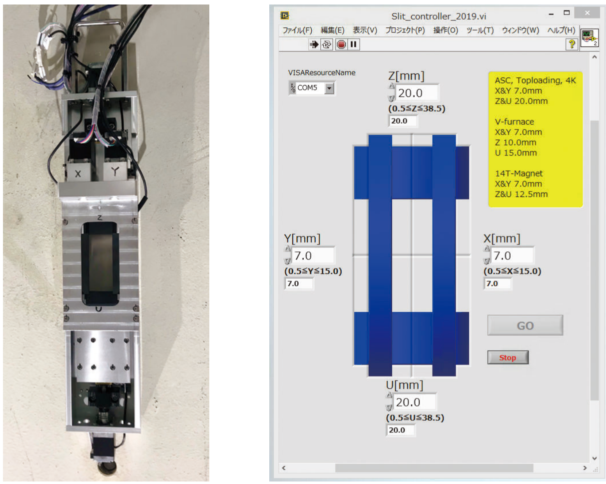

VISAResourceName COM5

Z[mm] 20.0 (0.5≦Z≦38.5) 20.0

Y[mm] 7.0 (0.5≦Y≦15.0) 7.0

X[mm] 7.0 (0.5≦X≦15.0) 7.0

U[mm] 20.0 (0.5≦U≦38.5) 20.0

ASC, Toploading, 4K
X&Y 7.0mm
Z&U 20.0mm

V-furnace
X&Y 7.0mm
Z 10.0mm
U 15.0mm

14T-Magnet
X&Y 7.0mm
Z&U 12.5mm

Figure 2. (Left) 4-quadrant slit system installed in SuperHRPD. A slim shape with a width of 10 cm was realized by devising the arrangement of the stepping motor. (Right) Slit control GUI created using LabVIEW.

changing the slit and improve the reproducibility of the slit size. On the incident side of the sample chamber, there was only a small space between the left and right backscattering banks, so a narrow-slit system was required. By efficiently arranging four stepping motors, we were able to complete a slit system with a width of only 10 cm. In addition, we built a slit control system using LabVIEW and completed a visually operable program with an emphasis on GUI.

A commissioning of 1K cryostat (Fig. 3) owned by the SuperHRPD group was carried out in the second half of FY2018. Since this cryostat was introduced at the time of the Great East Japan Earthquake, its commissioning was delayed because various restoration tasks had been prioritized. First, we performed background measurement and correction data measurement using a neutron beam without cooling. By adjusting the incident beam slit, we were able to suppress unnecessary reflections and obtain good background data. After that, we conducted a cooling test of the 1K cryostat system at the off-beam line. Compressors and other devices showed healthy operation were not affected by the earthquake disaster, but we found out that the essential ^{3}He gas line needle valve had a problem and did not reach the minimum temperature. Maintenance performed by the manufacturer is scheduled for 2019, and after that, the normal operation is expected to resume.

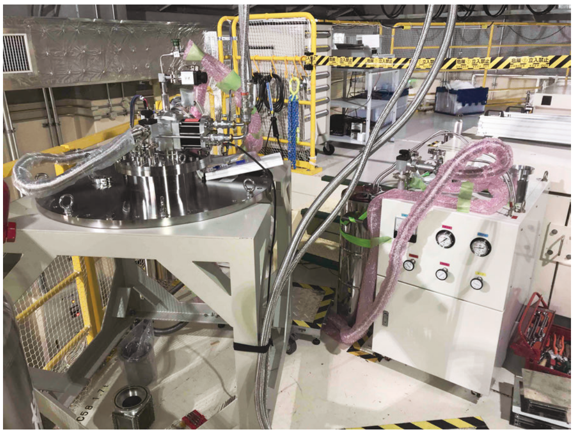

Figure 3. The 1K cryostat system during commissioning. A problem was found with the needle valve in the ^{3}He line, and repair is scheduled for FY2019.

References

[1] S. Torii *et. al.*, *J. Phys. Soc. Jpn.* **SB020** SB020-1-4 (2011).
[2] http://j-parc.jp/researcher/MatLife/en/applying/FTP_v01.html

S. Torii[1,2], M. Hagihala[1,2], and T. Kamiyama[1,2]
[1]*Neutron Science Section, Materials and Life Science Division, J-PARC Center;* [2]*Institute of Materials Structure Science, KEK*

Current Status of SPICA in 2018

1. Introduction

In the charge/discharge reaction of a real batteries, neutron diffraction with wavelengths of atomic distances is used to analyze the change of atomic arrangement including mobile ions at the atomic level. This method can provide the positional information of light elements with relatively high accuracy. The structural analysis of actual battery electrodes by neutron diffraction is an indispensable technique for elucidating degradation behavior. We are establishing the *operando* techniques of real batteries by non-destructive *in situ* observation, and proceeding with innovative battery research by relating electrode degradation with structural variation.

2. A new data processing computer system

One of features of MLF experiments is a data acquisition system called an event method where each neutron that enters into every detector pixels can be recorded as an event. After the experiment, the experimental data can be reproduced in various histograms depending on the specific objectives. However, since the event method generates a large amount of event data at the same time, the data processing is a big problem. The SPICA data processing computer system supports the data acquisition and data reduction. Over 7 years have passed since the old system started, and its service life has been exceeded, so a new system was introduced. The new system is designed to be faster with reduced cost while maintaining the performance. Furthermore, the virtual technology was introduced to reduce the number of data processing computers by half. The number of computers required for has been halved. Figure 1 shows the computer system. Data reduction performance such as time-dependent histogramming has improved as shown in Table 1, which is beneficial for operando experiments.

Figure 1. A new SPICA data processing computer system.

3. Bragg edge imaging

The Neutron Bragg-edge Imaging (NBI) has been expected to visualize a wide area of a real battery at once. There is no such technology for imaging the density of electrolyte solution which can be used for innovative batteries. In order to develop the NBI technology for visualizing electrolyte concentration in LIB, experiments were conducted using samples in which electrolytes were dissolved at different concentrations in the electrolyte solution. The specimens were prepared by dissolving 0.0 M, 0.5 M, 1.0 M, 2.0 M, and 3.0 M of electrolyte $LiPF_6$ in an electrolyte solution (mixed solution of ethylene carbonate, dimethyl carbonate, and ethyl methyl carbonate) placed in an aluminum container with a thickness of 5 mm. At SPICA, these specimens were placed in the neutron beam, and the neutrons that passed through the specimen were detected by an NBI two-dimensional neutron detector installed downstream of the specimen. Figure 2 shows the two-dimensional neutron distribution in various electrolyte concentrations. A bright area of 65 mm × 18 mm is the sample area containing the electrolyte of 0.0 M to 3.0 M while the outside is shielded against neutrons. For the region inside the red dashed line in Fig. 2, the neutron wavelength-dependent transmission was obtained by

Table 1. Data reduction performance.

	High speed processing (s)	Serial processing (s)	Time-dependent processing (s)
Old system	1184	2416	2282
New system	635	1247	878

dividing the data of 0.0 M–3.0 M electrolytes by that of the aluminum empty container. The obtained transmission is shown in Fig. 3. The longer the neutron wavelength, the lower the transmission, which is consistent with the neutron absorption by hydrogen and ^{6}Li.

The transmission spectra slightly vary depending on the electrolyte concentration. In order to extract the slight variation in area densities of the electrolyte solutions, transmission data were fitted with a function of the sum of the calculated $LiPF_6$ transmission and experimental transmission of 0.0 M. Here, this function includes the area densities of the electrolyte and the electrolyte solution as fit parameters. The results of fitting are shown in the solid line in Fig. 3. The broken line is a fit with a function that does not contain $LiPF_6$, indicating that the solid line is in better agreement with the experimental spectrum, especially for samples with higher electrolyte concentrations.

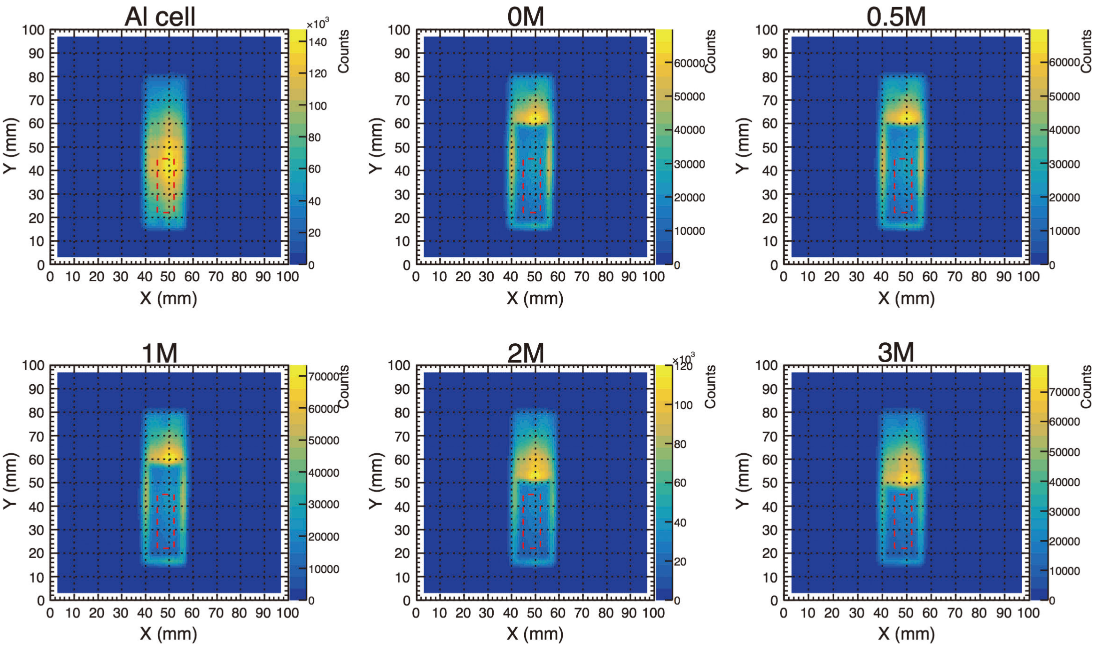

Figure 2. Two-dimensional neutron distribution in various electrolyte concentrations.

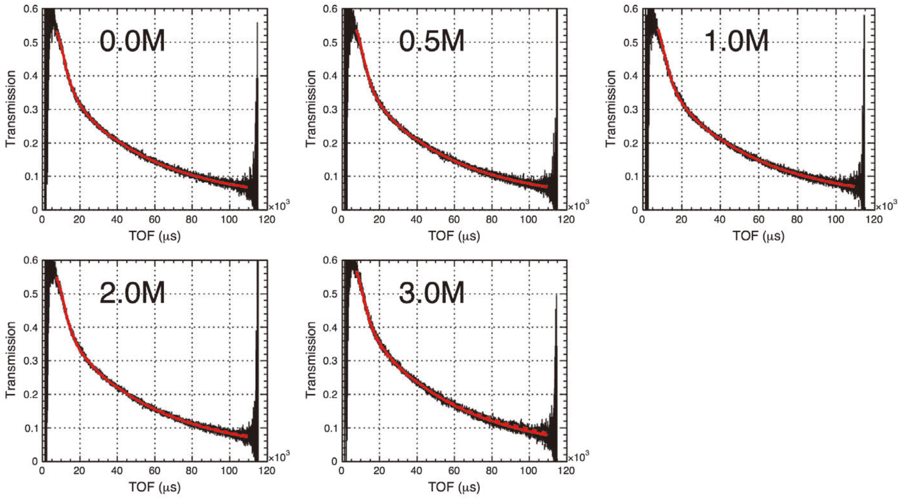

Figure 3. Transmission spectra in various electrolyte concentrations.

T. Kamiyama[1,2], M. Yonemura[1,2], S. Torii[1,2], T. Saito[1,2], and K. Kino[3]

[1]*Neutron Science Section, Materials and Life Science Division, J-PARC Center;* [2]*Institute of Materials Structure Science, KEK;* [3]*Research Institute for Measurement and Analytical Instrumentation, AIST*

BL10: NOBORU

1. Introduction

In FY2018, twelve general-use proposals and two project-use proposals, in addition to the postponed two proposals from FY2017B, were carried out at NOBORU. The user program was not disrupted by any technical problems with the instruments.

This year, we made an attenuation chopper which can selectively suppress the spectral peak of the thermal neutrons and helps to relax the counting limit of the imaging detectors [1]. Its basic design and performance test are described in Section 2.

2. Design and performance of the attenuation chopper

When performing Bragg-edge imaging experiments, the beam collimation ratio (*L*/*D*) is often set to very large values, for example *L*/*D* = 2000, not to prevent image blurring but rather to match the counting limit of the 2D detector. In practice, *L*/*D* values and field of view are determined by checking the direct beam spectrum to prevent event loss due to pile-up at a peak flux of about 2.3 Å. As a result, the detector is easily operated in the cold neutron region. Therefore, it is desirable to attenuate only the thermal peak region and make the spectrum flatter.

The specific requirements are as follows: a) attenuating thermal neutron by 1/2 ~ 1/3, b) low background of neutrons and gamma-rays, c) low electric noise, and d) table-top size and weight. To fulfill these requirements, we designed the attenuation chopper shown in Fig. 1. The chopper blade weighs about 0.4 kg and can be rotated by a 24 V DC motor, which produces negligible electrical noise inside the experiment room. The TEMPAX Float® scatters neutrons little, and generates low-energy gamma-rays compared with the sample's ones.

The design validation was performed by using a monitor counter under weak beam conditions. No event loss was confirmed for the spectrum obtained by open-stop position (blue dots in Fig. 2). Next, the attenuation chopper was kept in a close-stop position and the obtained neutron spectra (left axis) and its exponential decay ratio (right axis) were plotted by green dots. Finally, we obtained a red colored neutron spectrum. Its counting ratio was as expected by operating the attenuation chopper at 25 Hz and is shown in Fig. 2.

An example of Bragg-edge transmission spectra using the attenuation chopper is shown in Fig. 3. The chopper phase needs to be adjusted to a slightly shorter wavelength, but the transmission data was obtained as expected. No fake humps or unexpected background were found in the whole spectra.

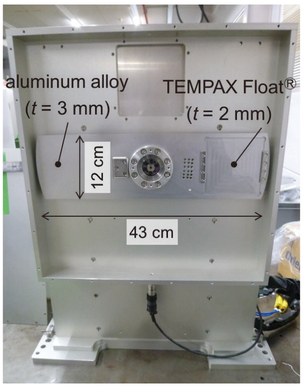

Figure 1. Picture of the attenuation chopper with the outer cover removed. The blade is in open-stop position.

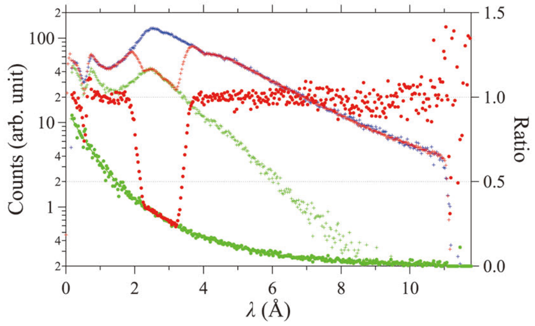

Figure 2. Measured neutron spectra and their ratios at three chopper conditions. Blue: open-stop position, green: close-stop position, and red: operating at 25 Hz.

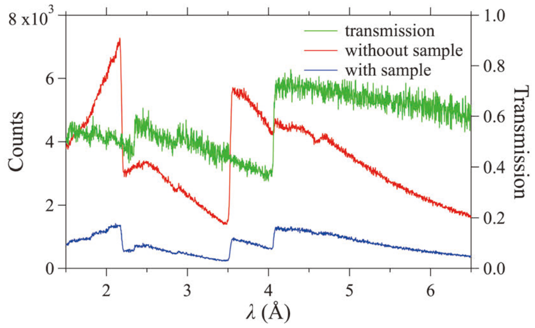

Figure 3. Incident neutron, transmitted neutron, and their transmission spectra of a ferrite steel sample obtained by a single pixel of nGEM detector.

Reference

[1] J. D. Parker et al., JPS Conf. Proc. **22**, 011022 (2018).

K. Oikawa
Neutron Science Section, Materials and Life Science Division, J-PARC Center

BL11: Development of Neutron Imaging Technique under High-Pressure Condition

1. Introduction

Radiography is an effective technique to see the internal structure of materials. Compared to X-ray radiography, neutron radiography has an advantage in observing light elements and isotopes via unique interaction of neutrons with them. These two characteristics enable observation of water distribution in minerals in a high-pressure cell as well as determination of diffusion constant under high-pressure and high-temperature condition. By conducting neutron radiography for samples at high pressures and high temperatures relevant to Earth's mantle condition, we can understand the role of water on materials cycle in the Earth's interior. This year we have tried to establish neutron radiography under high-pressure and high-temperature condition at PLANET [1].

2. Experimental setup

One of the problems in neutron radiography under high-pressure condition is the degradation in spatial resolution of the obtained images due to aberration. It is caused by a finite sample-camera distance *L* (i.e, neutron camera cannot be placed just behind sample because of interference with a high-pressure press) and a large divergence of the incident neutron beam. So far, we tried high-pressure neutron radiography by coupling a bulky neutron camera (Toshiba, Neutron Color I.I.$^{\mathrm{TM}}$) with the six-axis press ATSUHIME [2]. The achieved resolution was limited to ~400 μm because the large body of the camera prevented us from placing it close to the sample ($L = 146$ mm).

To overcome this problem, we newly employed a compact neutron camera (ADVACAM, MiniPix ver.1.0) with size similar to that of a USB stick. This makes it possible to reduce the sample-camera distance down to $L = 88$ mm (Fig. 1), which has significantly improved the spatial resolution as shown below.

3. Optimization of the parameter of beam optics

Prior to the radiography experiments at high pressures, we evaluated the effects of beam optics on the resolution without using a press. For the evaluation, we took images of a pattern lithographed with Gd on silica glass as functions of the sample-camera distance (*L*) and the width of 2nd beam narrower (S2), which was located at the exit of the beam transfer tube. The S2 defines the length-aperture (*L*/*D*) ratio that strongly affects the resolution. By reducing the S2 value from 10 mm to 2 mm, the *L*/*D* ratio can be changed from 200 to 1000 continuously.

Figure 2 shows the S2 and *L* dependence on the spatial resolution. Here, the resolution was estimated from the width of the fringe of the Gd pattern in the obtained images. The resolution was found to be 100 μm regardless of the S2 value when the camera was placed just behind the sample (i.e. $L = 0$ mm). The resolution became worse as the L increased, and the degree of the worsening became more prominent for the larger S2 value. This, however, does not necessarily mean that the smaller S2 is preferable because it also reduces the flux of the incident beam, which decreases the contrast of images. After several tests, we finally determined the optimum value for S2 as 6 mm. In this condition, we can obtain one image with the spatial resolution of 200 μm and the contrast resolution of 10% by a single shot with 10 min exposure.

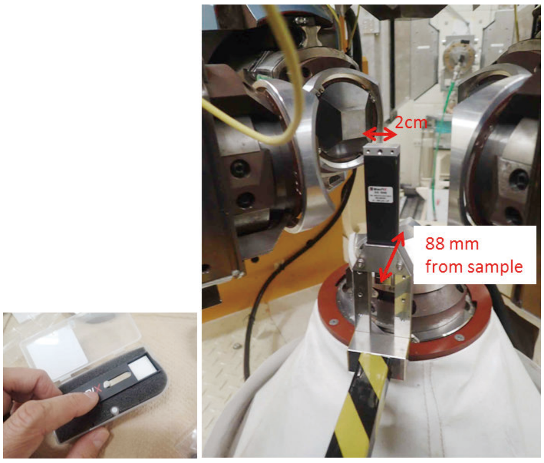

Figure 1. Neutron camera mounted on the six-axis press.

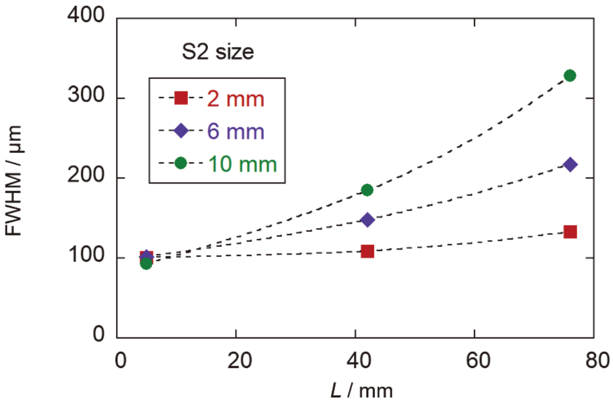

Figure 2. S2 and L dependence on the spatial resolution.

4. In-situ observation of H-D interdiffusion in brucite at 5 GPa and 1100 K

As a test of the neutron radiography under high pressure and temperature condition, we observed the interdiffusion of hydrogen and deuterium atoms in brucite ($Mg(OH)_2$) at 5 GPa and 1100 K. This substance is of geophysical importance because it is a simplified form of hydrous minerals, which play an important role in transporting water into the Earth's interior. The high-pressure cell used in this study is shown in Fig. 3. The pellets made of $Mg(OH)_2$ and $Mg(OD)_2$ powder were stacked and packed in a Pt capsule to seal the hydrogen. This was placed in a graphite tube heater and encased in a ZrO_2 pressure transmitting medium, together with a MgO electric insulator. This cell was compressed to 5 GPa and then heated to 1100 K for 27 hours. The neutron images were taken for 10 min per each at selected elapsed times. Figure 4 shows the obtained radiographs. The images were taken through the gap between the WC anvils opaque to neutrons. Thus, the field of view was limited to 1.4 mm in width. In spite of this limitation, a clear contrast originating from difference in the transmittance between H and D atoms was observed. With time, the boundary between them became obscure, suggesting that the inter-diffusion of H/D occurred at the interface. Figure 5 shows the diffusion profiles obtained by integrating the intensity in the center region along the vertical direction. By analyzing the profiles with the Boltzmann–Matano method, we obtained interdiffusion constant of 11.0 ± 0.2 m^2/s, which was consistent with the value reported so far [3].

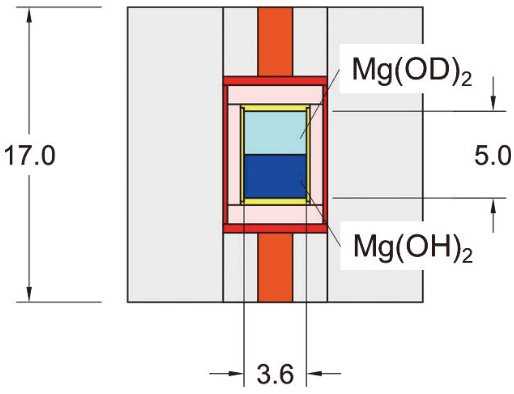

Figure 3. The high-pressure cell used in the experiment. The unit is mm.

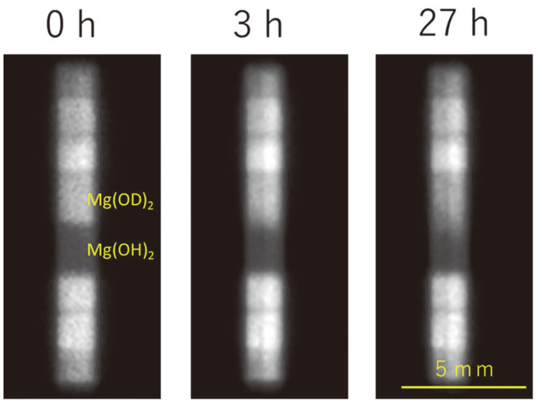

Figure 4. Time evolution of the radiograph.

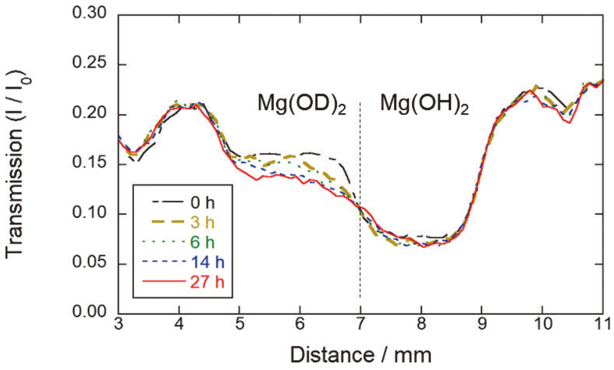

Figure 5. Diffusion profiles obtained by integrating intensity in the center region along the vertical direction.

References

[1] T. Hattori, et al., Nucl. Instrum. Methods. Phys. Res., Sect. A**780** 55 (2015).

[2] A. Sano-Furukawa et al., Rev. Sci. Instrum. **85** 113905 (2014).

[3] Guo et al., Amer. Mineral, **98** 1919 (2013).

H. Arima[1], T. Hattori[2], A. Sano-Furukawa[2], S. Machida[1], J. Abe[1], and K. Funakoshi[1]

[1]*Neutron Science and Technology Center, CROSS;* [2]*Neutron Science Section, Materials and Life Science Division, J-PARC Center*

High Resolution Chopper Spectrometer HRC

1. Introduction

The High Resolution Chopper Spectrometer (HRC) is being operated at BL12 in MLF to study dynamics in condensed matter, especially in wide range of correlated electron systems. The HRC delivers high-resolution and relatively high-energy neutrons, and we proposed three types of inelastic neutron scattering (INS) experiments on the HRC: high-resolution experiments in a conventional energy momentum space, neutron Brillouin scattering (NBS), and sub-eV neutron spectroscopy. In the first phase of the HRC project in the period between FY2008 and FY2013, we constructed the HRC and confirmed that it performed as expected. Based on the achievement in the first phase, we planned to improve further the performance of the HRC in the second phase in the period between FY2009 and FY2018. The improvements focused on two subjects: a realization of practical use of NBS experiments and a demonstration of INS under external fields. The results from the instrumentations for NBS and INS under external fields are the detections of Weyl fermions in metallic ferromagnet $SrRuO_3$ and novel excitations near quantum criticality in geometrically frustrated antiferromagnet $CsFeCl_3$, respectively.

2. Instrumentation

NBS is INS near the forward direction, and therefore, the performance of devices on the beamline, which are the low-angle detectors, the collimator system, and the Fermi chopper, is important [1]. In the low-angle detector bank at the secondary flight path of $L_2 = 5.2$ m, position sensitive detectors (PSDs) were aligned in a double-layered configuration to increase the counting rate. The distortion of the slit package of the Fermi chopper was improved. The geometry of the slit package of the high-resolution Fermi chopper was optimized to obtain a large intensity while keeping high resolutions. The collimator system, which is installed at the upper stream of the sample to reduce the background noise at low scattering angles, was improved. After these improvements, an intensity gain of a factor of 3.5 was achieved for the incident neutron energy of $E_i = 100$ meV with the energy resolution of $\Delta E = 2$ meV. Moreover, a resolution of nearly 1% was achieved with an acceptable intensity for $\Delta E = 1.4$ meV at $E_i = 100$ meV ($\Delta E/E_i = 1.4\%$).

A superconducting magnet was installed. Although an operation at 10 T was confirmed on the HRC, a vacuum leak occurred. The manufacturer evaluated the maximum magnetic field to be 5 T under the environment on the HRC. We will plan to perform experiments using the magnet below 5 T in the next phase of the HRC project. Realizing INS experiments under external fields is important issue on the HRC. We tried to perform INS experiments under high pressures instead of magnetic fields. A standard sample can, containing a cylindrical pressure cell with a sample crystal up to 1.5 GPa, was successfully cooled with a refrigerator.

We have constructed computing system and software environment to control accessories and to handle neutron signals from PSDs for the HRC. In the software environment, comprehensive control program YUI and visualization program HANA play central roles. During this period, we completed successfully YUI and HANA, and now we can conduct experiments confidently [2].

Other instrumentations are briefly described. In the first phase, we installed 128 pieces of PSDs with dimensions of 2.8 m long and 19 mm diameter and 1.8 MPa of ^{3}He gas pressure to cover the scattering angles $\phi = 3° - 42°$ at $L_2 = 4$ m. PSDs at $L_2 = 4$ m were increased to 256 pieces, which are mounted at $\phi = 3° - 62.5°$ and $\phi = -14° - -29.6°$. We have a variety of sample environments: a GM type refrigerator ($T \geq 3$ K), a ^{3}He sorption pumping type refrigerator ($T \geq 0.6$ K), a ^{3}He circulation type refrigerator ($T \geq 0.3$ K). In the ^{3}He refrigerators, background noise is generated at their outer vacuum chambers. By installing an oscillating radial collimator, the background noise has been reduced. Frequent maintenance works were performed for vacuum systems, choppers, refrigerators, and computing systems.

3. Scientific results

An anomalous Hall effect (AHE) is a Hall effect in a ferromagnet, where the Hall resistivity is proportional to the spontaneous magnetization M. However, the AHE in $SrRuO_3$ cannot be described by such a simple relation. $SrRuO_3$ exhibits a band structure including band crossing. The band crossing (Weyl fermion) produces the Berry phase, the Berry curvature takes the form of a magnetic monopole in the momentum space, and then, the fictitious magnetic field is an origin of the AHE. It is known that the Hall conductivity σ_{xy} in $SrRuO_3$ can be well described by this picture. For $SrRuO_3$, a large single crystal necessary for INS has not been synthesized. Therefore, NBS on the HRC using a powder sample is the only way to observe spin waves in $SrRuO_3$.

The observed spin wave dispersion relation can be well fitted to $E(Q) = DQ^2 + E_g$, and the spin wave gap E_g shows nonmonotonous temperature (T) dependence (Fig. 1). We found that the observed E_g is well explained by a theoretical form: $E_g(T) = aM(T)/[1+b\sigma_{xy}(T)/M(T)]$, where E_g can be described by the Berry curvature through σ_{xy}. We showed that the Berry curvature, that is the fictitious magnetic field produced by the Berry phase, is an observable of INS [3]. Correlated electronic systems have the internal degrees of freedom such as spin, charge, orbital, lattice, etc. The fluctuations of these degrees can be observed as spin waves, orbital waves, phonons etc. by means of INS, which are influenced by the quantal phase of electronic wavefunctions.

In a spontaneously symmetry-broken state near the quantum critical point (QCP), the phase and amplitude fluctuations of the order parameter are observed as the gapless Nambu-Goldstone and the gapped Higgs modes, respectively. We observed a hybridization of the phase and amplitude fluctuations near QCP in a frustrated magnet $CsFeCl_3$. A triangular-lattice antiferromagnet $CsFeCl_3$ shows a quantum disordered state at ambient pressure, and an ordered state with a noncolinear spin structure above the critical pressure (P_C = 0.9 GPa). We performed INS experiments under several pressures using HRC and the triple axis spectrometer CTAX at ORNL. Below P_C, a gapped spectrum was observed. On the other hand, we observed a gapless spectrum as well as characteristic excitations at 0.5 – 0.8 meV and 0.8 – 1.3 meV above P_C (Fig. 2). In order to discuss the observed spectra, the one-magnon cross section was calculated based on the extended spin-wave theory (ESW). One-magnon processes for the hybridization between the phase and amplitude fluctuations can only exist in a noncollinear state and the two characteristic excitation modes show level repulsion. The observed spectra agree well with this calculation. However, the two modes simply cross without the hybridization, and this calculation does not reproduce the observation. The hybridization plays an important role in magnon dynamics in noncollinear magnets near QCP. The INS measurements in $CsFeCl_3$ revealed this by the fine tuning of pressure through QCP [4].

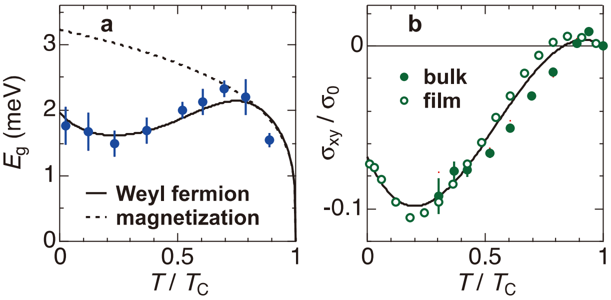

Figure 1. Spin wave gap $E_g(T)$ (a) and anomalous Hall conductivity $\sigma_{xy}(T)$ (b) in $SrRuO_3$ as a function of T/T_C with T_C = 165 K. The solid line in (a) is a fitted curve described in the text. (Reproduction from Ref. [3].)

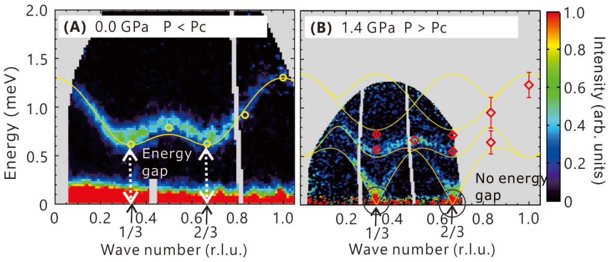

Figure 2. INS spectra from $CsFeCl_3$ obtained at HRC under (A) 0.0 GPa at 6 K and (B) 1.4 GPa at 0.9 K. The marks are the excitation peak positions obtained at CTAX. The solid yellow curves are calculated by ESW. (Reproduction from Ref. [4].)

Moreover, we have successfully investigated spin dynamics in correlated electron systems with the conventional method of INS [5–9].

References

[1] S, Itoh, et. al., Physica B, **568** 76 (2019).
[2] D. Kawana, et al., J. Phys.: Conf. Series, **1021** 012014 (2018).
[3] S. Itoh et al., Nat. Commun., **7** 11788 (2016).
[4] S. Hayashida et al., Sci. Adv., **5** eaaw5639 (2019).
[5] S. Hayashida et al., Phys. Rev. B **92**, 054402 (2015).
[6] Y. Ikeda et al., J. Phys. Soc. Jpn. **85**, 023701 (2016).
[7] S. Ibuka et al., Phys. Rev. B **95**, 224406 (2017).
[8] T. Haku et al., J. Phys. Conf. Series **828**, 012018 (2017).
[9] D. Ueta et al., Physica B **536**, 21 (2018).

S. Itoh[1,2], T. Masuda[1,3], T. Yokoo[1,2], S. Asai[3], H. Saito[1,2], D. Kawana[3], R. Sugiura[3], T. Asami[3], and Y. Ihata[4]
[1]*Institute of Materials Structure Science, KEK;* [2]*Neutron Science Section, J-PARC Center;* [3]*The Institute for Solid State Physics, The University of Tokyo;* [4]*Technology Development Section, J-PARC Center*

BL14 AMATERAS

1. Introduction

FY2018 was the tenth year of operation of AMATERAS [1, 2], a cold-neutron disk-chopper spectrometer. We continued the user program out-reach activities. As a part of our upgrade program, we have carried out detector and detector bank related equipment enhancement. In this FY, we did not encounter any serious mechanical problems with the equipment of AMATERAS.

2. User program, international activities and out-comes

The number of short-term general proposals submitted for the 2018A and 2018B periods was 31 (accepted: 14, reserved: 16, not approved: 1) and 24 (accepted: 13, reserved: 10, not approved: 1), respectively. We also had two long-term general proposals (accepted: 1, not approved: 1), three urgent proposals and three JAEA project proposals. The majority of the proposals dealt with studies on magnetism and strongly correlated systems, especially subjects related to quantum spin systems. As a result, in FY2018, 29 short-term general proposals, one long-term general proposal, three urgent proposals and three JAEA project proposals were carried out on AMATERAS.

In 2018, 14 refereed papers covering the woks at AMATERAS were published. The research topics included thermo-electric materials, novel superconductors, quantum spin liquids, 4f electron systems and other magnetisms. Furthermore, one press releases was issued, which covered the study on quantum paramagnet near spin-state transition in Co oxides done by a research group headed by Dr. Keisuke Tomiyasu of Tohoku University.

3. Instrumental activities

When we installed 10 position sensitive detectors (PSDs) in FY2017, six of them were installed to every other position in the high-angle side. This fiscal year, during the summer shutdown period, we additionally installed more PSDs to fill up the blankspots. As the result, the horizontal angle region up to 118° was covered (Fig. 1). This could be effective for various experiments, such as observations of phonon spectra and molecular dynamics. Furthermore, we added more vanes to the negative scattering angle side in the vacuum scattering chamber, though PSDs have not yet been installed to this side.

We also started to prepare the replacement of components of the main vacuum pump of the scattering chamber. Some of components have already been delivered. This upgrade will be completed in several years.

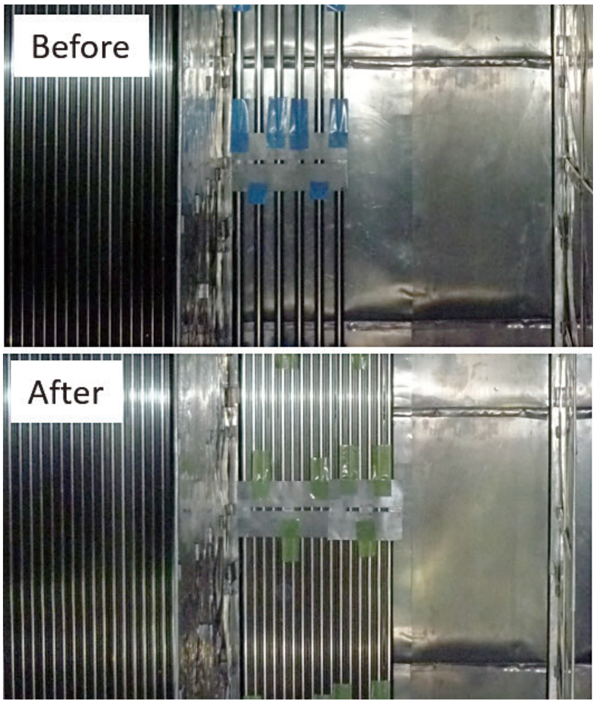

Figure 1. Detector banks at high-angle region before and after installing PSDs. Cadmium plates are stuck on the surface of the PSDs for calibration.

References

[1] K. Nakajima, S. Ohira-Kawamura, T. Kikuchi, M. Nakamura, R. Kajimoto, Y. Inamura, N. Takahashi, K. Aizawa, K. Suzuya, K. Shibata, T. Nakatani, K. Soyama, R. Maruyama, H. Tanaka, W. Kambara, T. Iwahashi, Y. Itoh, T. Osakabe, S. Wakimoto, K. Kakurai, F. Maekawa, M. Harada, K. Oikawa, R. E. Lechner, F. Mezei, and M. Arai, J. Phys. Soc. Jpn. **80**, SB028 (2011).

[2] K. Nakajima, RADIOISOTOPES **66**, 101 (2017).

K. Nakajima[1], S. Ohira-Kawamura[1], M. Kofu[1], T. Kikuchi[1,2], Y. Inamura[1], and D. Wakai[3]

[1]*Neutron Science Section, Materials and Life Science Division, J-PARC Center;* [2]*Chemical Analysis Center, Research & Development HQ, Sumitomo Rubber Industries, Ltd.;* [3]*Nippon Advanced Technology Co., Ltd.*

Upgrading TAIKAN

1. Introduction

The small and wide angle neutron scattering instrument TAIKAN (BL15) has been developed and upgraded at J-PARC to analyze precisely and efficiently the microstructures or hierarchical structures of substances in various scientific fields with a 1-MW spallation neutron source [1]. In FY2018, it was upgraded further to perform efficient low-*q* measurement and high precision gas/vapor adsorption measurements.

2. Upgrading for low-*q* measurement

The detector system of TAIKAN is composed of 5 detector banks: small-, middle-, high-, ultra-small-angle, and backward detector banks. On the small-angle detector bank, 144 ^{3}He PSD tubes were additionally installed. The measurement efficiency of the small-angle detector bank increased by about 19%. The number of ^{3}He tubes then increased to 912, 592, 200, and 40 for the small-, middle-, high-angle, and backward detector banks, respectively. The installation ratios of the ^{3}He tubes became 100, 82, 36, and 50% or the small-, middle-, high-angle, and backward detector banks, respectively. Figure 1 shows a photo of the small-angle detector bank after installing the ^{3}He tubes.

Figure 1. Small-angle detector bank.

3. Upgrading for high precision gas/vapor adsorption measurements

A high precision gas/vapor adsorption measurement instrument BELSORP-max (MicrotracBEL Corp.) with a quartz cell was introduced for the SANS measurement of porous materials, etc. (Fig. 2). The inside dimensions of the cell are 19 mm in diameter and 1 – 2 mm in depth. The sample volume is about 0.3 – 0.6 ml. The instrument has been used to measure specific surface area/pore size distribution, vapor adsorption and chemisorption of a sample. The adsorption gases/vapors to be measured are N_2, Ar, H_2O, D_2O, etc., and the measurement range of the pore size distribution is 0.35 – 500 nm in diameter.

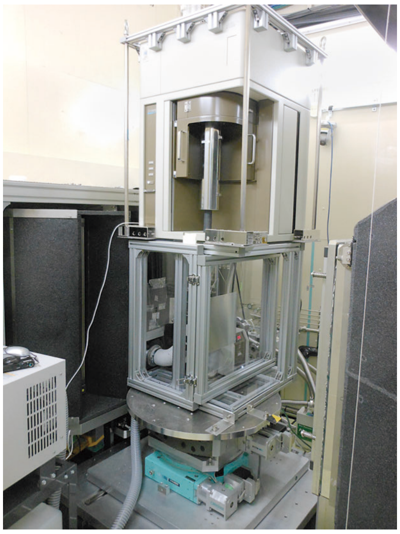

Figure 2. High precision gas/vapor absorption measurement instrument installed on a sample stage of TAIKAN.

4. Future prospects

The improvement of the measurement efficiency by the installation of small-angle detectors and the increase of the beam intensity makes precise measurement in a low-*q* range easier. In the future, TAIKAN is expected to contribute to the research of microstructures or hierarchical structures by precise measurement not only in a low-*q* range but also in a wide-*q* range.

Reference

[1] S. Takata, J. Suzuki, T. Shinohara, T. Oku, T. Tominaga, K. Ohishi, H. Iwase, T. Nakatani, Y. Inamura, T. Ito, K. Suzuya, K. Aizawa, M. Arai, T. Otomo and M. Sugiyama, JPS Conf. Proc. **8**, 036020 (2015).

J. Suzuki[1], S. Takata[2], K. Ohishi[1], H. Iwase[1], Y. Kawamura[1], K. Hiroi[2], T. Morikawa[1], and M. Sahara[1]

[1]*Neutron Science and Technology Center, CROSS;* [2]*Neutron Science Section, Materials and Life Science Division, J-PARC Center*

Installation of Focusing Mirror for Neutron Reflectometry at BL16 SOFIA

1. Introduction

Neutron reflectometry (NR) is very useful for investigations of structures of surfaces and buried interfaces composed of soft materials. SOFIA is a horizontal-type neutron reflectometer constructed at Beamline 16 (BL16) of the Materials and Life Science Experimental Facility (MLF) of the Japan Proton Accelerator Research Complex (J-PARC) [1, 2]. Due to the high-flux beam of J-PARC, less than one hour is needed for taking a full *Q*-range data and only a few seconds for a limited *Q*-range data in the case of a sample with 3 inches (76 mm) in diameter; even though the beam power is still one-third of the planned value, 1 MW. However, several hours are still needed for a small sample such as 10 mm × 10 mm, which is a typical size of a sample for X-ray reflectometry.

For further upgrade of the SOFIA reflectometer, we have developed an elliptical focusing mirror to illuminate a sample with a neutron beam with a large beam divergence. In the case of conventional double slit collimation, the optimal beam divergence decreases according to the sample size. Hence, the focusing optics with the mirror has an advantage on the beam flux especially for small samples. The planned specifications of the focusing mirror and detector are a beam size of 0.1 mm at a sample position with divergence of 2.5 mrad.

So far, we developed a prototype focusing supermirror capable of focusing neutrons with a width of 0.34 mm [3], and modified mirror with 0.17 mm in full width at half maximum (FWHM) [4]. These mirrors work well as focusing devices, however, the focusing size is insufficient for our demand. Last year, we reported the development of a focusing mirror having a potential to focus neutrons at a smaller spot size. This year, we report the performance of the mirror evaluated with neutrons.

2. Manufacture

We employed an aluminum alloy as a base plate for the focusing mirror. First, the base plate was machined with a single diamond tool to produce a rough surface shape, in which the surface follows the center part of an ellipse with a long axis of 4300 mm and a short axis of 430 mm. Then, the plate was coated with nickel phosphorous by electroless plating process, and finished by an ultrahigh precision cutting (UPC) process. The surface was polished before coating the super mirror to create a smooth surface of less than 1 nm in root mean square (RMS) roughness. The super mirror with the m-value of 3 was deposited on the substrate using an ion beam sputtering instrument at the institute for integrated radiation and Nuclear science, Kyoto University [5]. Since the mirror size, 550 mm in length and 60 mm in width, was too large to coat the super mirror, the mirror was divided into two pieces and assembled into one unit after the processes above were completed. The details were reported in the literature [6].

3. Results

First, we summarize the results reported last year. The surface roughness of the mirror substrate, which is sensitive to the reflectivity of neutrons was only 0.108 nm ± 0.009 nm (standard deviation), that is, the roughness was better than the commercially available Si substrates. The super-mirror coating deposited on the substrates was very homogeneous and equivalent to a good super-mirror guide: the critical momentum transfer was 0.628 nm^{-1} ± 0.007 nm^{-1} (standard deviation) and the reflectivity there was 86.2% ± 2.5% (standard deviation).

According to the surface shape of one mirror segment measured by a laser interferometer, the frequency distribution of the slope error followed Gaussian shape with the FWHM of 24 μrad. As the distance between the mirror and the focal point, that is, the sample position, is designed to be 2150 mm, the minimum beam size is expected to be 50 μm. However, we faced a problem with the assembly of the two segments last year: the focal images of the segments were not coincident at the focal point because of the misalignment of the relative tilt.

To overcome this problem, we changed the method for fixing the mirror segments. So far, we fixed the mirror segment gently with kinematic couplings. This enabled us to minimize the stress and deformation, but was not stable enough with respect to the vibration during transportation. Hence, we adopted direct fixing on the flange surrounding the mirror as shown in Fig. 1. The height of the flange at the fixing position was precisely adjusted by a spacer, of which the length was machined by an ultraprecision lathe with a positioning resolution of 10 nm.

The new mirror has been installed at the SOFIA reflectometer, and the focusing performance was evaluated. Owing to the high precision of the focusing mirror shape, neutrons diverged from the slit size of 0.05 mm were successfully converged at the sample position with the FWHM of 0.13 mm by the mirror. As the slit size is adjustable using pulse motors, the beam size at the sample position can be controlled depending on the size of the sample and incident angle to the sample plane by changing the aperture. Figure 2 shows the beam profiles for illuminating the samples having different sizes with the incident angle of 1.8 degrees. Remarkably, the integral of the profiles with the focusing optics was approximately two times larger than that with the conventional double slit optics. This indicates that the exposure time for the measurement can be shortened by half by using the focusing optics for the same data statistics.

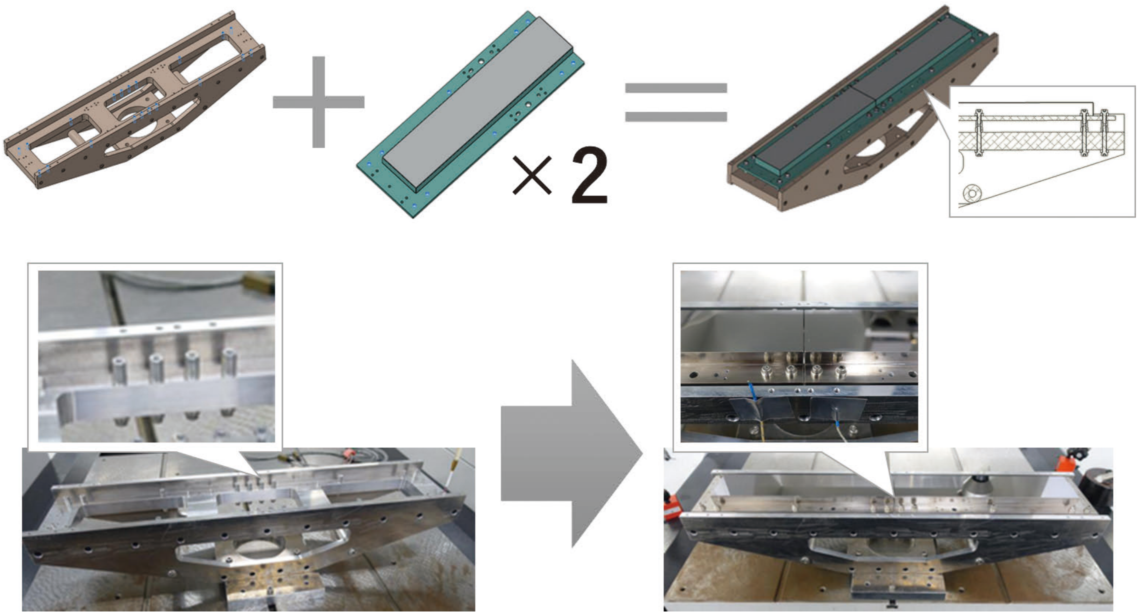

Figure 1. Schematic illustration of the focusing mirror assembly with the direct fixing method. Each mirror is tightly fixed at ten points on the flange with screws, and the height of the spacer is precisely machined to minimize the stress and deformation of the mirror segment.

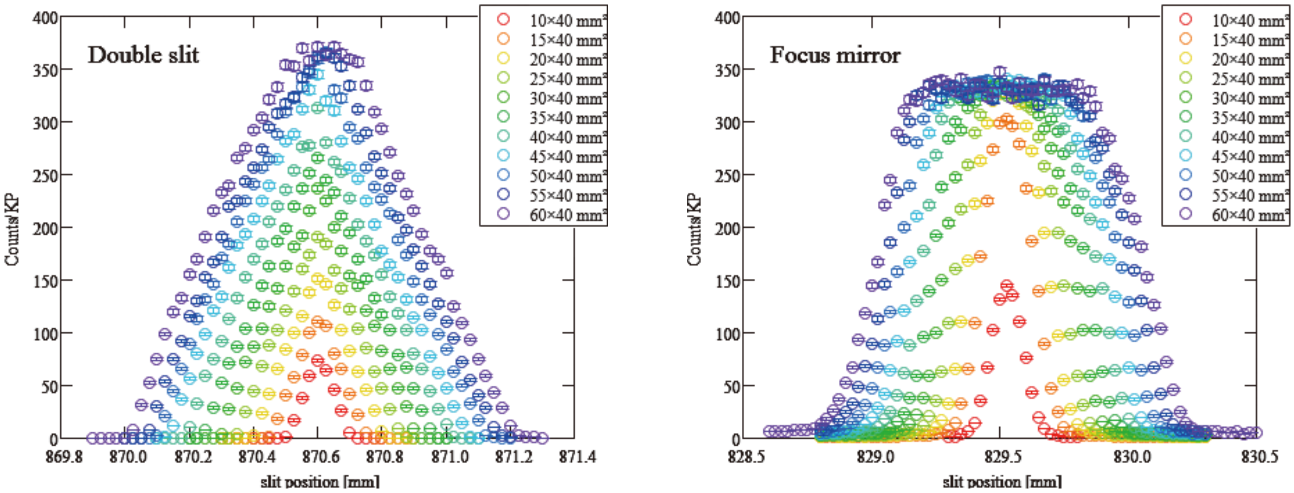

Figure 2. Beam intensity profiles for different illumination areas at the sample position with the conventional double slit optics and focusing optics with the mirror. The total intensity with the focusing optics is approximately twice stronger than that with the double slits, that is, the exposure time can be shorten by half with the focusing optics for the same data statistics.

4. Conclusion

Here, we reported the improvement of the focusing mirror developed for the neutron reflectometer SOFIA. The latest mirror we developed can converge neutrons on the sample position with a minimum FWHM of 0.13 mm. The beam intensity at the sample position with the focusing optics was approximately twice stronger than that with the conventional double slit optics for the same beam size, that is, the exposure time could be shortened by half with the focusing mirror. This mirror has already been installed at the SOFIA and used for the experiments with small samples.

References

[1] N. L. Yamada *et. al.*, *Euro. Phys. J. Plus*, **44** (2011) 9424.
[2] K. Mitamura *et. al.*, *Polymer J.*, **45** (2013) 100.
[3] S. Takeda *et. al.*, *Opt. Express*, **24**, (2016) 12478–12488.
[4] T. Hosobata *et. al.*, *Opt. Express*, **25**, (2017) 20012–20024.
[5] M. Hino *et. al.*, *Nucl. Instr. and Meth. A*, **797** (2015) 265.
[6] T. Hosobata *et. al.*, *Opt. Express*, **27**, (2019) 26807–26820.

N. L. Yamada[1,2], T. Hosobata[3], M. Hino[4], K. Hori[2,5], F. Nemoto[1,2,#], T. Kawai[3], and Y. Yamagata[3]
[1]*Neutron Science Section, Materials and Life Science Division, J-PARC Center;* [2]*Institute of Materials Structure Science, KEK;* [3]*RIKEN Center for Advanced Photonics;* [4]*Institute for Integrated Radiation and Nuclear Science, Kyoto University;* [5]*Sumitomo Rubber Industory*
#Present affiliation: National Defense Academy

BL17: Current Status of Polarized Neutron Reflectometer, SHARAKU

1. Introduction

Neutron reflectometry (NR) is a powerful technique to analyze the nanostructures of the surface and interface of thin films non-destructively. In the polarized neutron reflectometer, SHARAKU, installed at BL17 in the MLF, not only the depth profile of the chemical composition but also the magnetic structure can be analyzed. The large sample stage with high load capacity allows the use of various sample environment (SE) equipment, which enables the NR measurements in various conditions, such as high magnetic field, cryogenic temperature, humidity environment and UV/visible irradiation [1–5].

In this report, we describe the status of the SE devices newly available in the NR experiments at SHARAKU.

2. Humidity Control System

The interaction between water vapor and materials has attracted attention in industrial research and development. For example, the structure analysis of the material in an accelerated aging test under conditions of high temperature and humidity is necessary for the development of the performance and the quality assurance. The NR measurement in a wide range of temperature and humidity conditions is a key to the further improvement of the properties and functions of thin film materials such as adhesives and polyelectrolyte membranes in fuel cells.

In order to accelerate the NR studies in this field, we have introduced a SE system that can measure the neutron reflectivity in the controlled environment of temperature and humidity [6]. The photographs of the system are shown in Fig. 1. This system consists of a humidity generator (HUMICURUSE, Daiichi-kagaku Co. Ltd.) and a custom-made measurement chamber. The humidity generator produces water vapor at the desired humidity and temperature condition by combining dry air with saturated aqueous vapor by two mass flow controllers. The measurement chamber is made of stainless steel with a cavity of 85 mm diameter and 100 mm long and is covered with a heat insulator to introduce the temperature- and humidity-controlled gas without condensation. The sample is placed in the center of the cavity and water vapor flows in and out through the cavity. The incident and reflected neutron beams pass through the Al windows installed on the both sides of the chamber. This setting allows the NR measurement in a humidity range from 0 to 85% RH and a temperature range from 5 to 85°C.

Using this system, the structure of the polymer film under a controlled temperature and humidity environment was measured. Figure 2 shows the neutron reflectivity profiles for a thin film of poly (vinyl alcohol) (PVA) in vapor of heavy water at various humidity values [7]. From the analysis of the NR profile, the PVA film in the dry state (at 0% RH) showed a thickness of 46 nm and scattering length density (SLD) of 0.77. At high humidity, the critical *q* of the total reflection increased and the gap of the Kiessig fringe decreased. This indicates that the SLD of the film increased by the absorption of D_2O from the vapor phase and that the PVA film was swollen.

Figure 1. Photographs of the humidity-control system: sample chamber (left) and humidity generator (right).

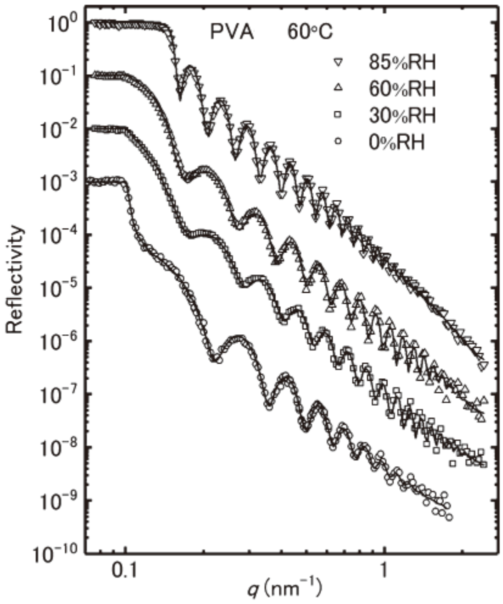

Figure 2. Neutron reflectivity profiles of a PVA film under humidity conditions of 0, 30, 60, and 85% RH at 60°C.

3. High-field magnets for PNR

In SHARAKU, polarized neutron reflectivity (PNR) experiments in various magnetic fields are realized using certain kinds of magnets in the MLF. The 1 T electromagnet with a vertical magnetic field is prepared for the usual use. For the experiments in a magnetic field higher than 1 T, high-field magnets in the MLF can be used in SHARAKU.

The 7 T superconducting magnet is one of the high-field magnets available as common SE equipment in MLF. The magnetic field is in the vertical direction and the sample is introduced from the top of the magnet using a sample stick. We carried out a commissioning of this magnet to provide it for user experiments in SHARAKU. Figure 3 shows the degree of polarization in a system using the magnet as a result of commissioning. The flipping ratio (I+/I–) is more than 40 in the wavelength range of 2.4–8.0 Å, indicating that the PNR measurement with a high polarization contrast can be conducted in SHARAKU. The 7-T magnet is open for user experiments as well as the 1-T and 4-T magnets.

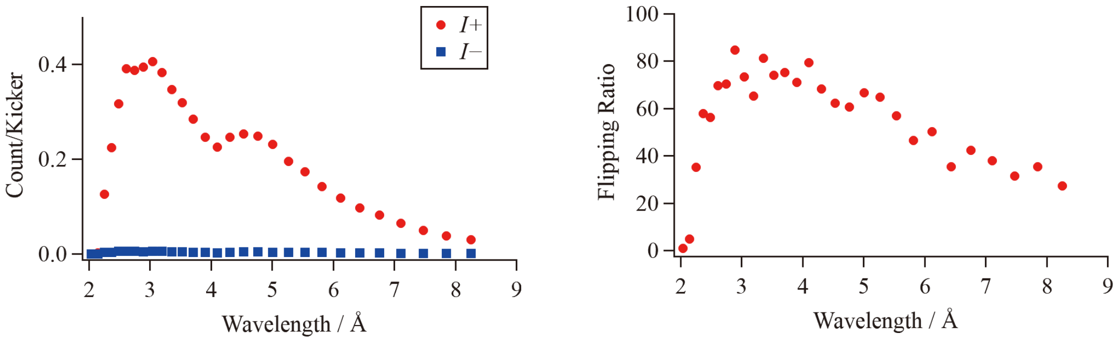

Figure 3. TOF spectra of polarized neutrons through an analyzer (a) and the flipping ratio in a magnetic field of 6.5 T. The red and blue dots in the panel (a) indicate the polarized neutron intensities at analyzer configurations for parallel and anti-parallel spin directions for the incident neutron, respectively.

References

[1] S. Itoh, M. Nakaji, Y. Uchida, M. Kitaguchi and H. M. Shimizu, Nuclear Inst. Meth. Phys. Res., A**908**, 78–81 (2018).

[2] V. Ukleev, S. Suturin, T. Nakajima, T.-H. Arima, T. Saerbeck, T. Hanashima, A. Sitnikova, D. Kirilenko, N. Yakovlev and N. Sokolov, Sci. Rep. **8**, 8741 (2018).

[3] Y. Sakaguchi, T. Hanashima, H. Aoki, H. Asaoka, A. Simon and M. Mitkova, Phys. Status Solidi A **215**, 1800049 (2018).

[4] K. Sakurai, M. Mizusawa, J. Jiang and T. Ito, Physica B: Condensed Matter **551**, 426–430 (2018).

[5] R. Maruyama, D. Yamazaki, K. Akutsu, T. Hanashima, N. Miyata, H. Aoki, M. Takeda and K. Soyama, Nuclear Inst. Meth. Phys. Res., A**888**, 70–78 (2018).

[6] S. O.-Kawamura, T. Hattori, S. Harjo, K. Ikeda, N. Miyata, T. Miyazaki, H. Aoki, M. Watanabe, Y. Sakaguchi and T. Oku, Neutron News **30**, 11–13 (2019).

[7] T. Miyazaki, N. Miyata, M. Asada, Y. Tsumura, N. Torikai, H. Aoki, K. Yamamoto, T. Kanaya, D. Kawaguchi and K. Tanaka, Langmuir **35**, 11099–11107 (2019).

N. Miyata[1], H. Aoki[2,3], K. Soyama[4], D. Yamazaki[2,5], K. Akutsu[1], T. Hanashima[1], and S. Kasai[1]

[1]Neutron Science and Technology Center, CROSS; [2]Neutron Science Section, Materials and Life Science Division, J-PARC Center; [3]Institute of Materials Structure Science, KEK; [4]Materials and Life Science Division, J-PARC Center; [5]Neutron Instrumentation Section, Materials and Life Science Division, J-PARC Center

Status of SENJU 2018

1. Introduction

SENJU is a TOF single-crystal neutron diffractometer designed for precise crystal and magnetic structure analyses under multiple extreme environments, such as low-temperature, high-pressure and high-magnetic field, as well as for taking diffraction intensities of small single crystals with a volume of less than 1.0 mm^3 down to 0.1 mm^3 [1]. Ever since SENJU was launched in 2012, continuous commissioning and upgrading operations have been carried out.

In 2018, we installed a new vacuum sample chamber for the future's installation of additional detectors, and successfully established the fine-calibration method of the detector position. In addition, we also report on the purposes for which the instrument beam-time for SENJU was used.

2. Installation of a new vacuum sample chamber

The detector arrangement of SENJU is almost cylindrical, 36 detectors are arranged cylindrically around the sample position and only one detector is positioned at the bottom of the sample position. Consequently, the obliquely downward direction of the sample position is not covered by the detector and the reciprocal space around the azimuth region of the f-axis was not measured without pulling out the goniometer and changing the sample orientation. To solve this problem, we have a plan to add detectors. As the first step of this plan, we manufactured and installed a new vacuum sample chamber. The new chamber has a dome-shaped basement made from aluminum. The thickness of the dome is 5 mm. The additional detectors will be set up in near future, as shown in Fig. 1.

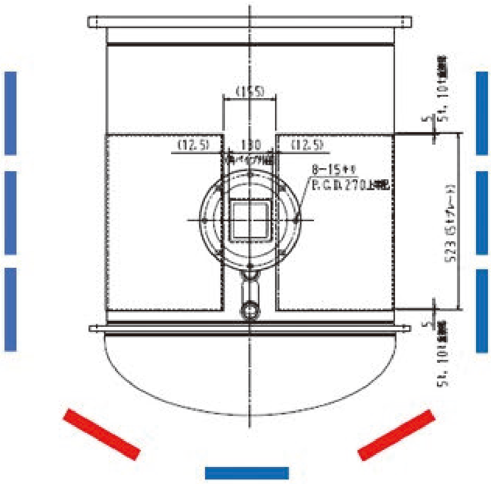

Figure 1. Schematic view of the new vacuum sample chamber and the detector arrangement. Blue boxes in the figure show the present detector arrangement and red boxes show the new detectors that will be installed in near future.

3. Fine calibration of the detector position

For single-crystal diffractometers, the ability to accurately determine the lattice constants of materials is one of the most important requirements, since the changes of lattice parameters are often indicative of phase transitions and bond lengths, which are directory related to the lattice parameters, determines the chemical properties. The accuracy of the lattice parameters largely depends on the accuracy of the instrumental parameters that define the positions of each detector with respect to the sample position and the incident beam. Therefore, the determination of the instrumental parameters, in other words "calibration", is very essential for the operation of instruments. Nevertheless, there is no established way to determine the instrumental parameters, and thus we developed a systematic procedure for calibration of SENJU.

There are 37 2D-detectors installed on SENJU. One module is composed of vertically aligned 3 detectors (top, middle and bottom), and 12 modules are cylindrically placed around the sample position (the rest of one detector is located underneath the sample position). 7 parameters for each detector describing the geometrical location of the detector and the distance between the target and the sample position (L_1) have to be determined (260 parameters in total). The calibration procedure was divided into two parts: the part to determine the parameters for the middle detectors and the part for the rest of detectors in order to avoid biases as much as possible. In the procedure, a single crystal of C12A7 (Maynite: $12CaO{\bullet}7Al_2O_3$) was used as a standard sample. The structure of this material is cubic, and the lattice constant was precisely measured by X-ray in advance ($a = 12.0018$ Å).

The sample was mounted on a one axis (omega) goniometer in a way that c-axis is aligned with the rotation axis (vertical axis). Under these conditions, number of Bragg reflections of (h k 0) can be measured on the middle detectors. By rotating the sample in small-angle steps such as 0.5°, the same Bragg reflections can be measured on the same detectors number of times and a series of Bragg reflections forming a line can be obtained. In addition, another series of Bragg reflections

(−h −k 0) can be measured by doing the same measurements after rotating the sample by 180°. Here, two lines of Bragg reflections have been recorded on the middle detectors, as shown in Fig. 2, as well as many other Bragg reflections on other detectors.

As the first part of the calibration, the distance between the sample and the detectors and the position of the equator on the detectors are calculated from the intervals of the Bragg reflections in the series and the gap between the two lines, respectively. Provided these parameters and the lattice parameters are fixed, the rest of parameters of the middle detectors and the orientation of the sample are determined based on the least-square method. By this process, all the parameters of the middle detectors and the orientation of the sample, that is the UB-matrix, are determined.

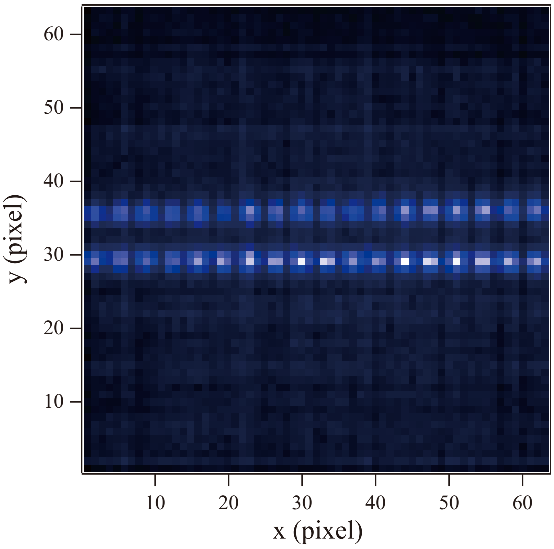

Figure 2. A typical example of a series of Bragg reflections measured during the calibration measurement by rotating the sample in small-angle steps.

As the second part of the calibration, the parameters of the rest of the detectors are refined based on the least-square method to best match the positions of the observed Bragg reflections and the predicted positions based on the UB-matrix. The flight path (L_1) is also refined simultaneously in this process.

All the processes mentioned above are integrated into one program, thus once the necessary measurements are conducted, the calibration will be done just by inputting the data into the program. One thing to be noted is that some parameters are not sensitive enough to be precisely determined with this process, thus further improvement is required.

4. Use of the instrument beam-time

In 2018, the instrument beam-time was used mainly for measurements of standard samples, a vanadium-nickel alloy for calibration of the detector efficiency. In addition, we used the instrument beam-time to compensate beam-time of some general-use proposals lost due to usage problems of sample environment devices.

Reference

[1] T. Ohhara et al., J. Appl. Cryst., **49** 120 (2016).

T. Ohhara[1], R. Kiyanagi[1], A. Nakao[2], K. Munakata[2], Y. Ishikawa[2], K. Moriyama[2], I. Tamura[1], and K. Kaneko[1]
[1]*Neutron Science Section, Materials and Life Science Division, J-PARC Center;* [2]*Neutron Science and Technology Center, CROSS*

TAKUMI and the Engineering Sciences

1. Introduction

TAKUMI is a neutron diffractometer dedicated for research in engineering materials sciences, which was installed at beamline 19 in the MLF of J-PARC. Careful analysis of the Bragg peaks in a neutron diffraction pattern can reveal important structural details of a sample material, such as internal stresses, phase conditions, dislocations, texture, etc. Experiments in TAKUMI vary from internal strain mapping in engineering components, microstructural evolutions during deformations of structural or functional materials at various temperatures, microstructural evolutions during manufacturing (thermo-mechanical) processes, to texture analyses of engineering materials.

TAKUMI has entered its 10th year since the start of commissioning. Many fruitful results using various materials from different engineering fields have been obtained through users experiments, internal project researches and instrumentation activities. Various sample environmental devices have been also developed independently by the TAKUMI team or together with users to realize numerous types of materials engineering experiments using neutron diffraction *ex situ* or *in situ*. They include several loading machines for high and low temperatures, as well as for room temperature, furnaces, a cryostat, a simulator for thermo-mechanical process (thermec-mastor), a cradle, radial collimators, and so on. Different kinds of data analyses have been also established to obtain the above structural details of the sample materials.

2. Statistics of experiments and sciences

In FY2018, thanks to users and collaborators, we were able to conduct various experiments, and several excellent refereed papers have been published. The experimental type statistics done during FY2018 are shown in Fig. 1. The experiments cover *ex situ* measurements, including strain mappings and diffraction measurements of samples with histories of deformations and/or heat treatments, and *in situ* measurements including loading experiments at temperatures covering 1273 K to 10 K, measurements during applications of a cyclic electric field, and so on.

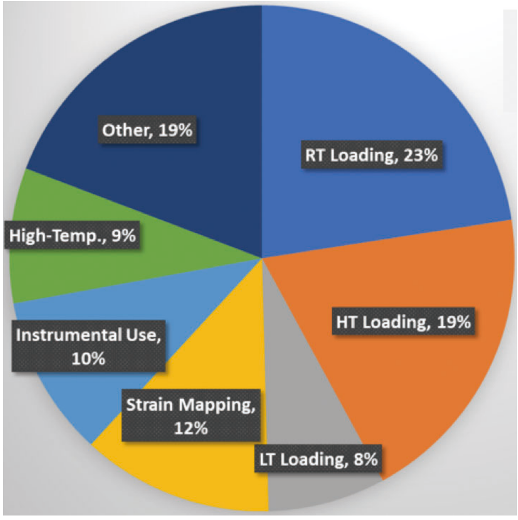

Figure 1. The experimental type statistics done during FY2018 in TAKUMI.

Many excellent papers have been published in FY2018, and the highlighted ones are as follows:

a. “Deformation behavior of as-cast and as-extruded $Mg_{97}Zn_1Y_2$ alloys during compression, as tracked by in situ neutron diffraction”, by Wu Gong et al. [1]. The yield strength of $Mg_{97}Zn_1Y_2$ alloy, containing a long period stacking ordered (LPSO) phase and an α-Mg phase, was found to be substantially enhanced by hot extrusion. The quantitative evaluation of phase stress partition confirmed that the LPSO phase was significantly enhanced by hot extrusion and kink deformation of the LPSO phase plays an important role in preserving ductility.

b. “In situ Neutron Diffraction Study on Ferrite and Pearlite Transformations for a 1.5 Mn-1.5 Si-0.2 C Steel”, by Yo Tomota et al. [2]. *In situ* neutron diffraction enables us to investigate the changes in lattice constants of ferrite and austenite, which are affected not only by thermal contraction but also by transformation strains, thermal misfit strains, and carbon enrichment in austenite. Pearlite transformation started after carbon enrichment in austenite reached approximately 0.7mass% and contributed to the broadening of the diffraction line.

c. “Deformation of CoCrFeNi high entropy alloy at large strain”, by Bing Wang et al. [3]. A three-stage deformation behavior was fully captured by lattice strain and texture evolution. In spite of the chemical complexity, the deformation in CoCrFeNi is dominated by dislocation activities. Analysis of diffraction and microscopy data shows that the deformation progresses from dislocation slip to severe entanglement, where a sharp increase in dislocation density is observed.

d. "Stroboscopic time-of-flight neutron diffraction during cyclic testing using the event data recording system at J-PARC", by Takuro Kawasaki et al. [4]. A time-resolved time-of-flight neutron diffraction technique to characterize the structural properties of materials during cyclic tests has been developed for the neutron diffractometers at J-PARC. Using this technique, diffracted neutrons and the applied cyclic conditions are recorded as event data together with time information. The developed technique enabled the collection and processing of diffraction data for all levels of the applied electric field, as opposed to only the highest and lowest levels.

e. "High stereographic resolution texture and residual stress evaluation using time-of-flight neutron diffraction", by Pingguang Xu et al. [5]. Pole figure evaluation of a limestone standard sample with a well-known texture suggested that the precision obtained for texture measurement is comparable to that of the established neutron beamlines utilized for texture measurement, such as the HIPPO diffractometer at the Los Alamos Neutron Science Center (New Mexico, USA) and the D20 angle-dispersive neutron diffractometer at the Institut Laue–Langevin (Grenoble, France). A high-strength martensite–austenite multilayered steel was employed for further verification of the reliability of simultaneous Rietveld analysis of multiphase textures and macro stress tensors.

3. New sample environmental devices

To understand the mechanism of grain refinement of metallic materials by thermo-mechanical process, our collaborators from Kyoto University developed a compressive loading device equipped with an induction heating system, called the thermec-mastor, enabling heating and cooling with fast rates (30 K/s), as well as a fast deformation rate (100 mm/s) [6]. The loading axis of the thermec-mastor can be, however, aligned vertically, measuring only the scattering vectors parallel to the radial direction of specimen. On the other hand, changes in the lattice parameters in the loading direction of the specimen are crucial to explore the internal stresses, as well as atomic partitioning during thermo-mechanical processes. To answer these demands, we developed a new sample environmental device for horizontal loading equipped with an induction heating system. The sample area of the new sample environmental device is shown in Fig. 2. The new device is still under commissioning.

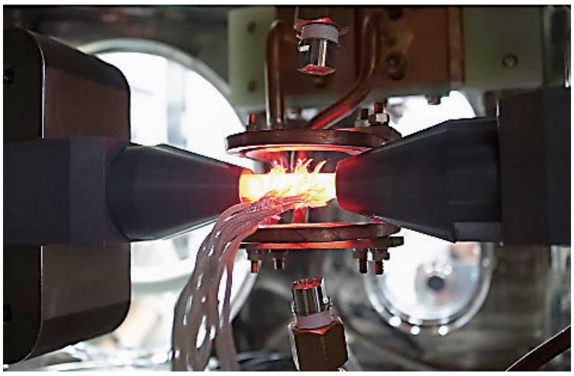

Figure 2. The sample area of a new sample environmental device for horizontal loading equipped with an induction heating system.

4. Future plans

We have developed and/or established many sample environmental devices as well as measurement and/or analyses methods. In the future, we will focus mainly on conducting engineering research together with our collaborators and users. In the same time, we will also continue to upgrade TAKUMI, which will include introducing new devices and further method development, taking into account the trends in engineering research.

References

[1] W. Gong et al., International Journal of Plasticity **111**, 288–306 (2018).

[2] Y. Tomota, et al., ISIJ International **58**, 2125–213 (2018).

[3] B. Wang et al., Scripta Materialia **155**, 54–57 (2018).

[4] T. Kawasaki et al., Journal of Applied Crystallography **51**, 630–634 (2018).

[5] P.G. Xu et al., Journal of Applied Crystallography **51**, 746–760 (2018).

[6] A. Shibata et al., Scripta Materialia **165**, 44–49 (2018).

S. Harjo[1], T. Kawasaki[1], and K. Aizawa[2]

[1]*Neutron Science Section, Materials and Life Science Division, J-PARC Center;* [2]*Technology Development Section, Materials and Life Science Division, J-PARC Center*

The Current Status of the Versatile Neutron Diffractometer, iMATERIA

1. Introduction

Ibaraki Prefecture, local government of Japan's area where the J-PARC sites are located, has decided to build a versatile neutron diffractometer (IBARAKI Materials Design Diffractometer, iMATERIA [1]) to promote industrial applications for the neutron beam in J-PARC. iMATERIA is planned to be a high-throughput diffractometer that could be used by materials engineers and scientists in their materials development work, including chemical analytical instruments.

The applications of neutron diffraction in materials science are designed (1) to do structural analyses of newly developed materials, (2) to clarify the correlation between structures and properties (functions), and (3) to clarify the relation between structural changes and improvements of functions, especially for practical materials. A diffractometer with super high resolution is not required to achieve those goals. The match of features like intermediate resolution around $\Delta d/d = 0.15\%$, high intensity and wide d coverage is more important.

This diffractometer is designed to look at a decoupled-poisoned liquid hydrogen moderator (36 mm, off-centered) (BL20), and it has an incident flight path (L1) of 26.5 m, with three wavelength selection disk-choppers and straight neutron guides with a total length of 14.0 m. The instrumental parameters are listed in Table 1. There are four detector banks, including a low-angle and small-angle scattering detector bank. The angular coverage of each detector bank is also shown in Table 1. The rotation speeds for the disk-choppers are the same, with a pulse repetition rate of 25 Hz for most applications (SF mode). In this case, the diffractometer covers $0.18 < d$ (Å) < 2.5 with $\Delta d/d = 0.16\%$ and covers $2.5 < d$ (Å) < 800 at three detector banks of 90°, low-angle and small-angle with gradually changing resolution. When the speed of the wavelength selection disk-choppers is reduced to 12.5 Hz (DF mode), we can access a wider d-range, $0.18 < d$ (Å) < 5 with $\Delta d/d = 0.16\%$, and $5 < d$ (Å) < 800 with gradually changing resolution and doubled measurement time compared to the SF mode.

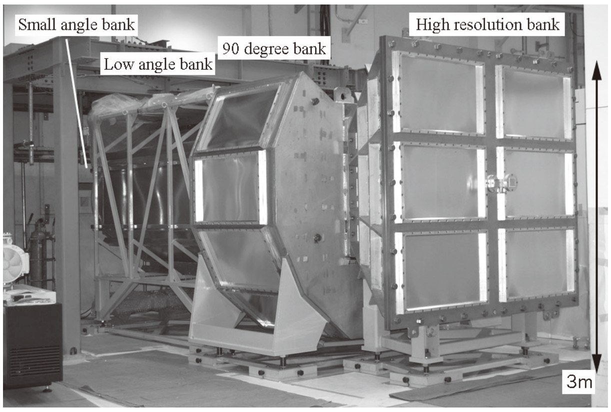

Figure 1. IBARAKI Materials Design Diffractometer, iMATERIA without detector for each bank and instrument shielding. The high-resolution bank, special environment bank (90°-bank), and low-angle bank, can be seen from right to left. The small-angle detector bank, which is not shown in the picture, is situated in the low-angle vacuum chamber (left-hand side of the picture).

Table 1. Instrumental parameters of iMATERIA. L2 is the scattered flight path. The *d*-range (*q*-range) for each bank is the maximum value for the 2-measurement mode.

L1	26.5 m	
Guide length		Total 14 m (3section)
Position of Disk choppers		7.5 m (double) 11.25 m (single) 18.75 m (single)
High-Resolution Bank	2θ	$150° \leq 2\theta \leq 175$
	L2	2.0 – 2.3 m
	d-range	$0.09 \leq d$ (Å) $\leq 5.0°$
Special Environment Bank	2θ	$80° \leq 2\theta \leq 100°$
	L2	1.5 m
	d-range	$0.127 \leq d$ (Å) ≤ 7.2
Low-Angle Bank	2θ	$10° \leq 2\theta \leq 40°$
	L2	1.2 – 4.5 m
	d-range	$0.37 \leq d$ (Å) ≤ 58
Small-Angle Bank	2θ	$0.7° \leq 2\theta \leq 5°$
	L2	4.5 m
	q-range	$0.007 \leq q$ (Å^{-1}) ≤ 0.6

2. Current status

All four banks, high-resolution bank (BS bank), special environment bank (90° bank), low-angle bank and small-angle bank, are operational. It takes about 5 minutes (in DF mode) to obtain a 'Rietveld-quality' data in the high-resolution bank at 500-kW beam power for about 1 g of standard oxide samples.

Figure 2 shows a typical Rietveld refinement pattern for a $LiCoO_2$ sample, cathode material for lithium ion batteries (LIB), at the high-resolution (BS) bank by the multi-bank analysis function of Z-Rietveld [2]. It takes 20 min in DF mode to collect the available

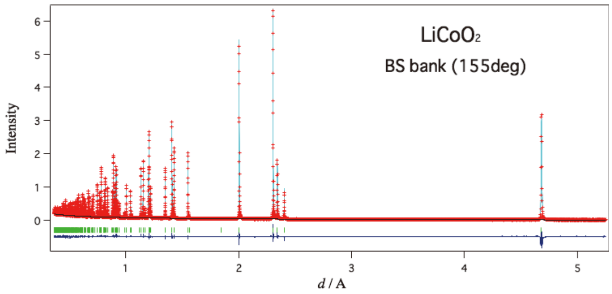

Figure 2. Rietveld refinement pattern for $LiCoO_2$ at the high-resolution bank of iMATERIA.

Rietveld data, due to the high neutron absorption cross section for natural Li ($\sigma_s^{Nat} = 70$ barn).

3. Sample Environments

The automatic sample changer is the most important sample environment for high-throughput experiments. Our automatic sample changer [3] consists of a sample storage, elevating system of two lines, two sets of pre-vacuum chambers and a sample sorting system. We can handle more than 600 samples continuously at room temperature without breaking the vacuum of the sample chamber.

The V-furnace (~900°C), the gas-flow furnace (~1000°C), the cryo-furnace (4K) and the 1K cryo are ready for experiments. The in-operando experiment system for LIB with a sample changer is available in cylindrical and coin types of batteries.

The rapid heating/quenching furnace with an automatic sample changer (RT – 1273 K with heating speed 10 K/s and cooling speed >20 K/s) and the universal deformation testing machine (max loading 50kN with RT – 1273 K) are available for texture measurement.

References

[1] T. Ishigaki et al., Nucl. Instr. Meth. Phys. Res. A **600** (2009) 189–191.
[2] R. Oishi et al., Nucl. Instr. Meth. Phys. Res. A **600** (2009) 94–96.
[3] A. Hoshikawa et al., J. Phys.: Conf. Ser. **251** (2010) 012083.

T. Ishigaki, A. Hoshikawa, T. Matsukawa, and Y. Onuki
Frontier Research Center for Applied Nuclear Sciences, Ibaraki University

Online Analysis System for NOVA

1. Introduction

The High-intensity neutron total diffractometer (NOVA) is able to measure the static structure factor $S(Q)$ with high precision in a very short time. The pair-distribution function $G(r)$ derived from the Fourier transform of the $S(Q)$, is used for the structure analysis of disordered materials, such as liquid, glass, amorphous and so on. The expected neutron intensity at NOVA is approximately 0.34×10^8 neutrons/s·cm^2·MW [1], and as common use, the neutron intensity is the most intense at MLF. NOVA is a wide-*Q* range machine to measure disordered material structures and is also a high-intensity powder diffractometer to measure crystalline material structures ($\Delta Q/Q \sim 0.35\%$). To figure out the experimental status at NOVA, an online monitor is a very useful tool. We developed a new online monitor modified with the current data acquisition (DAQ) system. In this report, we will describe the new tool.

2. DAQ-Middleware

DAQ-Middleware (DAQ-MW) [2] is a framework to realize the DAQ system in a network distributed environment easily and is standard DAQ software at MLF. DAQ-MW is able to integrate some DAQ machines in a network distributed environment. DAQ-MW is based on Robot Technology (RT) Middleware [3]. Users can customize the system configuration according to their requirements. The typical system configuration for DAQ-MW is shown in Fig. 1. DAQ-MW consists of a management part, including Daq Operator, and a function part, which includes a Gatherer component, Dispatcher component, Logger component and Monitor component. The functions of each component are shown in Table 1. Each component is designed as a state machine, and defined system control actions depending on the statements ('Load', 'Configure', 'Running', 'Pause'). The transition between the statements is carried out by control commands such as 'Configure', 'Unconfigure', 'Begin', 'End', 'Pause' and 'Resume'. DAQ components are connected with its input and output ports, for instance, the simplest DAQ system, which is constructed from Gatherer and Logger components, is can be created. The data transportation between the DAQ components is supported by Common Object Request Broker Architecture (CORBA) [4]. Since CORBA has a common interface definition language, it makes possible the data transportation between different computer languages and different operating systems. In general, since CORBA's processing overhead is bigger , the data transportation is less effective than that of Transmission Control Protocol and Internet Protocol (TCP/IP). By increasing the data size at one time, the performance will become closer to that of TCP/IP. DAQ-MW has two types of the parameter-set algorithm, and some parameters are written in parameter

Table 1. The functions of each component.

Gatherer	Connecting with read-out modules
Dispatcher	Splitting data flow
Logger	Data logging on the storage
Monitor	Online data processing

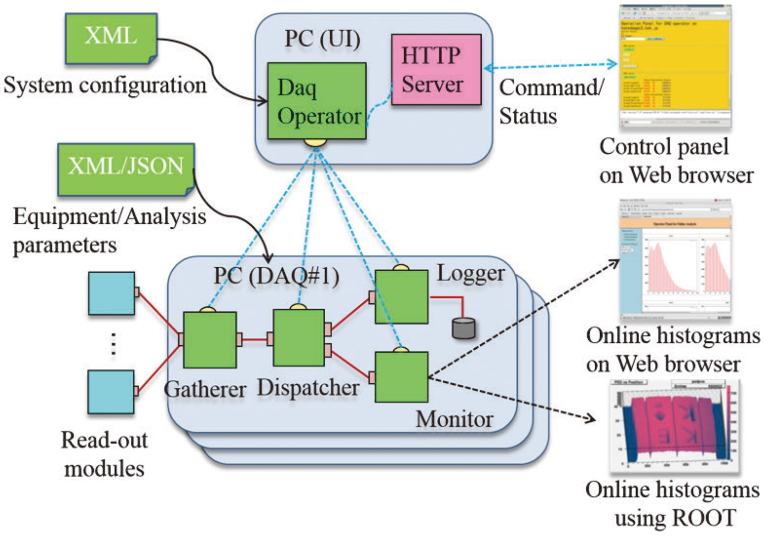

Figure 1. The typical system configuration for DAQ-MW.

files as Extensible Markup Language (XML) or JavaScript Object Notation (JSON). Those parameter-set algorithms are distinguished by the frequency of use. The system configuration will be set at one time when the DAQ machine restarts. On the other hand, the equipment and analysis parameters will be set after every 'Configure' statement. Since DAQ-MW has a Graphical User Interface (GUI) control panel, which runs on a web browser, we can control DAQ-MW via the network.

3. Improvement of DAQ-MW

Though DAQ-MW has been stably working at NOVA for several years, there are still some weak points in the online data processing. Since DAQ-MW is a tightly coupled system connected with some DAQ components, it is good at treating some regular tasks and not suitable to deal with an irregular task, such as a histogram drawing which is increasing CPU load gradually. Therefore, once Monitor component takes a long time to draw a histogram, the DAQ system will be down because of block data flow. Thus far, the measurement data has been usually decimated to keep the stability of the DAQ system during the online data processing. In order to monitor the experimental status within a short time, online data processing for all data (Live Data Reduction: LDR) is required. In the other large facility such as SNS and ESS, the development of LDR has already started. Therefore, we also started to develop a loosely coupled system to overcome our weak points. For our purpose, we applied redis [5] which can create Key-Value Store (KVS). Since KVS has a simple data structure of 'Key' and 'Value', it's useful to construct a database, which meets the requirement for handling a huge amount of data. A redis server works fast on computer memory. The data types such as a string type, a list type and so on, are used as a data type of 'Value'. And redis supports several computer program languages, such as C/C++, Python, Ruby and so on. Since redis is an open source program, the installation cost will be minimal. A redis server is used not only as a simple queue server (queue model), but also as a broker for publish-subscribe model. The typical usage of a redis server is shown in Fig. 2. The queue model is corresponding to one-to-one connection system, and some data setting into a redis server are kept until picking up. The stored data size is limited by the amount of computer memory. On the other hand, the publish-subscribe model is corresponding to an N-to-N connection system, if no subscribers are registered, the published data will be erased. As shown in Table 2, since the publish-subscribe model is also a spatially, temporally and synchronously separated system, those characteristics play an important role in improving the online data processing capability.

The new system configuration for DAQ-MW is shown in Fig. 3. Two new DAQ components, Publisher and DaqInfoPublisher, which use redis publish-subscribe model, have replaced the old Monitor component. The Publisher component publishes measurement data from the readout modules to a redis server. The DaqInfoPublisher component publishes the DAQ status, such as 'Begin', 'End' and so on to a redis server. A redis server, which is regarded as a large scale and fast

Table 2. The characteristics of redis publish-subscribe model.

Spatially	A publisher and a subscriber can be located anywhere in the network.
Temporally	Anytime, a publisher is able to publish, and a subscriber is able to subscribe.
Synchronously	A publisher and a subscriber can register and leave.

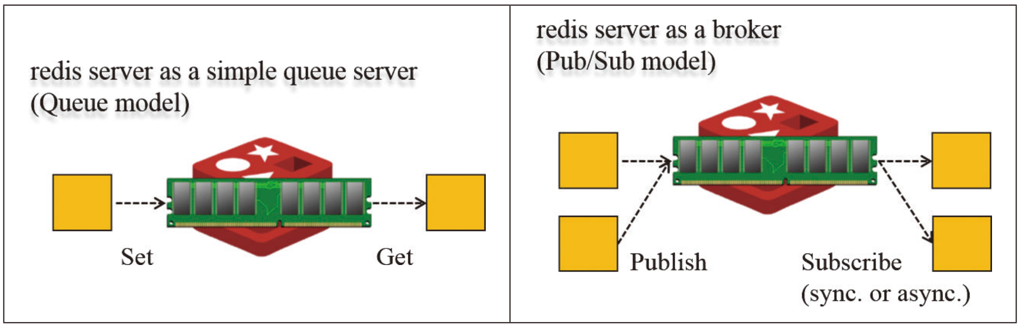

Figure 2. The typical usage of a redis server: (left) queue model, (right) publish-subscribe model.

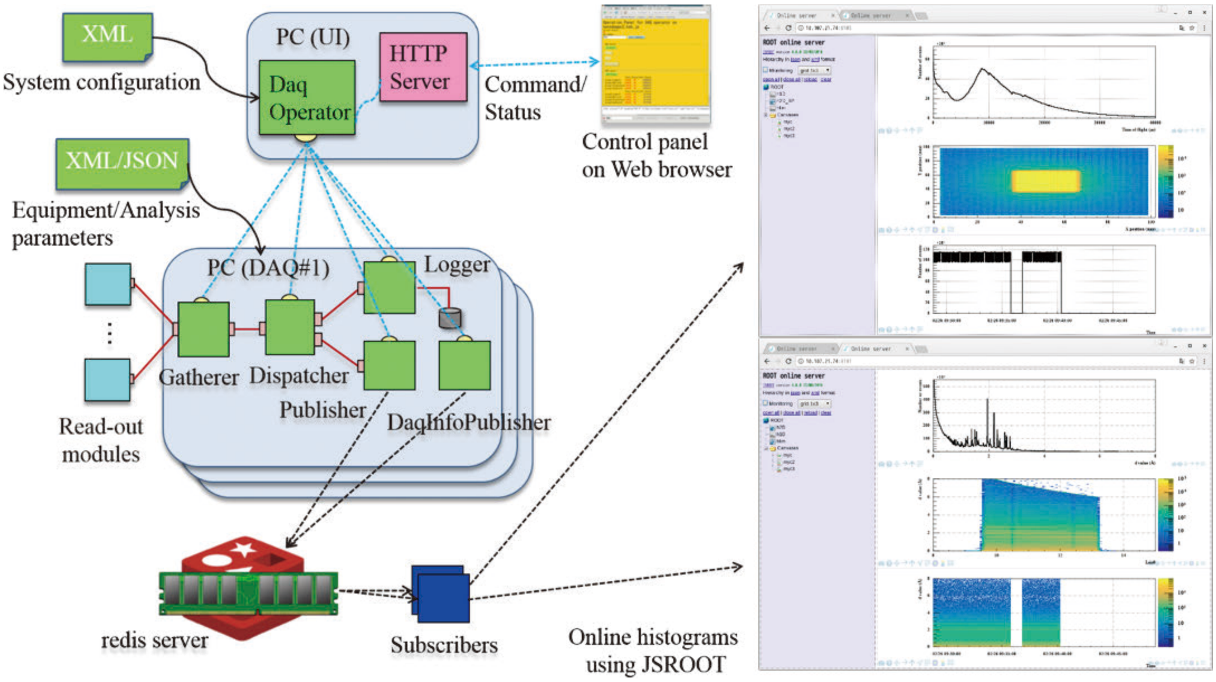

Figure 3. The new system configuration for DAQ-MW.

data buffer, plays an important role to separate clearly LDR from the DAQ system. A subscriber program subscribes some information, such as measurement data and the DAQ status, from a redis server. And a subscriber, which is the core program of LDR, is able to operate a higher CPU load task without blocking the DAQ system. Since a subscriber program obtains the DAQ status from a redis server, the DAQ system and a subscriber program works synchronously. The simple online monitor is created by JSROOT [6]. The time-of-flight distributions, the beam profile, the trend graphs and so on are displayed in the simple online monitor. Users can access the simple online monitor via network, and then obtain images of some histograms, change display conditions, and read statistic information.

Acknowledgement

This work was performed under the S1-type program (2014S06) approved by the Neutron Scattering Program Advisory Committee of IMSS, KEK.

References

[1] H. Ohshita, et al., JPS Conf. Proc. **8** (2015) 036019.
[2] K. Nakayoshi, et al., Nucl. Instr. and Meth. A **623** (2010) 537.
[3] Object Management Group, Specification of Robotic Technology Component (RTC), Version 1.0, http://www.omg.org/spec/RTC/1.0/.
[4] web page of CORBA, http://www.corba.org.
[5] web page of redis, http://redis.io.
[6] web page of JSROOT, https://root.cern.ch/js.

H. Ohshita[1,2], K. Ikeda[1,2,3], T. Honda[1,2,3], T. Otomo[1,2,3,4], Y. Yasu[1], T. Seya[1,2], N. Kaneko[1,2], K. Suzuya[2], S. Sashida[3], and M. Tsunoda[4]
[1]*Institute of Materials Structure Science, KEK;* [2]*Neutron Science Section, Materials and Life Science Division, J-PARC Center;* [3]*SOKENDAI;* [4]*Graduate School of Science and Engineering, Ibaraki University*

Status of the Energy-Resolved Neutron Imaging System RADEN

1. Introduction

The energy-resolved neutron imaging system "RADEN", installed at beamline BL22 in the Materials and Life Science Experimental Facility (MLF) of J-PARC, is a dedicated instrument for conducting wavelength/energy-dependent neutron imaging experiments with full utilization of the short-pulsed neutron's nature, such as broad available neutron energy range and narrow pulse shape [1]. RADEN has the capabilities to conduct the energy-resolved neutron imaging techniques, such as Bragg-edge, neutron resonance absorption, and polarized pulsed neutron imaging. In addition, the wavelength dependence analysis has been combined with the neutron phase imaging based on a Talbot-Lau interferometer by using pulsed neutrons [2]. In this report, we will cover the current status of RADEN's activities, including technical developments and application studies.

2. User programs

RADEN is accepting about 30 user programs every year, and more than half of them are using the energy-resolved neutron imaging technique. Especially the strain distribution measurement in metallic alloy samples made by the additive manufacturing technique is one of the increasing application studies of Bragg edge imaging. In addition, intensive developments in combining computed tomography and energy-resolved imaging have been carried out. Also, visualization of three-dimensional strain distribution in a deformed steel sample [3, 4] and magnetic field strength and direction generated in a small solenoid coil [5, 6] have been done. Another application that attracts attention is in-situ observation of the crystal growth process. Owing to the high penetration power of neutrons, it is possible to observe the solid/liquid interface directly through the furnace and to control the interface shape precisely during the observation, which is important in producing a high-quality crystal without defects or composition inhomogeneity [7]. Moreover, the neutron resonance absorption technique helps to quantitatively visualize the distribution of dopant element during the growth. This study is expected to accelerate the decisions necessary to make during the crystal growth process.

On the other hand, the demand for neutron imaging of objects, including large neutron absorption elements like Boron, has been increasing recently. Because RADEN can provide enough neutron intensity with energy larger than 1 eV, it is possible to obtain good transmission for such an object. To fulfil those requests, we conducted epi-thermal neutron imaging with parking the T0 chopper open and inserting Cd filter in the beam path to eliminate thermal and cold neutrons.

3. Development and improvement of the neutron imaging technique

High-spatial resolution imaging experiments have been demonstrated by means of the center-of-gravity technique using an MCP detector [8]. With this high-spatial imaging mode, 16 μm spatial resolution could be obtained, which was 4 times smaller than the pixel size of MCP detector of 55 μm (Fig. 1). The same technique

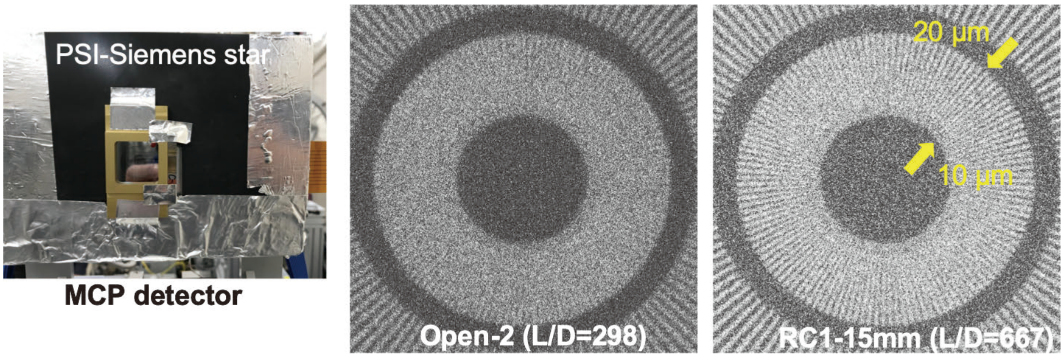

Figure 1. Results of the high-resolution imaging experiment. Photograph of the MCP detector and the test target (left), obtained image with coarse collimation (L/D=298) (center), and image with fine collimation (L/D=667) (right). It is possible to recognize the space smaller than 20 μm with a fine collimation condition.

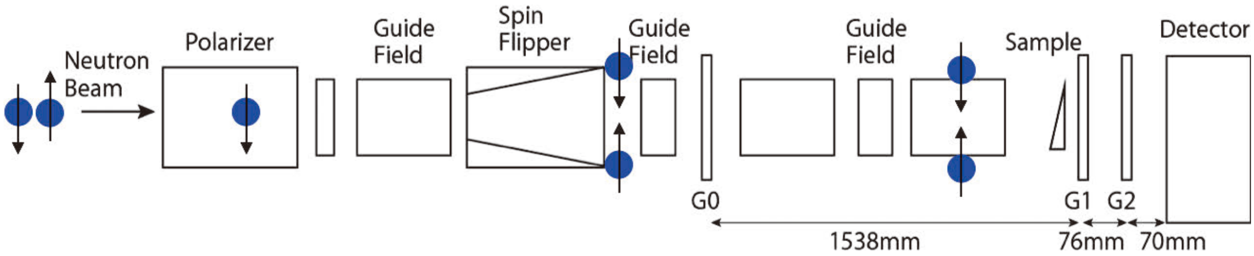

Figure 2. An illustration of polarized neutron phase imaging setup.

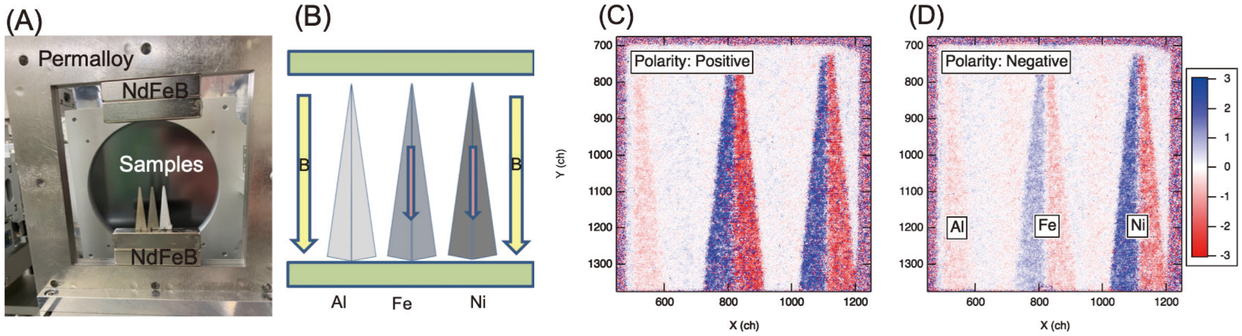

Figure 3. Results of the polarized phase imaging experiment. A photograph and a schematic illustration of samples (A), (B). Obtained differential phase image using polarized neutrons with positive spin polarity (C) and with negative spin polarity (D).

is going to be adapted to the normal neutron radiography using a CMOS camera. Next, the excessive time for a CT measurement has been improved drastically by a new dedicated measurement system composed of a pulse counter and a rotation stage controller. With this system, the required communication time between the control software and devices has been reduced to a few seconds. As a result, a typical CT measurement finishes in several hours.

Finally, the Talbot-Lau interferometer for the pulsed neutron phase imaging has been developed at RADEN [2]. Because a phase shift of a neutron wave depends on the neutron wavelength, the use of wavelength dependence analysis is beneficial to its accurate and precise evaluation. Moreover, the neutron phase imaging is sensitive to a magnetic field, since the phase shift occurs by optical potentials produced by nuclei and magnetic fields. Hence, we tried to use polarized neurons to detect magnetic information. Because the sign of the magnetic potential depends on the neutron polarity, unlike the nuclear potential, differential phase images obtained with flipping the spin polarity of a polarized neutron and subtracting each other enables us to extract the magnetic contribution. An illustration of the polarized neutron phase imaging set up is shown in Fig. 2. With this apparatus, we obtained successfully different contrast images by changing the neutron spin polarity for magnetic samples (Fig. 3).

4. Summary and future plans

Now, RADEN is under user operation and the application fields spread widely in both scientific and industrial disciplines. Especially the number of proposals about in-situ or in-operando observation experiments are increasing. Owing to the continuous improvement work, the basic imaging techniques become more sophisticated with every passing year. Also, we are developing new imaging techniques utilizing wavelength/energy dependence. In the near future, the energy-resolved neutron tomography is expected to become a general technique at RADEN, which visualizes the three-dimensional distribution of strain, magnetic field, elemental composition, and temperature.

Acknowledgements

This work was partially supported by the JST ERATO Momose Quantum Beam Phase Imaging Project.

References

[1] T. Shinohara et al., J. Phys: Conf. Series **746** 012007 (2016).

[2] Y. Seki et al., Europhys. Lett. **123**, 12002 (2018).

[3] J. N. Hendriks et al., Phys. Rev. Materials **1** 053802 (2017).

[4] A.W.T. Gregg et al., Phys. Rev. Applied **10** 064034 (2018).

[5] M. Sales et al., Scientific Reports **8** 2214 (2018).

[6] M. Sales et al., J. Phys. D: Appl. Phys. **52** 205001 (2019).

[7] A. S. Tremsin et al., Crystal Growth & Design **17** 6372 (2017).

[8] A. S. Tremsin et al., Nucl. Instr. Meth. A **787** 20 (2015).

T. Shinohara[1], T. Kai[1], K. Oikawa[1], M. Segawa[1], T. Nakatani[2], K. Hiroi[1], Y. Su[2], H. Hayashida[3], J. D. Parker[3], Y. Matsumoto[3], Y. Seki[1], and Y. Kiyanagi[4]

[1]*Neutron Science Section, Materials and Life Science Division, J-PARC Center;* [2]*Technology Development Section, Materials and Life Science Division, J-PARC Center;* [3]*Neutron Science and Technology Center, CROSS;* [4]*Graduate School of Engineering, Nagoya University*

On-Beam Commissioning on POLANO

1. Introduction

One of the remaining challenges in the pulsed neutron technique is the realization of polarization analysis, particularly with inelastic scattering. It is a promising technique that can be used for the recent research in the field of material science with entangled degrees of freedom. In order to accomplish advanced neutron experiments using intense pulsed neutrons at the Materials and Life Science Experimental Facility (MLF), J-PARC, POLANO has been dedicated for use as a polarization beam line. POLANO is a chopper type spectrometer with polarization analysis capability and is now under construction at the MLF [1–5]. The design and manufacture of the main components were completed by 2016. In 2016, the radiological assessment for acceptance of neutron beam was successfully conducted. Consequently, POLANO was approved as a proper neutron beam line and the on-beam commissioning process for future scientific program use has already started.

Our primary motive for designing POLANO is to achieve higher-energy polarization analysis of inelastic scattering beyond a reactor-based neutron source. A wide momentum and energy region are necessary to provide the research opportunities in the field of multiple degrees of freedom. Our final objective is to obtain up to 100 meV of the transfer energy and around 10 Å^{-1} in momentum space.

2. Spectrometer design

POLANO is located at BL23 in MLF, viewing the hydrogen decoupled moderator. The geometrical parameters of the spectrometer are as follows: distance from moderator to sample L1, distance from sample to detector L2, and distance from Fermi chopper to sample L3 are 17.5 m, 2.0 m, and 1.85 m, respectively. In order to gain more space after the Fermi chopper, a long L3 is used, without losing much resolution. An energy resolution of ΔE / Ei = 3 to 5% and momentum resolution of ΔQ / ki = 1 to 2% were achieved. These values are sufficient for observing most of the magnetic excitations in the so-called strongly correlated electron systems, where the magnetic excitations are scaled by exchange or super exchange coupling constant J = 100 meV. A resolution of a few meV could be enough to see the detailed structures even at higher incident energy. Also, in order to observe the incommensurate structure in cuprate high-Tc superconductors, the incommensurability is in the range of a tenth in reciprocal lattice unit, which corresponds to the order of 0.1 to 0.2 Å^{-1}. The incommensurate structure can be observed separately with our resolution.

After passing the moderator, the neutrons are transported by supermirror guide tubes with m = 4, optimized for around 110 meV neutron intensity with a McStas simulation [6, 7]. An elliptical guide, which is optimized section wise (section length = 50 cm) can yield a neutron flux of 3.9×10^5 [n/sec/meV/cm^2/MW], which is almost comparable with a coupled moderator beam line at E = 100 meV.

A SEOP ^{3}He filter cell will be placed at L = 16.435 m from the moderator. The ^{3}He filter has a beam width of 8 cm at the bottom, and 4 cm at the half height. In the early stages, ^{3}He cells with a diameter of 5 cm will be used, because the ^{3}He polarizing technique has already been established for 5 cm cells [8].

3. On-beam Commissioning

In 2018, we started on-beam commissioning on POLANO in order to evaluate all the devices and instruments and ensure that they operate properly. Figure 1 depicts the neutron beam cross section at POLANO sample position both simulation (left) and measurement (right). In the left upper panel different values of neutron energy from 5 to 200 meV were taken into account for the simulation. The lower panel depicts

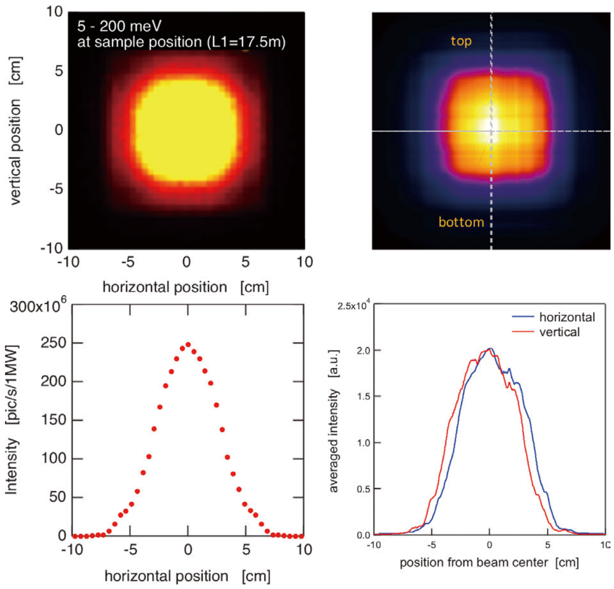

Figure 1. (left) Simulated beam cross section at sample position. (right) Measured neutron intensity by imaging plate.

one-dimensional integrated intensity along horizontal position. Comparison of the simulation and measurement data shows that the 1D peak profiles are very similar to each other. The peak width of the measured 1D peaks on both horizontal and vertical can be well reproduced by the simulation. Transportation designing with 4 Qc supermirror guide tube is, thus, successfully tested by using neutron beam. The transported neutron intensity (absolute flux) is measured in two different ways: by using gold foil, and also using ^{3}He detectors. The corrected values of these two absolute fluxes are evaluated 1.58×10^8 and 3.3×10^8 [n/cm^2/s/MW] for gold-foil and ^{3}He detectors, respectively. The neutron energy dependence of the measured flux is in good agreement with that calculated by McStas Monte Carlo simulation. Thus, the neutron transportation ability on POLANO is assessed by on-beam test as we expected on guide tube designing.

Figure 2 shows the neutron scattering data measured on a real material $CsVCl_3$, which is known as a one-dimensional (1D) quantum spin magnet. $CsVCl_3$ has S = 3/2 spins arranged antiferromagnetically along c-direction. Those spins are 3D ordered at low temperature T_N = 13.3 K [9,10]. In order to see the dynamics of the 1D spin chains, the inelastic spectrum at T = 20 K was measured with "unpolarized" neutrons. In addition to the phononic excitation lying at lower energy, a clearly observed palm tree structure originated from magnetic 1D chains at Q_{1D} = 1.0 and 3.0, which corresponded to the 1D magnetic first and second Brillouin zone center.

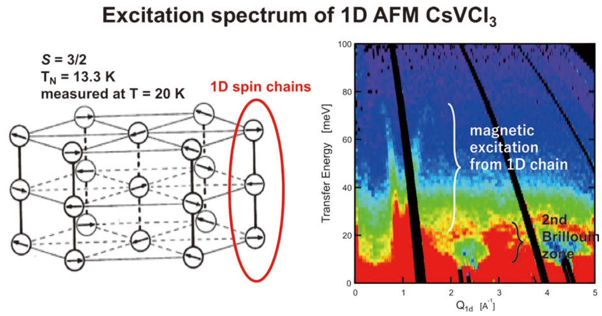

Figure 2. The first inelastic signals by the POLANO spectrometer.

4. Future plans

We have to seriously consider unexpected contaminations (background) when analyzing the data. We plan to install a direct beam catcher, and collimators to reduce that accidental scattering. Polarization analysis is of course the main purpose of this instrument. We are continuing our efforts to make possible the polarization experiments in the near future. R&D of the crucial devices as SEOP polarizer and magnetic guide field system are now in the final stage of installation at the beam line [11].

References

[1] T. Yokoo, et. al., J. Phys. Soc. Jpn. **82** (2013) SA035.
[2] K. Ohoyama, et. al., J. Phys. Soc. Jpn. **82** (2013) SA036.
[3] T. Yokoo, et. al., Journal of Physics Conf. Series **502** (2014) 012046.
[4] T. Yokoo, et. al., EPJ Web of Conferences **83** (2015) 03018.
[5] T. Yokoo, et. al., AIP conference proceedings **1969** (2018) 050001.
[6] K. Lefmann and K. Nielsen Neutron News **10/3** (1999) 20.
[7] P. Willendrup, E. Farhi, K. Lefmann, Physica B **350** (2004) 735.
[8] T. Ino, et. al., ibid.
[9] H. Kadowaki, et. al., J. Phys. Soc. Jpn. **52** (1983) 1799.
[10] S. Itoh, et. al., Phys. Rev. Lett. **74** (1995) 2375.
[11] N. Kaneko, et. al., ibid.

T. Yokoo[1,2], N. Kaneko[1,2], Y. Ikeda[3], S. Itoh[1,2], M. Fujita[3], M. Ohkawara[3], T. Ino[1,2], and K. Hayashi[1]
[1]Neutron Science Section, Materials and Life Science Division, J-PARC Center; [2]Institute of Materials Structure Science, KEK; [3]Institute for Materials Research, Tohoku University

^{3}He Neutron Spin Filter Cells

1. Introduction

A polarized ^{3}He neutron spin filter (NSF) is a key component in POLANO [1]. An *in-situ* polarized ^{3}He NSF functions as the incident neutron beam polarizer, where ^{3}He gas is continuously spin-polarized on the instrument by spin-exchange optical pumping (SEOP) to obtain steady neutron beam polarization. Another polarized ^{3}He gas will be employed for the spin-analysis of the scattered neutrons on the next stages of the POLANO project. To achieve the best quality of neutron polarization or neutron spin-analyzing power, the highest ^{3}He polarization as well as a very long spin relaxation time of polarized ^{3}He gas is of great importance. One of the crucial techniques in ^{3}He gas polarization by SEOP is manufacturing of high quality ^{3}He gas container cells.

In SEOP, alkali metal atoms are polarized by optical pumping, and the angular momentum of polarized alkali atoms is transferred to ^{3}He nuclei by hyperfine interaction [2]. The alkali metals are confined in a container cell with ^{3}He gas, and the cell is heated to 200–250°C to maintain appropriate alkali number density. Listed below are some of the essential requirements for such SEOP cells:

(1) Transparent to the optical pumping light.
(2) Transparent to neutrons.
(3) No helium leakage.
(4) No magnetic impurities.
(5) Alkaline resistant in high temperatures.
(6) Tolerate high pressure.

Aluminosilicate glass containing no boron can be the only candidate material for SEOP cells today. Single crystals [3] or transparent ceramics can be an alternative choice, but cells made of these materials can hardly satisfy all the requirements.

2. Fabrication of GE180 cells

We use a type of aluminosilicate glass named GE180 to fabricate SEOP cells. This aluminosilicate glass fulfills all the above requirements, and almost all the SEOP cells used today all over the world are made of this material. Spin-relaxation times of polarized ^{3}He gas in GE180 cells can occasionally approach the theoretical limit; ^{3}He polarizations of more than 80% are regularly achieved. The only drawback of using GE180 is glassblowing, which is very difficult to work with. Compared to Pyrex, commonly used glass in scientific researches, the softening temperature of GE180 is higher, and the working temperature range, where the glass keeps appropriate viscosity for glassblowing, is narrower.

We have been making SEOP cells using GE180 in a collaboration between J-PARC and Tohoku University. Shown in Fig. 1 is one of our SEOP cells, glassblowing by Mr. Tomomi Kudo of Tohoku University (Fig. 2) and ^{3}He gas filling at KEK. The cell contains ^{3}He gas of 3.4 atm to polarize 100 meV neutrons. The glass cell was designed using the finite element method so as to withstand an internal gas pressure of >6 atm, which is expected during the optical pumping at 250°C.

A blown GE180 cell is attached to the string part made of Pyrex that is to be connected to a high vacuum system for the gas filling (Fig. 3). GE180 and Pyrex tubes are connected together using glasses that have thermal expansion coefficients between those of GE180

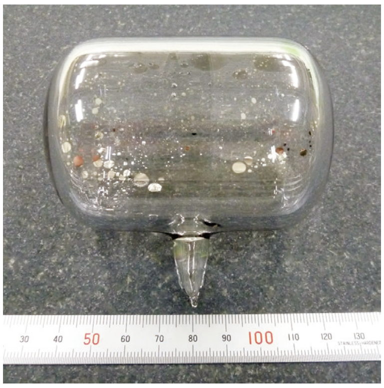

Figure 1. A cylindrical shape ^{3}He SEOP cell made of GE180 with ^{3}He gas of 3.4 atm and alkali metals inside. The shiny metallic spots are a mixture of rubidium and potassium.

Figure 2. GE180 cells are fabricated at the IMRAM glass workshop of Tohoku University.

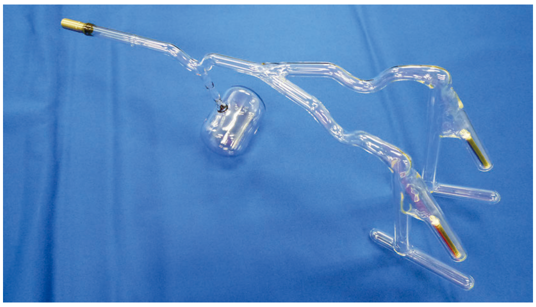

Figure 3. A GE180 cell with the string part.

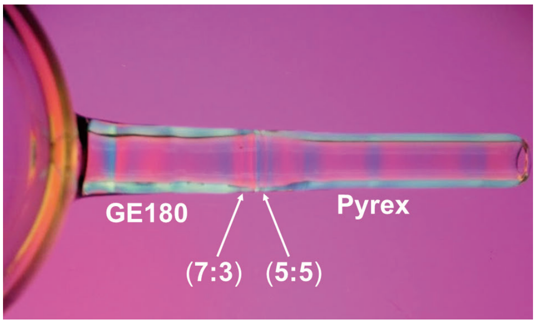

Figure 4. Connection of GE180 and Pyrex tubes.

and Pyrex to reduce the residual stress. The connecting glasses are prepared by mixing GE180 and Pyrex at ratios of 7:3 and 5:5 and placed between the two tubes (Fig. 4). The use of these connecting glasses significantly suppresses cell failures.

3. Gas filling

A GE180 cell with the string is thoroughly cleaned and then connected to a high vacuum system at KEK. They are baked out until the pressure reaches the minimum. The alkali metals are then evaporated and chased into the GE180 cell using heaters. Finally, the cell is filled with a small amount of nitrogen gas and ^{3}He gas through heated getter gas purifiers and sealed off using a gas torch. For a ^{3}He cell with a gas pressure of >1 atm, the cell is soaked into liquid nitrogen during the tip-off. Up to 3.6 atm of ^{3}He gas can be filled with liquid nitrogen. The whole gas filling process takes a few weeks.

4. What's next?

We have been making cylindrical shape ^{3}He cells using GE180. The next milestones are the enlargement of the cell diameter to expand the usable neutron beam size, the increase of the pressure resistance to boost the polarizable neutron energies, and achieving the longest spin relaxation time for the *ex-situ* applications, where ^{3}He gas is not polarized in the instrument, but a polarized ^{3}He cell is transported from an optical pumping station in a laboratory to the neutron beamline, which considerably simplifies the ^{3}He NSF apparatus.

Another important demand is the spin analysis of scattered neutrons. POLANO covers a wide solid angle for scattered neutron detection, and the same angle coverage is desired for the spin analysis. A horseshoe-shaped or doughnut-shaped ^{3}He cell will cover such a wide scattering angle [4, 5] though it is extremely difficult to fabricate.

An alternative direction of the spin-analyzer development can be a double chamber cell. It consists of two chambers connected together with a gas transfer tube; one chamber is for the optical pumping, and the other for the NSF. A ^{3}He gas is polarized in the optical pumping chamber, and the polarized ^{3}He gas diffuses into the NSF chamber. The advantage of using a double chamber cell is that the NSF part can be separated from the hot optical pumping chamber, yet the polarization of ^{3}He is kept constant as the ^{3}He gas is continuously polarized in the optical pumping chamber.

The fabrication of GE180 aluminosilicate glass cells is an important key technique in the ^{3}He neutron spin filter development. Glass cells in various shapes and sizes will be needed for POLANO as well as for other neutron scattering measurements. The growth of the ^{3}He NSF applications depends strongly on the advances in glassblowing techniques.

References

[1] T. Ino, M. Ohkawara, K. Ohoyama, T. Yokoo, S. Itoh, Y. Nambu, M. Fujita, H. Kira, H. Hayashida, K. Hiroi, K. Sakai, T. Oku, and K Kakurai, J. Phys.: Conf. Ser. **862** 012011 (2017).
[2] T. R. Gentile, P. J. Nacher, B. Saam, and T. G. Walker, Rev. Mod. Phys. **89**, 045004 (2017).
[3] Y. Masuda, T. Ino, V. R. Skoy, and G. L. Jones, Appl. Phys. Lett. **87**, 053506 (2005).
[4] W. C. Chen *et al.*, J. Phys.: Conf. Ser. **746**, 012016 (2016).
[5] E. Babcock *et al.*, AIP Conf. Proc. **1969**, 050005 (2018).

T. Ino[1,2], T. Kudo[3], Y. Ikeda[4], Y. Ohkawara[4], M. Fujita[4], T. Yokoo[1,2], S. Itoh[1,2], and N. Kaneko[1,2]
[1]*Neutron Science Section, Materials and Life Science Division, J-PARC Center;* [2]*Institute of Materials Structure Science, KEK;* [3]*Institute of Multidisciplinary Research for Advanced Materials, Tohoku University;* [4]*Institute for Materials Research, Tohoku University*

Magnetic Devices and Environment for Polarization Experiment on POLANO

1. Introduction

Although the polarized neutron spectrometer, POLANO, is still under commissioning, a part of the user program was opened for public use with unpolarized neutron experiments. POLANO is a chopper type spectrometer originally designed with polarization analysis capability [1–5]. Our primary motive for designing POLANO is to achieve higher-energy polarization analysis of inelastic scattering beyond a reactor-based neutron source. A wide momentum and energy region is necessary for physics in multiple degrees of freedom. Our final goal is to realize polarization experiments up to 100 meV of the transfer energy and around 10 Å^{-1} in momentum space.

The total polarization system on POLANO is now under development, specifically, the development of a spin exchange optical pumping (SEOP) spin filter used for a polarizer, and a magnetic field system. Both are now in the process of off-line testing. The magnetic field system involves magnetic guide fields for maintaining spin polarization, Helmholtz coil system for applying a magnetic field on a sample, and analyzer mirror. Last year, we reported on the newly developed cooling system for the Helmholtz coil system [6]. In this report, we present the follow-up magnetic field measurement test results of the system.

2. Magnetic field system

The magnetic field system being installed in the beam line of POLANO is combined with several magnetic devices such as, permanent magnets before the Fermi chopper, a solenoid coil in the SEOP system, a vertical guide field, Helmholtz coil system, permanent guide field after the sample, and a magnetic yoke of analyzer mirror. The Helmholtz coil system is composed of three magnetic coils for applying horizontal magnetic fields and a pair of coils for applying vertical magnetic fields. Since the three horizontal magnetic coils are positioned triangularly in the horizontal plane, applying magnetic field can be controlled by tuning the current of each coil.

We conducted the magnetic field measurement tests with a three-dimensional (3D) probe in order to check accurately the applied magnetic field on the sample. The system will be used in a large vacuum chamber of POLANO, precisely controlling the magnetic field by changing the electric current of the Helmholtz coils. The test probe with a mechanical translation system to measure the magnetic field at entire positions in the coils was developed as shown in Fig. 1.

By tuning the current ratio, the magnetic field direction can be controlled three-dimensionally in the range of ±50 Gauss. Figure 2 shows the results of measured magnetic moments (dotted signals) at various positions from the sample ($x = 0$). Also, the optimized alignments of the magnetic-field devices were evaluated using the finite elements method software, FEMTET, shown by lines in the figure. Figure 2(a) represents scattering angle dependence of the magnetic moments in the horizontal plane, applied to the vertical field. Position 0 in the x-axis corresponds to the sample position. The calculation by FEMTET can almost reproduce the measured results, except for deviations at large x. Near the sample position $x = 0$, where near the sample, the magnetic field is from the Helmholtz coil only. The dip in between $x = 30$ to 40, corresponds to the gap of the Helmholtz coil and the fan-shaped guide magnet (FSM). At $x = 55$ cm, the position of the FSM makes a large field again. In Fig. 2(b), measured and calculated results of the vertical height dependence are depicted in the same way. Also, the electrical current dependences are plotted in Fig. 2(c). The reason why we have small differences between measured and calculated data is currently unknown. However, the discrepancy of about 5 Gauss cannot be a serious problem for the guide field. Figure 3 is a horizontal field result plotted similarly to the vertical. In this measurement, there are some differences between calculated and measured results at the Helmholtz and FSM position. Again, the differences do not much affect neutron spin polarization.

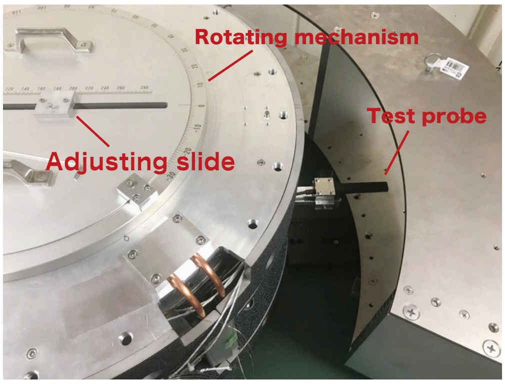

Figure 1. Newly developed test probe flange. The probe can be translated by adjusting the slide and rotation mechanism. Radial: from sample position to 600 mm, rotation angle: from beam center to 120 degrees, height: from beam center to ±30 mm.

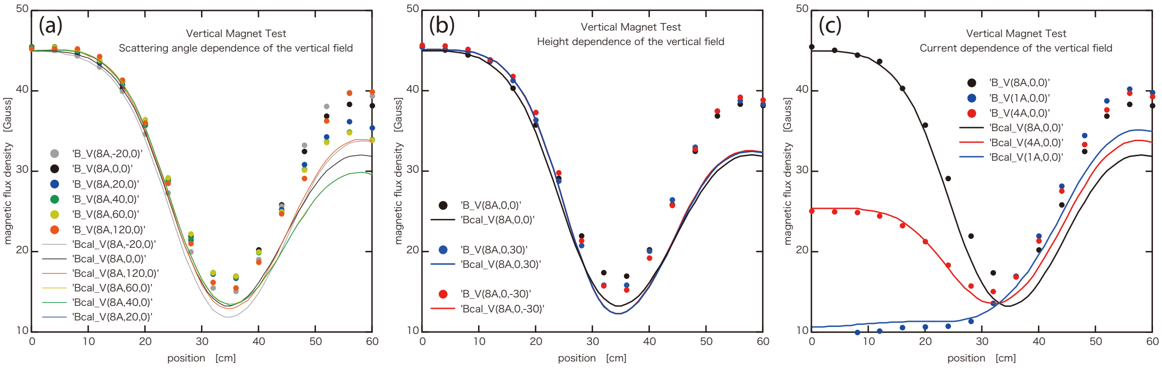

Figure 2. (a) Scattering angle dependence (current: 8 A, scattering angle: −20 to +120 deg., height: beam center). (b) Height dependence (current: 8 A, scattering angle: 0 deg., height: −30, 0, 30 mm). (c) Current dependence (coil current:1, 4, and 8 A, scattering angle: 0 deg., height: 0 mm)

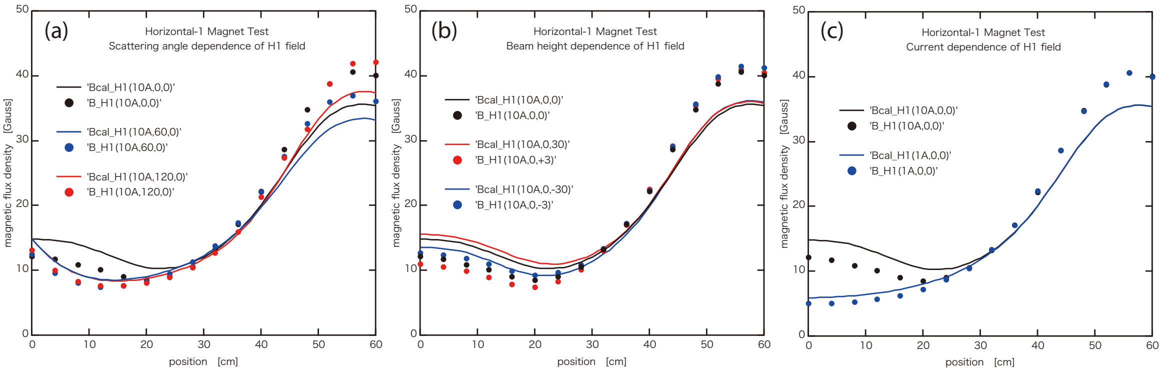

Figure 3. (a) Scattering angle dependence (current: 10 A, scattering angle: 0 to 120 deg., height: beam center). (b) Height dependence (current: 10 A, scattering angle: 0 deg., height: −30, 0, +30 mm). (c) Current dependence (coil current: 1 and10 A, scattering angle: 0 deg., height: 0 mm)

Through this series of tests, we concluded that the calculation using FEMTET can evaluate with high precision the magnetic field with POLANO magnetic condition.

3. Future installation into beam line

Based on this test, we can control applied magnetic field by YUI device control program. Now, the system is under safety assessment by MLF. The whole system will be eventually installed in the beam line, and the polarization commissioning will start soon thereafter.

References

[1] T. Yokoo, K. Ohoyama, S. Itoh, J. Suzuki, K. Iwasa, T.J. Sato, H. Kira, Y. Sakaguchi, T. Ino, T. Oku, K. Tomiyasu, M. Matsuura, H. Hiraka, M. Fujita, H. Kimura, T. Sato, J. Suzuki, M. Takeda, K. Kaneko, M. Hino, S. Muto, J. Phys. Soc. Jpn. **82** (2013) SA035.

[2] K. Ohoyama, T. Yokoo, S. Itoh, J. Suzuki, K. Iwasa, T.J. Sato, H. Kira, Y. Sakaguchi, T. Ino, T. Oku, K. Tomiyasu, M. Matsuura, H. Hiraka, M. Fujita, H. Kimura, T. Sato, J. Suzuki, H.M. Shimizu, T. Arima, M. Takeda, K. Kaneko, M. Hino, S. Muto, H. Nojiri, C.H. Lee, J.G. Park, S. Choi, J. Phys. Soc. Jpn. **82,** (2013) SA036.

[3] T. Yokoo, K. Ohoyama, S. Itoh, J. Suzuki, M. Nanbu, N. Kaneko, K. Iwasa, T.J. Sato, H. Kimura, M. Ohkawara, Journal of Physics Conf. Series **502** (2014) 012046.

[4] T. Yokoo, K. Ohoyama, S. Itoh, K. Iwasa, N. Kaneko, J. Suzuki, M. Ohkawara, K. Aizawa, S. Tasaki, T. Ino, K. Taketani, S. Ishimoto, M. Takeda, T. Oku, H. Kira, K. Hayashi, H. Kimura, T. J. Sato, EPJ Web of Conferences **83** (2015) 03018.

[5] T. Yokoo, S. Itoh, N. Kaneko, M. Fujita, T. Ino, M. Ohkawara, K. Ohoyama, M. Sakaguchi, AIP conference proceedings **1969** (2018) 050001.

[6] M.Ohkawara et al. MLF annual report 2017, p.120–121.

N. Kaneko[1,2]**, T. Yokoo**[1,2]**, Y. Ikeda**[3]**, M. Ohkawara**[3]**, K. Hayashi**[2]**, S. Itoh**[1,2]**, and M. Fujita**[3]

[1]*Neutron Science Section, Materials and Life Science Division, J-PARC Center;* [2]*Institute of Materials Structure Science, KEK;* [3]*Institute for Materials Research, Tohoku University*

Sample Environment at MLF

1. Introduction

The sample environment (SE) team operates the beamline (BL)-common SE equipment, prepares and develops new SE equipment, and aids the users in operating the equipment. The SE team consists of 17 members: 8 from JAEA, 1 from KEK, 6 from CROSS and 2 from an outsourcing company, and is divided into sub-teams of cryogenics and magnets, high temperature, soft-matter, pulsed magnet, light irradiation, ^{3}He spin filter, and high pressure. The status and activities of the SE team in JFY2018 are summarized in this report.

2. Cryogenics and magnets

We have supported users' experiments using the SE equipment that is commonly used at several beamlines: the superconducting magnet was operated for 16 experiments, the ^{3}He cryostat for 16 experiments and the dilution refrigerator (DR) insert for seven experiments, including instrument proposals. The ^{4}He cryostat fabricated by ICEoxford had been under repair due to serious leakages found in January 2018. The cryostat was returned to our facility after finishing the repair in March 2019, and we confirmed that all the problems were solved. Note that another ^{4}He cryostat fabricated by Suzuki Shokan Co., Ltd. was introduced for users' experiments twice when the cryostat by ICEoxford was not available.

3. High temperature equipment

We have two furnaces: a niobium furnace for inelastic and quasi-elastic neutron scattering measurements, and a furnace for small-angle neutron scattering (SANS) measurements.

In JFY2018, the niobium furnace was used for two users' experiments on BL14 and BL18. On BL21, we measured the background level from the furnace, and found that it was acceptable for experiments.

We have upgraded the SANS furnace, installing a new heater, which contains B_4C shielding blocks and can cover both a small-angle detector bank and a middle-angle detector bank. From a test measurement, we found out that the background level was quite small.

4. A pulsed magnet system

In the last fiscal year, we have already developed a prototype compact and transportable pulsed magnet system for high magnetic fields of up to 30 Tesla using for the commercial liquid helium (LHe)-cooled cryostat, named 'Orange-cryostat', with a 70 mm bore (AS Scientific Products Ltd.). Although a system using cryostats can generally achieve low temperatures (i.e., below 2 K), handling LHe is relatively difficult and inconvenient.

Therefore, in this fiscal year, we are developing a new insert and a coil using a Gifford-McMahon (GM) refrigerator instead of cryostats. Even users who are not accustomed to LHe can use the pulsed magnet system, thus improving both convenience and practicality. Figure 1 shows the appearance of the pulsed magnet system, the insert and the GM refrigerator (HE-05, ULVAC, Inc.). Neutron scattering experiments using this system were tested and demonstrated at BL10. An example of an output pulsed current waveform of the coil is shown in Fig. 2. The current value at the peak is 3.6 kA at 29.2 Tesla. In this experiment, the automatic repetitive operation of this system was also confirmed to be successful.

Figure 1. The pulsed magnet system.

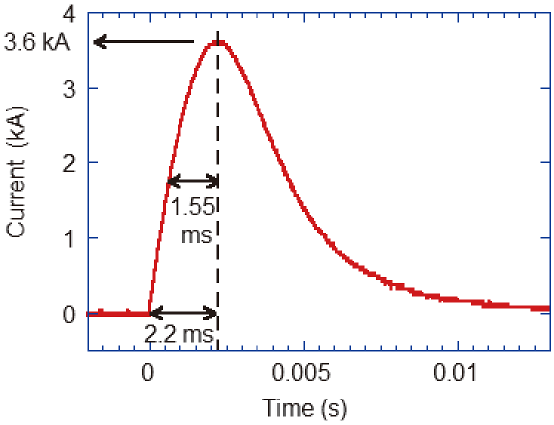

Figure 2. Example of an output pulsed current waveform.

5. Light irradiation

The mercury lamp light source of the MLF SE common equipment (REX-250, Asahi spectra) was used in the neutron reflectivity experiment for the first time. The light shutter can be controlled from the operation cabin under the device control and data acquisition system to make possible subsequent automatic measurements under different conditions.

6. ^{3}He spin filter

We have been developing a spin-exchange optical-pumping (SEOP) based polarized ^{3}He neutron spin filter (^{3}He-NSF) for efficient utilization of pulsed neutrons at J-PARC.

In JFY2018, we have completed the assembly of a ^{3}He gas filling station with a vacuum system to fill ^{3}He gas and alkali metals of Rb and K for the hybrid spin filter cells (Fig. 3). We were able to achieve vacuum pressure lower than 1×10^{-6} Pa within the filling station after baking at 250°C for stainless parts and 450°C for glass parts for almost a week. Such a level of low pressure is considered to be necessary to fabricate high-quality spin filter cells. We have also developed and introduced an electron paramagnetic resonance (EPR) and frequency sweep NMR into our ^{3}He-NSF system to monitor the polarization degree of the ^{3}He nuclear spin.

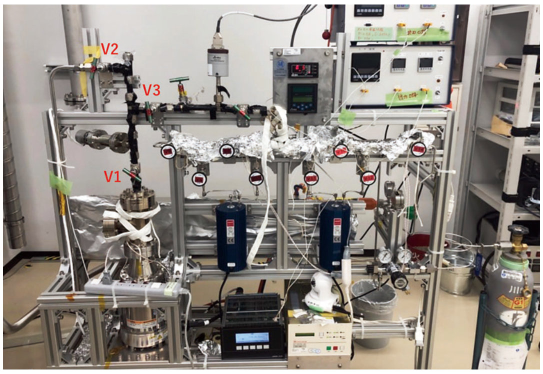

Figure 3. The assembled ^{3}He gas filling station with a vacuum system.

7. High pressure

We have constructed a low-temperature and high-pressure (LTHP) system based on the one developed by Klotz et al. [1]. The system consists of a Paris-Edinburgh (P-E) cell (VX-5) suspended from the vacuum flange equipped with a rotation goniometer and a GM refrigerator. Feasibility tests demonstrated pressure generation of 20 GPa at room temperature. Also, we succeeded in cooling to 5 K in the low-temperature generation test. When the P-E cell is precooled with liquid nitrogen, the cooling time to 5 K from room temperature is about 6.5 hours. Until 2017, we used a manual hand pump to pressurize the pressure transmission medium, but it was difficult to control the pressure for prolonged measurements. We newly installed an automatic pressure pump (Teledyne ISCO, 30D syringe pump) for precise control of the pressure. In JFY2018, we carried out an inelastic scattering experiment at BL01 using this system.

8. Soft matter tensile testing machine

We newly installed the tensile testing machine with a humidity control unit (Fig. 4). The maximum length of stroke is 100 mm, the load range from 100 N to 1 kN can be measured, and the relative humidity in the sample chamber can be changed from 0% to 85%RH. In JFY2018, we supported the research on ion exchange membranes using in-situ small-angle neutron scattering experiment at BL15 with this equipment.

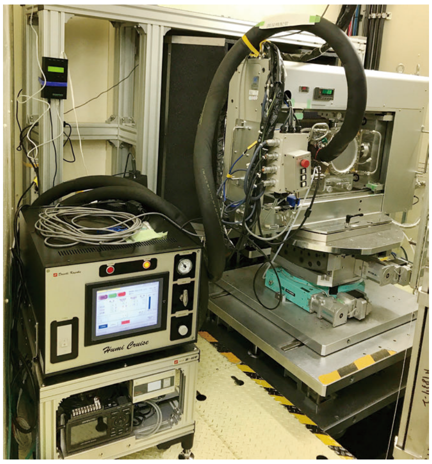

Figure 4. Tensile testing machine equipped with humidity control unit.

Reference

[1] S. Klotz et al, High Press. Res., **36**, 73 (2016).

M. Watanabe[1], T. Oku[1], R. Takahashi[1], Y. Su[1], T. Okudaira[1], T. Ino[1,2], S. Ohira-Kawamura[1,2], S. Takata[1,2], K. Sakai[1,3], M. Ishikado[4], K. Ohuchi[4], H. Arima[4], T. Morikawa[4], S. Zhang[4], Y. Sakaguchi[4], Y. Yamauchi[5], M. Nakamura[5], and K. Aizawa[1]

[1]*Technology Development Section, Materials and Life Science Division, J-PARC Center;* [2]*Neutron Science Section, Materials and Life Science Division, J-PARC Center;* [3]*Neutron Source Section, Materials and Life Science Division, J-PARC Center;* [4]*Neutron Science and Technology Center, CROSS;* [5]*Nippon Advanced Technology co.*

MLF Advanced Computational Environment

1. Introduction

The requirements of the instrument scientists and users to the infrastructure of the MLF computational environment include the following:

- Management of large volumes of data generated in MLF:
  - ➢ Making it possible to manage reliably measurement data that will increase dramatically as the proton beam power increases.
  - ➢ As the analysis becomes more intermediate, data and result data (secondary data) generated during the analysis may become very large, it is necessary to access users' data quickly and easily under the authorized access.
  - ➢ Business continuity plan (BCP) in case of a disaster.
- Support for advanced data analysis of the new measurement methods developed in MLF, such as the Multi-Ei measurement, 4D single crystal measurement, and stroboscopic measurement.

To satisfy these requests, the MLF computing group started to develop the infrastructure from FY2012. The construction of the infrastructure, called MLF Advanced Computational Environment (MLF-ACE), began in FY2017. In this article, we cover the details of the MLF-ACE installed in FY2017 – 2018.

2. Solution

The solution for the requests mentioned above is the MLF-ACE, composed of the following four components:

- Broadband and redundant network
- Large scale parallel access storage
- File sharing system
- Analysis factory

Figure 1 is the schematic view of the MLF-ACE. In FY2017 – 2018, the broadband and high availability network, a part of the large-scale parallel access storage and the file sharing system have been installed. It is a fault tolerant system. The specification of these components is shown in Table 1. In compliance with the BCP, the components in the J-PARC Research Building (JRB) are installed on the second floor.

The network includes two layers. One is the main layer and the other is a branch. The main layer is the network between the four core switches at JRB and the

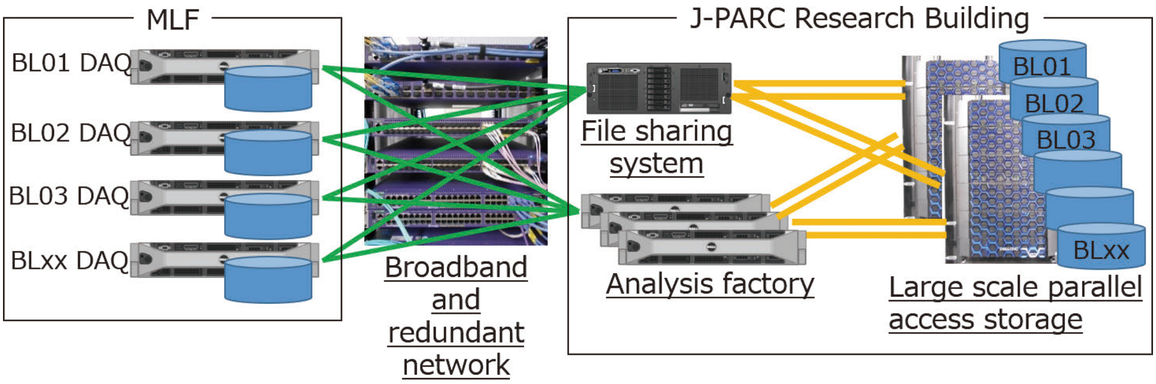

Figure 1. The schematic view of the MLF-ACE.

Table 1. Specifications of the MLF-ACE introduced in FY2017 – 18.

Component	Specifications
Network	Instruments (BL switches×27) – Aggregation switches×4 at MLF: 10 Gbps/BL Aggregation switches×4 – Core switches×4 at JRB: 40 Gbps×2 Core switch – File sharing system: 10 Gbps×4
Storage	200 TB×2 (Volume: 100 TB×4) Fiber channel switch×2 File sharing system: Metadata×2, Gateway File sharing system – Storage: 16 Gbps×4 (Fiber Channel)
Monitor	Network traffic monitoring server, Traffic visualization software

four aggregation switches at MLF. The branch layer connects the aggregation switches and 27 BL switches at each instrument including 23 neutron beamlines and four muon beamlines. The network bandwidth is broadband, which is that the main layer is double 40 Gbps and the branch layer is 10 Gbps. All network lines are wired with optical fibers except in the server room in JRB. The main layer has high availability, every core switch, aggregation switch and wire is paralleled. The paths between the switches are a cross-over connection. So, if a single failure occurs, the paths are automatically switched and the network communication continues. All switches have duplicated power supply units.

The storage consists of two units to balance the load. One unit will store the data generated with the instruments at the MLF first experimental hall, the other will be stored at the second experimental hall in parallel. Currently, one storage unit consists of two 100 TB data volumes. The storage is also redundant. In each unit, there are duplicated storage processor and Raid6 disk volumes distributed in six enclosures. The power supply units of each enclosure are also duplicated.

The file sharing system is not maintained by a software service such as NFS and something similar, but by a dedicated appliance. Currently, the appliance consists of two metadata servers and one gateway server. As the data traffic amount increases, we will be able to add gateway servers. They are connected with the storage via Fiber Channel switches. The bandwidth is 16 Gbps×4 per Fiber Channel. The connection between the core switches and the file sharing system is 40 Gbps Ethernet. All connections are also redundant.

In addition, a network traffic monitoring system has been installed. The system consists of a network traffic monitoring server and a visualization workstation with traffic visualization software. The operator can watch all network traffic in the MLF-ACE in real time.

3. Current status

In the instruments introduced at the MLF-ACE, it is possible to reduce the time allocated to data management. For example, the instrument staff currently handle the data backup for each instrument. After the MLF-ACE is installed, the data generated from the DAQ system will be stored directly in the available high-capacity storage of the MLF-ACE. Thus, because the instrument staff do not need to manage the data, they will concentrate on other tasks, such as data analysis.

4. Future plans

The DAQ system in several instruments and the storage of the MLF-ACE will be connected in FY2019. The storage will be expanded, and the analysis factory will be introduced as soon as possible. In the analysis factory Live Data Reduction will be performed. In the future, the so-called "data mining" and "Materials Informatics" methods will be applied to the data stored in the MLF-ACE.

T. Nakatani
Technology Development Section, Materials and Life Science Division, J-PARC Center

A 200-Micron Spatial Resolution Scintillation Detector for Time-of-Flight Neutron Diffraction Imaging

1. Introduction

Neutron diffraction imaging is a powerful technique to evaluate spatial distribution within materials, such as texture, grain orientation, and gain size. With a combination of a pulsed neutron source energy-selective neutron images can be measured, providing us with spectroscopic information about the transmission or diffraction spectra. More precise diffraction images can be obtained by using well defined, high-intensity pulsed neutron beam in the J-PARC MLF.

Our purpose is to develop a high-resolution, two-dimensional neutron detector for time-of-flight diffraction imaging. Although superior high-resolution detectors have been developed, such as n-MCP [1], they are not always available or do not suit perfectly our requirements. We introduce here our solution to provide such detectors with a scintillator / wavelength shifting (WLS) fiber detector technology.

2. A scintillator / WLS fiber detector

The scintillator / WLS fiber detector has a great flexibility in designing the detector head. This technique has proven to work well to develop a position-sensitive neutron detector [2, 3]. The detector specifications, such as pixel size and spatial resolution, can be designed by selecting properly tuned detector components. A two-dimensional neutron detector is required in our experiment with a spatial resolution of about 100 μm and with a neutron-sensitive area of more than 20 × 20 mm. In order to meet these requirements, the neutron-detecting head was made by using WLS fibers with a diameter of 100 μm. These fibers are specially manufactured for this purpose. Figure 1 shows a photograph of the prototype detector. In order to make fiber arrays, the WLS fibers were aligned in flat without air gap between them. Two of these fiber arrays were produced and each array contained 224 fibers. They were arranged diagonally in contact with each other, making fiber channels for x and y directions. On top of the crossed fiber arrays a single ^{6}Li:ZnS scintillator screen was implemented. The scintillator screen was grinded down to 0.17 mm to lower the light spread within the scintillator. It ensures a high spatial resolution of the detector. The detector specifications are summarized in Table 1.

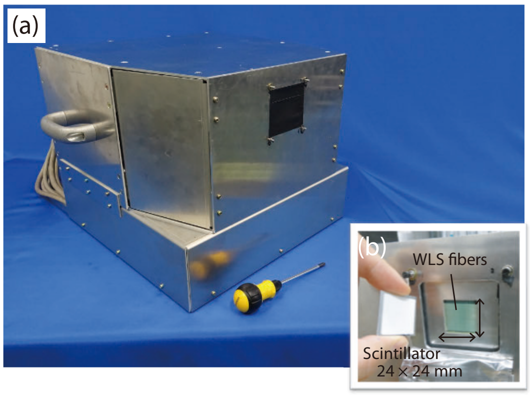

Figure 1. (a) Photograph of the 200-μm spatial resolution scintillation detector. (b) Inside view of the neutron detecting head.

Table 1. Detector specifications.

Neutron-sensitive area	: 24 × 24 mm
Pixel size	: 107 × 107 μm
Channel number	: 224 × 2 ch
No. of pixel	: 50176
Photomultipliers	: MaPMT (64 ch) × 8
Physical size	: $40^{w} \times 45^{d} \times 30^{h}$ cm
Weight	: 25 kg
Power dissipation	: 135 W

3. Detector performances

The detector performances were evaluated by using a pulsed neutron beam in the BL10 of the J-PARC MLF. In order to check the image reconstruction, the detector measured the neutron beam with a Cd cut-out mask placed on the detector window. The detector was positioned at the distance of 13 m from the moderator. Figure 2 shows (a) a photograph of the Cd mask and (b) the measured transmission image. Only the limited area shown by the dot line in (a) was irradiated with neutrons. The detector reproduced the shape of cutout letter well, confirming the proper positioning scheme of the detector system.

A spatial resolution of the detector was evaluated by measuring the beam-edge of the collimated beam. A Cd mask covered the part of the neutron-sensitive area as the mask edge was placed normal to the WLS fibers. The measured transmission profiles were then analyzed by fitting with a linear-spread function. The spatial resolutions are represented in full width at half maximum (FWHM). Figure 3 shows the measured spatial resolution in (a) x-direction and (b) y-direction for

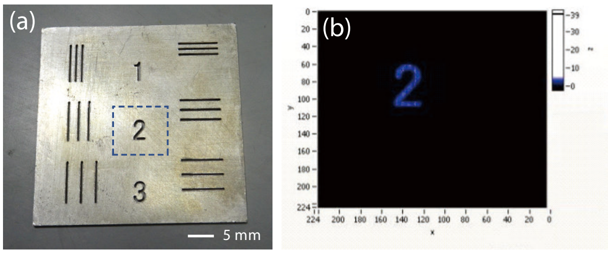

Figure 2. (a) Photograph of the Cd mask. Only the area with the dot line was irradiated with neutrons. (b) the measured transmission neutron image with the mask.

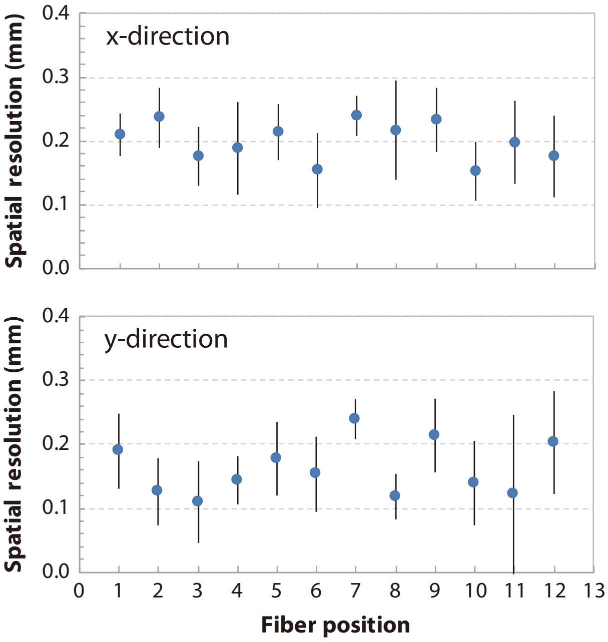

Figure 3. Spatial resolution (FWHM) of the detector [4].

neighboring 12 points. The detector exhibited spatial resolutions of 0.20±0.06 mm and 0.16±0.06 mm in average for x and y directions, respectively.

The detection efficiency of the detector was evaluated to be ~7% for thermal neutrons (1.8 Å). This value was about half of the neutron absorption rate in the scintillator screen. The trigger rate could be increased by lowering the threshold of discriminator electronics with a cost for gamma-ray sensitivity. Under this operational condition, the ^{60}Co gamma-ray sensitivity reached 1×10^{-6} for 1.17 and 1.33 MeV gamma rays. This was acceptable for our demonstrative experiment.

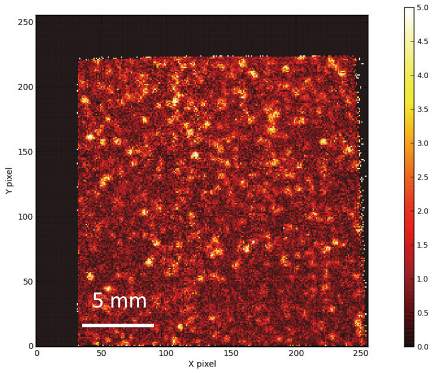

Figure 4. Example of neutron diffraction images measured with the prototype detector [5].

Figure 4 shows one of the time-of-flight neutron diffraction images measured in the BL10 of the J-PARC MLF. Details of the experiments can be found in [5]. The coarse-grained electromagnetic steel plate was set as a sample at the distance of 13.4 m from the pulsed neutron source. The detector was located close to the sample at a distance of 7 cm from the sample at 90°. Many diffraction spots were traced clearly in the measured images, confirming the feasibility of the detector.

4. Conclusions and future works

The high-resolution neutron detector was developed by using the scintillator / WLS fiber detector technology. The developed detector was implemented successfully into the demonstrative experiment for time-of-flight neutron diffraction imaging in the J-PARC MLF. In the future, the detection efficiency will be improved by adjusting the ^{6}Li content in the scintillator and/or by equipping multiple scintillator / WLS detecting heads.

References

[1] A. S. Tremsin, et al., Nucl. Instrum. & Meth. A **787** (2015) 20.

[2] T. Nakamura, et al., Nucl. Instrum. & Meth. A **737** (2014) 176.

[3] T. Kawasaki, et al., Nucl. Instrum. & Meth. A **735** (2014) 444.

[4] T. Nakamura, et al., Conference record, 2018 IEEE Nuclear Science and Medical Imaging Conference.

[5] T. Kawasaki, et al., Physica B: Condensed Matter **551** (2018) 460.

T. Nakamura[1], K. Toh[1], T. Kawasaki[2], and K. Sakasai[1]

[1]*Neutron Instrumentation Section, Materials and Life Science Division, J-PARC Center;* [2]*Neutron Science Section, Materials and Life Science Division, J-PARC Center*

Muon Science

Status of J-PARC MUSE: Overview

Muon Science Division is responsible for the inter-university user program and the operation, maintenance and construction of the muon beamlines; the D-Line, S-Line, U-Line, and H-Line as well as the muon source at MLF.

1. D-line

At the D-Line, variety of new scientific activities such as archeology, industrial application, and fundamental physics by using the world's most intense negative and positive muon beam have been performed, with budgetary support from the collaborative research of Inter-University Research Institute Corporation and by "Toward new frontiers: Encounter and synergy of state-of-the-art astronomical detectors and exotic quantum beams" (Grant-in-Aid for Scientific Research on Innovative Areas from Ministry of Education, Culture, Sports, Science and Technology). The high-intensity negative muon (μ–) beam and counting system has drastically increased the data acquisition rate for μ–SR to over 2×10^4 events/s (72 M events/hr), allowing the completion of a μ–SR experiment within an acceptable time. For example, the first observation with μ–SR of the nuclear magnetic field in MgH2 is featured in the research highlights of this volume.

2. S-line

At the S-Line, the stable operation at the S1 area continues. Thirty-four experiment proposals in 2018 have been carried out, including one urgent proposal and three P-type proposals. During the 1-MW test operation in July 2018, the integrity of the μSR data acquisition system and the beamline equipment at the S-line was confirmed. It was successfully demonstrated that the μSR spectrometer, ARTEMIS, can handle a data acquisition rate as high as 370 million events per hour.

3. U-line

At the U-line, the depth profile experiments using decelerated ultra-slow muons were successfully performed in a silver film on a silicon dioxide plate in June 2018. The double permalloy magnetic shield for the tungsten target was installed in September 2018 for suppressing muon-spin depolarization by stray field from the beamline magnets. A muon reacceleration experiment using an induction accelerator will soon be conducted at the U1B area.

4. H-line

At the H-Line, electric power of about 5 MW is necessary to operate all components of the H-line, so, a new electric power sub-station is being constructed in the northeast side of MLF. In FY2018, the platform of the sub-station was completed and high voltage cables were laid. The electric construction, including cabling work from the new sub-station to the experimental hall of the MLF, is planned for FY2019.

Y. Miyake[1,2], S. Takeshita[1,2], A. Koda[1,2],Y. Ikedo[1,2], T. Yamazaki[1,2], K. Shimomura[1,2] , N. Kawamura[1,2], P. Strasser[1,2], Y. Oishi[1,2], Y. Nagatani[1,2], H. Fujimori[1,2], S. Makimura[1,2], Y. Kobayashi[1,2], J. Nakamura[1,2], T. Adachi[1,2], M. Tampo[1,2], W. Higemoto[2,3], and T. U. Ito[2,3]

[1]*Institute of Materials Structure Science, KEK;* [2]*Muon Science Section, Materials and Life Science Division, J-PARC Center;* [3]*Muon Science Section, Materials and Life Science Division, J-PARC Center*

Report on the Trouble of the Rotation System and the Taken Measures

1. Introduction

A pulsed muon beam with unprecedented intensity will be generated by a 3 GeV 333 μA proton beam on a muon target made of 20 mm thick isotropic graphite at J-PARC MLF MUSE (Muon Science Establishment). The energy deposited by a 1 MW proton beam is estimated to be 3.9 kW in the muon target. The first muon beam was successfully produced on September 26, 2008. Gradually upgrading the beam intensity, a continuous 300 kW proton beam has been operated by a fixed target method without replacements till June 2014. However, the proton-irradiation damage to the graphite caused by the 1-MW proton beam operation, will reduce the lifetime of the fixed target to less than a year. To extend the lifetime, a muon rotating target, in which the radiation damage is distributed to a wider area, had been developed. The muon rotating target was installed in September 2014. The rotating target has been successfully used for five years without replacement. Since 2018, a continuous and stable 500-kW proton beam has been operated successfully. The accumulated operational period and the number of revolutions have reached 13500 hours and 12.5 million, respectively, by March 2019. Furthermore, on July 3, 2018, a 1-MW beam operation for 1 hour (beam power, 935 kW: 1 MW equivalent for one pulse) was successfully achieved. Meanwhile, a failure on the rotation system, which could potentially lead to a loss of the transmission, was discovered during the long shutdown in September 2018. At present, the operation of the rotating target is being monitored carefully and measures have been taken to prevent the loss of the transmission. In this report, the trouble of the rotation system and the measures taken at J-PARC MLF MUSE will be covered.

2. Failure on the rotation system

When the rotation feedthrough between a vacuum and air was replaced as part of the regular maintenance in September 2018, the damage on the flexible coupling that connects the feedthrough and the rotation shaft was discovered. Though the coupling had survived in spite of the damage, it broke into pieces completely during the replacement process. We recognized that the damage originated from the drawing instructions for the machining of the coupling. Inappropriate couplings were employed on the two positions of the rotation system. Figure 1 shows pictures of the rotating target assembly (right), the replacement of the vacuum feedthrough with the glove box (left-up), and the broken flexible coupling (left-down). While the broken coupling was replaced immediately with the appropriate one, it was difficult to replace the other one before the restart of the beam operation because of its hard accessibility, the high residual radiation dose, and the high contamination of tritium. Consequently, we decided to keep using the inappropriate coupling with careful monitoring and planning for measures to take in case of loss of the transmission.

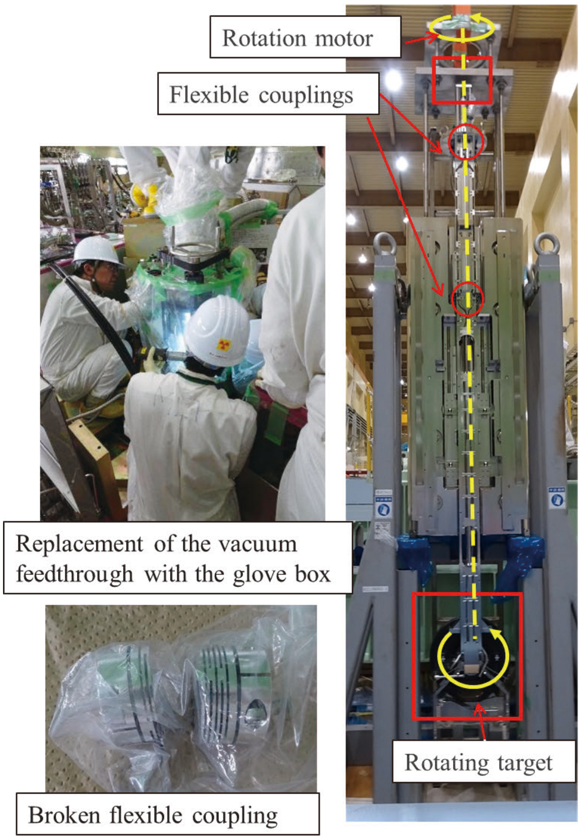

Figure 1. Pictures of the rotating target assembly (right), the replacement of the vacuum feedthrough with the glove box (left-up), and the broken flexible coupling (left-down).

3. Analysis of the rotation stop

The most reliable way of detecting the rotation stop during the proton beam operation is by observing the increment of the torque of the rotation motor.

When the coupling breaks down, the detection might not work as expected. Therefore, the variations of the temperature and the subsequent thermal stress were carefully evaluated through a finite element method, ANSYS.

The graphite itself is divided into three pieces to release thermal stress caused by the temperature difference on the graphite. The divided three pieces are held together as a target wheel by the centrifugal-force ring made of Inconel 600 (Daido Special Metal Co. LTD.).

The weight of the target wheel is 3 kg, and its temperature reaches 930 K. The target wheel is supported by the rigid wheel support through the nine flat bars made of Inconel 600. The cutting section of the flat bar is rectangular of 1 mm by 10 mm, and the length of the rectangle is 35 mm. The rectangle is located in parallel with the circumferential direction of the target wheel to release the thermal stress originating from the large temperature difference between the target wheel and the wheel support, as well as to support the weight of the target wheel. Figure 2 shows a picture of the rotating target. To validate the effect of the rotation stop, the maximum temperature of the graphite, the thermal stress on the graphite, and the thermal stress on the flat bar are evaluated. To save time for the simulation, the simplified 3-dimensional model of the graphite wheel is used for FEM code since the results are similar to those of the full model. The thermal stress on the flat bar is evaluated by a theoretical calculation with a double supported beam model, where the rotation is restricted on the both ends. The criteria of the maximum temperature of the graphite, the thermal stress on the graphite, and the thermal stress on the flat bar are 2300 K, 25 MPa, and 200 MPa, respectively.

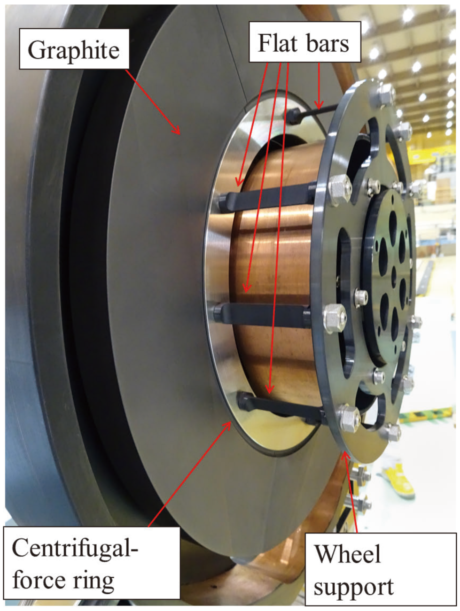

Figure 2. Pictures of the rotating target.

As a result of the simulations, it was confirmed that the allowable beam intensity without rotation was 500 kW. When the beam intensity exceeds 500 kW without rotation, the graphite will probably crack and the flat bar will be plasticly deformed. However, even if the temperature of the graphite reaches 2300 K, the evaporation rate of the graphite is still low enough (1.4 μm/hour). Furthermore, the used rotating target can be replaced with a new one, because the aperture of the target chamber is large enough to extract the rotating target, even if the flat bars are plastically deformed. On the other hand, the radioactive gases, including tritium, are produced and stored in the graphite during the beam operation. The radioactive gases from the graphite at high temperature should be taken into account.

4. Restart of the beam operation

Because the results showed that 500 kW power of the beam operation was acceptable, we decided to keep using the current rotating target with the inappropriate couplings. To detect the rotation stop immediately, the sensitivity of the machine protection system, such as the quadrupole mass spectrometer, the torque monitor of the rotation system, and the temperature measurement has been improved [1]. To avoid the release of the emitted radioactive gases to the outside of the facility via the vacuum pumping system, a buffer

Table 1. Results of the analyses under the conditions of 500 kW and 1000 kW with rotation (W/R) and the conditions of 500 kW, 700 kW, and 1000 kW without rotation (W/O/R).

	Criteria	500 kW W/R	1000 kW W/R	500 kW W/O/R	700 kW W/O/R	1000 kW W/O/R
Max. temp. of Graphite (G.) (K)	2300	740	880	1690	1990	2390
Temp. difference on G. (K)	-	30	50	950	1220	1600
Equivalent stress on G. (MPa)	25	0.7	1.1	22	29	38
Temp. of CF ring	-	-	450	910	1000	-
Equivalent stress on flat bar	200	-	80	180	240	-

tank was employed to keep the pumped gas tentatively until confirming its activity to be low enough [2]. The rotating target had retreated to the escape position from October 20 to November 6 to validate the new vacuum pumping system and the buffer tank. At present, a 500-kW proton beam has been stably operated with the rotating target. In the long shutdown of 2019, the replacement of the inappropriate coupling or the replacement of the entire rotating target assembly is planned.

5. Acknowledgement

I would like to thank to support of the dedicated staffs from The NIPPON ADVANCED TECHNOLOGY CO., LTD (NAT).

References

[1] S. Matoba et al., ibid.
[2] N. Kawamura et al., ibid.

S. Makimura[1,2], S. Matoba[1,2], and N. Kawamura[1,2]
[1]*Institute of Materials Structure Science, KEK;* [2]*Muon Science Section, Materials and Life Science Division, J-PARC Center*

Negative Muon at D Line – Beamline Commissioning

1. Introduction

The D line, which is a beamline located at MUSE, MLF, has a long superconducting solenoid and therefore can supply positive and negative decay muons from several MeV/c to ~100 MeV/c in addition to surface muons. Since the energy of the primary proton beam of MLF is as high as 3 GeV, the generation efficiency of negative muons is high. In particular, because the power of the primary proton beam has been incrementally increased in recent years, the D line now supplies the world's highest intensity negative muon beam. Using the high-intensity negative muons, applications for various experiments such as non-destructive elementary analysis using muonic X-rays, and negative muon spin relaxation, are being developed. In this report, we cover the current status of commissioning the negative muon beam at D line.

2. Kicker tuning for negative muons

MLF provides double bunch beams with a period of 25 Hz. Each bunch has an FWHM of 100 ns and a bunch interval of 600 ns. By dividing the double bunch beam into two single bunches with an electro-magnetic kicker (DKKR1, 2) installed at the branch section, it becomes possible to supply a single bunch beam simultaneously in areas D1 and D2.

The branch section consists of two switchyard magnets (DSY1, 2, the so-called bending magnet), two kicker electromagnets (DKKR1, 2), and septum magnets, which conduct the muon beam toward areas D1 and D2 (DSPTM1, 2) (Fig. 1(a)).

Without kicker excitation, the beam trajectory is slightly bent toward DSPTM2 by DSY1 and 2 and led to area D2 by the DSPTM2 (Fig. 1(a)). If the kicker is excited with an appropriate voltage when the second bunch of this beam passes through DKKR1 and 2, only the second bunch is bent toward the DSPTM1 and then conducted to the area D1 (Fig. 1(b)). Since DKKR is unipolar, the single bunch operation for negative muons requires that the kicker be operated to the double bunch beam supplied to the D2 area.

The optimal kicker excitation voltage and excitation timing depend on the momentum of the muon beam. The kicker excitation voltage and the excitation timing were tuned for the negative muon beam of 30 MeV/c. Regarding excitation timing tuning, we measured by installing scintillation counters in both D1 and D2. While changing the delay of the kicker excitation trigger, we found the condition that the first bunch was conducted to D2 without any loss and the second bunch was also conducted to D1 without loss. The kicker excitation voltage was tuned by measuring the intensity of the negative muon at D1 with the scintillator while changing the excitation voltage. As a result, an excitation voltage of ±27 kV was optimal at 30 MeV/c. The result of this tuning is shown in Fig. 2. The double bunch beam observed at D2 without the kicker operation is supplied as a single bunch beam to D1 and D2 by the kicker operation. Considering that the kicker rating is ±40 kV, it can be expected that a beam of about 40 MeV/c can be kicked.

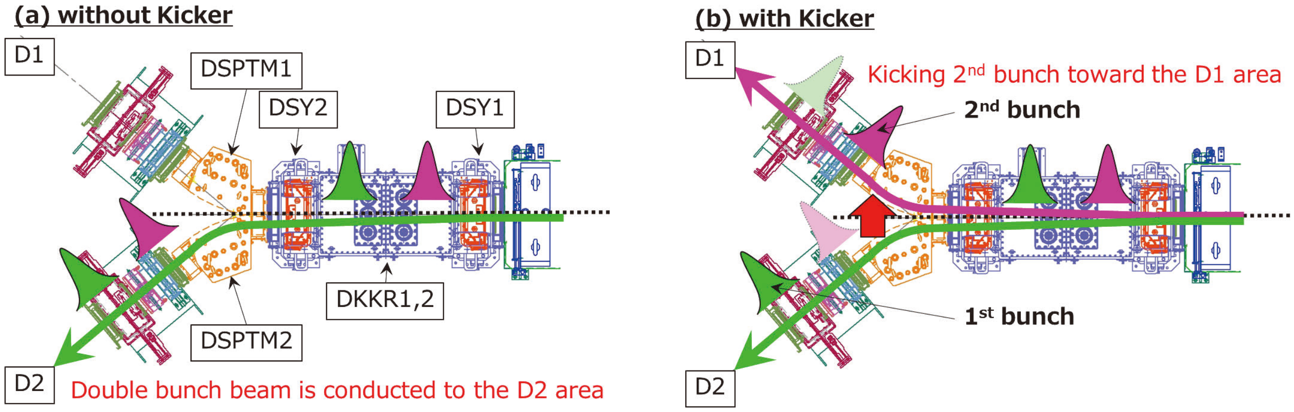

Figure 1. Schematic view of the branch section with the kicker system and its operation (a) without and (b) with kicker excitation.

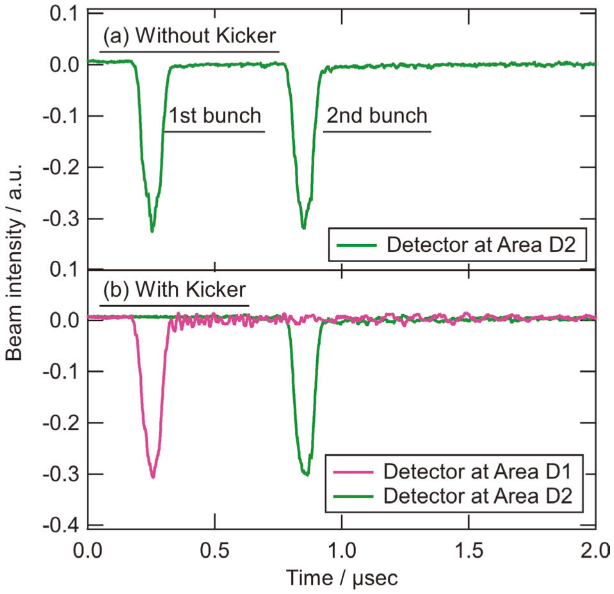

Figure 2. Muon intensities as a function of time observed by scintillation counter at areas D1 and D2. (a) Double-bunch structure of the negative muon beam observed at area D2 and (b) Single-bunch structure by exiting DKKR1 and 2 observed at both areas.

3. Separator upgrading

In measurements, such as elementary analysis by muonic X-rays and muon spin relaxation, contamination of prompt electrons becomes a noise source and must be filtered as much as possible. For this reason, a DC separator (DSEP, the so-called Wien filter) has been installed in the D line. The DSEP consists of high-field electrodes for applying a high electric field, and correction coils for applying correction magnetic field to correct the trajectory of the muon bent by the high electric field, where the direction of the magnetic field is orthogonal to the electric field. However, discharge had frequently happened during the operation, and therefore the operation voltage of the electric field has been limited to ±170 kV for stable operation. During the summer maintenance in 2018, the high-voltage power supply was replaced with a revised new system so that a higher electric field can be applied, and this upgrade improves the efficiency of reduction of the prompt electron.

The high-voltage power supply for DSEP had been located next to area D2 and connected to the electrodes of the DSEP via a high-voltage cable with length of approximately 10 m. Since frequent discharge happened in this electrode connection part, the high-voltage power supply was replaced with the one that had been tested and approved at the U and S line (Fig. 3). This high-voltage power supply is of the Cockcroft type and is placed directly above and below the main body of the DSEP. The electrodes of the high-voltage power supply are directly connected to the separator electrodes inside the chamber. As a result, it was possible to apply an electric field of up to ±250 kV.

In order to measure the effect of the high electric field, a stacked pair of scintillation counters were installed in area D2. The intensities of the negative muons and contaminated electrons in the beam were measured by the counter of the upstream and downstream, respectively. The upstream scintillator has enough thickness to stop all muons, so that the downstream counter observes only the signal of the electrons.

Figure 4 shows the intensities of the negative muons and the electrons as a function of the correction coil current at DSEP with applied voltages of ±170 kV and ±240 kV at 30 MeV/c. From the muon intensity, the optimal correction coil current was ~60 A at an applied voltage of ±170 kV, while it increased to ~60 A at ±240 kV. As a result, the ratio of the intensity of the contaminated electrons at ±240 kV compared to that at ±170 kV is 13% (87% of electrons are thoroughly filtered). However, due to the failure of the high-voltage power supply, which happened in February 2019, currently, the applied voltage is limited again to ±170 kV. This power supply will be replaced with a new one during the 2019 summer shutdown.

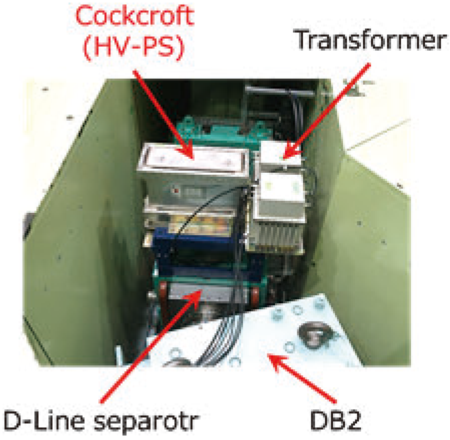

Figure 3. Installed Cockroft type high-voltage power supply on the DC Separator (DSEP).

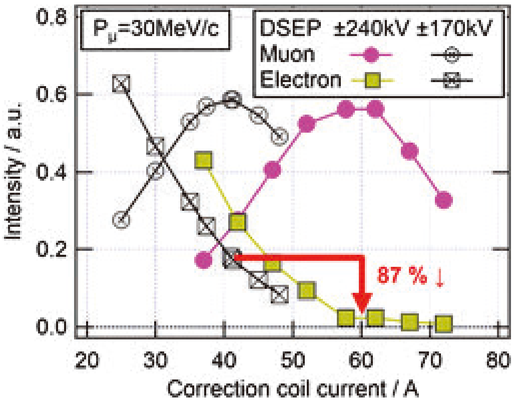

Figure 4. Intensities of muon and contaminated electron at ±240 kV and ±170 kV excitation.

S. Takeshita[1,2], P. Strasser[1,2], Y. Ikedo[1,2], M. Tampo[1], S. Doiuchi[1], A. Hashimoto[1], I. Umegaki[3], T. U. Ito[4], S. Nishimura[1,2], N. Kawamura[1,2], K. Shimomura[1,2], and Y. Miyake[1,2]

[1]*Institute of Materials Structure Science, KEK;* [2]*Muon Science Section, Materials and Life Science Division, J-PARC Center;* [3]*Toyota Central Research & Development Laboratories, Inc.;* [4]*Advanced Science Research Center, JAEA*

Development of the Ultra-Slow Muon Beam at the U-line

1. Overview of the U-Line

The Ultra-Slow Muon (USM) beam, which has quite low kinetic-energy, small beam-size, and small-time distribution, is needed to probe surface and inter- face of materials. In J-PARC, a muon beamline (U-Line) for USM was constructed and currently is under commissioning [1]. In the U-Line, an intense surface muon beam is transported by superconducting solenoids and incidents to a muon production target. A part of the muons stopped in the tungsten evaporate as muoniums. A resonant laser ionizes muoniums to produce a USM beam. Then, the USM beam is accelerated up to 30 keV and is transported to the U1A area or the U1B area. At the U1A area, the USM beam is provided to a μSR spectrometer on a high voltage stage. To control the penetration depth to a sample, the kinetic energy of the USM beam is controlled by the deceleration voltage, which is applied to the stage.

2-1. Improvement of the magnetic shield

Strong stray field from the superconducting solenoids affects the extraction of USM. The magnetic shielding of the muonium production chamber was improved during the summer shutdown of 2018. A double-layered permalloy shield was installed in between the muonium chamber and existing iron shields. The iron shields were also improved as forming triple layers. The layout of the shield is shown in Fig. 1. The magnetic field under the shield was calculated and measured. The results are shown in Fig. 2. The measured fields agree with the calculated fields within 0.1 mT.

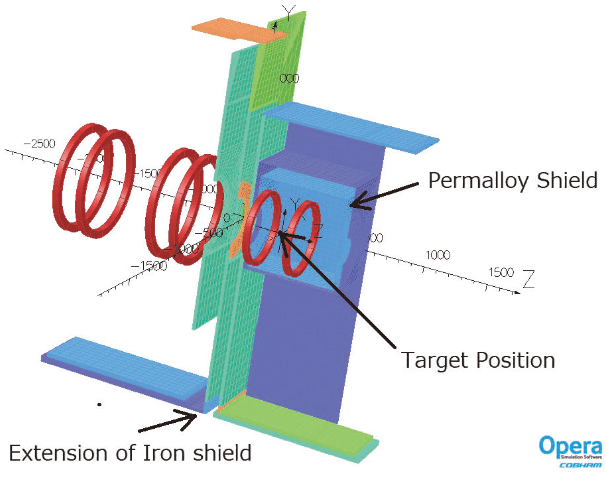

Figure 1. The layout of the magnetic shield calculated and measured.

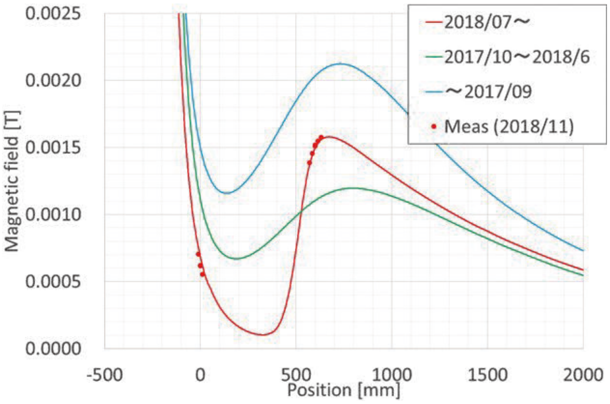

Figure 2. Magnetic field without using correction coil. Fields in the center of the beamline are shown. Lines are showing the calculated field with each season's magnetic shield. Dots are the measured field with the latest magnetic shield.

2-2. Control of penetration depth

Following the last year's successful observation of muon-spin-rotation of USM [2], we tested scanning of penetration depth. The test sample was 50 nm Ag coated SiO2 plate. A schematic of the test is shown in Fig. 3. According to the deceleration of USM, the asymmetry increased. It means the stopping region of USM changed from SiO2 to Ag.

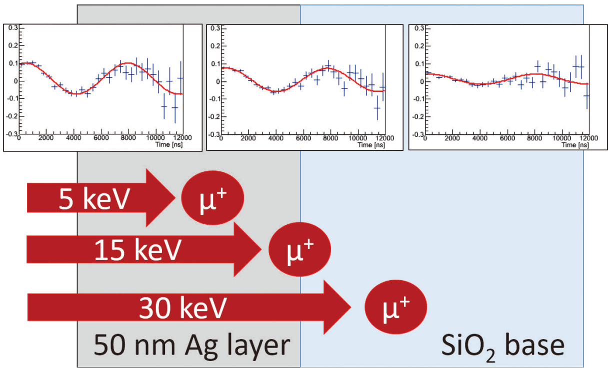

Figure 3. Schematics of the penetration-depth controlling test.

3. The progress of the laser system

Lyman-α laser system has been operated so far by making minor upgrades. In order to increase the stability of the output pulse energy, a few major upgrades were applied to the laser system.

3-1. Laser system for ultra-slow muon generation

Ultra-slow muons can be generated by resonant optical ionization of thermal muonium from hot-W foil target using 122.09 nm coherent light pulse for 1s-2p excitation and 355 nm coherent light pulse for ionization. The high-energy pulsed coherent Lyman-α light (122.09 nm) source is a very important element for the efficient generation of high-power ultra-slow muons.

The design of the Lyman-α light source is described in Ref. 1 and schematic of the light source is shown in Fig. 4. The pulsed Lyman-α is generated by 2-photon resonant four-wave mixing in krypton gas. The required 2-photon-resonant 212.556 nm and 820 nm pulses are obtained by nonlinear wavelength conversions of intense 1062.78 nm pulse. The intense 1062.78 nm pulse is provided from wavelength locked all-solid-state laser amplifiers with Nd:YGAG ceramics as an efficient gain mediums. The all-solid-state laser amplifiers and subsequent wavelength converters that were placed in the temperature-controlled laser room require minimal monthly adjustment, and have been working stably for several months. Even if the laser's operation is very stable, the problem of the slow intensity suppression of Lyman-α intensity by Kr-Ar mixture gas degradation still remains, which was pointed out in the previous year's facility report. In order to reduce that effect, the mixture is automatically exchanged every 3 hours.

3-2. Improvement of the laser beam's pointing stability

Since the Lyman-α generation by four-wave-mixing requires the spatiotemporal overlapping of 212 nm and 820 nm pulses in the gas cell, laser pointing stability is important. When the temperature in the laser room rises due to unexpected blackouts, summer long shutdown and/or thermal condition changing of flash lamp pumped Nd:YAG laser for 355 nm generation, an irreversible misalignment of the optical pass in the laser system appears. A stress transformation is mainly introduced by the difference of thermal expansion coefficient between breadboards and optical table. The laser system was modularized on the 15 mm thickness aluminum solid breadboards. Three amplifier modules (Regenerative, intermediate and power amplifier) and wavelength conversion stages (212.556 nm wavelength converter and 820 nm parametric amplifier) were placed on the optical table made of stemless steel. In order to avoid this problem, all optomechanical components were relocated from breadboards to the optical table directory during the summer shutdown in 2018. The effect of this is under evaluating in the day by day operation. In addition, the optical setup displays instability at the height adjustment periscopes matching

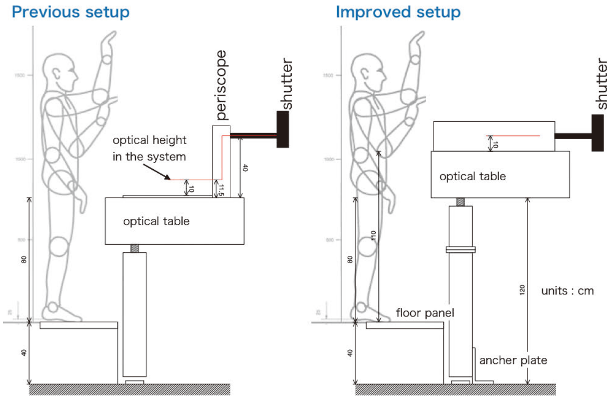

Figure 5. Side view of the optical table and optical pass setup.

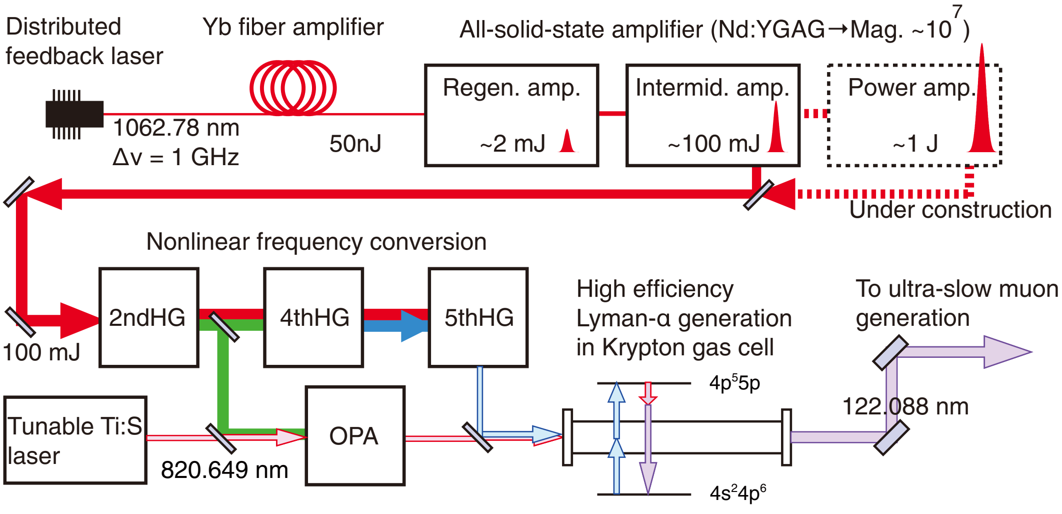

Figure 4. Schematic of the Lyman-α laser system for the Ultra-slow muon generation.

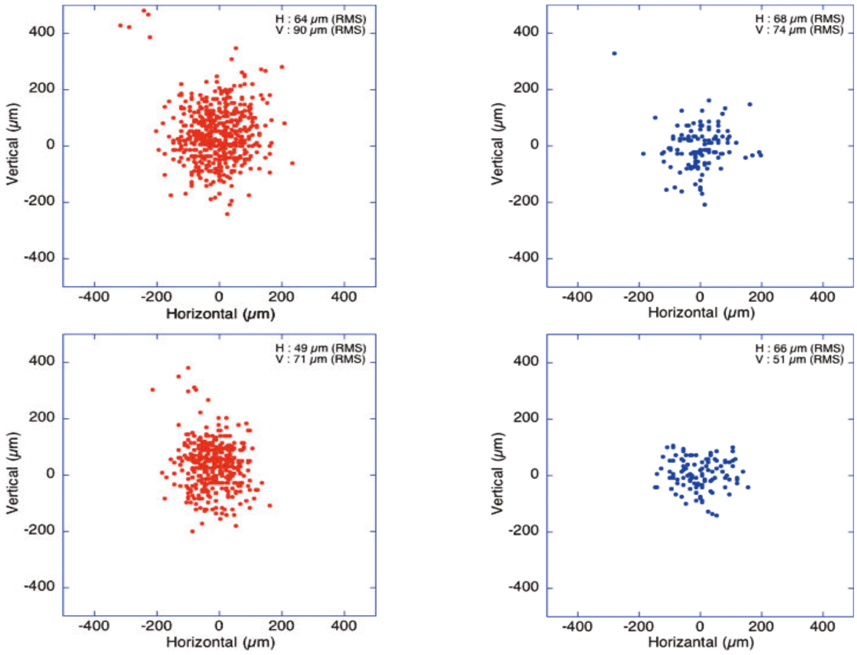

Figure 6. Variation of beam pointing in the beam diameter of ~4 mm for 212 nm pulses and ~6 mm for 820 nm pulses.

the height with the Kr gas cell and the muon beam line. In order to reduce the beam pointing instability, the height of the optical table was padded by just 300 mm. We measured the beam pointing stability before and after the changing of the height of optical table by a CCD camera which placed at Kr gas cell. Figure 6 shows the variation of shot to shot laser beam center position for (a) 212 nm pulses and (b) 820 nm pulses, respectively. For both wavelength pulses, the beam pointing stability was improved by almost 20%. We will continue to improve the pointing stability to realize stable Ultra-slow muon generation.

4. U1B Area

We are developing transmission muon microscopies at the U1B area. The final goal of the transmission muon microscopies is visualizing thick object (> 10 μm) in nanometer resolution. The re-acceleration of the ultra-slow muon beam provides quantum coherence of the beam and deep penetration through a specimen. Coherent muon beams can visualize electromagnetic fields in thick specimens in high resolution. The transmission muon microscopy will become a unique research method.

4-1. Prototype of the transmission muon microscopy

This year, a prototype of the transmission muon microscopy is being constructed at the U1B area. The purpose of the prototype is to obtain a direct proof of the quantum interference of muons, by detecting diffraction patterns of the ultra-slow muon beam. The experiment will be the first direct proof of the wave-particle duality beyond the second generation of the Standard Model. A camera-chamber with a 2-dimensional image sensor is installed after the object lens, including a specimen stage. The prototype employs the 30keV ultra-slow muon without any additional acceleration. We have confirmed that the incoming muons can be visualized as dot-images by the system.

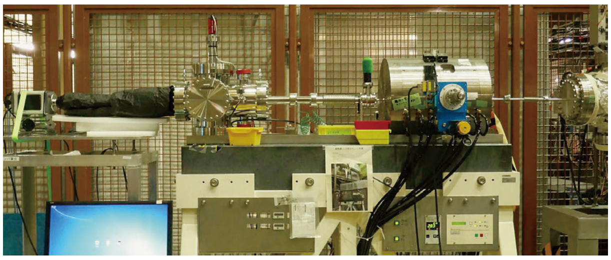

Figure 7. The prototype of the transmission muon microscopy in the U1B area. The optical devices of the microscopy are constructed on a surface-plate of stone. The ultraslow muon beam is coming from the right side. An object lens and a specimen-stage are stored in the silver cylinder. A multi-channel plate (MCP) and a phosphor plate are installed in the left chamber. The MCP converts incoming muons into electrons conserving position of muons. The electrons are converted into lights by the phosphor plate. Amplification of the MCP is enough high for visualizing single muon for naked eyes. The image on the phosphor is taken by a CCD camera at the left end.

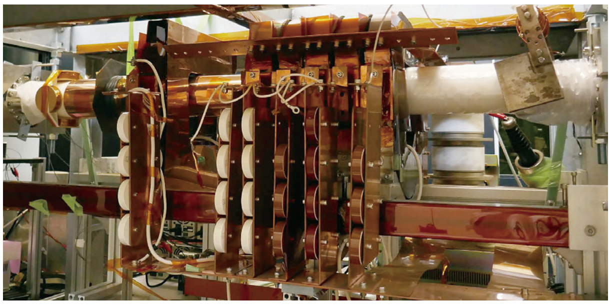

Figure 8. Principal part of the induction accelerator. The horizontal white duct is a beam pipe. The duct is passing through 6 induction cores. Each core is made by finemet material and accelerate particles up to 6 kV. The vertical white tube behind the beam pipe is a thyratron, which discharges ceramic capacitors (brown and white cells) into the induction cores.

4-2. Induction accelerator for muons

We have constructed an induction accelerator for muons. The main aim of the induction accelerator is to conduct a muon diffraction experiment for different energies of muon-beams. The diffraction pattern should be shrinking due to the increase of the beam energy. By accelerating more than 30 keV, we can choose more kinds of specimens for diffraction-experiments due to increasing its penetration.

The induction accelerator has been constructed and tested in the Tsukuba campus. In the test, we employed a pulse electron beam generated by a photocathode, and a magnetic deflector as an energy spectrometer. It was confirmed that the accelerator fully works, and it has been transported from the Tukuba campus to J-PARC/MLF.

References

[1] A. D. Pant et al., JPS Conf. Proc. **21** (2018) 011060.
[2] T. Adachi et al., KEK-MSL Progress Report 2017 (2018) 13.
[3] N. Saito et. al., Opt. Express **24**, 7566–7574 (2016).

T. Adachi[1,2], Y. Ikedo[1,2], Y. Oishi[1,2], Y. Nagatani[1,2], and M. Yoshida[3]

[1]*Institute of Materials Structure Science, KEK;* [2]*Muon Science Section, Materials and Life Science Division, J-PARC Center;* [3]*Accelerator Laboratory, KEK*

Development of Sample Environment at the S1 Area

1. Introduction

There is a growing demand for the μSR experiment at low temperatures below 1 K at MUSE, which leads to the chronic shortage of beam time for ^{3}He-^{4}He dilution refrigerator (DR) installed to the D1 instrument. In order to settle this issue, we have commissioned a new ^{3}He evaporation cryostat, which has certain advantages (e.g., portability, cooling efficiency) against DR. The cryostat is based on a commercially available model (Heliox AC-V supplied by Oxford Instruments plc), which was customized for passing a muon beam through the outer vacuum chamber and related parts around the sample space (see Fig. 1).

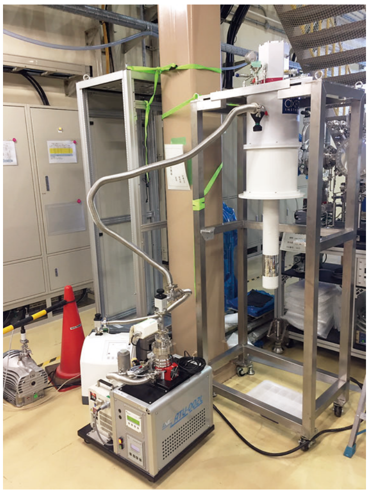

Figure 1. A snapshot of the new ^{3}He evaporation cryostat placed at the test bench.

2. Cooling performance

The cryostat consists of a ^{3}He insert and a two-stage pulse tube cryocooler (PTC) operated by a dedicated compressor (Fig. 2), which allows cryogen-free cooling system. The ^{3}He insert consists of a sorption pump (sorb), a ^{3}He pot, and a heat switch (HSW). A sample is mounted on the base of the ^{3}He pot for temperature control by thermal conduction. A muon beam is delivered to the sample in vacuum through a 30-mmϕ aluminized mylar window. The ^{3}He condensation is realized by the PTC second stage (~3 K) and an outgassing sorb, while the cooling is attained by pumping ^{3}He gas using the sorb cooled via HSW.

An example of cooling-down trend for the sample temperature is shown in Fig. 3. Apart from the holding time attained by heater control, it takes 1.5 days to reach the base temperature (0.3 K) from ambient temperature. Since the cryostat is not designed for the top-loading holder, it needs warming up to the room temperature upon sample exchange (taking ca. 9 hours).

We also examined the influence of eddy current induced by changing magnetic field. Figure 4 (left) shows the temperature trend at the base temperature, where the its rise is observed with various ramping rates for changing a magnetic field in 50 G step. The right side of Fig. 4 shows the trend with ramping the field from 3450 to 50 G with 4 G/s, where temperature levels are off because of the balance between heating due to the eddy current and cooling by ^{3}He evaporation. This suggests that the temperature rise during the field ramping is ~20 mK at the base temperature.

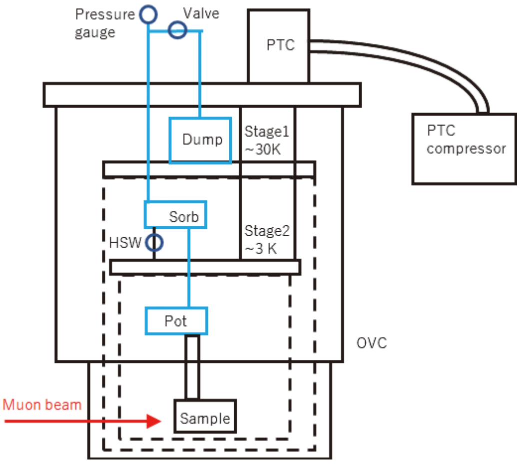

Figure 2. Schematic diagram of the ^{3}He cryostat with blue lines showing ^{3}He flow paths, where PTC, OVC, sorb, and HSW, respectively, denote the pulse tube cryocooler, the outer vacuum chamber, the ^{3}He sorption pump, and the heat switch.

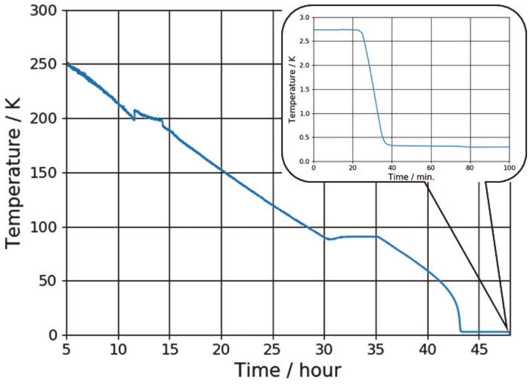

Figure 3. Cooling down trend of the ^{3}He cryostat. The origin of the horizontal axis represents the time when PTC was turned on. The plateau at 90 K is that artificially attained by heater control. The inset shows a magnified view near the base temperature.

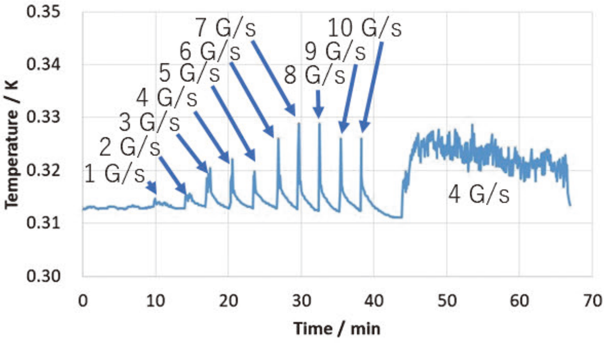

Figure 4. Temperature trend at the base temperature observed at different ramping rates for the external magnetic field.

3. Performance for the μSR experiment

The ^{3}He cryostat was then loaded to the ARTEMIS spectrometer in the S1 area to examine the performance for the μSR experiment. A slab of holmium metal (20×20×0.3 mm) was mounted on a silver holder made with the common design for DR at the D1 area (Fig. 5) [1–4]. The observed μ-e event rate was 95 M/hour with 20 mmϕ collimator, double-pulse, and proton beam power of 300 kW. Figure 6(a) shows some examples of μSR spectra observed at around 150 K with a variable inner diameter for the beam collimator. The fast-relaxing component corresponds to the signal coming from the Ho sample, while the time-independent component is backgrounds primarily from the sample holder. Curve-fit of the asymmetry [$A(t)$] using a form, $A(t) = A_s \exp(-\lambda t) + A_b$ yields the signal to noise (S/N) ratio $A_s/(A_s + A_b)$ as shown in Fig. 6(b).

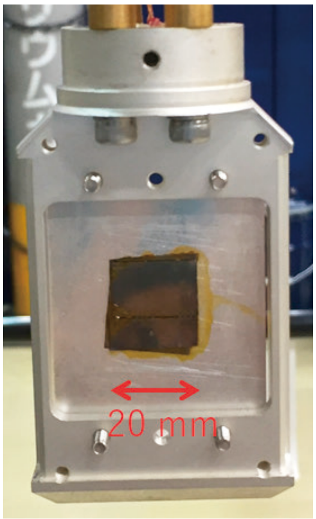

Figure 5. Sample holder for the ^{3}He cryostat.

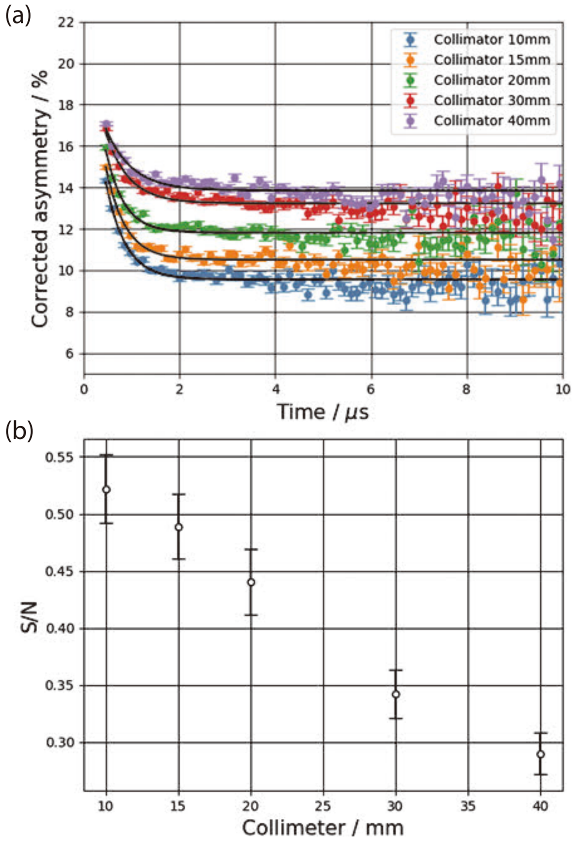

Figure 6. (a) Some examples of the μSR spectra obtained for Ho sample (20×20×0.3 mm) using the ^{3}He cryostat. (b) The signal to noise ratio obtained from (a) by curve-fit (see text).

Besides the installation of the ^{3}He cryostat, we worked on the maintenance of other cryostats including their thermometers that may deviate from their original specifications after being subjected to prolonged heat cycles. The resistivity of some Cernox resistors (Lake Shore Cryortronics, Inc.) was measured to update the calibration tables. We also plan to ensure the traceability and to keep track of the health condition of thermometers by calibration during their regular cycles.

References

[1] W. Higemoto et. al., KEK Progress Report 2011-3 KEK-MSL REPORT 2010 (2011) 13.
[2] W. Higemoto et. al., KEK Progress Report 2013-3 KEK-MSL REPORT 2012 (2013) 34.
[3] W. Higemoto et. al., KEK Progress Report 2015-4 KEK-MSL REPORT 2014 (2015) 24.
[4] W. Higemoto et. al., KEK Progress Report 2018-2 KEK-MSL REPORT 2017 (2018) 9.

J. G. Nakamura[1,2], A. Koda[1,2], S. Nishimura[1,2], H. Li[2], S. Doiuchi[2], A. Hashimoto[2], H. Okabe[2], H. Hiraishi[2], and R. Kadono[1,2]
[1]*Muon Science Section, Materials and Life Science Division, J-PARC Center;* [2]*Institute of Materials Structure Science, KEK*

H-Line Construction – Recent Progress

A new beam line named H-line [1] is being constructed in the east section of Experimental Hall #1 of the MLF. The H-line is planned to be used for various experiments, which need high statistics, i.e. high-intensity beam and long beamtime. These characteristics enable precise measurements such as muon g-2/EDM experiment [2] and high-precision measurement of the hyperfine splitting of the ground state of muonium (MuSEUM experiment [3]), and is also best suited for the rare decay search like DeeMe experiment [4], which searches for charged lepton flavor violation (cLFV) using muonic atoms. A transmission muon microscope, which is an unprecedented tool to obtain 3D images of a living cell non-destructively, is planned as well.

In order to deliver a high-intensity beam to experimental areas, the H-line has a large-aperture capture solenoid (HS1). It is located 600 mm from the muon production target and its acceptance is 108 mSr. Coils of HS1 are wound with radiation resistant mineral insulation cables (MIC) [5]. Because MIC is a normal conducting wire, HS1 needs high electric power (~ 1 MW). Other beamline components, such as the bending magnets (HB1, HB2), the transportation solenoids (HS2, HS3), and the focusing quadrupole triplet (HQ1–3), also have large aperture for efficient muon transportation. Figure 1 is a layout drawing of the H-line in the first phase.

The front-end apparatuses of the H-line (HS1, HB1, HGV1) were installed during the summer shutdowns in 2012 and 2014. In 2016, all radiation shields until the first branch of the H-line, H1 area, were placed. A beam blocker (HBB1) was also installed. With the beam blocker inserted, the dose rate inside the H1 area is expected to be about 10 μSv/h, even when the beam is on.

The construction of a new electric power sub-station for the H-line has been in progress since FY2017. The capacity of the electric sub-station is about 5 MW, which is necessary to operate the H-line. The construction site is located in the northeast side of the MLF, as shown in Fig. 2.

During the summer shutdown in 2017, a through-hole for electric transmission lines was drilled on the MLF wall. The size of the aperture is 2 m × 1 m (Fig. 3). The hole is now covered with an iron plate to keep the experimental hall airtight. Then we started building the platform of the electric sub-station and it was almost completed in FY2018. Figure 4 is a picture of the electric sub-station taken in the end of FY2018. In FY2019, electrical construction, including installation of transformers and cabling work inside the MLF building, is scheduled and all the construction of the new electric sub-station will be completed.

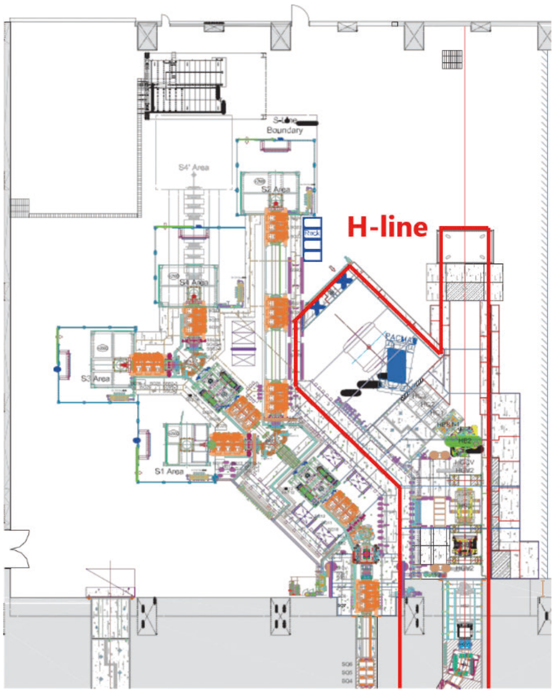

Figure 1. A layout plan of Experimental Hall #1 in the first phase of the H-line construction.

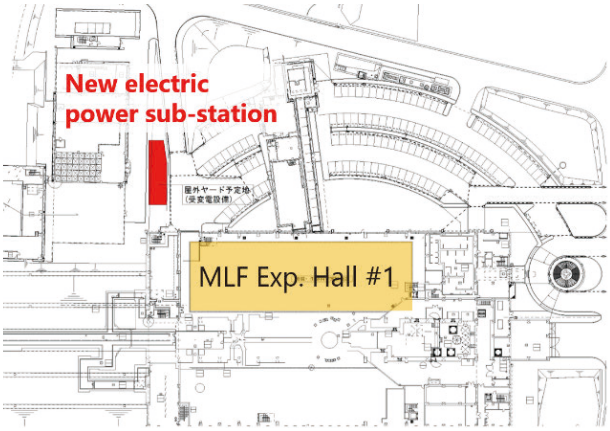

Figure 2. Construction site of a new electric power sub-station. It is located outside the MLF building.

Figure 3. Aperture for the electric transmission lines. It is located above the carry-in entrance of the east #1 experimental hall of the MLF.

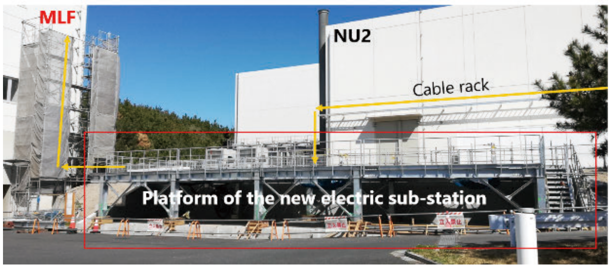

Figure 4. The platform of the new electric sub-station was almost completed in FY2018.

References

[1] N. Kawamura, et al., Prog. Theor. Exp. Phys. 2018, 113G01 (2018).
[2] T. Mibe, et al., Chin. Phys. C **34**, 745 (2010).
[3] K. Shimomura, AIP conf. proc. **1382**, 245 (2011).
[4] H. Natori, et al., Nucl. Phys. B (Proc. Suppl.) **248–250**, 52 (2014).
[5] H. Fujimori, et al., Nucl. Instrum. Methods Phys. Res. Sect. A **600**, 114 (2009).

T. Yamazaki[1,2] and N. Kawamura[1,2]
[1]*Institute of Materials Structure Science, KEK;* [2]*Muon Science Section, Materials and Life Science Division, J-PARC Center*

MLF Safety

Research Safety

1. Radiation safety

Radiation safety for users

The low-surface contamination area has been adopted at the MLF Experimental halls from November 2016 to avoid surface-contamination problems caused by a sample, an environmental atmosphere and so on, and to expand the flexibility of the experiments conducted at the MLF. The number of conducted experiments using gaseous or liquid samples or atmospheres has gradually increased.

On the other hand, samples have been radio-activated by neutron irradiations because the stable proton beam power increased to 500 kW. Especially, ^{60}Co ($T_{1/2} = 5.271$ y) and ^{110m}Ag ($T_{1/2} = 249.8$ d) can be found in radio-activated samples well, resulting that the radio-active samples cannot be brought for long time. It is required to minimize the parent nuclei ^{59}Co and ^{109}Ag and/or the irradiated neutrons.

The four monitors for take-out articles work smoothly to bring an article out from the controlled area without significant trouble. However, hand-foot-clothe monitors had several troubles due to damage of the light shielding sheets. The devices are hoped to be used carefully and softly.

Distribution of survey-meters to each neutron beam line

From the introduction of the low-surface contamination area, to check dose rates around the sample, and surface contamination at sample environment devices, survey-meters are distributed at each neutron beam lines, resulting that the radiation exposure of users can be reduced. All survey-meters are inspected and calibrated annually.

Radiological license upgrade

The applications for radiological license upgrades in FY2018 were approved on August 22, 2018, and February 4, 2019.

The following items were updated after the application approval in FY2018:

(1) Addition of a sealed radioactive isotope (^{237}Np, 10 MBq) for nuclear data measurements

(2) Consideration of movable shields of a muon beam line by re-evaluation of shielding and addition of safety devices

(3) Reduction of the storage area of radio-active materials to install a large detector to find sterile neutrinos at the 3rd floor of the maintenance area in the MLF

2. Chemical safety

An annual task of the chemical-safety team is to check the chemical safety of user-brought chemical materials, such as specimen and reagents, to evaluate their toxicity and the stability of their actual physical state – powder, solid, liquid or gas. The task was performed successfully, followed by the approval of the actual materials for use by the individual beamline staffs. As a result, the experiments were performed without serious chemical problems. Figure 1 shows a trend for the amount of chemical materials subjected to safety check for over 10 years. As the beam power increases, the number of user-brought chemical materials is also increasing. Since a stable operation at 500 kW was achieved for the first time during the planned beam-operation schedule for the last year, a record amount of chemical materials was brought. Over 8,000 chemical materials were brought in the MLF, which was about 10 times more than at the start of the MLF operation. However, the total number tends to flatten recently. Therefore, by using the last year's data, we evaluated the expected number of the user-brought chemical materials at 1 MW, which is full power, and we can also estimate the total number of necessary equipment for chemical handling for sample preparation, consumables, radioactive wastes after experiments at 1 MW operation, which is planned within several years.

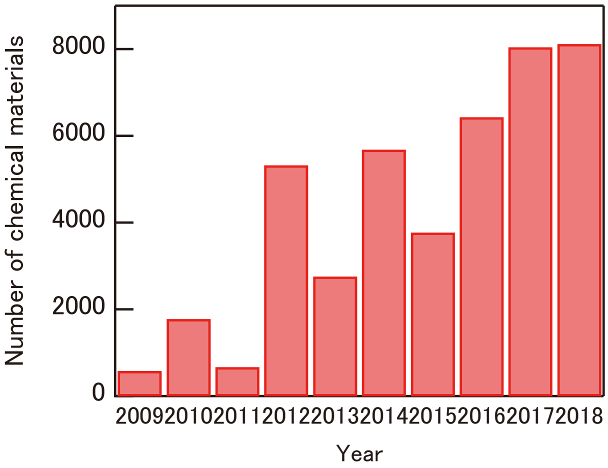

Figure 1. Trend of amount of user-brought chemical materials for chemical safety check from the start of the MLF operation to the last year.

3. Sample environment safety

Table 1 shows last year's statistics of the common sample environment, such as a magnetic field apparatus, various kinds of cryostats and various kinds of furnaces. The common sample environment equipment was used 50 times and 256 days in total. The common sample environment is maintained by the sample environment team whose members include JAEA, KEK and CROSS staffs. Each common sample environment must take a safety check by technology development section, MLF until regular operation and pass it. The safety check examines the maximum controllable value, for example, temperature of the equipment, the interlock system, electrical integrity and structural integrity. If the specifications of each common sample environment are changed, it is necessary to conduct the safety check again. As a result of those measures, all common sample environment equipment operated well, and there were no safety problems.

Table 1. Statistics of the common sample environment.

equipment	times	total days
7 T magnet	16	86
2 K cryostat	3	5
3He cryostat	16	95
dilution cryostat	7	41
cryostat for residual stress measurement	2	7
GM cryo-furnace	2	10
Nb furnace	3	11
SANS furnace	1	1
Total	50	256

4. Crane safety

Throughout the year, we use cranes to change sample environment equipment for experiments and to perform various kinds of maintenance of the neutron instruments. There are 50 t and 7.5 t cranes in experimental hall No.1 and there are 50 t, 7.5 t and 15 t cranes in experimental hall No.2 and its extension building. Those cranes can be operated only by crane operators who have been licensed by the government, additionally, they must be trained by our crane safety staff and pass our skill test. In addition, before each individual crane operation, the crane working group must submit a dedicated usage sheet for crane operation whose content includes information of the suspended load, weight, total number and method of slinging by the crane staff. The usage sheet must be approved before proceeding. As a result, last year, there were no problems with the crane operations. Figure 2 shows last year's statistics of use of cranes. From April to June and from November to March, which is the beamtime period, the MLF staffs operated cranes for changing sample environment equipment and the frequency was almost same. On the other hand, from June to October, which is the period of maintenance of the neutron instruments, the MLF staffs and constructors used cranes, therefore, cranes were used most frequently in that period. During that time, the MLF managed the coordination of the crane-use schedule to accommodate the needs of staffs and constructors.

Figure 2. Trend of the total crane usage in one year.

M. Harada[1], M. Ooi[1], M. Sekijima[1], K. Kawakami[2], K. Aizawa[2], A. Hori[2], H. Tanaka[2], W. Kambara[2], M. Sawabe[2], K. Suzuya[3], N. Kawamura[4], Y. Sakaguchi[5], R. Takahashi[2], Y. Yamaguchi[5], and K. Soyama[6]

[1]*Neutron Source Section, Materials and Life Science Division, J-PARC Center;* [2]*Technology Development Section, Materials and Life Science Division, J-PARC Center;* [3]*Neutron Science Section, Materials and Life Science Division, J-PARC Center;* [4]*Muon Science Section, Materials and Life Science Division, J-PARC Center;* [5]*Neutron Science and Technology Center, CROSS;* [6]*Materials and Life Science Division*

MLF Operations in 2018

Beam Operation Status at MLF

Overall:

In Japanese Fiscal Year (JFY) 2018, the beam operation at the MLF started on April 1, 2018, with a beam power of 150 kW and ended on April 2, 2019. Table 1 shows the scheduled time and availability in JFY2018. In the schedule, 2018A switched to 2018 on November 8. Since the neutron Target #8, which was replaced in the summer of 2018, had the helium bubbler to mitigate cavitation erosion at the target vessel, the beam power was increased beyond 300 kW. The records of the beam power and the availability are shown in Fig. 1. In JFY2018, the beam operation started with the power of 400 kW from April 3 and was maintained at that level until the end of April. After confirmation of the operational status with a beam power of 500 kW, the power was increased from 400 kW to 500 kW with a double-bunch beam in time structure.

The operation continued until June 28, just before the summer outage period. Meanwhile, continuous beam operation with high stability and R&D for a high-intensity beam operation were carried out. In order to minimize the influence on the user caused by the target failure, we made a demonstration of the high-intensity beam operation after user beam delivery. A beam operational demonstration with 1-MW power was successfully completed within 1 hour on July 3. The memorial photo is shown in Fig. 2. After the summer outage period, the beam operation resumed on October 20. Due to the failure of the helium bubbler, the beam power was decreased from 500 kW to 300 kW. After the bubbler

Figure 2. Memorial photo after the completed demonstration of 1-MW beam operation on June 3, 2018.

Table 1. Run cycle, scheduled time, and availability.

Run	Duration	Scheduled time (h)	Beamtime (h)	Availability (%)
79	Apr 3 – Jun 29	1812	1669.0	92.1
80	Oct 22– Dec 16	1188	1120.1	94.3
81	Jan 22 – Mar 25	1294	1191.5	92.1
2018A	Apr 3 – Nov 7	2163	1974.9	92.0
2018B	Nov 8 – Mar 25	2131	2287.6	93.4
Overall		4294	4179.4	92.7

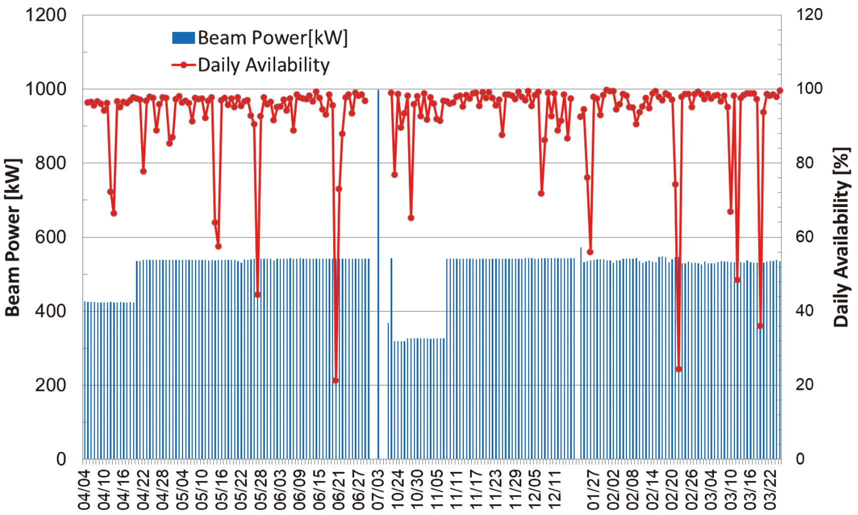

Figure 1. Beam power trend (blue line) at the MLF and availability per day (red line).

Table 2. Events that stopped the beam and made the daily availability of less than 80%.

Stop date	Cause of beam stop	Stop duration for each event [h]
4/12	RCS charge exchange foil failure	3.3
4/13	RCS RF failure	8.1
4/22	LINAC water flow shortage	4.5
5/14	LINAC vaccum pump failure	8.7
5/15	LINAC water flow shortage	10.2
5/27	3NBT magnet layer short failure	13.3
6/20	LINAC water leak at klystron gallery	18.9
6/21	Oarai facility radiation failure event	3.3
10/23	RCS kicker magnet #2 power supply failure	5.6
10/28	RCS kicker magnet #5 power supply failure	8.4
12/7	RCS kicker magnet #3 power supply failure	6.8
1/25 and 1/26	RCS shift bump magnet power supply failure	13.4
2/21 and 2/22	LINAC ion source failure and replacement	21.3
3/10	RCS RF power supply failure	8.0
3/12	LINAC water flow shortage and the power supply for the klystron	12.4
3/14	3-50BT bending magnet (B15D) failure surveirance	15.4

was repaired, the operation was continued with the beam power of 500 kW.

Since no significant failures occurred in JFY2018, the achieved average availability was as high as 92.7%. In the past, a relatively long beam shutdown period was required to complete the purification of the cryogenic system for the neutron moderator. In the summer of 2016, the impurities in the loop of the cryogenic system were removed completely; after that, the periodical purification is not required. Thus, a long uninterrupted work period of 4,179 h was attained in JFY2018.

The beam operation was stopped on several occasions due to minor failures. Typical causes of the beam stops with daily availability of less than 80% are summarized in Table 2 and described below.

LINAC:

During JFY2018, a shortage of water flow for the magnet and power supplies at LINAC occurred three times, on April 22, May 15, and March 12, respectively. A vacuum pump at LINAC for the beam dump (90-degree beam dump) failed on May 14. A controller of the high-voltage power supply to the klystron also failed. After the replacement of the controller, the beam operation was resumed. The ion source at LINAC was stopped on February 21. It took a long time to replace the ion source, which caused the most prolonged downtime of the operation in JFY2018.

3-GeV Rapid Cycling Synchrotron (RCS):

The power supplies to the kicker magnet at RCS failed three times, on October 23 and 28, and December 7, respectively. Also, the power supply for the shift bump magnet failed on January 25. Power supplies for the RCS RF also failed on April 13 and March 10.

Beam transport from RCS to MLF (3NBT) :

A malfunction of the quadruple magnet's coil happened on May 27 at 3NBT. Without the use of the failed magnet, the beam transport was resumed after the change of the beam optics at 3NBT.

30-GeV Synchrotron (MR):

A beam-bending magnet failed at the 3–50 BT, which delivers the beam from the RCS to MR. The coil also had malfunction due to the layer short. Without the usage of the bending magnet, the beam cannot continue the delivery. In order to survey the magnet failure preciously, the beam operation to MLF was stopped.

Other facilities:

The outside facility of J-PARC, Oarai, had a failure event involving radiation safety on June 21. JAEA decided to stop the operation of all facilities before the safety of each facility was confirmed. After the confirmation of the safety, the beam operation was resumed on June 22.

Users at the MLF

In fiscal year (FY) 2018, the MLF was running stably with beam power of 500 kW throughout the year, except for the first two weeks' 400-kW operation from April 3 and the first two weeks' 300-kW operation from October 22. That led to an average availability up to 92.7%. In addition, the 1-MW beam test was successfully operated for one hour on July 3, 2018, before the summer maintenance period. The total number of users of the neutron and muon experimental facilities in FY2018 reached 965, which was the highest number to date.

The trend for the number of users at the MLF since the start of the operations in FY2008 is summarized in Table 1 and Fig. 1.

Table 1. The number of domestic and foreign users by fiscal year.

	FY2008		FY2009		FY2010		FY2011		FY2012		FY2013	
	Domestic Users	Foreign Users	Domestic Users	Foreign Users	Domestic Users	Foreign Users	Domestic Users	Foreign Users	Domestic Users	Foreign Users	Domestic Users	Foreign Users
Neutron	107		317		476		259		708		449	
	95	12	303	14	432	44	238	21	628	80	399	50
Muon	18		40		50		23		56		61	
	18	0	38	2	42	8	21	2	46	10	50	11

	FY2014		FY2015		FY2016		FY2017		FY2018	
	Domestic Users	Foreign Users	Domestic Users	Foreign Users	Domestic Users	Foreign Users	Domestic Users	Foreign Users	Domestic Users	Foreign Users
Neutron	824		559		852		927		965	
	711	113	476	83	744	108	742	185	789	176
Muon	91		69		99		179		161	
	78	13	59	10	83	16	149	30	146	15

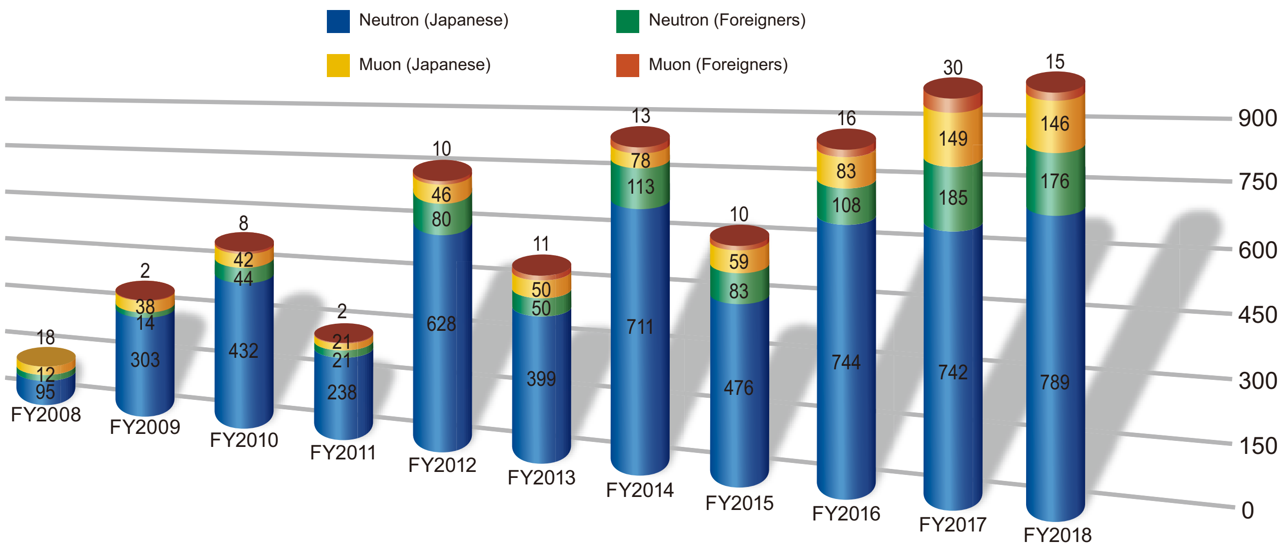

Figure 1. The number of domestic and foreign users by fiscal year.

MLF Proposals Summary – FY2018

Table 1. Breakdown of Proposals Numbers for the 2018 Rounds.

Beam-line	Instrument		2018A		2018B		Full Year			
			Submitted	Approved	Submitted	Approved	Submitted		Approved	
			GU	GU	GU	GU	PU/S	IU	PU/S	IU
BL01	4D-Space Access Neutron Spectrometer - ***4SEASONS***		18(0)	10(0)	18(0)	13(0)	1	1	1	1
BL02	Biomolecular Dynamics Spectrometer - ***DNA***		14(1)	12(1)	25(2)	13(2)	2	1	2	1
BL03	Ibaraki Biological Crystal Diffractometer - ***iBIX***	(100–β)‡	4	2	2	1	0	0	0	0
		(β)†	0	0	0	0	33	0	33	0
BL04	Accurate Neutron-Nucleus Reaction Measurement Instrument - ***ANNRI***		6	4	10	4	1	1	1	1
BL05	Neutron Optics and Physics - ***NOP***		3	3	5	5	0	0	0	0
BL06	Neutron Resonance Spin Echo Spectrometers - ***VIN ROSE***		2	2	7	4	0	0	0	0
BL08	Super High Resolution Powder Diffractometer - ***S-HRPD***		8	7	9	8(0)	0	0	0	0
BL09	Special Environment Neutron Power Diffractometer - ***SPICA***		4	1	2	2	0	0	0	0
BL10	Neutron Beamline for Observation and Research Use - ***NOBORU***		4	4	10	7	2	1	2	1
BL11	High-Pressure Neutron Diffractometer - ***PLANET***		9(0)	7(0)	7(0)	7	0	1	0	1
BL12	High Resolution Chopper Spectrometer - ***HRC***		8	6	7	7	1	0	1	0
BL14	Cold-neutron Disk-chopper Spectrometer - ***AMATERAS***		34	17	24	13	3	1	3	1
BL15	Small and Wide Angle Neutron Scattering Instrument - ***TAIKAN***		34(3)	17(3)	36(3)	22(3)	3	3	3	3
BL16	High-Performance Neutron Reflectometer with a horizontal Sample Geometry - ***SOFIA***		20	18	20	19	0	1	0	1
BL17	Polarized Neutron Reflectometer - ***SHARAKU***		16(0)	11(0)	20(1)	14(1)	2	3	2	3
BL18	Extreme Environment Single Crystal Neutron Diffractometer - ***SENJU***		24(0)	12(0)	18(0)	5(0)	1	2	1	2
BL19	Engineering Diffractometer - ***TAKUMI***		20	18	22	15(0)	1	1	1	1
BL20	Ibaraki Materials Design Diffractometer - ***iMATERIA***	(100–β)‡	8	7	7	7	0	0	0	0
		(β)†	31	31	31	31	25	0	25	0
BL21	High Intensity Total Diffractometer - ***NOVA***		15	13	25	19	0	0	0	0
BL22	Energy Resolved Neutron Imaging System - ***RADEN***		13(1)	12(1)	20(2)	15(2)	0	3	0	3
BL23	Polarization Analysis Neutron Spectrometer - ***POLANO***		0	0	0	0	0	0	0	0
D1	Muon Spectrometer for Materials and Life Science Experiments - ***D1***		9(1)	6(1)	15(1)	4(1)	0	1	0	1
D2	Muon Spectrometer for Basic Science Experiments - ***D2***		8(0)	6(0)	9(0)	6(0)	0	1	0	1
S1	General purpose μSR spectrometer - ***ARTEMIS***		13(0)	12(0)	25(2)	18(2)	0	1	0	1
UA	Muon U		0	0	0	0	0	1	0	1
Total			**325**	**238**	**374**	**266**	**75**	**23**	**75**	**23**

GU : General Use **PU :** Project Use or Ibaraki Pref. Project Use **S :** S-type Proposals
IU : Instrument Group Use
† : Ibaraki Pref. Exclusive Use Beamtime (β = 80% in FY2018)
‡ : J-PARC Center General Use Beamtime (100–β = 20% in FY2018)
( ) : Proposal Numbers under New User Promotion or P-type proposals (D1,D2) in GU

Table 2. Proposals Numbers of Long Term Proposal.

Application FY	Submitted	Approved
2017	24	8
2018	9	5

In addition, you can check the MLF experimental Report 2018 via the following links:
http://j-parc.jp/researcher/MatLife/en/lists/2018A.html
http://j-parc.jp/researcher/MatLife/en/lists/2018B.html
http://j-parc.jp/researcher/MatLife/en/lists/2018AB.html
http://j-parc.jp/researcher/MatLife/en/lists/2018LTP.html

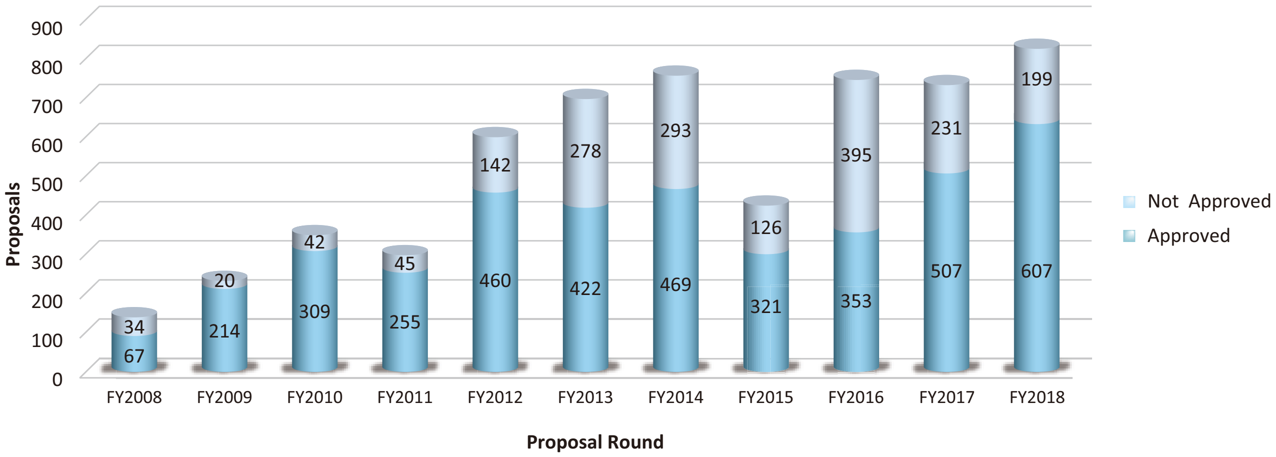

Figure 1. MLF Proposal Numbers over Time.

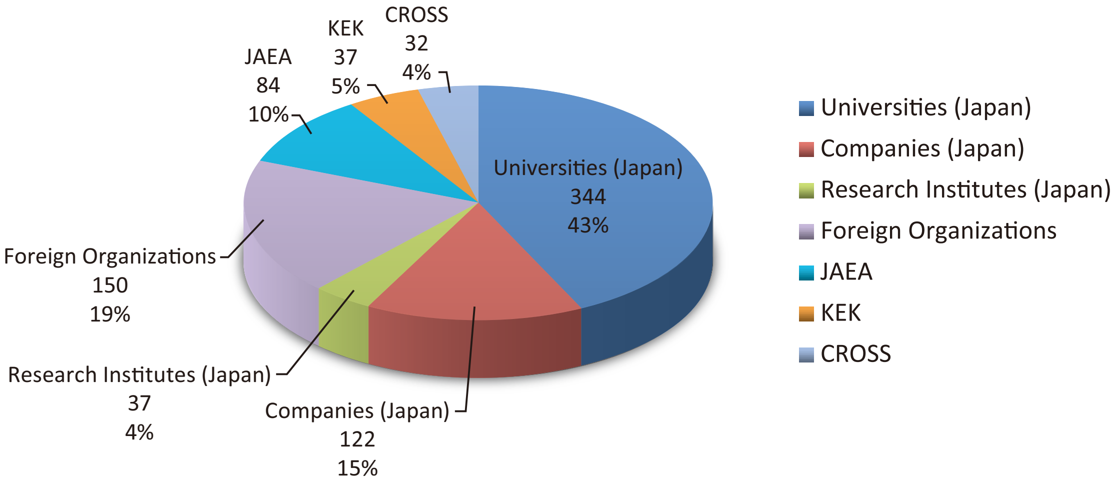

Figure 2. Origin of Submitted Proposals by affiliation - FY2018.

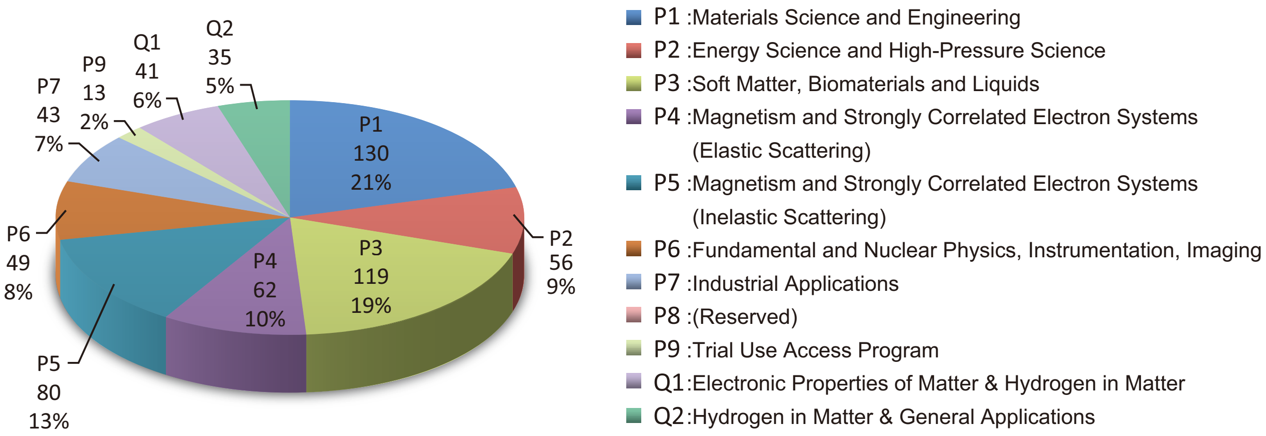

Figure 3. Submitted Proposals by Sub-committee/Expert Panel - FY2018.

MLF Division Staff 2018

Toshiji Kanaya (Head)
Kazuhiko Soyama (Deputy Head)
Toshiya Otomo (Deputy Head)
Yasuhiro Miyake (Deputy Head)
Kazuya Aizawa (Deputy Head)
Eiichi Wakai
Izumi Kuwahara

Neutron Source Section

*: additional duties

<JAEA>

Katsuhiro Haga (Leader)
Kenji Sakai (Sub-Leader)
Masahide Harada
Makoto Teshigawara
Hiroyuki Kogawa
Tomokazu Aso
Motoki Ooi
Takashi Naoe
Takashi Wakui
Masakazu Seki
Shiho Masuda
Motonori Takagi
Hideyuki Nemoto
Akihiko Watanabe
Hideki Muto
Kouhei Hanano
Mitsuaki Sekijima
Katsuhiro Aoyagi
Yoshinori Kikuchi
Masakazu Nakamura
Hidemitsu Hosokawa
Atsushi Akutsu
Toshiyuki Yasuhra
Hiromi Inoue
Noriyuki Morikawa
Shizuka Yoshinari
Miyuki Hoshino
Hiroshi Takada *
Shoichi Hasegawa *
Eiichi Wakai *
Shin-ichiro Meigo *
Hidetaka Kinoshita *
Kenichi Oikawa *
Tetsuya Kai *
Hiroyuki Uehara *

Neutron Science Section

*: additional duties

<JAEA>

Kenji Nakajima (Leader)
Yukinobu Kawakita (Sub-Leader)
Kentaro Suzuya
Ryoichi Kajimoto
Takanori Hattori
Mitsutaka Nakamura
Stefanus Harjo
Kenichi Oikawa
Takashi Ohhara
Takenao Shinohara
Tetsuya Kai
Seiko Kawamura
Shinichi Takata
Ryoji Kiyanagi
Kaoru Shibata
Asami Sano
Yasuhiro Inamura
Hiroyuki Aoki
Takuro Kawasaki
Kousuke Hiroi
Maiko Kofu
Naoki Murai
Yoshichika Seki
Takayuki Yamashita
Tatsuya Kikuchi
Takeshi Harada
Hideaki Isozaki
Kazuhiro Aoyama
Misono Fujii
Naoko Shimizu
Mariko Ohtake
Miho Igarashi
Itaru Tamura *
Kouji Kaneko *
Hiroshi Nakagawa *
Hideo Harada *
Atsushi Kimura *
Shoji Nakamura *
Yosuke Toh *
Mariko Segawa *
Masahide Harada *
Kazuya Aizawa *
Masao Watanabe *
Dai Yamazaki *
Hiroshi Suzuki *
Satoshi Morooka *
Atsushi Moriai *
Kazuo Kurihara *
Tarou Tamada *
Yuu Hirano *

<KEK>

Shinichi Ito (Sub-Leader)
Hideki Seto
Toshiya Otomo *
Takashi Kamiyama
Hitoshi Endo
Testuya Yokoo
Takashi Ino
Norifumi Yamada
Takashi Honda
Naokatsu Kaneko
Shuki Torii
Hidetoshi Oshita
Kaoru Taketani
Kenji Mishima
Kazutaka Ikeda
Masao Yonemura
Masato Hagihala
Fumiya Nemoto
Hiraku Saito
Seiji Sugai

Technology Development Section

*: additional duties

<JAEA>

Kazuya Aizawa * (Leader)
Takayuki Oku (Sub-Leader)
Takeshi Nakatani
Masao Watanabe
Yuhua Su
Takuya Okudaira
The Dang Vu
Wataru Kambara
Akihiro Hori
Hideaki Takahashi
Ryuta Takahashi
Wu Gong
Kazuhiro kawakami
Hiromichi Tanaka
Masaki Sawabe
Yukiko Nagai
Kenji Sakai *
Tetsuya Kai *
Hiroyuki Kogawa *
Motoki Ooi *
Kentaro Suzuya *
Mitsutaka Nakamura *
Shinichi Takata *
Kaoru Sakasai *
Tatsuya Nakamura *
Yasuhiro Inamura *
Masahide Harada *
Tomokazu Aso *
Seiko Kawamura *
Fumiaki Kono *
Rumi Shimizu *
Tatsuhito Matsuo *
Satoru Fujiwara *
Motoyasu Adachi *
Shigeki Arai *
Yoshiteru Yonetani *

<KEK>

Setsuo Sato
Tomohiro Seya
Testuya Yokoo *
Shuki Torii *
Takashi Ino *
Naokatsu Kaneko *
Kaoru Taketani *
Naritoshi Kawamura *
Hiroshi Fujimori *
Shunsuke Makimura *

Neutron Instrumentation Section

*: additional duties

<JAEA>

Kaoru Sakasai (Leader)
Dai Yamazaki
Kentaro Toh
Tatsuya Nakamura
Ryuji Maruyama *
Noriaki Tsutsui
Yukiko Uno
Masumi Ebine *

Muon Science Section

*: additional duties

<KEK>

Ryosuke Kadono (Leader)
Naritoshi Kawamura (Sub-Leader)
Yasuhiro Miyake *
Koichiro Shimomura
Patrick Strasser
Akihiro Koda
Takayuki Yamazaki
Yu Oishi
Yukinori Nagatani
Shiro Matoba
Soshi Takeshita
Hiroshi Fujimori
Shunsuke Makimura
Yasuo Kobayashi
Yutaka Ikedo
Junpei Nakamura
Taihei Adachi
Shoichiro Nisimura
Masatoshi Hiraishi
Hirotaka Okabe
Motonobu Tanpo
Tatsuhiko Tachibana
Hua Li
Masato Tabe
Shogo Doiuchi
Akiko Hashimoto
Izumi Umegaki

<JAEA>

Wataru Higemoto *
Takashi Ito *

CROSS Staff 2018

Director **Hideaki Yokomizo**

Science Coordinators

Kazuhisa Kakurai
Mikio Kataoka
Makoto Hayashi
Takashi Noma

Research & Development Division

*: additional duties

Jun-ichi Suzuki (Head)
Kenichi Funakoshi (Deputy Head)
Tsukasa Miyazaki *(Deputy Head)
Sayaka Suzuki

<BL01 Group>
Kazuya Kamazawa (Leader)
Kazuhiko Ikeuchi
Kazuki Iida

<BL02 Group>
Masato Matsuura (Leader)
Takeshi Yamada
Taiki Tominaga

<BL11 Group>
Kenichi Funakoshi *(Leader)
Jun Abe
Shinichi Machida

<BL15 Group>
Kazuki Ohishi (Leader)
Jun-ichi Suzuki *
Hiroki Iwase
Yukihiko Kawamura

<BL17 Group>
Noboru Miyata (Leader)
Kazuhiro Akutsu
Takayasu Hanashima

<BL18 Group>
Akiko Nakao (Leader)
Koji Munakata
Yoshihisa Ishikawa

<BL22 Group>
Hirotoshi Hayashida (Leader)
Joseph Don Parker
Yoshihiro Matsumoto

<Technical Support Group>
Koji Kiriyama (Leader)
Takayoshi Ito (Sub-Leader)
Yoshifumi Sakaguchi
Hiroshi Kira
Motoyuki Ishikado
Nobuo Okazaki
Shuoyuan Zhang
Makoto Kobayashi
Satoshi Kasai
Toshiaki Morikawa
Hideyuki Hiramatsu
Yutaka Ebara
Kentaro Moriyama
Hiroshi Arima
Yasuji Masuda
Keiichi Ohuchi
Masae Sahara

Safety Division

*: additional duties

Yasuhiro Yamaguchi (Head)
Koji Kiriyama *
Tazuko Mizusawa *
Masae Sahara *

Utilization Promotion Division

*: additional duties

Junichi Sato (Head)
Tsukasa Miyazaki (Deputy Head)
Atsuko Irie
Seiya Konishi (Leader)
Tazuko Mizusawa
Miho Igarashi
Toshiki Asai (Leader)
Emi Goto
Taeko Ishikawa
Maya Endo
Junko Ohta
Yutaka Ebara *
Takayoshi Ito *
Nobuo Okazaki *

Administration Division

Michihiko Murasawa (Head)
Takashi Hikita (Leader)
Rei Ohuchi
Tomoko Sakuma
Mutsumi Shiraishi
Shinobu Matsumoto

Proposals Review System, Committees and Meetings

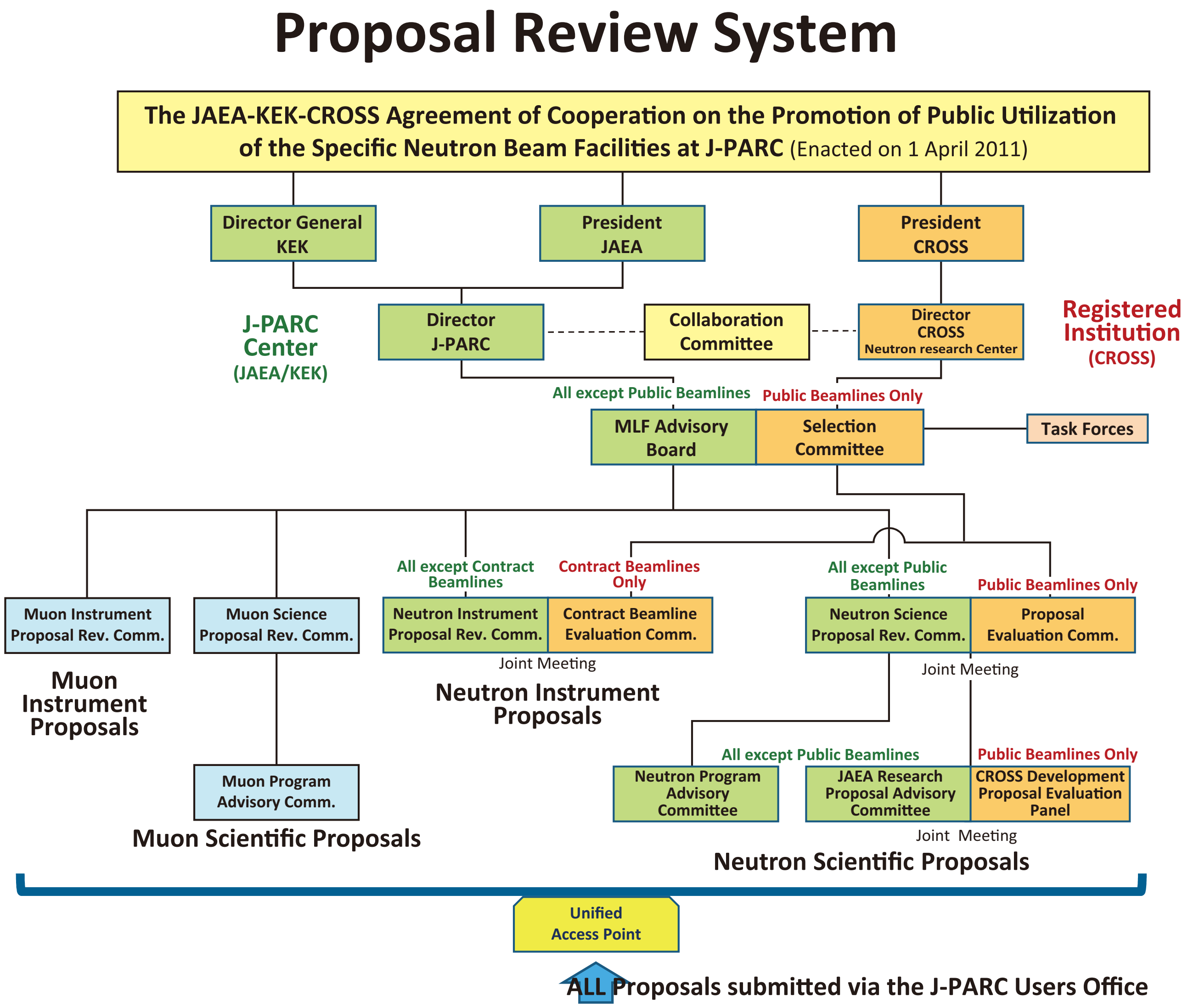

Figure 1. Proposals Review System Framework.

Materials and Life Science Facility Advisory Board

Kazuya Aizawa	Japan Atomic Energy Agency
Hiroshi Amitsuka	Hokkaido University
Taka-hisa Arima	The University of Tokyo
Masatoshi Futakawa	Japan Atomic Energy Agency
Ryosuke Kadono	High Energy Accelerator Research Organization
Kazuhisa Kakurai	Comprehensive Research Organization for Science and Society
Takashi Kamiyama	High Energy Accelerator Research Organization
Takashi Kamiyama	Hokkaido University
Toshiji Kanaya	High Energy Accelerator Research Organization
Yukinobu Kawakita	Japan Atomic Energy Agency
Takamitsu Kohzuma	Ibaraki University
Yoji Koike	Tohoku University
Kenya Kubo	International Christian University
Yasuhiro Miyake	High Energy Accelerator Research Organization
Kenji Nakajima	Japan Atomic Energy Agency
Toshiya Otomo	High Energy Accelerator Research Organization
Yoshiharu Sakurai	Japan Synchrotron Radiation Research Institute
Taku Sato	Tohoku University
Hideki Seto	High Energy Accelerator Research Organization
Mitsuhiro Shibayama	The University of Tokyo
Kazuhiko Soyama	Japan Atomic Energy Agency
Masaaki Sugiyama (chair)	Kyoto University
Jun-ichi Suzuki	Comprehensive Research Organization for Science and Society
Atsushi Takahara	Kyushu University
Masayasu Takeda	Japan Atomic Energy Agency
Toshio Yamaguchi	Fukuoka University

Term: through March 31, 2021

Neutron Science Proposal Review Committee

Hiroyuki Kagi	The University of Tokyo
Ryosuke Kadono	High Energy Accelerator Research Organization
Toshiji Kanaya	High Energy Accelerator Research Organization
Yoshiaki Kiyanagi	Nagoya University
Tsukasa Miyazaki	Comprehensive Research Organization for Science and Society
Kenji Nakajima	Japan Atomic Energy Agency
Kenji Ohoyama	Ibaraki University
Hideki Seto	High Energy Accelerator Research Organization
Shinichi Shamoto	Japan Atomic Energy Agency
Yuichi Shimakawa	Kyoto University
Hirohiko Shimizu	Nagoya University
Masaaki Sugiyama (chair)	Kyoto University
Masayasu Takeda	Japan Atomic Energy Agency
Ichiro Tanaka	Ibaraki University

Term: through September 30, 2019

Muon Science Proposal Review Committee

Tadashi Adachi	Sophia University
Kenta Amemiya	High Energy Accelerator Research Organization
Hiroshi Amitsuka	Hokkaido University
Hidehito Asaoka	Japan Atomic Energy Agency
Toshiyuki Azuma	Institute of Physical and Chemical Research
Katsuyuki Fukutani	The University of Tokyo
Wataru Higemoto	Japan Atomic Energy Agency
Adrian Hillier	Rutherford Appleton Laboratory
Ryosuke Kadono	High Energy Accelerator Research Organization
Toshiji Kanaya	High Energy Accelerator Research Organization
Naritoshi Kawamura	High Energy Accelerator Research Organization

Yasushi Kino	Tohoku University
Akihiro Koda	High Energy Accelerator Research Organaization
Kenya Kubo (chair)	International Christian University
Roderick Macrae	Marian University
Yasuyuki Matsuda	University of Tokyo
Tsutomu Mibe	High Energy Accelerator Research Organization
Yasuhiro Miyake	High Energy Accelerator Research Organization
Kenji Nakajima	Japan Atomic Energy Agency
Chihiro Ohmori	High Energy Accelerator Research Organization
Toshiya Otomo	High Energy Accelerator Research Organization
Hideki Seto	High Energy Accelerator Research Organization
Tatsushi Shima	Osaka University
Koichiro Shimomura	High Energy Accelerator Research Organaization
Jun Sugiyama	Toyota Central R&D Labs.
Masaaki Sugiyama	Kyoto University Research Reactor Institute
Toshiyuki Takayanagi	Saitama University
Hideki Tou	Kobe University

Term: through March 31, 2019

Proposal Evaluation Committee

Hiroyuki Kagi	The University of Tokyo
Toshiji Kanaya	High Energy Accelerator Research Organization
Yoshiaki Kiyanagi	Nagoya University
Tsukasa Miyazaki	Comprehensive Research Organization for Science and Society
Kenji Ohoyama	Ibaraki University
Shinichi Shamoto	Japan Atomic Energy Agency
Yuichi Shimakawa	Kyoto University
Hirohiko Shimizu	Nagoya University
Masaaki Sugiyama (chair)	Kyoto University
Ichiro Tanaka	Ibaraki University

Term: through September 30, 2019

Selection Committee

Taka-hisa Arima	The University of Tokyo
Yasuhiro Iye (chair)	Japan Society for Promotion of Science
Takashi Kamiyama	Hokkaido University
Hiroyuki Kishimoto	Sumitomo Rubber Industries, LTD.
Hideaki Kitazawa	Research Center for Strategic Materials
Yoji Koike	Tohoku University
Takamitsu Kohzuma	Ibaraki University
Yoshiharu Sakurai	Japan Synchrotron Radiation Research Institute
Taku Sato	Tohoku University
Mitsuhiro Shibayama	The University of Tokyo
Masaaki Sugiyama	Kyoto University
Atsushi Takahara	Kyushu University
Shinji Tsuneyuki	The University of Tokyo
Toshio Yamaguchi	Fukuoka University

Term: through March 31, 2021

Neutron Advisory Committee (NAC)

NAC convened 18–19 February, 2019 at the J-PARC Research Center, Tokai


Group photo of NAC


Neutron Advisory Committee (18–19 Feb. 2019)

Robert McGreevy (chair)	Rutherford Appleton Laboratory
Bertrand Blau	Paul Scherrer Institut (PSI)
Mark Wendel	Oak Ridge National Laboratory
oshiaki Kiyanagi	Nagoya University
Christiane Alba Simionesco	The Laboratoire Leon Brilloin
Jamie Schulz	Australian Nuclear Science and Technology Organization
Andreas Schreyer	European Spallation Source
Sung-Min Choi	Korea Advanced Institute of Science and Technology
Yoshie Otake	Institute of Physical and Chemical Research
Masaaki Sugiyama	Kyoto University
Christian Rüegg	Paul Scherrer Institut

Muon Advisory Committee (MAC)

MAC convened 1 - 2 March, 2019 at the KEK Tokai Campus, Tokai


Group photo of MAC


Muon Advisory Committee (1–2 Mar. 2019)

Prokscha Thomas (chair)	The Paul Scherrer Institute
Martin Månsson	KTH Royal Institute of Technology
Andrew Macfarlane	The University of British Columbia
Klaus Kirch	ETH Zurich and Paul Scherrer Institute
Kenya Kubo	International Christian University
Tadayuki Takahashi	The University of Tokyo
Takashi Nakano	Osaka University
Hiroshi Amitsuka	Hokkaido University

Workshops, Conferences, Seminars and Schools in 2018

Conferences held jointly by J-PARC MLF and CROSS

The 21th Conference on Superionic Conductor (The 70th Solid State Ionics Society of Japan)
1–2 Jun. 2018, IBARAKI Quantum Beam Research Center, Ibaraki

The 1st Workshop on Deuterium Materials
10, Jul. 2018, Nagoya Institute of Technology, Aichi

2018 Meeting on J-PARC MLF Industrial Use
23–24 Jul. 2018, Akihabara Convention Hall, Tokyo


Photo of the 2018 Meeting on J-PARC MLF Industrial Use (photo courtesy of J-PARC Center)

The 6th Workshop on Pulsed Neutron Imaging
10 Oct. 2018, Essam Kanda Hall, Tokyo

User Group Meeting on MLF Spectrometers DIRECTION 2018
10–11 Oct. 2018, IBARAKI Quantum Beam Research Center, Ibaraki


Group photo of User Group Meeting on MLF Spectrometers DIRECTION 2018

User Group Meeting on TOF near Backscattering Spectrometer DNA 2018
12 Oct. 2018, IBARAKI Quantum Beam Research Center, Ibaraki


Photo of User Group Meeting on TOF near Backscattering Spectrometer DNA 2018

2018 Z-Code Intermediate Level Training Course
16 Nov. 2018, Essam Kanda Hall, Tokyo

J-PARC Workshop: Deuterated Materials Enhancing Neutron Science for Structure Function Applications
15–16 Jan. 2019, IBARAKI Quantum Beam Research Center, Ibaraki


Photo of the J-PARC Workshop (photo courtesy of J-PARC Center)

2018 Z-Code Beginner Level Training Course
2 Feb. 2019, Essam Kanda Hall, Tokyo

Meeting on Evaluation Technology of Reinforced Concrete Using Neutron
15 Feb. 2019, Tokyu Construction Co., Ltd., Tokyo

3rd Workshop on the Collaborative Use of Large Research Institutions and the KEI Super Computer 2018
25 Feb. 2019, Public Relation Center SPring-8, Hyogo

2018 Quantum Beam Science Festival (The 10th MLF Symposium and The 36th PF Symposium)
12–13 Mar. 2019, Tsukuba International Congress Center, Ibaraki

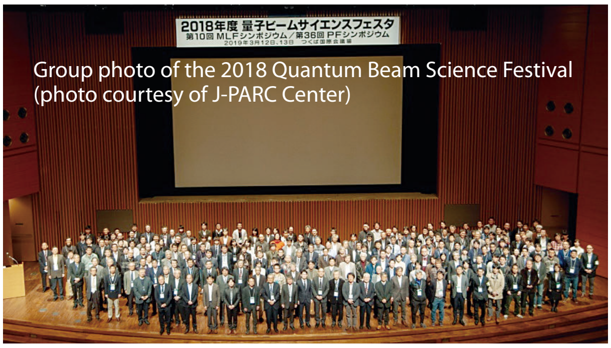

Group photo of the 2018 Quantum Beam Science Festival (photo courtesy of J-PARC Center)

Workshops held by KEK

Workshop for Negative Muon Research
1–3 Jul. 2018 KEK Tokai Campus, Ibaraki

Workshop for Neutron Spin Echo Research (BL06)
30 Oct. 2018, KEK Tokai Campus, Ibaraki

Structural Study for Functional Materials using SPICA (BL09)
26 Nov. 2018, KEK Tsukuba Campus, Ibaraki

Fundamental Physics with Pulsed Cold Neutrons (BL05)
21 Dec. 2018, Nagoya University, Nagoya

High-Resolution Neutron Powder Diffraction Method using SuperHRPD (BL08)
25 Dec. 2018, KEK Tsukuba Campus, Ibaraki

Workshops and Seminars held by CROSS and other organizations

The 21th CROSSroads Workshop “Dynamics and Neutron Scattering of Biological Materials and Hydrated Water”
2 Jul. 2018, IBARAKI Quantum Beam Research Center and KEK Tokai Campus, Ibaraki

Group photo of the CROSSroad 21 (photo courtesy of CROSS)

2018 1st Workshop on Structural Biology
2 Sep. 2018, Essam Kanda Hall, Tokyo

2018 1st Workshop on Polymer Science under Humidity Control
1 Oct. 2018, TKY Conference Center, Tokyo

2018 1st Workshop on Residual Stress and Strain
9 Oct. 2018, Essam Kanda Hall, Tokyo

2018 2nd Workshop on iMATERIA “Neutron Scattering of Electrode Material on Charge/discharge”
18 Oct. 2018, Essam Kanda Hall, Tokyo

Neutron Experiment Technique Training Course
2 Nov. 2018, Essam Kanda Hall, Tokyo

Workshop on Magnetc Materials
9 Nov. 2018, Essam Kanda Hall, Tokyo

Workshop on Non-destructive Visualization and Analysis Methods
14 Nov. 2018, Essam Kanda Hall, Tokyo

Meeting on Deuterium Labeled Compound for Neutron Science

15 Nov. 2018, J-PARC Center and IBARAKI Quantum Beam Research Center, Ibaraki

Group photo of the CROSSroad 21 (photo courtesy of J-PARC Center)

2018 Workshop on Materials Science

14 Dec. 2018, Essam Kanda Hall, Tokyo

2018 Workshop on Soft Matter Neutron Scattering

25 Dec. 2018, Essam Kanda Hall, Tokyo

2018 Workshop on Battery Materials

15 Jan. 2019, KENKYUSHA EIGO Center, Tokyo

2018 Workshop on Surfaces and Interfaces

30 Jan. 2019, Essam Kanda Hall, Tokyo

2018 Workshop on Metallographic Structure

22 Feb. 2019, Essam Kanda Hall, Tokyo

2018 Workshop on Liquids and Amorphous Materials

11 Mar. 2019, Tsukuba International Congress Center, Ibaraki

5th Symposium on the Collaborative Use of Large Research Institutions and the KEI Super Computer 2018

15 Mar. 2018, Akihabara UDX, Tokyo

2018 2nd Workshop on Residual Stress and Strain

19 Mar. 2019, Essam Kanda Hall, Tokyo

2018 2nd Workshop on Structural Biology

27 Mar. 2019, Essam Kanda Hall, Tokyo

Schools in 2018

Hello Science from J-PARC: Investigation "Water" Deep in the Earth with Neutrons

14 May. 2018, iVil, Tokai

The 3rd Neutron and Muon School

20–24 Nov. 2018, J-PARC Center and IBARAKI Quantum Beam Research Center, Ibaraki

Group photo of the 3rd Neutron and Muon School (photo courtesy of J-PARC Center)

Hello Science from J-PARC: Observing the Force Supporting Reinforced Concrete by Neutrons

30 Nov. 2018, iVil, Tokai

Hello Science from J-PARC: Visualization of Lithium Ion Secondary Battery using Neutron Beam

22 Feb. 2019, iVil, Tokai

Award List

51st The Atomic Energy Society of Japan Award : Best Paper Award
Measurements of neutron total and capture cross sections of ^{241}Am with ANNRI at J-PARC
K. Terada, A. Kimura, T. Nakao (2019-03-21)

The Journal of Nuclear Science and Technology Most Cited Article Award 2018
Neutron-capture cross-sections of ^{244}Cm and ^{246}Cm measured with an array of large germanium detectors in the ANNRI at J-PARC/MLF
K. Terada, A. Kimura, T. Nakao, S. Nakamura, K. Mizuyama, N. Iwamoto, O. Iwamoto, H. Harada, T. Katabuchi, M. Igashira, T. Sano, Y. Takahashi, C.H. Pyeon, S. Fukutani, T. Fujii, T. Yagi, K. Takamiya & J. Hori (2019-03-21)

JSNS President's Choice
Clarification of refrigerant boiling behavior in an evaporator utilizing neutron imaging.
T. Fuse, T. Okamura, S. Inoue, T. Matsuno, R. Iwata, T. Yamauchi, T. Shimazu, Y. Matsumoto, T. Shinohara, T. Kai (2018-12-05)

The18th JSNS Poster Prize
Expansion of application of neutron atomic resolution holography
S. Uechi (2018-12-04)

The18th JSNS Poster Prize
Simulation Software for Neutron Holography Apply to B doped 6H-SiC
Y. Fukumoto (2018-12-04)

73rd Ceramic Society of Japan Awards for advancements in ceramic science and technology (2018)
High-performance ferroelectric perovskites by controlling defect and polarization structures
Y. Kitanaka (2018-11-29)

73rd The Ceramic Society of Japan Academic Award (2018)
Materials design and new function development of polar perovskites
Y. Noguchi (2018-11-29)

JAEA President Award 2018 [R & D Achievement Prize]
Construction and Leading Research of the Energy-Resolved Neutron Imaging System, RADEN
T. Shinohara, T. Kai, K. Oikawa, M. Segawa, T. Nakatani, M. Harada, M. Ooi, K. Hiroi, Y.H. Su, Y. Kiyanagi, T. Kamiyama, H. Sato, J.D. Parker, H. Hayashida, Y. Matsumoto (2018-10-01)

School of High Energy Accelerator Science Dean's Award
The investigation of negative thermal expansion and magnetic structure in $La_{0.5}Ba_{0.5}CoO_{3-x}$ *by neutron powder diffraction.*
Z.J. Tan (2018-09-29)

APS Fellow
K. Tanaka (2018-09)

Jacek Grochowski Memorial Poster Prize
Local structure observation of Sm doped RB6 (R: rare earth) by white neutron atomic resolution holography
S. Uechi (2018-08-27)

The Adhesion Society of Japan Award
Study on molecular picture of adhesive interface
K. Tanaka (2018-06)

Award of The Society of Fiber Science and Technology, Japan
A Novel Design Concept of Bio-scaffolds Based on Dimension Controlled Polymers
H. Matsuno (2018-06)

Atom Indonesia Best Paper Award 2017(I-AIBPA 2017)
Synthesis, Structural and Magnetic Properties of $La_{0.5}Ba_{0.5}CoO_{2.75+x}$
Z.J. Tan, P. Miao, Y. Ishikawa, M. Hagihala, S. Lee, S. Torii, M. Yonemura, T. Kamiyama
Atom Indonesia **44** 49 (2018) (2017-12-5)

MLF Publication 2018

1 S. Lee, M.-C. Lee, Y. Ishikawa, P. Miao, S. Torii, C. Won, K. Lee, N. Hur, D.-Y. Cho, and T. Kamiyama
Crystal and Magnetic Structures of La_2CoPtO_6 *Double Perovskite*
ACS Omega **3** 11624 (2018)

2 N. Yano, T. Yamada, T. Hosoya, T. Ohhara, I. Tanaka, N. Niimura, and K. Kusaka
Status of the neutron time-of-flight single-crystal diffraction data-processing software STARGazer
Acta Crystallographica Section D STRUCTURAL BIOLOGY **D74** 1041–1052 (2018)

3 J.W. Bae, J.B. Seol, J. Moon, S.S. Sohn, M.J. Jang, H.Y. Um, B.-J. Lee, and H.S. Kim
Exceptional phase-transformation strengthening of ferrous medium-entropy alloys at cryogenic temperatures
Acta Materialia **161** 388–399 (2018)

4 K. Tomiyasu, N. Ito, R. Okazaki, Y. Takahashi, M. Onodera, K. Iwasa, T. Nojima, T. Aoyama, K. Ohgushi, Y. Ishikawa, T. Kamiyama, S. Ohira-Kawamura, M. Kofu, and S. Ishihara
Quantum paramagnet near spin-state transition
Advanced Quantum Technologies **2018** 1800057 (2018)

5 K. Suekuni, C.-H. Lee, H.I. Tanaka, E. Nishibori, A. Nakamura, H. Kasai, H. Mori, H. Usui, M. Ochi, T. Hasegawa, M. Nakamura, S. Ohira-Kawamura, T. Kikuchi, K. Kaneko, H. Nishiate, K. Hashikuni, Y. Kosaka, K. Kuroki, and T. Takabatake
Retreat from stress: rattling in a planar coordination
Advansed Materials **30** 1706230 (2018)

6 K. Ikeuchi, K. Nakajima, S. Ohira-Kawamura, R. Kajimoto, S. Wakimoto, and M. Fujita
Al-impurity-induced magnetic excitations in heavily over-doped $La_{1.7}Sr_{0.3}Cu_{0.95}Al_{0.05}O_4$
AIP Advances **8** 101318 (2018)

7 T. Okuda, R. Kajimoto, M. Noda, and H. Kuwahara
Schottky specific heat of the lightly Mn-substituted electron-doped $SrTiO_3$
AIP Advances **8** 101339 (2018)

8 T. Yokoo, S. Itoh, N. Kaneko, M. Fujita, T. Ino, M. Ohkawara, and M. Sakaguchi
Ready to Roll? Time to Launch POLANO
AIP Conf. Proc. **1969** 050001 (2018)

9 S. Itoh, T. Yokoo, T. Masuda, H. Yoshizawa, M. Soda, S. Ibuka, Y. Ikeda, M. Yoshida, T. Hawai, D. Kawana, R. Sugiura, T. Asami, Y. Kawamura, T. Shinozaki, and Y. Ihata
High Resolution Chopper Spectrometer HRC and Neutron Brillouin Scattering
AIP Conf. Proc. **1969** 050002 (2018)

10 R. Kajimoto, K. Sato, Y. Inamura, and M. Fujita
Instrumental Resolution of the Chopper Spectrometer 4SEASONS Evaluated by Monte Carlo Simulation
AIP Conf. Proc. **1969** 050004 (2018)

11 Y. Fukushima, K. Yamada, K. Tamura, and K. Shibata
Dynamic of organic species in organo-clay / polypropyrene composite by quesi-elastic neutron scattering
Appl. Clay. Sci. **155** 15–19 (2018)

12 H. Iwase, T. Ogura, H. Sakuma, K. Tamura, and Y. Fukushima
Structural investigation of hectorite aqueous suspensions by dielectric microscopy and small-angle neutron scattering coupling with rheological measurement
Appl. Clay. Sci. **157** 24–30 (2018)

13 T. Takami, Y. Morita, M. Yonemura, Y. Ishikawa, S. Tanaka, M. Mori, T. Fukunaga, and E. Matsubara
Appearance of Lithium-Ion Conduction in a La–Li–Co–O Band Insulator: Possible Route to Oxide Electrolyte
Applied Energy Materials **1** 2546 (2018)

14 C.H. Lee, A. Nishida, T. Hasegawa, H. Nishiate, H. Kunioka, S. Ohira-Kawamura, M. Nakamura, K. Nakajima, and Y. Mizuguchi
Effect of rattling motion without cage structure on lattice thermal conductivity in $LaOBiS_{2-x}Se_x$
Applied Physics Letters **112** 023903 (2018)

15 Z.J. Tan, P. Miao, Y. Ishikawa, M. Hagihala, S. Lee, S. Torii, M. Yonemura, and T. Kamiyama
Synthesis, Structural and Magnetic Properties of $La_{0.5}Ba_{0.5}CoO_{2.75+x}$
Atom Indonesia **44** 49 (2018)

16 M. Hirai, S. Ajito, M. Sugiyama, H. Iwase, S. Takata, N. Shimizu, N. Igarashi, A. Martel, and L. Porcar
Direct evidence for the effect of glycerol on protein hydration and thermal structural transition
Biophys. J. **115** 313–327 (2018)

17 Y. Kameda, Y. Amo, T. Usuki, Y. Umebayashi, K. Ikeda, and T. Otomo
Neutron Diffraction Study on Partial Pair Correlation Functions of Water at Ambient Temperature
Bull. Chem. Soc. Jpn. **91** 1586–1595 (2018)

18 H. Nishihara, H. Fujimoto, H. Itoi, K. Nomura, H. Tanaka, M.T. Miyahara, P.A. Bonnaud, R. Miura, A. Suzuki, N. Miyamoto, N. Hatakeyama, A. Miyamoto, K. Ikeda, T. Otomo, and T. Kyotania
Graphene-based ordered framework with a diverse range of carbon polygons formed in zeolite nanochannels
Carbon **129** 854–862 (2018)

19 K. Kataoka and J. Akimoto
High ionic conductor member of garnet-type oxide $Li_{6.5}La_3Zr_{1.5}Ta_{0.5}O_{12}$
Chem. Electro. Chem. **5** 2551–2557 (2018)

20 M. Yoshimoto, Y. Yoshida, Y. Noda, S. Koizumi, S. Takata, J. Suzuki, A. Hoshikawa, T. Ishigaki, S. Ozeki, and T. Iiyama
Mesoscopic investigation of an "immiscible" cyclohexane and water micro-mixture in carbon micropores by contrast variation small-angle neutron scattering
Chem. Lett. **47** 336–339 (2018)

21 A. Chanyshev, K. Litasov, S. Rashchenko, A. Sano-Furukawa, H. Kagi, T. Hattori, A. Shatskiy, A. Dymshits, I. Sharygin, and Y. Higo
High-Pressure - High-Temperature Study of Benzene: Refined Crystal Structure and New Phase Diagram up to 8 GPa and 923K
Crystal Growth & Design **18** 3016–3026 (2018)

22 Y. Muraba, S. Iimura, S. Matsuishi, H. Hiramatsu, T. Honda, K. Ikeda, T. Otomo, and H. Hosono
Phase transition in CaFeAsH: bridging 1111 and 122 iron-based superconductors
Dalton Trans. **47** 12964–12971 (2018)

23 N. Naganawa, T. Ariga, S. Awano, M. Hino, K. Hirota, H. Kawahara, M. Kitaguchi, K. Mishima, H.M. Shimizu, S. Tada, S. Tasaki, and A. Umemoto
A Cold/Ultracold Neutron Detector using Fine-grained Nuclear

Emulsion with Spatial Resolution less than 100 nm
European Physical Journal C **78** 959 (2018)

24 Y. Seki, T. Shinohara, J.D. Parker, W. Ueno, T. Samoto, W. Yashiro, A. Momose, Y. Otake, and Y. Kiyanagi
Efficient phase imaging using wavelength-resolved neutron Talbot-Lau interferometry with TOF method
Europhysics Letters **123** 12002 (2018)

25 K. Mishima, H. Sumino, T. Yamada, S. Ieki, N. Nagakura, H. Otono, and H. Oide
Accurate determination of the absolute 3He/4He ratio of a synthesized helium standard gas (Helium Standard of Japan, HESJ): Towards revision of the atmospheric 3He/4He ratio
Geochemistry, Geophysics, Geosystems **19** 3995–4005 (2018)

26 T. Nakamura, T. Kawasaki, K. Toh, M. Ebine, A. Birumachi, and K. Sakasai
A sub-millimeter spatial resolution scintillation neutron detector for time-of-flight neutron diffraction imaging
IEEE Nuclear science symposium and medical imaging conference, conference record N07-197 (2018)

27 W. Liao, M. Hashimoto, S. Manabe, Y. Watanabe, S. Abe, K. Nakano, H. Sato, T. Kin, K. Hamada, M. Tampo, and Y. Miyake
Measurement and Mechanism Investigation of Negative and Positive Muon-Induced Upsets in 65nm Bulk SRAMs
IEEE Trans. Nucl. Sci. **65** 1734 (2018)

28 S. Manabe, Y. Watanabe, W. Liao, M. Hashimoto, K. Nakano, H. Sato, T. Kin, S. Abe, K. Hamada, M. Tampo, and Y. Miyake
Negative and Positive Muon-Induced Single Event Upsets in 65-nm UTBB SOI SRAMs
IEEE Trans. Nucl. Sci. **65** 1742 (2018)

29 T. Suwa, T. Hemmi, T. Saito, Y. Takahashi, K. Norikiyo, V. Luzin, H. Suzuki, and S. Harjo
Evaluation of Thermal Strain Induced in Components of Nb3Sn Strand During Cooling
IEEE Transactions on Applied Superconductivity **28** 1–4 (2018)

30 Y. Higaki, Y. Inutsuka, H. Ono, N.L. Yamada, Y. Ikemoto, and A. Takahara
Counteranion-Specific Hydration States of Cationic Polyelectrolyte Brushes
Ind. Eng. Chem. Res. **57** 5268–5275 (2018)

31 K. Asano, H. Kim, K. Sakaki, K. Jimura, S. Hayashi, Y. Nakamura, K. Ikeda, T. Otomo, A. Machida, and T. Watanuki
Structural Variation of Self-Organized Mg Hydride Nanoclusters in Immiscible Ti Matrix by Hydrogenation
Inorg. Chem. **57** 11831–11838 (2018)

32 F. Takeiri, T. Yamamoto, N. Hayashi, S. Hosokawa, K. Arai, J. Kikkawa, K. Ikeda, T. Honda, T. Otomo, C. Tassel, K. Kimoto, and H. Kageyama
A Fluorine-rich Perovskite Oxyfluoride $AgFeOF_2$
Inorg. Chem. **57** 6686–6691 (2018)

33 W. Gong, K. Aizawa, S. Harjo, R.X. Zheng, T. Kawasaki, J. Abe, T. Kamiyama, and N. Tsuji
Deformation behavior of as-cast and as-extruded $Mg_{97}Zn_1Y_2$ *alloys during compression, as tracked by in situ neutron diffraction*
International Journal of Plasticity **111** 288–306 (2018)

34 K. Yoshida, T. Inoue, M. Torigoe, T. Yamada, K. Shibata, and T. Yamaguchi
Thermal behavior, structure, dynamic properties of aqueous glycine solutions confined in mesoporous silica MCM-41 investigated by x-ray diffraction and quasi-elastic neutron scattering
J . Chem. Phys. **149** 124502 (2018)

35 K. Itoh, J. Saida, and T. Otomo
Inhomogeneity of local packing density and atomic bonding of Ni67Zr33 amorphous alloy
J. Alloys. Comp. **732** 585–592 (2018)

36 Y. Nagata, T. Nishikawa, M. Suginome, S. Sato, M. Sugiyama, L. Porcar, A. Martel, R. Inoue, and N. Sato
Elucidating the solvent effect on the switch of the helicity of poly(quinoxaline-2,3-diyl)s: A conformational analysis by small-angle neutron scattering
J. Am. Chem. Soc. **140** 2722–2726 (2018)

37 A. Shinozaki, K. Komatsu, H. Kagi, C. Fujimoto, S. Machida, A. Sano-Furukawa, and T. Hattori
Behavior of intermolecular interactions in a-glycine under high pressure
J. Chem. Phys. **148** 044507 (2018)

38 F. Nemoto, M. Kofu, M. Nagao, K. Ohishi, S. Takata, J. Suzuki, T. Yamada, K. Shibata, T. Ueki, Y. Kitazawa, M. Watanabe, and O. Yamamuro
Neutron scattering studies on short- and long-range layer structures and related dynamics in imidazolium-based ionic liquids
J. Chem. Phys. **149** 054502 (2018)

39 K. Fujii, M. Yashima, K. Hibino, M. Shiraiwa, K. Fukuda, S. Nakayama, N. Ishizawa, T. Hanashima, and T. Ohhara
High oxide-ion conductivity by the overbonded channel oxygens in Si-deficient $La_{9.565}(Si_{5.826}\square_{0.174})O_{26}$ *apatite without interstitial oxygens*
J. Mater. Chem. A **6** 10835–10846 (2018)

40 H. Abe, T. Yamada, and K. Shibata
Dynamic properties of nano-confined water in an ionic liquid
J. Mol. Liq. **264** 54–57 (2018)

41 A. Mori, H. Mamiya, M. Ohnuma, J. Ilavsky, K. Ohishi, J. Wozniak, A. Olszyna, N. Watanabe, J. Suzuki, H. Kitazawa, and M. Lewandowska
Manufacturing and characterization of Ni-free N-containing ODS austenitic alloy
J. Nucl. Mater. **501** 72–81 (2018)

42 M. Hirai, S. Ajito, H. Iwase, S. Takata, N. Ohta, N. Igarashi, and N. Shimizu
Restoration of myoglobin native fold from its initial state of amyloid formation by trehalose
J. Phys. Chem. B **122** 11962–11968 (2018)

43 Y. Kameda, S. Maeda, Y. Amo, T. Usuki, K. Ikeda, and T. Otomo
Neutron Diffraction Study on the Structure of Hydrated Li(+) in Dilute Aqueous Solutions
J. Phys. Chem. B **122** 1695–1701 (2018)

44 S. Ajito, H. Iwase, S. Takata, and M. Hirai
Sugar-mediated stabilization of protein against chemical or thermal denaturation
J. Phys. Chem. B **122** 8685–8697 (2018)

45 J. Kijima, Y. Shibuya, K. Katayama, T. Itoh, H. Iwase, Y. Fukushima, M. Kubo, and A. Yamaguchi
Structural characterization of myoglobin molecules adsorbed within mesoporous silicas
J. Phys. Chem. C **122** 15567–15574 (2018)

46 S. Taminato, M. Hirayama, K. Suzuki, K.S. Kim, K. Tamura, and R. Kanno
Reversible Structural Changes and High-Rate Capability of Li3PO4-Modified Li2RuO3 for Lithium-Rich Layered Rocksalt Oxide Cathodes
J. Phys. Chem. C **122** 16607 (2018)

47 H. Kadowaki, M. Wakita, B. Fak, J. Ollivier, S. Ohira-Kawamura, K. Nakajima, H. Takatsu, and M. Tamai
Continuum excitation and pseudospin wave in quantum spin-liquid and quadrupole ordered states of $Tb_{2+x}Ti_{2-x}O_{7+y}$

J. Phys. Soc. Jpn. **87** 064704 (2018)

48 N. Metoki, H. Yamauchi, H.S. Suzuki, H. Kitazawa, K. Kamazawa, K. Ikeuchi, R. Kajimoto, M. Nakamura, and Y. Inamura
Neutron Inelastic Scattering Study of the f-Electron States in NdPd$_5$*Al*$_2$
J. Phys. Soc. Jpn. **87** 084708 (2018)

49 Y. Oba, T. Shinohara, H. Sato, Y. Onodera, K. Hiroi, Y.H. Su, and M. Sugiyama
Imaging Measurement of Neutron Attenuation by Small-Angle Neutron Scattering Using Soller Collimator
J. Phys. Soc. Jpn. **87** 094004 (2018)

50 T. Nakajima, V. Ukleev, K. Ohishi, H. Oike, F. Kagawa, S. Seki, K. Kakurai, Y. Tokura, and T. Arima
Uniaxial-stress effects on helimagnetic orders and skyrmion lattice in Cu_2OSeO_3
J. Phys. Soc. Jpn. **87** 094709 (2018)

51 K. Iwasa, F. Iga, T. Moyoshi, A. Nakao, and T. Ohhara
Magnetic-Ordering Propagation Vectors of Terbium Hexaboride Revisited
J. Phys. Soc. Jpn. **87** 64705 (2018)

52 D. Kawana, M. Soda, M. Yoshida, Y. Ikeda, T. Asami, R. Sugiura, H. Yoshizawa, T. Masuda, T. Hawai, S. Ibuka, T. Yokoo, and S. Itoh
YUI and HANA: Control and Visualization Programs for HRC in J-PARC
J. Phys.: Conf. Ser. **1021** 012014 (2018)

53 Y. Inamura, T. Ito, and J. Suzuki
Applications of the differential events reading method at MLF, J-PARC
J. Phys.: Conf. Ser. **1021** 012015 (2018)

54 S. Itoh, T. Yokoo, T. Masuda, H. Yoshizawa, M. Soda, M. Yoshida, T. Hawai, D. Kawana, R. Sugiura, T. Asami, and Y. Ihata
Improvement for Neutron Brillouin Scattering Experiments on High Resolution Chopper Spectrometer HRC
J. Phys.: Conf. Ser. **1021** 012028 (2018)

55 R. Kajimoto, M. Nakamura, Y. Inamura, K. Kamazawa, K. Ikeuchi, K. Iida, M. Ishikado, N. Murai, H. Kira, T. Nakatani, S. Ohira-Kawamura, R. Takahashi, N. Kubo, W. Kambara, K. Nakajima, and K. Aizawa
Status report of the chopper spectrometer 4SEASONS
J. Phys.: Conf. Ser. **1021** 012030 (2018)

56 Y. Miki, H. Yamaguchi, Y. Iizawa, H. Shishido, K.M. Kojima, K. Oikawa, M. Harada, S. Miyajima, M. Hidaka, T. Oku, K. Soyama, and T. Ishida
Neutron signal features of Nb-based kinetic inductance detector with 10B convertor
J. Phys.: Conf. Ser. **1054** 012054 (2018)

57 T. Koyama and T. Ishida
Electrodynamic theory for the operation principle of a superconducting kinetic inductance stripline detector
J. Phys.: Conf. Ser. **1054** 012055 (2018)

58 Y. Iizawa, H. Yamaguchi, Y. Miki, K. Nishimura, H. Shishido, K.M. Kojima, K. Oikawa, M. Harada, S. Miyajima, M. Hidaka, T. Oku, K. Soyama, T. Koyama, and T. Ishida
Physical characteristics of delay-line current-biased kinetic inductance detector
J. Phys.: Conf. Ser. **1054** 012056 (2018)

59 K. Ninomiya, M. Kitanaka, A. Shinohara, M. Tampo, Y. Miyake, Y. Sakai, and M.K. Kubo
Muonic X-ray measurements on mixtures of CaO/MgO and Fe3O4/MnO
J. Radioanal. Nucl. Chem. **316** 1107–1111 (2018)

60 N.V. Mdlovu, Y. Chen, K.-S. Lin, M.-W. Hsu, S.S.-S. Wang, C.-M. Wu, Y.-S. Lin, and K. Ohishi
Multifunctional nanocarrier as a potential micro-RNA delivery vehicle for neuroblastoma treatment
J. Taiwan Inst. Chem. Eng. **96** 526–537 (2018)

61 Y. Kitanaka, M. Ogino, Y. Noguchi, M. Miyayama, A. Hoshikawa, and T. Ishigaki
Crystal Structure and ferroelectric polarization of tetragonal $(Bi_{1/2}Na_{1/2})TiO_3$*–12*$BaTiO_3$
Japanese Journal of Applied Physics **57** 11UD05 (2018)

62 T. Okuchi, N. Tomioka, P. Narangoo, and K. Shibata
Quasielastic neutron scattering of brucite to analyse hydrogen transport on the atomic scale
Journal of Applied Crystallography **51** 1564–1570 (2018)

63 T. Kawasaki, Y. Inamura, T. Ito, T. Nakatani, S. Harjo, W. Gong, and K. Aizawa
Stroboscopic time-of-flight neutron diffraction during cyclic testing using the event data recording system at J-PARC
Journal of Applied Crystallography **51** 630–634 (2018)

64 P.G. Xu, S. Harjo, M. Ojima, H. Suzuki, T. Ito, W. Gong, S.C. Vogel, J. Inoue, Y. Tomota, K. Aizawa, and K. Akita
High stereographic resolution texture and residual stress evaluation using time-of-flight neutron diffraction
Journal of applied crystallography **51** 746–760 (2018)

65 K. Mochiki, T. Uragaki, J. Koide, Y. Kushima, J. Kawarabayashi, A. Taketani, Y. Otake, Y. Matsumoto, Y.H. Su, K. Hiroi, T. Shinohara, and T. Kai
Pulsed-neutron imaging by a high-speed camera and center-of-gravity processing
Journal of Instrumentation **13** C01038 (2018)

66 S. Takada, T. Okudaira, F. Goto, K. Hirota, A. Kimura, M. Kitaguchi, J. Koga, T. Nakao, K. Sakai, H.M. Shimizu, T. Yamamoto, and T. Yoshioka
Characterization of germanium detectors for the measurement of the angular distribution of prompt γ-rays at the ANNRI in the MLF of the J-PARC
Journal of Instrumentation **13** P02018 (2018)

67 Y. Iwasaki, N. Matsui, K. Suzuki, Y. Hinuma, M. Yonemura, G. Kobayashi, M. Hirayama, I. Tanaka, and R. Kanno
Synthesis, crystal structure, and ionic conductivity of hydride ion-conducting Ln_2LiHO_3 *(Ln = La, Pr, Nd) oxyhydrides*
Journal of Materials Chemistry A **6** 23457–23463 (2018)

68 T. Wakui, E. Wakai, T. Naoe, Y. Shintaku, T. Li, K. Murakami, K. Kanomata, H. Kogawa, K. Haga, H. Takada, and M. Futakawa
Recent studies for structural integrity evaluation and defect inspection of J-PARC spallation neutron source target vessel
Journal of Neuclear Materials **506** 3–11 (2018)

69 H. Muta, R. Nishikane, Y. Ando, J. Matsunaga, K. Sakamoto, S. Harjo, T. Kawasaki, Y. Ohishi, K. Kurosaki, and S. Yamanaka
Effect of hydrogenation conditions on the microstructure and mechanical properties of zirconium hydride
Journal of Nuclear Materials **500** 145–152 (2018)

70 K. Terada, A. Kimura, T. Nakao, S. Nakamura, K. Mizuyama, N. Iwamoto, O. Iwamoto, H. Harada, T. Katabuchi, M. Igashira, T. Sano, Y. Takahashi, C.H. Pyeon, S. Fukutani, T. Fujii, T. Yagi, K. Takamiya, and J. Hori
Measurements of neutron total and capture cross sections of ^{241}*Am with ANNRI at J-PARC*
Journal of Nuclear Science and Technology **55** 1198–1211 (2018)

71 T. Tsuchiya, R. Kobayashi, T. Kubota, K. Saito, K. Ono, T. Ohhara, A. Nakao, and K. Takanashi
Mn2VAl Heusler alloy thin films: Appearance of antiferromagnetism and exchange bias in a layered structure with Fe
Journal of Physics D: Applied Physics **51** 065001 (2018)

72 H. Matsuda, S. Meigo, and H. Iwamoto
Measurement of activation cross sections of the target and the proton beam window materials at J-PARC
Journal of Physics: Conference Series **1021** 012016 (2018)

73 K. Nakajima, S. Ohira-Kawamura, T. Kikuchi, M. Kofu, Y. Kawakita, Y. Inamura, W. Kambara, K. Aoyama, D. Wakai, M. Harada, and M. Ooi
Recent issues encountered by AMATERAS: A cold-neutron disk-chopper spectrometer
Journal of Physics: Conference Series **1021** 012031 (2018)

74 T. Kai, T. Uchida, H. Kinoshita, M. Seki, M. Ooi, T. Wakui, K. Haga, Y. Kasugai, and H. Takada
Off-gas processing system operations for mercury target vessel replacement at J-PARC
Journal of Physics: Conference Series **1021** 012042 (2018)

75 M. Teshigawara, M. Harada, M. Ooi, and H. Takada
Present fabrication status of spare moderators and reflector in J-PARC spallation neutron source
Journal of Physics: Conference Series **1021** 012061 (2018)

76 T. Aso, M. Teshigawara, S. Hasegawa, H. Muto, K. Aoyagi, K. Nomura, and H. Takada
Recovery of helium refrigerator performance for cryogenic hydrogen system at J-PARC MLF
Journal of Physics: Conference Series **1021** 012085 (2018)

77 K. Ikeuchi, T. Kikuchi, K. Nakajima, R. Kajimoto, S. Wakimoto, and M. Fujita
Fe-impurity-induced magnetic excitations in heavily over-doped $La_{1.7}Sr_{0.3}Cu_{0.95}Fe_{0.05}O_4$
Journal of Physics: Conference Series **969** 012024 (2018)

78 Y. Idemoto, T. Hiranuma, N. Ishida, and N. Kitamura
Effect of operating temperature on local structure during first discharge of $0.4Li_2MnO_3\text{-}0.6LiMn_{1/3}Ni_{1/3}Co_{1/3}O_2$ *electrodes*
Journal of Power Sources **378** 198–208 (2018)

79 T. Ohkubo
Insights from ab initio molecular dynamics simulations for a multicomponent oxide glass
Journal of the American Ceramic Society **101** 1122–1134 (2018)

80 N. Matsui, G. Kobayashi, K. Suzuki, A. Watanabe, A. Kubota, Y. Iwasaki, M. Yonemura, M. Hirayama, and R. Kanno
Ambient pressure synthesis of La_2LiHO_3 *as a solid electrolyte for a hydrogen electrochemical cell*
Journal of the American Ceramic Society **102** 3228–3235 (2018)

81 H. Yamashita, T. Broux, Y. Kobayashi, F. Takeiri, T. Zhu, M.A. Hayward, K. Fujii, M. Yashima, T. Murakami, and H. Kageyama
Chemical Pressure-induced Anion Order-disorder Transition in LnHO Enabled by Hydride Size Flexibility
Journal of the American Chemical Society **140** 11170–11173 (2018)

82 W. Uno, K. Fujii, E. Niwa, S. Torii, P. Miao, T. Kamiyama, and M. Yashima
Experimental visualization of oxide-ion diffusion paths in pyrochlore-type $Yb_2Ti_2O_7$
Journal of the Ceramic Society of Japan **126** 341–345 (2018)

83 K. Fujii and M. Yashima
Discovery and development of $BaNdInO_4$ *- A brief review -*
Journal of the Ceramic Society of Japan **126** 852–859 (2018)

84 T. Matsushita, T. Muro, F. Matsui, N. Happo, S. Hosokawa, K. Ohoyama, A. Sato-Tomita, Y.C. Sasaki, and K. Hayashi
Principle and Reconstruction Algorithm for Atomic-Resolution Holography
Journal of the Physical Society of Japan **87** 061002 (2018)

85 K. Oyama, M. Sugishima, K. Tanabe, A. Mitsuda, H. Wada, K. Ohoyama, T. Matsukawa, Y. Yoshida, A. Hoshikawa, T. Ishigaki, and K. Iwasa
Neutron Diffraction Studies on Valence Ordering Compound YbPd
Journal of the Physical Society of Japan **87** 114705 (2018)

86 S. Ohira-Kawamura, K. Tomiyasu, A. Koda, D.P. Sari, R. Asih, S. Yoon, I. Watanabe, and K. Nakajima
Magnetic Properties of One-Dimensional Quantum Spin System $Rb_2Cu_2Mo_3O_{12}$ *Studied by Muon Spin Relaxation*
JPS Conf. Proc. **21** 011007 (2018)

87 M. Fujita, K.M. Suzuki, S. Asano, A. Koda, H. Okabe, and R. Kadono
μSR Study of Magnetism in the As-Prepared and Non-Superconducting $T^*\text{-}La_{0.9}Eu_{0.9}Sr_{0.2}CuO_4$
JPS Conf. Proc. **21** 011026 (2018)

88 T. Sumura, T. Ishimoto, H. Kuwahara, K. Kurashima, Y. Koike, I. Watanabe, M. Miyazaki, A. Koda, R. Kadono, and T. Adachi
Reduction Effects on the Cu-Spin Correlation in the Electron-Doped T'-Cuprate $Pr_{1.3-x}La_{0.7}Ce_xCuO_{4+\delta}$ $(x = 0.10)$
JPS Conf. Proc. **21** 011027 (2018)

89 K. Nishimura, K. Matsuda, N. Nunomura, T. Namiki, S. Lee, D. Hatakeyama, W. Higemoto, Y. Miyake, T. Matsuzaki, G. Itoh, K. Ihara, H. Toda, and M. Yamaguchi
Muon Spin Relaxation of an Al–3.4%Zn–1.9%Mg alloy
JPS Conf. Proc. **21** 011030 (2018)

90 M. Mihara, H. Araki, M. Mizuno, K. Shimomura, W. Higemoto, K. Sugita, K. Atsushi, M. Kondo, Y. Tanaka, T. Matsuzaki, R. Kadono, W. Sato, T. Nakano, and T. Fukuda
μSR Study on Hydrogen Behavior in Palladium
JPS Conf. Proc. **21** 011031 (2018)

91 T. Kiyotani, M. Kobayashi, I. Tanaka, and N. Niimura
Visualization of proton and electron transfer processes of a biochemical reaction by μSR
JPS Conf. Proc. **21** 011037 (2018)

92 A.D. Pant, Y. Sugawara, H. Nakanishi, E. Torikai, W. Higemoto, K. Shimomura, and K. Nagamine
Theoretical Calculations of Charge States and Stopping Sites of Muons in Glycine and Triglycine
JPS Conf. Proc. **21** 011038 (2018)

93 G.D. Liu, Y.G. Chen, A.H. Morrison, A. Koda, P.W. Percival, and K. Ghandi
Supercritical Water Experimental Setup for μSR
JPS Conf. Proc. **21** 011039 (2018)

94 I. Umegaki, Y. Higuchi, H. Nozaki, K. Ninomiya, M.K. Kubo, M. Tampo, K. Hamada, S. Doiuchi, P. Strasser, N. Kawamura, Y. Miyake, and J. Sugiyama
Detection of Li in Li-ion Battery Electrode Materials by Muonic X-ray
JPS Conf. Proc. **21** 011041 (2018)

95 K. Ninomiya, M.K. Kubo, P. Strasser, A. Shinohara, M. Tampo, N. Kawamura, and Y. Miyake
Isotope Identification of Lead by Muon Induced X-ray and Gamma-ray Measurements
JPS Conf. Proc. **21** 011043 (2018)

96 G. Yabu, M. Katsuragawa, M. Tampo, K. Hamada, A. Harayama, Y. Miyake, S. Oshita, S. Saito, G. Sato, T. Takahashi, S. Takeda, and S. Watanabe
Imaging of Muonic X-ray of Light Elements with a CdTe Double-Sided Strip Detector
JPS Conf. Proc. **21** 011044 (2018)

97 P. Strasser, K. Shimomura, and H.A. Torii
Possibility of New Precise Measurements of Muonic Helium Atom HFS

at J-PARC MUSE
JPS Conf. Proc. **21** 011045 (2018)

98 G. Yoshida, K. Ninomiya, M. Inagaki, M. Toyoda, J. Aoki, N. Kawamura, Y. Miyake, and A. Shinohara
Development of Muonic Atom Beam Extraction System and First Evaluation by Intense Negative Muon Beam of J-PARC MUSE
JPS Conf. Proc. **21** 011046 (2018)

99 Y. Miyake, K. Shimomura, N. Kawamura, A. Koda, P. Strasser, K.M. Kojima, H. Fujimori, S. Makimura, Y. Ikedo, Y. Kobayashi, J. Nakamura, Y. Oishi, S. Takeshita, T. Adachi, A.D. Pant, H. Okabe, S. Matoba, M. Tampo, M. Hiraishi, K. Hamada, S. Doiuchi, W. Higemoto, T.U. Ito, and R. Kadono
J-PARC Muon Facility, MUSE
JPS Conf. Proc. **21** 011054 (2018)

100 D. Tomono, M. Fukuda, K. Hatanaka, W. Higemoto, Y. Kawashima, K.M. Kojima, Y. Kuno, Y. Matsuda, T. Matsuzaki, Y. Miyake, K. Miyamoto, Y. Morita, T. Motoishi, Y. Nakazawa, K. Ninomiya, R. Nishikawa, S. Ohta, A. Sato, K. Shimomura, K. Takahisa, Y. Weichao, and M.L. Wong
Muon Beamline Commissioning and Feasibility Study for μSR at a New DC Muon Beamline, MuSIC-RCNP, Osaka University
JPS Conf. Proc. **21** 011057 (2018)

101 S. Makimura, S. Matoba, N. Kawamura, Y. Matsuzawa, M. Tabe, H. Aoyagi, H. Kondo, Y. Kobayashi, H. Fujimori, Y. Ikedo, R. Kadono, A. Koda, K.M. Kojima, Y. Miyake, J.G. Nakamura, Y. Oishi, H. Okabe, K. Shimomura, and P. Strasser
Perspective of Muon Production Target at J-PARC MLF MUSE
JPS Conf. Proc. **21** 011058 (2018)

102 S. Matoba, S. Makimura, N. Kawamura, Y. Matsuzawa, M. Tabe, Y. Kobayashi, R. Kadono, and Y. Miyake
Renovation of a Scraper Unit of a Muon Production Target at J-PARC
JPS Conf. Proc. **21** 011059 (2018)

103 A.D. Pant, T. Adachi, Y. Ikedo, Y. Oishi, J. Nakamura, P. Strasser, K.M. Kojima, S. Makimura, N. Kawamura, A. Koda, T.U. Ito, W. Higemoto, K. Shimomura, R. Kadono, Y. Miyake, and E. Torikai
Transportation of Ultra Slow Muon on U-line, MLF, J-PARC
JPS Conf. Proc. **21** 011060 (2018)

104 P. Strasser, A. Koda, K.M. Kojima, T.U. Ito, H. Fujimori, Y. Irie, M. Aoki, Y. Nakatsugawa, W. Higemoto, M. Hiraishi, H. Li, H. Okabe, S. Takeshita, K. Shimomura, N. Kawamura, R. Kadono, and Y. Miyake
Status of the New Surface Muon Beamline at J-PARC MUSE
JPS Conf. Proc. **21** 011061 (2018)

105 K.M. Kojima, M. Hiraishi, A. Koda, H. Okabe, S. Takeshita, H. Li, R. Kadono, M.M. Tanaka, M. Shoji, T. Uchida, and S.Y. Suzuki
Development of General Purpose μSR Spectrometer ARTEMIS at S1 Experimental Area, MLF J-PARC
JPS Conf. Proc. **21** 011062 (2018)

106 R. Katayama, K. Mishima, S. Yamashita, M. Kitaguchi, T. Yoshioka, Y. Seki, M. Mitsuhashi, M. Sugihara, M. Hino, E. Watanabe, D. Tsuya, M. Saito, and N.L. Yamada
Development of new neutron mirrors for measuring the neutron electric dipole moment
JPS Conf. Proc. **22** 011009 (2018)

107 R. Maruyama, D. Yamazaki, and K. Soyama
Effect of the interfacial roughness correlation on the reflectivity in a neutron multilayer mirror
JPS Conf. Proc. **22** 011011 (2018)

108 J.D. Parker, M. Harada, H. Hayashida, K. Hiroi, T. Kai, Y. Matsumoto, T. Nakatani, K. Oikawa, M. Segawa, T. Shinohara, Y.H. Su, A. Takada, T. Takemura, T. Taniguchi, T. Tanimori, and Y. Kiyanagi
Development of Energy-Resolved Neutron Imaging Detectors at RADEN
JPS Conf. Proc. **22** 011022 (2018)

109 S. Tada, S. Awano, M. Hino, K. Hirota, H. Kawahara, M. Kitaguchi, K. Mishima, N. Naganawa, H.M. Shimizu, S. Tasaki, and A. Umemoto
Development of High Spatial Resolution Cold/Ultra-Cold Neutron Detector Using Nano Imaging Tracker
JPS Conf. Proc. **22** 011023 (2018)

110 T. Uragaki, J. Koide, J. Kawarabayashi, K. Mochiki, Y. Matsumoto, Y.H. Su, K. Hiroi, T. Shinohara, and T. Kai
Evaluation of high-frame-rate camera with digital accumulation system combined with neutron color image intensifier for energy resolved neutron imaging
JPS Conf. Proc. **22** 011027 (2018)

111 M. Segawa, K. Oikawa, T. Kai, T. Shinohara, H. Hayashida, Y. Matsumoto, J.D. Parker, T. Nakatani, K. Hiroi, Y.H. Su, and Y. Kiyanagi
Spatial Resolution Test Targets Made of Gadolinium and Gold for Conventional and Resonance Neutron Imaging
JPS Conf. Proc. **22** 011028 (2018)

112 K. Hiroi, T. Shinohara, H. Hayashida, J.D. Parker, K. Oikawa, Y.H. Su, T. Kai, and Y. Kiyanagi
Development of a Polarization Analysis Method for Visualization of the Magnetic Field Distribution in a Small Electric Transformer using Pulsed Polarized Neutron Imaging
JPS Conf. Proc. **22** 011030 (2018)

113 K. Mishima, S. Awano, Y. Fuwa, F. Goto, C.C. Haddock, M. Hino, M. Hirose, K. Hirota, S. Ieki, S. Imajo, T. Ino, Y. Iwashita, R. Katayama, H. Kawahara, M. Kitaguchi, R. Kitahara, J. Koga, A. Morishita, T. Nagae, N. Nagakura, N. Naganawa, N. Oi, H. Oide, H. Otono, Y. Seki, D. Sekiba, T. Shima, H.M. Shimizu, W.M. Snow, N. Sumi, H. Sumino, S. Tada, K. Taketani, S. Tasaki, T. Tomita, A. Umemoto, T. Yamada, S. Yamashita, M. Yokohashi, and T. Yoshioka
Fundamental physics activities with pulsed neutron at J-PARC(BL05)
JPS Conf. Proc. **22** 011033 (2018)

114 N. Sumi, H. Otono, T. Yoshioka, K. Mishima, and Y. Makida
Precise Neutron Lifetime Measurement with a Solenoidal Coil
JPS Conf. Proc. **22** 011036 (2018)

115 S. Imajo, Y. Iwashita, K. Mishima, M. Kitaguchi, H.M. Shimizu, T. Ino, S. Yamashita, K. Hirota, F. Goto, Y. Fuwa, R. Katayama, and NOP Collaboration
Time-focus Experiment of Ultracold Neutron by Improved UCN Rebuncher at J-PARC/MLF
JPS Conf. Proc. **22** 011038 (2018)

116 N. Oi, H.M. Shimizu, K. Hirota, M. Kitaguchi, C.C. Haddock, W.M. Snow, T. Yoshioka, K. Mishima, T. Ino, and T. Shima
A Search for Possible Deviations from Newtonian Gravity at the nm Length Scale Using Neutron-Noble Gas Scattering
JPS Conf. Proc. **22** 011039 (2018)

117 T. Kumada, K. Akutsu, K. Ohishi, T. Morikawa, Y. Kawamura, M. Sahara, J. Suzuki, and N. Torikai
Development of Dynamic Nuclear Polarization System for Spin-Contrast-Variation Neutron Reflectometry
JPS Conf. Proc. **22** 11015 (2018)

118 Y. Ogata, T. Abe, S. Yonemori, N.L. Yamada, D. Kawaguchi, and K. Tanaka
Impact of the Solid Interface on Proton Conductivity in Nafion Thin Films
Langmuir **34** 15483–15489 (2018)

119 K. Shimokita, I. Saito, K. Yamamoto, M. Takenaka, N.L. Yamada, and T. Miyazaki
Effect of Preferential Orientation of Lamellae in Interfacial Region between Block Copolymer-based Pressure-Sensitive Adhesive and

Solid Substrate on the Peel Strength
Langmuir **34** 2856–2864 (2018)

120 K. Yanagi, N.L. Yamada, K. Kato, K. Ito, and H. Yokoyama
Polyrotaxane brushes dynamically formed at a water/elastomer interface
Langmuir **34** 5297–5302 (2018)

121 F. Endo, R. Okoshi, K. Takaesu, N. Kurokawa, H. Iwase, T. Maeda, and A. Hotta
Mechanically tough syndiotactic polypropylene (sPP) gels realized by fast quenching using liquid nitrogen
Macromolecules **51** 2321–2327 (2018)

122 Y. Shudo, A. Izumi, K. Hagita, T. Yamada, K. Shibata, and M. Shibayama
Diffusion Behavior of Methanol Molecules Confined in Cross-linked Phenolic Resins Studied using Neutron Scattering and Molecular Dynamics Simulations
Macromolecules **51** 6334–6343 (2018)

123 T. Iwamoto, Y. Doi, K. Kinoshita, A. Takano, Y. Takahashi, E. Kim, T. Kim, S. Takata, M. Nagao, and Y. Matsushita
Conformations of ring polystyrenes in semidilute solutions and in linear polymer matrices studied by SANS
Macromolecules **51** 6836–6847 (2018)

124 T. Koyama, K. Ueno, M. Sekine, Y. Matsumoto, T. Kai, T. Shinohara, H. Iikura, H. Suzuki, and M. Kanematsu
Deformation Analysis of Reinforced Concrete using Neutron Imaging Technique
Materials Research Proceedings **4** 155–160 (2018)

125 M. Kumagai, T. Uchida, K. Murasawa, M. Takamura, Y. Ikeda, H. Suzuki, Y. Otake, T. Hama, and S. Suzuki
Convergence Behavior in Line Profile Analysis Using Convolutional Multiple Whole-Profile Software
Materials Research Proceedings **6** 57–62 (2018)

126 T.Z. Sun, A.S. Tremsin, M.J. Roy, M. Hofmann, P.B. Prangnell, and P.J. Withers
Investigation of residual stress distribution and texture evolution in AA7050 stationary shoulder friction stir welded joints
Materials Science & Engineering A **712** 531–538 (2018)

127 Y. Sato, Y. Murakami, I. Satoshi, and N. Ishikawa
Critical Conditions of Cold Cracking in High Strength Steel Weld Based on the Local Stress Distribution and Hydrogen Accumulation
Materials Science Forum **941** 153–157 (2018)

128 K. Murasawa, M. Takamura, M. Kumagai, Y. Ikeda, H. Suzuki, Y. Otake, T. Hama, and S. Suzuki
Determination Approach of Dislocation Density and Crystallite Size Using a Convolutional Multiple Whole Profile Software
Materials Transactions **59** 1135–1141 (2018)

129 A. Taketani, Y. Wakabayashi, Y. Otake, Y. Ikeda, T. Wakabayashi, K. Kono, T. Kai, K. Oikawa, H. Sunaga, M. Yamada, and T. Nakayama
Quantification of localized water image in under-film corroded steel with high spatial resolution, high time resolution, and wide view by neutron radiography
Materials Transactions **59** 976–983 (2018)

130 B. Li, H. Wang, Y. Kawakita, Q. Zhang, M. Feygenson, H.L. Yu, D. Wu, K. Ohara, T. Kikuchi, K. Shibata, T. Yamada, X.K. Ning, Y. Chen, J.Q. He, D. Vaknin, R.Q. Wu, K. Nakajima, and M.G. Kanatzidis
Liquid-like thermal conduction in intercalated layered crystalline solids
Nature Materials **17** 226–230 (2018)

131 W.L. Yao, C.Y. Li, L.C. Wang, S.J. Xue, Y. Dan, K. Iida, K. Kamazawa, K.K. Li, C. Fang, and Y. Li
Topological spin excitations in a threedimensional antiferromagnet
Nature Physics **14** 1011–1015 (2018)

132 T. Fujiwara, Y. Mitsuya, and H. Takahashi
Radiation imaging with glass gas electron multipliers (G-GEMs)
Nucl. Instrum. Methods Phys. Res., Sect. A **878** 40–49 (2018)

133 R. Maruyama, D. Yamazaki, K. Akutsu, T. Hanashima, N. Miyata, H. Aoki, M. Takeda, and K. Soyama
Development of high-polarization Fe/Ge neutron polarizing supermirror: Possibility of fine-tuning of scattering length density in ion beam sputtering
Nucl. Instrum. Methods Phys. Res., Sect. A **888** 70–78 (2018)

134 W.H. Guan, E. Wakai, T. Naoe, H. Kogawa, T. Wakui, K. Haga, H. Takada, and M. Futakawa
Optimization study on structural analyses for the J-PARC mercury target vessel
Nucl. Instrum. Methods Phys. Res., Sect. A **894** 8–19 (2018)

135 B. Kim, S. Bae, H. Choi, S. Choi, N. Kawamura, R. Kitamura, H. Sanko, Y. Kondo, T. Mibe, M. Otani, G.P. Razuvaev, and E. Won
Development of a microchannel plate based beam profile monitor for a re-accelerated muon beam
Nucl. Instrum. Methods Phys. Res., Sect. A **899** 22–27 (2018)

136 M. Harada, M. Teshigawara, M. Ohi, E. Klinkby, L. Zanini, K. Batkov, K. Oikawa, Y. Toh, A. Kimura, and Y. Ikeda
Experimental validation of the brightness distribution on the surfaces of coupled and decoupled moderators composed of 99.8% parahydrogen at the J-PARC pulsed spallation neutron source
Nucl. Instrum. Methods Phys. Res., Sect. A **903** 38–45 (2018)

137 S. Itoh, M. Nakaji, Y. Uchida, M. Kitaguchi, and H.M. Shimizu
Pendellosung interferometry by using pulsed neutrons
Nucl. Instrum. Methods Phys. Res., Sect. A **908** 78 (2018)

138 M. Teshigawara, Y. Ikeda, M. Ooi, M. Harada, H. Takada, M. Kakishiro, G. Noguchi, T. Shimada, K. Seita, D. Murashima, K. Fukatani, K. Kanomata, and T. Teraoku
Implementation of a low-activation Au-In-Cd decoupler into the J-PARC 1 MW short pulsed spallation neutron source
Nuclear Materials and Energy **14** 14–21 (2018)

139 T. Takamuku, T. Tokuda, T. Uchida, K. Sonoda, B.A. Marekha, A. Idrissi, O. Takahashi, Y. Horikawae, J. Matsumura, T. Tokushima, H. Sakurai, M. Kawano, K. Sadakane, and H. Iwase
Hydrogen bonds of the imidazolium-ring of ionic liquids with DMSO studied by NMR, soft X-ray spectroscopy, and SANS
Phys. Chem. Chem. Phys. **20** 12858 (2018)

140 Y. Ishii, K. Komatsu, S. Nakano, S. Machida, T. Hattori, A. Sano-Furukawa, and H. Kagi
Pressure-induced stacking disorder in boehmite
Phys. Chem. Chem. Phys. **20** 16650 (2018)

141 S. Bae, H. Choi, S. Choi, Y. Fukao, K. Futatsukawa, K. Hasegawa, T. Iijima, H. Iinuma, K. Ishida, N. Kawamura, B. Kim, R. Kitamura, H.S. Ko, Y. Kondo, S. Li, T. Mibe, Y. Miyake, T. Morishita, Y. Nakazawa, M. Otani, G.P. Razuvaev, N. Saito, K. Shimomura, Y. Sue, E. Won, and T. Yamazaki
First muon acceleration using a radio-frequency accelerator
Phys. Rev. Accel. Beams **21** 050101 (2018)

142 H. Shishido, Y. Miki, H. Yamaguchi, Y. Iizawa, T.D. Vu, K.M. Kojima, T. Koyama, K. Oikawa, M. Harada, S. Miyajima, M. Hidaka, T. Oku, K. Soyama, S.Y. Suzuki, and T. Ishida
High-Speed Neutron Imaging Using a Current-Biased Delay-Line Detector of Kinetic Inductance
Phys. Rev. Applied **10** 044044 (2018)

143 A.W.T. Gregg, J.N. Hendriks, C.M. Wensrich, A. Wills, A.S. Tremsin, V.

Luzin, T. Shinohara, O. Kirstein, M.H. Meylan, and E.H. Kisi
Tomographic Reconstruction of Two-Dimensional Residual Strain Fields from Bragg-Edge Neutron Imaging
Phys. Rev. Applied **10** 064034 (2018)

144 S. Shamoto, T.U. Ito, H. Onishi, H. Yamauchi, Y. Inamura, M. Matsuura, M. Akatsu, K. Kodama, A. Nakao, T. Moyoshi, K. Munakata, T. Ohhara, M. Nakamura, S. Ohira-Kawamura, Y. Nemoto, and K. Shibata
Neutron scattering study of yttrium iron garnet
Phys. Rev. B **97** 054429 (2018)

145 K. Horigane, M. Fujii, H. Okabe, K. Kobayashi, R. Horie, H. Ishii, Y.F. Liao, Y. Kubozono, A. Koda, R. Kadono, and J. Akimitsu,
Magnetic phase diagram of $Sr_{2-x}La_xIrO_4$ synthesized by mechanical alloying
Phys. Rev. B **97** 064425 (2018)

146 T. Hattori
Is there a pressure-induced discontinuous volume change in liquid Cs?
Phys. Rev. B **97** 100101(R) (2018)

147 I. Yamauchi, M. Hiraishi, H. Okabe, S. Takeshita, A. Koda, K.M. Kojima, R. Kadono, and H. Tanaka
Local spin structure of the a-$RuCl_3$ honeycomb-lattice magnet observed via muon spin rotation/relaxation
Phys. Rev. B **97** 134410 (2018)

148 S. Hayashida, O. Zaharko, N. Kurita, H. Tanaka, M. Hagihala, M. Soda, S. Itoh, Y. Uwatoko, and T. Masuda
Pressure-induced quantum phase transition in the quantum antiferromagnet $CsFeCl_3$
Phys. Rev. B **97** 140405(R) (2018)

149 T. Kim, J.C. Leiner, K. Park, J. Oh, H. Sim, K. Iida, K. Kamazawa, and J.-G. Park
Renormalization of spin excitations in hexagonal $HoMnO_3$ by magnon-phonon coupling
Phys. Rev. B **97** 201113(R) (2018)

150 N. Murai, K. Suzuki, S. Ideta, M. Nakajima, K. Tanaka, H. Ikeda, and R. Kajimoto
Effect of electron correlations on spin excitation bandwidth in $Ba_{0.75}K_{0.25}Fe_2As_2$ as seen via time-of-flight inelastic neutron scattering
Phys. Rev. B **97** 241112(R) (2018)

151 T. Nakajima, Y. Inamura, T. Ito, K. Ohishi, H. Oike, F. Kagawa, A. Kikkawa, Y. Taguchi, K. Kakurai, Y. Tokura, and T. Arima
Phase-transition kinetics of magnetic skyrmions investidated by stroboscopic small-angle neutron scattering
Phys. Rev. B **98** 014424 (2018)

152 H. Okabe, M. Hiraishi, S. Takeshita, A. Koda, K.M. Kojima, and R. Kadono
Local electronic structure of interstitial hydrogen in iron disulfide
Phys. Rev. B **98** 075210 (2018)

153 P. Wu, B. Zhang, K.L. Peng, M. Hagihala, Y. Ishikawa, M. Kofu, S.H. Lee, H. Kumigashira, C.S. Hu, Z.M. Qi, K. Nakajima, G.Y. Wang, Z. Sun, and T. Kamiyama
Investigation of the electronic structure and lattice dynamics of the thermoelectric material Na-doped SnSe
Phys. Rev. B **98** 094305 (2018)

154 S. Lee, M.-C. Lee, Y. Ishikawa, P. Miao, S. Torii, C.J. Won, K.D. Lee, N. Hur, D.-Y. Cho, and T. Kamiyama
Magnetoelastic octahedral breathing mode in the ferrimagnetic La_2CoIrO_6 double perovskite
Phys. Rev. B **98** 104409 (2018)

155 S. Torigoe, T. Hattori, K. Kodama, T. Honda, H. Sagayama, K. Ikeda, T. Otomo, H. Nitani, H. Abe, H. Murakawa, H. Sakai, and N. Hanasaki
Nanoscale ice-type structural fluctuation in spinel titanates
Phys. Rev. B **98** 134443 (2018)

156 H. Tamatsukuri, H. Hiraka, K. Ikeuchi, S. Iimura, Y. Muraba, M. Nakamura, H. Sagayama, J. Yamaura, Y. Murakami, Y. Kuramoto, and H. Hosono
Gapless magnetic excitation in a heavily electron-doped antiferromagnetic phase of $LaFeAsO_{0.5}D_{0.5}$
Phys. Rev. B **98** 174415 (2018)

157 T. Moyoshi, K. Kamazawa, M. Matsuda, and M. Sato
Inelastic neutron scattering study on the electronic transition in $(Pr_{1-y}Y_y)_{1-x}Ca_xCoO_3$ single crystals
Phys. Rev. B **98** 205105 (2018)

158 T. Okudaira, S. Takada, K. Hirota, A. Kimura, M. Kitaguchi, J. Koga, K. Nagamoto, T. Nakao A. Okada, K. Sakai, H.M. Shimizu, T. Yamamoto, and T. Yoshioka
Angular distribution of γ rays from neutron-induced compound states of 140La
Phys. Rev. C **97** 034622 (2018)

159 C.C. Haddock, N. Oi, K. Hirota, T. Ino, M. Kitaguchi, S. Matsumoto, K. Mishima, T. Shima, H.M. Shimizu, W.M. Snow, and T. Yoshioka
A Search for deviations from the inverse square law of gravity at nm range using a pulsed neutron beam
Phys. Rev. D **97** 062002 (2018)

160 R. Inoue, T. Kanaya, T. Yamada, K. Shibata, and K. Fukao
Experimental investigation of the glass transition of polystyrene thin films in a broad frequency range
Phys. Rev. E **97** 012501 (2018)

161 T. Xie, D.L. Gong, H. Ghosh, A. Ghosh, M. Soda, T. Masuda, S. Itoh, F. Bourdarot, L.-P. Regnault, S. Danilkin, S.L. Li, and H.Q. Luo
Neutron Spin Resonance in the 112-Type Iron-Based Superconductor
Phys. Rev. Lett. **120** 137001 (2018)

162 T. Xie, Y. Wei, D.L. Gong, T. Fennell, U. Stuhr, R. Kajimoto, K. Ikeuchi, S.L. Li, J.P. Hu, and H.Q. Luo
Odd and Even Modes of Neutron Spin Resonance in the Bilayer Iron-Based Superconductor $CaKFe_4As_4$
Phys. Rev. Lett. **120** 267003 (2018)

163 K. Kurashima, T. Adachi, K.M. Suzuki, Y. Fukunaga, T. Kawamata, T. Noji, H. Miyasaka, I. Watanabe, M. Miyazaki, A. Koda, R. Kadono, and Y. Koike
Development of Ferromagnetic Fluctuations in Heavily Overdoped $(Bi,Pb)_2Sr_2CuO_{6+\delta}$ Copper Oxides
Phys. Rev. Lett. **121** 057002 (2018)

164 J. Sugiyama, I. Umegaki, H. Nozaki, W. Higemoto, K. Hamada, S. Takeshita, A. Koda, K. Shimomura, K. Ninomiya, and M.K. Kubo
Nuclear magnetic field in solids detected with negative-muon spin rotation and relaxation
Phys. Rev. Lett. **121** 087202 (2018)

165 Y. Sakaguchi, T. Hanashima, H. Aoki, H. Asaoka, A.-A.A. Simon, and M. Mitkova
Kinetics of Silver Photodiffusion Into Amorphous $Ge_{20}S_{80}$ Films: Case of Pre-Reaction
Phys. Status Solidi A **215** 1800049 (2018)

166 K. Ohoyama and K. Hayashi
White Neutron Holography in Pulsed Neutron Facilities
Phys. Status Solidi B **255** 1800143 (2018)

167 D. Ueta, T. Kobuke, M. Yoshida, H. Yoshizawa, Y. Ikeda, S. Itoh, and T. Yokoo
Crystalline electric field level scheme of the non-centrosymmetric $CePtSi_3$
Physica B **536** 21–23 (2018)

168 M. Yoshida, D. Ueta, Y. Ikeda, T. Yokoo, S. Itoh, and H. Yoshizawa
Magnetic and thermodynamic studies on the charge and spin ordering in the highly hole-doped $La_{2-x}Sr_xCoO_4$
Physica B **536** 338–341 (2018)

169 K. Matsuura, H. Sagayama, A. Uehara, Y. Nii, R. Kajimoto, K. Kamazawa, K. Ikeuchi, S. Ji, N. Abe, and T. Arima
Magnetic excitations in the orbital disordered phase of MnV_2O_4
Physica B **536** 372–376 (2018)

170 K. Ikeuchi, T. Kikuchi, K. Nakajima, R. Kajimoto, S. Wakimoto, and M. Fujita
Detailed study of the structure of the low-energy magnetic excitations in overdoped $La_{1.75}Sr_{0.25}CuO_4$
Physica B **536** 717–719 (2018)

171 Z.J. Tan, P. Miao, X.H. Lin, S. Lee, Y. Ishikawa, M. Hagihala, S. Torii, Y.X. Wang, M. Yonemura, and T. Kamiyama
The investigation of magnetic phase transition in cobaltite perovskites byhigh-resolution neutron powder diffraction under 14 T magnetic field
Physica B **551** 111–114 (2018)

172 K. Nakajima and R. Kajimoto
High-energy magnetic excitations in lightly oxygen-doped lanthanum nickel oxides
Physica B **551** 142–145 (2018)

173 K. Hiroi, T. Shinohara, H. Hayashida, J.D. Parker, Y.H. Su, K. Oikawa, T. Kai, and Y. Kiyanagi
Study of the magnetization distribution in a grain-oriented magnetic steel using pulsed polarized neutron imaging
Physica B **551** 146–151 (2018)

174 M. Hirai, S. Ajito, M. Sugiyama, H. Iwase, S. Takata, N. Shimizu, N. Igarashi, A. Martel, and L. Porcar
Macromolecular crowding effect on protein structure and hydration clarified by using X-ray and neutron scattering
Physica B **551** 212–217 (2018)

175 S. Itoh, T. Hawai, S. Ibuka, T. Yokoo, and Y. Endoh
Magnetic excitations in metallic antiferromagnets $Fe_{0.5}Mn_{0.5}$ *and* $Fe_{0.7}Mn_{0.3}$
Physica B **551** 21–23 (2018)

176 N.L. Yamada, M. Sferrazza, and S. Fujinami
In-situ measurement of phospholipid nanodisk adhesion on a solid substrate using neutron reflectometry and atomic force microscopy
Physica B **551** 222–226 (2018)

177 S. Ajito, M. Hirai, H. Iwase, N. Shimizu, N. Igarashi, and N. Ohta
Protective action of trehalose and glucose on protein hydration shell clarified by using X-ray and neutron scattering
Physica B **551** 249–255 (2018)

178 K. Akutsu, M. Cagnes, T. Niizeki, Y. Hasegawa, and T.A. Darwish
Penetration behavior of an ionic liquid in thin-layer silica coating: Ionic liquid deuteration and neutron reflectivity analysis
Physica B **551** 262–265 (2018)

179 M. Mizusawa, K. Sakurai, D. Yamazaki, and M. Takeda
An electrochemical cell with vertical geometry for neutron reflectivity measurements
Physica B **551** 270–273 (2018)

180 J. Abe, K. Sekine, S. Harjo, T. Kawasaki, and K. Aizawa
Effect of gauge volume on strain measurement in rock materials using time-of-flight neutron diffraction
Physica B **551** 283–286 (2018)

181 Y. Kawakita, T. Kikuchi, Y. Inamura, S. Tahara, K. Maruyama, T. Hanashima, M. Nakamura, R. Kiyanagi, Y. Yamauchi, K. Chiba, S. Ohira-Kawamura, Y. Sakaguchi, H. Shimakura, R. Takahashi, and K. Nakajima
Anomaly of structural relaxation in complex liquid metal of bismuth - Dynamic correlation function of coherent quasi-elastic neutron scattering -
Physica B **551** 291–296 (2018)

182 M. Nakamura, T. Kikuchi, K. Kamazawa, and Y. Kawakita
Phonon dynamics of NaI investigated by G(r, E) analysis
Physica B **551** 351–354 (2018)

183 K. Iwasa, T. Onimaru, T. Takabatake, R. Higashinaka, Y. Aoki, S. Ohira-Kawamura, and K. Nakajima
Inelastic neutron scattering study on 4 f -electron multipole system $PrTr_2X_{20}$ *(Tr : transition metal, X : Al and Zn)*
Physica B **551** 37–40 (2018)

184 W.R. Puspita, H. Takeya, T. Mochiku, Y. Ishikawa, S. Lee, S. Torii, M. Yonemura, and T. Kamiyama
Temperature Dependence of Structural Disorder in Thermoelectric Clathrate $Ba_8Al_{16}Ge_{30}$
Physica B **551** 41–45 (2018)

185 K. Sakurai, M. Mizusawa, J. Jiang, and T. Ito
Hadamard coding of time-of-flight neutron reflectogram at grazing incidence
Physica B **551** 426–430 (2018)

186 K. Oikawa, Y.H. Su, R. Kiyanagi, T. Kawasaki, T. Shinohara, T. Kai, K. Hiroi, S. Harjo, J.D. Parker, Y. Matsumoto, H. Hayashida, S.Y. Zhang, Y. Tomota, and H. Sato
Recent progress on practical materials study by Bragg edge imaging at J-PARC
Physica B **551** 436–442 (2018)

187 N. Miyata and T. Miyazaki
Relatively thick (few micrometers) film structure estimated by back-incidence neutron reflectometry
Physica B **551** 449–451 (2018)

188 Y. Ishikawa, J.R. Zhang, R. Kiyanagi, M. Yonemura, T. Matsukawa, A. Hoshikawa, T. Ishigaki, S. Torii, R. Oishi-Tomiyasu, and T. Kamiyama
Z-MEM, Maximum Entropy Method software for electron/nuclear densitydistribution in Z-Code
Physica B **551** 472–475 (2018)

189 M. Nakamura, W. Kambara, K. Iida, R. Kajimoto, K. Kamazawa, K. Ikeuchi, M. Ishikado, and K. Aoyama
Performances of oscillating radial collimator for the Fermi chopper spectrometer 4SEASONS at J-PARC
Physica B **551** 480–483 (2018)

190 T. Kai, S. Sato, K. Hiroi, Y.H. Su, M. Segawa, J.D. Parker, Y. Matsumoto, H. Hayashida, T. Shinohara, K. Oikawa, and Y. Kiyanagi
Characteristics of the 2012 model lithium-6 time-analyzer neutron detector (LiTA12) system as a high efficiency detector for resonance absorption imaging
Physica B **551** 496–500 (2018)

191 H. Iwase, S. Takata, T. Morikawa, M. Katagiri, A. Birumachi, and J. Suzuki
Installation of a high-resolution position-sensitive scintillation detector in the small and wide angle neutron scattering instrument (TAIKAN), MLF, J-PARC
Physica B **551** 501–505 (2018)

192 Y. Seki, T. Shinohara, W. Ueno, J.D. Parker, and Y. Matsumoto
Effect of upstream beam collimation on neutron phase imaging with a Talbot-Lau interferometer at the RADEN beam line in J-PARC
Physica B **551** 512–516 (2018)

193 P. Wu, Y. Ishikawa, M. Hagihala, S. Lee, K.L. Peng, G.Y. Wang, S. Torii,

and T. Kamiyama
Crystal structure of high-performance thermoelectric materials by high resolution neutron powder diffraction
Physica B **551** 64–68 (2018)

194 S. Lee, S. Torii, Y. Ishikawa, M. Yonemura, T. Moyoshi, and T. Kamiyama
Weak-ferromagnetism of CoF$_3$ *and* FeF$_3$
Physica B **551** 94–97 (2018)

195 S. Satoh
Development of a Flat-Panel and Resistor-Type Photomultiplier Tube System for High Position-Resolution Two-Dimensional Neutron Detector
Plasma and Fusion Research **13** 2405056 (2018)

196 F.A. Mavuso, N.V. Mdlovu, K.-S. Lin, K. Ohishi, K. Dehvari, N.B. Mdlovu, and Y.-S. Lin
Synthesis and structural characterization of polymer-magnetic nanocomposites as carriers for drug delivery system
Proc. of 450th International Conference on Recent Advances in Medical Science (ICRAMS) (2018)

197 K. Moriyama, T. Nakatani, Y. Yasu, H. Ohshita, and T. Seya
Development of status analysis system based on ELK stack at J-PARC MLF
Proceedings of 16th Int. Conf. on Accelerator and Large Experimental Control Systems 1423–1427 (2018)

198 T. Kumada, K. Akutsu, K. Ohishi, Y. Kawamura, T. Morikawa, M. Sahara, J. Suzuki, and N. Torikai
Development of closed-cycle dynamic nuclear polarization system for small-angle neutron scattering and neutron reflectometry
Proceedings of Science **324** 9 (2018)

199 K. Akutsu, M. Sahara, T. Niizeki, S. Suzuki, Y. Hasegawa, M. Yoshii, A. Shimomura, and H. Komatsuzaki
Development of new waterproof thin-layers for the magnetic alloy core and structural study by neutron reflectometry
Proceedings of the 15th Annual Meeting of Particle Accelerator Society of Japan 1198–1201 (2018)

200 Y. Nakamura, A. Shibata, W. Gong, S. Harjo, T. Kawasaki, A. Ito, and N. Tsuji
In Situ Neutron Diffraction Study on Microstructure Evolution During Thermo-Mechanical Processing of Medium Manganese Steel
Proceedings of the International Conference on Martensitic Transformations: Chicago 155–158 (2018)

201 N. Tsuchida and S. Harjo
TRIP Effect in a Constant Load Creep Test at Room Temperature
Proceedings of the International Conference on Martensitic Transformations: Chicago 43–46 (2018)

202 N. Kawamura, M. Aoki, J. Doornbos, T. Mibe, Y. Miyake, F. Morimoto, Y. Nakatsugawa, M. Otani, N. Saito, Y. Seiya, K. Shimomura, A. Toyoda, and T. Yamazaki
New concept for a large-acceptance general-purpose muon beamline
Progress of Theoretical and Experimental Physics **2018** 113G01 (2018)

203 A. Sano-Furukawa, T. Hattori, K. Komatsu, H. Kagi, T. Nagai, J.J. Molaison, A.M. dos Santos, and C.A. Tulk
Direct observation of symmetrization of hydrogen bond in δ-AlOOH under mantle conditions using neutron diffraction
Scientific Reports **8** 15520 (2018)

204 M. Ishikado, S. Shamoto, K. Kodama, R. Kajimoto, M. Nakamura, T. Hong, and H. Mutka
High-energy spin fluctuation in low-Tc iron-based superconductor LaFePO$_{0.9}$
Scientific Reports **8** 16343 (2018)

205 M. Sales, M. Strobl, T. Shinohara, A. Tremsin, L.T. Kuhn, W.R.B. Lionheart, N.M. Desai, A.B. Dahl, and S. Schmidt
Three Dimensional Polarimetric Neutron Tomography of Magnetic Fields
Scientific Reports **8** 2214 (2018)

206 V. Ukleev, S. Suturin, T. Nakajima, T.-H. Arima, T. Saerbeck, T. Hanashima, A. Sitnikova, D. Kirilenko, N. Yakovlev, and N. Sokolov
Unveiling structural, chemical and magnetic interfacial peculiarities in ε-Fe$_2$O$_3$*/GaN (0001) epitaxial films*
Scientific Reports **8** 8741 (2018)

207 R. Kajimoto, M. Nakamura, N. Murai, S. Shamoto, T. Honda, K. Ikeda, T. Otomo, H. Hata, T. Eto, M. Noda, H. Kuwahara, and T. Okuda
Elastic and dynamical structural properties of La and Mn-doped SrTiO$_3$ *studied by neutron scattering and their relation with thermal conductivities*
Scientific Reports **8** 9651 (2018)

208 K. Kataoka, H. Nagata, and J. Akimoto
Lithium-ion conducting oxide single crystal as solid electrolyte for advanced lithium battery application
Scientific Reports **8** 9965 (2018)

209 B. Wang, H.Y. He, M. Naeem, S. Lan, S. Harjo, T. Kawasaki, Y.X. Nie, H.W. Kui, T. Ungár, D. Ma, A.D. Stoica, Q. Li, Y.B. Ke, C.T. Liu, and X.L. Wang
Deformation of CoCrFeNi high entropy alloy at large strain
Scripta Materialia **155** 54–57 (2018)

210 J.-J. Kang, T.-Y. Yang, Y.-K. Lan, W.-R. Wu, C.-J. Su, S.-C. Weng, N.L. Yamada, A.-C. Su, and U.-S. Jeng
Directed Vertical Diffusion of Photovoltaic Active Layer Components into Porous ZnO-based Cathode Buffer Layers
Small **14** 1704310 (2018)

211 H. Tanoue, K. Inoue, N.L. Yamada, K. Kohzo, S. Miyao, T. Ishizone, and H. Yokoyama
Thermoresponsive Dynamic Polymer Brush Fabricated by the Segregation of Amphiphilic Diblock Copolymers
Soft matter **14** 5930–5935 (2018)

212 N. Ishida, K. Miyazawa, N. Kitamura, J. Akimoto, and Y. Idemoto
Average and local structure analysis of metastable Li$_x$Mn$_{0.9}$Ti$_{0.1}$O$_2$ *by synchrotron X-ray and neutron sources*
Solid State Ionics **325** 209–213 (2018)

Editorial Board - MLF Annual Report 2018

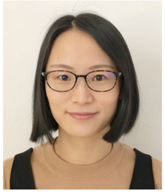

Chief Editor
Yuhua Su
Technology Development Section

Tazuko Mizusawa
CROSS

Jun Abe
CROSS

Yukinori Nagatani
Muon Science Section

Akinori Hoshikawa
Ibaraki University

Takashi Naoe
Neutron Source Section

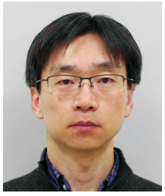

Kazutaka Ikeda
Neutron Science Section

Kenichi Oikawa
Neutron Science Section

Yoshihisa Ishikawa
CROSS

Kaoru Sakasai
Neutron Instrumentation Section

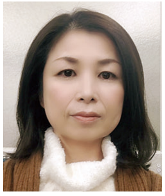

Yukiko Nagai
Technology Development Section

J-PARC

JAPAN PROTON ACCELERATOR RESEARCH COMPLEX

High Energy Accelerator Research Organization (KEK)
Japan Atomic Energy Agency (JAEA)

http://j-parc.jp/

Materials and Life Science Division
J-PARC Center

https://mlfinfo.jp/en

CROSS
Comprehensive Research Organization for Science and Society

https://neutron.cross.or.jp/en